Mechanisms of Adipocyte Loss in Familial Partial Lipodystrophy 2

by

Jessica Nanda Maung

A dissertation submitted in partial fulfillment
of the requirements for the degree of
Doctor of Philosophy
(Molecular and Integrative Physiology)
in the University of Michigan
2025

Doctoral Committee:

Professor Ormond A. MacDougald, Chair
Professor Carey N. Lumeng
Professor Elif A. Oral
Professor Yatrik Shah

Jessica Nanda Maung

jmaung@umich.edu

ORCID iD: 0000-0003-4289-0614

© Jessica Nanda Maung 2025

Dedication

This doctoral dissertation is dedicated to my sister, Hannah Maung, who is my best friend and light of my world. It is also dedicated to my father, Min Maung and my mother, Meritje Maung, who sacrificed everything to immigrate to the United States and provide me and Hannah with the best resources, education, and support. Finally, this dissertation is dedicated to my fiancé and future husband, David Cahana, who is my unwavering rock and companion. This accomplishment is shared by all of us, as I would not be here without any of you.

Acknowledgements

First, I want to acknowledge and thank my doctoral advisor, Dr. Ormond MacDougald. Thank you for teaching me how to be a scientist and a "seeker of truth." Your mentorship has instilled confidence in me as I have navigated learning how to design rigorous experiments and push the limits of creativity. Thank you for helping me grow into a self-assured and outspoken leader, and for encouraging me to take initiative in everything I do. Your constant emphasis on perseverance, resilience, and adaptability have taught me how to "function at the level of a Ph.D." ☺ We have spent many hours editing papers and grants, scratching our heads at puzzling mouse phenotypes, and debating the best next experiments to perform. These writing and brainstorming sessions have been challenging, humbling, and rewarding, and I will fondly remember these times that we laughed (and cursed) together. This Ph.D. would not have been possible without your guidance, so thank you.

Thank you to my committee members and academic mentors for shaping me professionally and personally (and for writing the endless recommendation letters ☺) Thank you to Dr. Elif Oral for providing a helpful clinical perspective and focusing our attention on the bigger picture. Your passion has been incredibly inspirational, and your excitement and joy are contagious. Thank you to Dr. Carey Lumeng for your insights: I always looked forward to your perspectives at our committee meetings and thank you for your generosity in offering assistance. Finally, thank you to Dr. Yatrik Shah: thank you for offering extra time and help to work through any technical or scientific issues, and offering great career advice.

Next, I want to acknowledge my family: my sister, Hannah Maung, my dad, Min Maung, and my mom, Meritje Maung. Hannah, you have been my best friend and biggest cheerleader throughout life. Thank you for the endless FaceTimes and phone calls, often for hours on end. You are always there for me during my anxious and stressful moments, and to celebrate my accomplishments and wins. I am so thankful for your positivity, generosity, and humor, and I love you b. To Dad: thank you for your sacrifices, for pursing an education in the U.S. and setting us up for success and happiness, and for your support of me pursuing my dreams. To

Mom: thank you for your constant presence and sacrifices for us, especially during the hardest years. I always appreciate your enthusiasm about my research and Ph.D journey. I'm so proud of how far we have all come together.

An extra big thank you to my fiancé and future husband, David Cahana. We embarked on this journey together five years ago and had no idea what it was going to bring us. We are leaving here with a whole doctorate, two cats, and lots of memories. Your steady composure, kind and generous heart, hilarious dad jokes, and ability to pick me up on the hardest days has been instrumental in this pursuit. Thank you for always being there for me, I love you. Thank you to the Cahanas: Ida Rae and Michael for taking me in and cheering me on at every step, and to Sarit, Casper, and Lee for being very awesome future siblings-in-law.

To my lab mates: this dissertation would not have been completed without you, either. Your scientific input and constructive criticism are very appreciated, and helped make all my projects infinitely better. Thank you to Hiro and Ziru, who taught me all the bench and animal work skills that I know and were consistently encouraging and positive. Thank you to Romi for being a consistent light inside and outside the lab. I'm so glad we shared many years together through both happy and sad tears as sisters. I love that we celebrated all our scientific and personal accomplishments on sticky notes posted on the best office's door ☺ Thank you to Hadla to being a hilarious and iconic companion and one of the few who can match my drama. I will cherish our Lowertown dates, long animal room days, and our horrible wordplay that only we find funny. Thank you to Isabel for always being down for anything, like our adventures around Detroit watching live music and eating delicious food, and our constant chats about racism, the state of the world, and lab gossip. Thank you all the other MacLabbers throughout the years who have made the day-to-day super fun and bearable when things were hard.

To my MIP cohort: we entered our PhD program at the height of the COVID-19 pandemic, an incredibly difficult time. I'm very proud of how far we have all come. I'm thankful for our cohort hangouts and hilarious game nights where we could share our trials and tribulations. To my Michigan friends: you are all very special to me. Thank you for the memories at the MIP tailgates, bar crawls around town, and for eating lots of hot pot while chatting about life with me and David. Thank you for being there through absolutely everything! A special shout to my lifelong friends around the country and world – the constant FaceTime check-ins and girls' trips always filled my cup when I needed it the most.

A special acknowledgement to my funding sources: my doctoral work was funded by the Training Program in Organogenesis (T32 HD007505) and an NIH Predoctoral Individual National Research Service Award (F31 DK135181). Thank you to the MIP Grants Team for helping process all the administrative tasks and for answering my many questions. Thank you to Michele Boggs and Jeannie Worrall for your help in navigating the MIP program.

Thank you to the many mice that sacrificed their life for this dissertation. I did my very best to maximize your lives to further human health and scientific advancement, and it was a privilege and honor to be able to conduct animal work.

There are many more people not specifically mentioned here that were instrumental in this dissertation journey. A heartfelt thank you to every single one of you for your help and support.

Table of Contents

Dedication ii

Acknowledgements iii

List of Figures ix

Abstract xxiii

Chapter 1 Introduction 1

1.1 Adipose tissue is a key metabolic organ and contributes to whole-body metabolism 1

1.2 The paradox of too much versus too little adipose tissue 2

1.3 Familial partial lipodystrophy 2: prevalence and clinical characteristics 3

1.4 Lamins are regulators of nuclear function and gene expression 5

1.5 Laminopathies: diseases beyond FPLD2 caused by lamin A/C variants 9

1.6 Lamin A/C knockout studies to study fundamental roles of lamins 11

1.6.1 Lmna KO MEFs 11

1.6.2 Lamin KO in embryonic stem cells (ESCs), mesenchymal stem cells (MSCs), and other cellular models 13

1.6.3 Global Lmna KO mouse models 14

1.6.4 Tissue-specific Lmna KO mouse models 15

1.7 Studying disease mechanisms caused by *LMNA* variants 17

1.7.1 Pathogenic LMNA variants that cause laminopathies: structure and function relationship 17

1.7.2 LMNA R482 variants in vitro 19

1.7.3 Other LMNA variants in vitro 22

1.7.4 LMNA FPLD2 variants in vivo 24

1.7.5 Other laminopathy-causing LMNA variants in vivo 26

1.8 Human tissue experiments to study mechanisms of FPLD2 28

1.9 New studies to fill in existing knowledge gaps 29

1.10 Figures and legends..... 31

1.11 References..... 36

Chapter 2 Bridging Human and Mouse Lipodystrophy: The Requirement of Functional Lamin A/C for Adipocyte Homeostasis 45

2.1 Abstract..... 45

2.2 Introduction..... 46

2.3 Results..... 49

2.4 Discussion..... 65

2.5 Materials and methods 70

2.6 Figures and legends..... 84

2.7 References..... 104

Chapter 3 Effects of FGF21, Soluble TGFβR2, and Environmental Temperature on Metabolic Dysfunction in Lipodystrophic Mice 108

3.1 Abstract..... 108

3.2 Introduction..... 109

3.3 Results..... 112

3.4 Discussion..... 120

3.5 Materials and methods 125

3.6 Figures and legends..... 131

3.7 References..... 148

Chapter 4 Creation and Characterization of Novel Pathogenic *Lmna* Variant Mouse Lines 152

4.1 Abstract..... 152

4.2 Introduction..... 153

4.3 Results 156
4.4 Discussion 165
4.5 Materials and methods 169
4.6 Figures and legends 173
4.7 References 193
Chapter 5 Discussion and Future Perspectives 196
5.1 Molecular basis of shared transcriptomic signatures in lipodystrophic WAT 197
5.2 Other unexplored potential mechanisms of adipocyte loss in FPLD2 201
5.3 How do *Lmna*-deficient adipocytes eventually disappear and die? 203
5.4 Is FGF21/sTGFBR2 gene treatment a viable option for patients with FPLD2? 204
5.5 Impaired exercise capacity in *Lmna* T10I variant mice 206
5.6 How can we trigger lipodystrophy in *Lmna* variant mice? 209
5.7 Final remarks 210
5.8 References 212

List of Figures

Figure 1.1. Adipose tissue is a key metabolic organ, and obesity and lipodystrophy are caused by an imbalance of adipose tissue amount and impaired function. (**A**) White adipose tissue (WAT) is the most abundant type of adipose tissue in the body, comprised of multiple cell types beyond adipocytes like adipose stem and progenitor cells (ASPCs), immune cells like macrophages and T cells, and endothelial and lymphatic endothelial cells (LECs). WAT has multiple key functions including storing energy in the form of triacylglycerols (TAGs) and orchestrating lipid uptake and breakdown. WAT is also an endocrine organ, and secretes many adipokines like leptin, adiponectin, and adipsin, along with fatty acid binding protein 4 (FABP4) and fatty acid esters of hydroxy fatty acids (FAHFAs). These adipokines and other cytokines (interleukin 6 (IL-6), tumor necrosis factor alpha (TNFα) and C-C motif chemokine ligand 2 (CCL2)) can crosstalk with other organs like the brain, liver, and heart to influence metabolism. (**B**) Obesity is caused by excess adipose tissue, which causes WAT to become overloaded with lipid, unable to expand further, which causes ectopic lipid deposition and metabolic dysfunction. Lipodystrophy, a rare disease that causes a loss of adipose tissue, leads to the same deficiency in a safe lipid storage depot, causing the same metabolic dysfunction as observed in obesity. Figure adapted from Lim et al. 2021. 31

Figure 1.2. Familial partial lipodystrophy 2 (FPLD2) is caused by mutations in LMNA, leading to adipose tissue loss and redistribution and many clinical features, including metabolic dysfunction and cardiac issues. (**A**) Patient with FPLD2 showing pattern of adipose tissue loss and redistribution. Picture from Akinci et al. 2018. (**B**) Dual energy X-ray absorptiometry (DEXA) scans of adipose tissue distribution in control patients or patients with FPLD2 (either harboring *LMNA* R482W or T528M variant. Red = areas of high adipose, yellow = areas of medium adipose, green = areas of low adipose tissue. Data from Araujo-Vilar et al. 2021. (**C**) Clinical features of FPLD2 affecting different peripheral and central organs. Data from Akinci et al. 2018. 32

Figure 1.3. Lamin A/C undergoes post-translational processing and modifications to be assembled into the nuclear lamina to influence nuclear stability and structure, and to associate with chromatin to affect gene expression. (**A**) The lamin A/C gene, *LMNA*, encodes both lamin A and lamin C, which are alternatively spliced. Prelamin A, the precursor to mature lamin A, undergoes multiple post-translational processing steps to reach its final form. Alternatively, lamin C is translated as its mature form without post-translational processing. (**B**) Both lamin A and C undergo multiple post-translational modifications including phosphorylation and acetylation to allow for normal function, data from review by Zheng et al. 2022. (**C**) Schematic of lamin A/C within the nucleus as part of the nuclear lamina. Lamin A/C interacts with nuclear pore complexes (NPCs) to control nuclear transport, with other transmembrane proteins like emerin and lamin B receptor (LBR), and indirectly with the cytoskeleton through the Linker of Nucleoskeleton and Cytoskeleton (LINC)

complex. Finally, lamin A/C interacts with chromatin at lamina-associated domains (LADs), typically gene-poor regions of heterochromatin. Figure adapted from Gaillard and Reddy 2018..... 33

Figure 1.4. Variants throughout LMNA cause a wide spectrum of laminopathy diseases beyond FPLD2. Map of amino acid mutations that cause different diseases in patients, like muscular dystrophy (pink), cardiomyopathy (yellow), lipodystrophy (green), neuropathy (orange), and progeria (gray). Boxes with two colors (e.g. yellow and green) indicate that *LMNA* variant causes both disease phenotypes. Variants with a black underline indicates published *in vitro* studies in the literature, and a magenta underline indicates *in vivo* studies. If variants are underlined with both black and magenta, both *in vitro* and *in vivo* studies are published. Adapted from Mckenna et al. 2013. 34

Figure 1.5. Summary of key literature findings about lamin A/C knockout (KO) and variant models. Many studies have explored the effects of *Lmna* KO in culture or *in vivo*, which leads to nuclear abnormalities, dysfunctional mitochondria, and premature death in mice. Variant studies investigating the common R482 residue site for mutations also show nuclear abnormalities *in vitro* along with reduced adipogenic capacity. Mouse models harboring the *Lmna* R482Q variant lose adipose tissue, albeit a mild phenotype, and have increased extracellular matrix (ECM) deposition in WAT. 35

Figure 2.1. **Clinical, metabolic, and molecular characterization of individuals with familial partial lipodystrophy type 2 (FPLD2).** (**A**) Study design and patient groups. Groups include unaffected family members (Control, Group C, n = 6), genetically affected but clinically unaffected individuals (Developing, Group B, n = 9), and patients with FPLD2 (FPLD2, Group A, n = 7). (**B**) Pedigrees from multiple families with FPLD2. Filled symbols represent affected individuals, open symbols indicate unaffected individuals, question marks denote unknown phenotypic status. (**C**) Images of patients with developing FPLD2 with early signs of fat redistribution. (**D**) Images of patients with FPLD2 phenotypes with peripheral lipoatrophy and upper trunk fat accumulation. (**E**) Whole body fat shadows. Quantification of fat mass percentage in (**F**) total body, (**G**) leg, and (**H**) trunk. (**I**) Magnetic resonance imaging (MRI)-based hepatic fat fraction maps with (**J**) quantification. (**K**) Hemoglobin A1c percentages. (**L**) Triglyceride concentrations. (**M**) Non-esterified fatty acid (NEFA) concentrations. (**N**) Homeostatic Model Assessment for Insulin Resistance (HOMA-IR) scores. (**O**) Leptin concentrations. (**P**) Adiponectin concentrations. (**Q**) Fibroblast growth factor 21 (FGF21) concentrations. Data are represented as mean ± SD. *P < 0.05. Statistical analyses were performed using one-way ANOVA, followed by Bonferroni's post-hoc test 84

Figure 2.2. Biopsies from patients with FPLD2 have no change in adipocyte size, but bulk RNA-sequencing suggests decreased metabolism and increased inflammation in patient adipose tissue. (**A**) Representative adipose tissue histological images and Picrosirius Red-stained tissue for collagens from biopsies across patient groups in abdominal biopsies. (**B**) Frequency distribution of adipocyte size and (**C**) frequency of adipocytes less or greater than 2500 μm^2 from abdominal biopsies. (**D**) Histological images and Picrosirius Red analyses on upper neck biopsies. (**E**) Frequency distribution of adipocyte size and (**F**) frequency of adipocytes less or greater than 2500 μm^2 from upper neck biopsies. Bulk RNA-sequencing on patient biopsies. Biopsies from Group A and B were combined to compare to Group C. n = 4-5

samples (upper neck and abdomen combined) per group. Gene set enrichment analysis (GSEA) identified (**G**) up and (**H**) downregulated pathways with normalized enrichment scores (NES). Data are represented as mean ± SD. *P < 0.05. Statistical analyses were performed using two-way ANOVA, followed by Bonferroni's post-hoc test. 85

Figure 2.3. Single nuclei RNA-sequencing identifies changes in cell proportions and subclustering analyses between subcutaneous abdomen and upper neck adipose tissue in unaffected patients. (**A**) Uniform Manifold Approximation and Projection (UMAP) of abdomen and upper neck biopsies across all patient groups (A, B and C); ASPC = adipose stem and progenitor cells, LEC = lymphatic endothelial cells. (**B**) Marker genes for each cell population. (**C**) Permutation tests to identify changes in cell proportions in the upper neck relative to the abdominal biopsies from control patients (Group C); changes were statistically significant if the log2fold change was less or greater than 0.32, and the false discovery rate (FDR) was less than 0.05. (**D**)Adipocyte subclusters and corresponding GSEA pathways. (**E**) Adipocyte subclusters changes between the upper neck and abdomen in control patients. (**F**) ASPC subclusters with GSEA pathways. (**G**) ASPC subcluster changes in the upper neck relative to abdomen. (**H**) Macrophage subclusters with GSEA pathways. (**I**) Subcluster changes in macrophages in upper neck relative to abdomen. (**J**) T cell subclusters with GSEA pathways. (**K**) Subcluster changes in T cells in upper neck relative to abdomen. 86

Figure 2.4. Single nuclei RNA-sequencing identifies changes in cell proportions and identity with progression of FPLD2. (A) UMAP of combined upper neck and abdomen biopsies across disease states; cell type markers are the same as in Figure 3. Permutation tests identified changes in cell proportion from abdominal biopsies from patients with (**B**) developing FPLD2 and (**C**) FPLD2 relative to control, and from upper neck biopsies in (**D**) developing FPLD2 and (**E**) FPLD2 relative to control. Cell proportion changes in the upper neck relative to abdomen were identified in (**F**) developing and (**G**) FPLD2 disease states. (**H**) All adipocytes from developing or FPLD2 biopsies were analyzed via GSEA and compared to controls to identify population-level changes in cell identity. Sig = signaling; Org = organization. (**I**) Adipocyte subcluster analyses with corresponding GSEA pathways (same as in Figure 3) and subcluster changes with disease. (**J**) ASPC GSEA in developing or FPLD2 biopsies relative to controls. (**K**) ASPC subcluster changes with disease. (**L**) Macrophage GSEA in developing or FPLD2 biopsies relative to controls. (**M**) Macrophage subcluster changes with disease. 87

Figure 2.5. Tamoxifen-inducible adipocyte-specific *Lmna* knockout causes transient adipose tissue loss, and *Lmna*-deficient adipocytes shrink and disappear. All data from male mice besides histology from female mice. (**A**) Gene schematic of $Lmna^{fl/fl}$ control mice and $Lmna^{iADKO}$ inducible *Lmna* adipocyte-specific knockout mice. Adult mice were administered tamoxifen intraperitoneally (i.p.) for five consecutive days to induce recombination. (**B**) Fat mass after tamoxifen administration (n = 6). (**C**) Posterior subcutaneous white adipose tissue (psWAT) weights and (**D**) epididymal white adipose tissue (eWAT) weights at two-, four-, and 16-weeks post-tamoxifen (n = 3-6). (**E**) Representative histology of psWAT and gonadal WAT (gWAT) two weeks post-tamoxifen. Scale bar = 40 μm. (**F**) Insulin tolerance test (ITT) six weeks post-tamoxifen (n = 6). (**G**) Glucose tolerance test (GTT) seven weeks post-tamoxifen (n = 6). (**H**) Serum adiponectin immunoblot at zero- and four-weeks post-tamoxifen (n = 4-5). (**I**) Schematic of mTmG reporter system induced by tamoxifen-

mediated Cre activity. (**J**) Representative fresh confocal micrographs of psWAT and (**K**) quantification of psWAT adipocyte size at two-weeks post-tamoxifen (n = 3-4). (**L**) Quantification of psWAT GFP+ or tdTomato+ adipocytes. (**M**) Confocal micrographs of eWAT and (**N**) quantification of eWAT adipocyte size at two weeks post-tamoxifen. (**O**) Quantification of eWAT GFP+ or tdTomato+ adipocytes. Data are represented as mean ± SD. *P < 0.05. Statistical analyses were performed using two-way ANOVA, followed by Bonferroni's post-hoc test. 88

Figure 2.6. Bulk RNA-sequencing and proteomics of *Lmna*^{iADKO} WAT reveals increased inflammation and reduced fatty acid metabolism and mitochondrial pathways, similar to human FPLD2 biopsies. *Lmna*^{iADKO} and *Lmna*$^{fl/fl}$ parametrial white adipose tissue (pmWAT) two-weeks post-tamoxifen was used for RNA-sequencing (n = 6-7) and proteomics (n = 5). (**A**) Integrative GSEA on bulk RNA-sequencing (RNA-seq) and proteomics. Pink dots symbolize that NES were significantly changed in both RNA-seq and proteomics datasets, orange dots = NES only changed in proteomics, blue = NES only changed in RNA-seq. (**B**) Highlighted GSEA pathways changed in both proteomics and RNA-seq. Numbers on bars represent number of overlapping genes driving pathways. (**C**) Highlighted GSEA pathways changed in proteomics only. Heatmaps showing selected changes in genes driving (**D**) lipid biosynthesis, (**E**) mitochondrial function, (**F**) inflammation, and (**G**) cell death. (**H**) Integrative GSEA of *Lmna*^{iADKO} pmWAT bulk RNA-seq compared to FPLD2 bulk RNA-seq (Figure 2). (**I**) Highlighted GSEA pathways changed in both mouse and human RNA-seq datasets. 89

Figure 2.7. *Lmna*^{iADKO} adipocytes have reduced oxygen consumption and dysfunctional mitochondrial dynamics and structure. Immunoblot analyses two-weeks post-tamoxifen of lipid metabolism and lipogenesis proteins in (**A**) psWAT and (**B**) eWAT (n = 4-5). (**C**) Immunoblot of mitochondrial proteins in eWAT two-weeks post-tamoxifen (n = 4-5). Oroboros Oxygraph-2k analyses of (**D**) baseline and (**E**) maximum respiration in floated adipocytes from pmWAT two-weeks post-tamoxifen (n = 6). (**F**) Immunoblot of mitochondrial function and dynamics proteins in floated adipocytes and stromal vascular fraction (SVF) from pmWAT two-weeks post-tamoxifen (n = 3-5). * indicates non-specific band. (**G**) Confocal micrographs of floated adipocytes from pmWAT stained for nuclei (Hoechst), lipid (BODIPY), and mitochondria (MitoTracker Red) and (**H**) Transmission electron micrographs of eWAT two-weeks post-tamoxifen. Scale bar = 1 μM for 3000x; 200 nm for 10000x magnification images. Data are represented as mean ± SD. *P < 0.05. Statistical analyses were performed using Student's t-test. 90

Figure 2.8. *Lmna* KO mouse embryonic fibroblasts (MEFs) and adipocytes have shared patterns of altered gene expression, correlated with changes in chromatin accessibility. (**A**) Schematic of dataset integration between *Lmna*^{iADKO} pmWAT RNA-seq and *Lmna* KO MEFs microarray and Assay for Transposase-Accessible Chromatin (ATAC)-seq. Overlapping changed genes in RNA-seq of *Lmna*^{iADKO} WAT (iADKO), *Lmna* KO MEF microarray (MEF) and *Lmna* KO MEF ATAC-seq (ATAC) were identified, and GSEA was ran to identify changes in (**B**) lipid metabolism Gene Ontology (GO) terms with their corresponding (**C**) overlapping leading edge genes, along with (**D**) inflammatory GO terms with (**E**) corresponding overlapping leading edge genes. (**F**) Distribution of chromatin features represented by percentage of overall chromatin composition compared between *Lmna* control (CTRL) and KO MEF ATAC-seq. (**G**) Enriched motifs in *Lmna* KO MEFs, stratified into four

bins based on microarray gene expression changes, from most downregulated to most upregulated. (**H**) ATAC-seq signal tracks and visualization of significantly enriched regions and their predicted target genes. Red lines represent enhancers with a positive fold change upon *Lmna* KO, and blue lines are negative. 91

Figure 3.1. FGF21/sTGFBR2 reduces body weight, improves insulin sensitivity, and reduces plasma TAG in high fat diet-fed mice, with greatest effects in mice housed at 26°C and 30°C. (**A**) Schematic illustration of housing conditions and experimental timeline. (**B**) Concentrations of FGF21 in plasma pre-transduction (Pre) and at euthanasia (Euth). (**C**) Concentrations of sTGFBR2 in plasma 3, 5, 7, and 9 weeks after transduction. Body weight over time in 60% HFD-fed female mice housed at (**D**) 22°C, (**E**) 26°C, or (**F**) 30°C (n = 6-7). Insulin tolerance tests (0.75 U/kg) in mice housed at (**G**) 22°C, (**H**) 26°C, or (**I**) 30°C (n = 6-7), data presented as mean ± SEM. #Mice in (E) were given intraperitoneal glucose because their blood glucose concentrations dropped below 30 mg/dL. (**J**) Plasma TAG concentrations eight weeks post-treatment in mice housed at 22°C, 26°C, or 30°C (n = 6-7). *P < 0.05. Statistical analyses were performed using two-way ANOVA, followed by Bonferroni's post-hoc test. ... 131

Figure 3.2. FGF21/sTGFBR2 decreases adiposity and plasma insulin concentrations, with highest efficacy at housing temperatures of 26°C and 30°C. Female mice were euthanized ten weeks after transduction with FGF21/sTGFBR2 (n = 5-7). (**A**) Body weight of mice transduced with FGF21/sTGFBR2 at euthanasia. (**B**) Posterior subcutaneous white adipose tissue (psWAT) and (**C**) brown adipose tissue (BAT) weights. (**D**) Representative histological images of mouse BAT stained with H&E. Scale bar = 50 μm. Fed (**E**) blood glucose concentrations, (**F**) plasma TAG and (**G**) insulin concentrations prior to euthanasia. Tibial (**H**) cortical thickness (Ct.Th), (**I**) cortical area (Ct.Ar), and (**J**) cortical bone volume fraction (Ct.BV/TV) analyzed via nanoCT. *P < 0.05. Statistical analyses were performed using two-way ANOVA, followed by Bonferroni's post-hoc test. 132

Figure 3.3. FGF21/sTGFBR2 decreases liver weights and hepatic steatosis, with highest efficacy at housing temperatures of 26°C and 30°C. (**A**) Liver weights in vehicle and FGF21/sTGFBR2 treated mice at all housing temperatures ten weeks after transduction (n = 6-7). (**B**) Liver TAG concentration normalized to protein amount (n = 6-7). (**C**) Representative histological images of mouse livers stained with H&E. Scale bar = 50 μm. (**D**) Representative images of mouse livers stained with Picrosirius Red to identify collagen. Scale bar = 50 μm. *P < 0.05. Statistical analyses were performed using two-way ANOVA, followed by Bonferroni's post-hoc test. 133

Figure 3.4. Adipose tissue is required for FGF21/sTGFBR2 to mediate metabolic improvements at thermoneutrality. (**A**) Schematic illustration of housing conditions and experimental timeline; $Lmna^{Fl/Fl}$ = control mice and $Lmna^{ADKO}$ = lipodystrophic mice. Plasma (**B**) FGF21 and (**C**) sTGFBR2 concentrations in mice 12 weeks after transduction (n = 4-7). (**D**) Body weight in vehicle and FGF21/sTGFBR2 mice four weeks after transduction (n = 5-7). (**E**) Fat and (**F**) lean mass measured by EchoMRI four weeks post-transduction (n = 4-7). (**G**) Plasma TAG, and (**H**) blood glucose concentrations four weeks post-treatment (n = 5-7). (**I**) Insulin tolerance tests (0.75 U/kg; n = 5-7), data presented as mean ± SEM. *P < 0.05. Statistical analyses were performed using two-way ANOVA, followed by Bonferroni's post-hoc test. 134

Figure 3.5. FGF21/sTGFBR2 does not improve metabolic dysfunction of lipodystrophic mice housed at thermoneutrality. Female mice were euthanized 12 weeks after FGF21/sTGFBR2 transduction (n = 4-7). (**A**) Body weight, (**B**) psWAT, (**C**) parametrial white adipose tissue (pmWAT), (**D**) BAT, (**E**) spleen, and (**F**) heart weights in mice at euthanasia. Fed (**G**) blood glucose, (**H**) plasma TAG, and (**I**) plasma insulin concentrations prior to euthanasia. (**J**) Representative tibial osmium-nanoCT images. (**K**) rBMAT normalized to marrow volume. (**L**) cBMAT normalized to marrow volume. *P < 0.05. Statistical analyses were performed using two-way ANOVA, followed by Bonferroni's post-hoc test. 135

Figure 3.6. FGF21/sTGFBR2 reduces liver weight, total hepatic TAG, and liver collagen deposition in lipodystrophic mice housed at 30°C. Female mice were euthanized 12 weeks after FGF21/sTGFBR2 transduction (n = 4-7). (**A**) Liver weights at euthanasia. (**B**) Liver TAG normalized to protein content. (**C**) TAG amount normalized to total liver weight. (**D**) Representative histological images of mouse livers stained with H&E. Scale bar = 50 μm. (**E**) Representative images of mouse livers stained with Picrosirius Red for collagen. Scale bar = 50 μm. (**F**) Machine learning quantification of area stained by Picrosirius Red in the liver. *P < 0.05. Statistical analyses were performed using two-way ANOVA, followed by Bonferroni's post-hoc test. 136

Figure 3.7. FGF21 improves insulin sensitivity of lipodystrophic mice housed at 22°C. (A) Schematic illustration of housing conditions and experimental timeline. (**B**) Plasma FGF21 concentrations eight weeks post-transduction (n = 3-16). (**C**) Body weight, (**D**) fat mass, and (**E**) lean mass measured by EchoMRI seven weeks post-transduction (n = 3-13). (**F**) Glucose tolerance test (1 mg/kg; n = 3-13), data presented as mean ± SEM. (**G**) Insulin tolerance test (0.75U/kg; n = 3-13), data presented as mean ± SEM. #Mice in (G) received intraperitoneal glucose because their blood glucose dropped below 30 mg/dL. Indirect calorimetry was measured for three days using the Promethion System. (**H**) Energy expenditure (EE) averaged during dark or light cycles, (**I**) fat oxidation averaged during the first four hours of dark or light cycles, and (**J**) distance traveled averaged during dark or light cycles. *P < 0.05. Statistical analyses were performed using two-way ANOVA, followed by Bonferroni's post-hoc test. ... 137

Figure 3.8. FGF21 does not improve metabolic dysfunction of lipodystrophic mice housed at 22°C. Female mice were euthanized eight weeks after FGF21 administration (n = 3-15). (**A**) Body weights, (**B**) psWAT, (**C**) pmWAT, (**D**) BAT, and (**E**) heart weights at euthanasia. Fed (**F**) blood glucose, (**G**) plasma TAG, (**H**) plasma insulin, and (**I**) plasma leptin concentrations prior to euthanasia. *P < 0.05. Statistical analyses were performed using two-way ANOVA, followed by Bonferroni's post-hoc test..... 138

Figure 3.9. FGF21 reduces liver weight, total hepatic TAG content, and liver collagen deposition in lipodystrophic mice housed at 22°C. Female mice were euthanized eight weeks after FGF21 administration (n = 3-15). (**A**) Liver weights at euthanasia. (**B**) Liver TAG normalized to protein content. (**C**) Total liver TAG normalized to liver weights. (**D**) Representative histological images of H&E-stained mouse livers. Scale bar = 50 μm. (**E**) Representative images of mouse livers stained with Picrosirius Red for collagen. Scale bar = 50 μm. (**F**) Machine learning quantification of area stained by Picrosirius Red in the liver. *P < 0.05. Statistical analyses were performed using two-way ANOVA, followed by Bonferroni's post-hoc test. 139

Figure 3.10. RNA-sequencing analyses of livers reveal that livers from lipodystrophic mice have increased cell proliferation and increased fibrosis, and that FGF21 treatment increases mitochondrial and translation pathways. (**A**) Summary of key GSEA pathways in hepatic mRNA of CTRL vs. ADKO mice eight weeks after treatment with FGF21 or vehicle. (**B**) GSEA pathways changed in CTRL mice dependent on treatment, padj<0.05. (**C**) GSEA pathways changed in ADKO mice dependent on treatment, padj<0.05. (**D**) GSEA pathways changed in vehicle-treated mice dependent on genotype, padj<0.05. (**E**) GSEA pathways changed in FGF21-treated mice dependent on genotype, padj<0.05. 140

Figure 4.1. Creation and validation of seven pathogenic *Lmna* variant mouse lines. (**A**) Schematic of lamin A/C and location of seven amino acid mutations knocked into mice. Sequencing validation of (**B**) T10I, (C) R482Q, (D) P485R, (E) K486N, (F) S573L, (G) N582H, (H) R584H, (I) R584H*. Some wobble sites in WT sequences were changed back to the normal WT sequence, as marked in red. R584H* has two base pair deletions and one substitution downstream of R584H mutation site..... 173

Figure 4.2. Body composition analyses of different *Lmna* variant lines revealed no changes in body weight, fat mass, or lean mass. All mice were on normal chow and housed at 22°C and were 20 weeks of age. +/+ = wildtype controls, m/+ = heterozygous, m/m = homozygous. (**A**) Body weight, (**B**) fat mass, and (**C**) lean mass in male and female *Lmna* T10I mice as measured by EchoMRI. (**D**) Body weight, (**E**) fat mass, and (**F**) lean mass in 10-week-old male and female *Lmna* R482Q mice. (**G**) Body weight, (**H**) fat mass, and (**I**) lean mass in 12-week-old *Lmna* P485R mice. (**J**) Body weight, (**K**) fat mass, and (**L**) lean mass in 16-week-old *Lmna* N582H mice. (**M**) Body weight, (**N**) fat mass, and (**O**) lean mass in 14-week-old *Lmna* R584H mice. All data represented as mean ± SD. Data were analyzed with two-way ANOVA with a Bonferroni post-hoc test. 174

Figure 4.3. *Lmna* T10I mice had no change in white adipose tissue (WAT) mass in males or females on normal chow (NC) or high-fat diet (HFD) at 22°C or 30°C. Necropsy data of male and female *Lmna* T10I mice on NC at 22°C at 20 weeks of age, including (**A**) fed glucose, (**B**) posterior subcutaneous white adipose tissue (psWAT) weights, (**C**) gonadal white adipose tissue (gWAT) weights, and (**D**) liver weights. Male mice were challenged with 60% HFD and housed at 30°C, and (**E**) fat mass and (**F**) lean mass were measured. Female mice were housed at 30°C, with their (**G**) fat mass and (**H**) lean mass measured. Data at euthanasia of T10I male mice at 26 weeks of age: (**I**) psWAT, epididymal white adipose tissue (eWAT), retroperitoneal white adipose tissue (rpWAT), perirenal white adipose tissue (prWAT), and brown adipose tissue (BAT), and (**J**) fasted triacylglycerol concentrations. Data at euthanasia of female T10I mice at 26 weeks of age of (**K**) adipose depots and liver, and (**L**) fasted triacylglycerol concentrations. All data represented as mean ± SD. Data were analyzed with two-way ANOVA with a Bonferroni post-hoc test. 175

Figure 4.4. No difference in adipocyte turnover rates but bulk RNA-seq analyses reveal *Lmna* T10I WAT has decreased adipogenic and skeletal muscle pathways, and increased protein translation and mTORC1 signaling pathways. Adiponectin-CreERT2 and mTmG background crossed with T10I mice: 24-week-old *Lmna* T10I WAT 12-weeks post-tamoxifen from male and female mice and imaged fresh via confocal of (**A**) psWAT and (**B**) gWAT, with quantification of GFP+ and tdTomato+ adipocytes in (**C**) and (**D**). Gene set enrichment

analysis (GSEA) of bulk RNA-seq performed on gWAT from male and female T10I mice housed at 22°C and 30°C, with comparisons of (**E**) T10I/+ vs. +/+ and (**F**) T10I/T10I vs. +/+. Numbers on bars are the number of genes driving each pathway. All data represented as mean ± SD. Data were analyzed with two-way ANOVA with a Bonferroni post-hoc test. 176

Figure 4.5. *Lmna* T10I homozygous mice run less voluntarily but have no impairment in muscle strength or forced running capacity. At 20 weeks of age, female *Lmna* T10I mice were placed in cages with running wheels, and (**A**) time ran per day, (**B**) distance ran per day, (**C**) average speed, and (**D**) maximum (max) speed was measured. (**E**) Total time ran over 30 days. (**F**) Total distance ran over 30 days. (**G**) Grip strength measurements in 24-week-old *Lmna* T10I mice. Uphill treadmill assay was performed on female *Lmna* T10I mice and (**H**) total run time, (**I**) max speed, and (**J**) total distance on treadmill was measured. A downhill treadmill assay was performed to cause muscle injury, and (**K**) run time, (**L**) max speed, and (**M**) distance ran was measured. All data represented as mean ± SD. Data were analyzed with two-way ANOVA with a Bonferroni post-hoc test. 177

Figure 4.6. Female *Lmna* T10I mice have decreased running activity, energy expenditure, and fat oxidation. At 20 weeks of age, mice were placed into SABLE Promethion cages for three days with a running wheel, data shown is from the third day of indirect calorimetry. (**A**) Distance ran on running wheel was measured over time. (**B**) Total distance ran on the third day. (**C**) Energy expenditure over time. (**D**) Average energy expenditure for the six middle hours of each light cycle on the third day. (**E**) Respiratory exchange ratio (RER) over time. (**F**) Average RER during the eight middle hours of each light cycle. (**G**) Fat oxidation measured over time. (**H**) Average fat oxidation for first four hours of each light cycle. All data represented as mean ± SD. Data were analyzed with two-way ANOVA with a Bonferroni post-hoc test. 178

Figure 4.7. Female *Lmna* T10I mice have decreased energy expenditure and fat oxidation during different metabolic stressors. Mice at 20 weeks of age were placed into SABLE Promethion cages for seven days, and metabolic responses to fasting, refeeding, and the indicated temperature changes were determined. All data was averaged over the full 12 hours of each light cycle. (**A**) Distance traveled. (**B**) Energy expenditure. (**C**) RER. (**D**) Fat oxidation. All data represented as mean ± SD. Data were analyzed with two-way ANOVA with a Bonferroni post-hoc test..... 179

Figure 4.8. *Lmna* R482Q mice do not have lipodystrophy when fed normal chow, HFD, or western-style diet (WSD). Male and female mice at 10 to 12 weeks of age on normal chow housed at 22°C were euthanized. (**A**) Body weight. (**B**) Fed glucose. (**C**) psWAT weights. (**D**) gWAT weights. Eight to 10-week-old male *Lmna* R482Q mice were challenged with 60% HFD at 26°C with measures of (**E**) body weight, (**F**) fat mass, and (**G**) lean mass. Eight to 10-week-old female *Lmna* R482Q mice were challenged with 60% HFD housed at 26°C and (**H**) body weight, (**I**) fat mass, and (**J**) lean mass determined. Male mice at 20 weeks of age were challenged with WSD at 26°C and (**K**) body weight, (**L**) fat mass, and (**M**) lean mass was measured. Female mice at 20 weeks of age were challenged with WSD at 26°C and (**N**) body weight, (**O**) fat mass, and (**P**) lean mass was measured. All data represented as mean ± SD. Data were analyzed with two-way ANOVA with a Bonferroni post-hoc test..... 180

Figure 4.9. Homozygous *Lmna* R482Q mice die by P14, and RNA-seq analyses of Lmna R482Q/+ adipocytes reveal decreased adipogenesis and metabolism pathways, and an increased inflammatory signature. Serum adiponectin in 10-12-week-old (**A**) female and (**B**) male mice. (**C**) Fed serum insulin concentrations in 10-12-week-old female mice. (**D**) Image of homozygous R482Q mice compared to +/+ and R482Q/+ littermates at post-partum day 14 (P14). (**E**) Adiponectin-CreERT2 and mTmG background crossed with +/+ or R482Q/+ mice and imaged four weeks post-tamoxifen via confocal microscopy. Scale bar = 50 μm. (**F**) Bulk RNA-seq analyses of floated adipocytes (ads) from psWAT of male and female mice at 10 to 12 weeks of age. Numbers on graph bars are the number of genes driving each pathway. All data represented as mean ± SD. Data were analyzed with two-way ANOVA with a Bonferroni post-hoc test. 181

Figure 4.10. Female *Lmna* R482Q mice have decreased fat oxidation and increased glucose oxidation when fasted and exposed to cold temperatures. One year old female mice were placed into SABLE Promethion cages for five days and exposed to metabolic stressors like fasting, refeeding, and cold exposure. (**A**) Energy expenditure. (**B**) RER. (**C**) Fat oxidation. (**D**) Glucose oxidation. All data represented as mean ± SD. Data were analyzed with two-way ANOVA with a Bonferroni post-hoc test. 182

Figure 4.11. Female *Lmna* P485R mice have a trending decrease in WAT weights, accompanied by decreased adipogenic and oxidative phosphorylation gene pathways in WAT. Body composition of P485R mice over time on NC housed at 22°C: (**A**) Body weight, (**B**) fat mass and (**C**) lean mass. Necropsy data at euthanasia of female *Lmna* P485R mice at 17 to 19 weeks of age. (**D**) Body weight. (**E**) Body length. (**F**) Fed glucose. (**G**) psWAT weight. (**H**) Parametrial white adipose tissue (pmWAT) weight. (**I**) rpWAT weight. (**J**) prWAT weight. (**K**) Liver weight. (**L**) Heart weight. (**M**) BAT weight. (**N**) Gastrocnemius muscle diameter. Fasted serum (**O**) triacylglycerol and (**P**) insulin concentrations before euthanasia. (**Q**) Serum adiponectin immunoblot. Bulk RNA-seq performed on psWAT of 17-19-week-old female *Lmna* P485R mice and analyzed with GSEA. (**R**) P485R/+ vs. +/+ comparison. (**S**) P485R/P485R vs. +/+ comparison. All data represented as mean ± SD. Data were analyzed with one or two-way ANOVA with a Bonferroni post-hoc test. 183

Figure 4.12. Female HFD-fed *Lmna* P485R mice have no change in fat mass but have decreased voluntary running capacity. Mice were started on HFD at 12 weeks of age and housed at 26°C. (**A**) Body weight, (**B**) fat mass, and (**C**) lean mass was measured over time. Mice were then placed into cages with voluntary running wheels when they were at 40 weeks of age. Mice were kept on HFD for 14 days of running, and then were switched to NC. (**D**) Time ran per day. (**E**) Cumulative time ran for 28 days. (**F**) Distance ran per day. (**G**) Cumulative distance ran for 28 days. (**H**) Average speed and (**I**) maximum speed per day. (**J**) Grip strength measured in mice at 44 weeks of age. All data represented as mean ± SD. Data were analyzed with two-way ANOVA with a Bonferroni post-hoc test. 185

Supplemental Figure 2.1. Patients with FPLD2 have impaired glucose tolerance and increased GDF15 concentrations with otherwise comparable clinical characteristics to controls. (A) Additional fat shadow scans from all patients. (**B**) Area under the curve (AUC) from an oral glucose tolerance test (OGTT). (**C**) Insulin AUC during OGTT. (**D**) NEFA AUC during OGTT. (**E**) Fasted insulin concentrations. (**F**) Adipose tissue insulin resistance index (ADIPO-IR). (**G**) Growth differentiation factor 15 (GDF15) concentrations. (**H**) Histological images of skin from subcutaneous adipose tissue biopsies. Scale bar = 50 mm. 92

Supplemental Figure 2.2. Single nuclei RNA-sequencing identifies changes in cell proportions and clusters in upper neck and abdominal subcutaneous adipose tissue biopsies from control patients. (A) Endothelial subclusters with all disease states and biopsy location combined and their GSEA pathways. (**B**) Endothelial subcluster changes in the upper neck relative to abdomen in control biopsies. (**C**) Pericyte subclusters with GSEA pathways. (**D**) Subcluster changes in pericytes in the upper neck versus the abdomen. (**E**) LEC subclusters with GSEA pathways. (**F**) Subcluster changes in LECs in the upper neck relative to the abdomen. 93

Supplemental Figure 2.3. Single nuclei analyses reveal cell proportion changes and identity with disease state. (A) UMAP projection of combined upper neck and abdomen biopsies from patients with different *LMNA* variants, or separated by (**B**) female and male individuals. (**C**) All endothelial cells from developing or FPLD2 biopsies were analyzed via GSEA and compared to controls to identify population-level changes in cell identity. (**D**) Endothelial subclusters with corresponding GSEA pathways and subcluster changes with disease. (**E**) T cell GSEA in developing or FPLD2 biopsies relative to controls. (**F**) T cell subcluster changes with disease. (**G**) Pericyte GSEA in developing or FPLD2 biopsies relative to controls. (**H**) Pericyte subcluster changes with disease. (**I**) LEC GSEA in developing or FPLD2 biopsies. (**J**) LEC subcluster changes with disease. 94

Supplemental Figure 2.4. Subcluster analyses reveal depot-specific shifts in cellular identity. Subcluster changes in the upper neck relative to the abdomen in biopsies from patients with developing and developed FPLD2 in (**A**) adipocytes, (**B**) ASPC, (**C**) macrophages, (**D**) endothelial cells, (**E**) T cells, (**F**) pericytes, and (**G**) LECs. 95

Supplemental Figure 2.5. *Lmna*^{iADKO} mice do not have changes in body weight, lean mass, or develop metabolic dysfunction. All data from male mice except histology from female mice in D. (**A**) Body weight and (**B**) lean mass post-tamoxifen over time (n = 6). (**C**) Weights of perirenal white adipose tissue (prWAT), retroperitoneal white adipose tissue (rpWAT), brown adipose tissue (BAT), and liver two-weeks post-tamoxifen (n = 6). (**D**) psWAT and pmWAT weights of female mice two-weeks post-tamoxifen (n = 12). (**E**) Histology of psWAT, gWAT, liver, BAT, and tibial regulated bone marrow adipose tissue (rBMAT) and constitutive bone marrow adipose tissue (cBMAT). (**F**) Quantification of serum adiponectin immunoblot four-weeks post-tamoxifen (n = 4-5). (**G**) Insulin tolerance test 12 weeks post-tamoxifen (n = 6). (**H**) Glucose tolerance test 13 weeks post-tamoxifen (n = 6). Data are represented as mean ± SD. *P < 0.05. Statistical analyses were performed using two-way ANOVA with a Bonferroni post-hoc test. 96

Supplemental Figure 2.6. *Lmna* knockout adipocytes do not de-differentiate and reside in adipose tissue after adipocyte shrinkage. All data from male mice. (**A**) Fresh confocal micrographs of small GFP-positive cells only present in *Lmna*^{iADKO} mTmG psWAT and eWAT six-weeks post-tamoxifen with (**B**) quantification. Scale bar = 100 μm. (**C**) Backgating strategy to identify tdTomato+ and GFP+ stromal vascular cells (SVC) in *Lmna*^{iADKO} mTmG WAT six-weeks post-tamoxifen. Flow cytometry analyses of tdTomato+ and GFP+ SVCs in (**D**) psWAT and (**E**) eWAT..... 97

Supplemental Figure 2.7. Integrative RNA-seq analyses of *Lmna*^{iADKO} compared to *Lmna*^{ADKO} WAT reveals conserved patterns of gene expression across *Lmna* knockout models and depots. (A) Integrative GSEA comparison of RNA-seq *Lmna*^{iADKO} pmWAT two-weeks post-tamoxifen compared to *Lmna*^{ADKO} psWAT from four-week-old female mice (n= 5-6). Pink dots symbolize that NES were significantly changed in both RNA-seq and proteomics datasets, orange dots = NES only changed in proteomics, blue = NES only changed in RNA-seq. (**B**) Overlapping GSEA pathways in both *Lmna*^{iADKO} and *Lmna*^{ADKO} RNA-seq. Numbers on bars represent number of overlapping genes driving pathways. GSEA pathways changed in only (**C**) *Lmna*^{iADKO} or (**D**) *Lmna*^{ADKO} WAT. 98

Supplemental Figure 2.8. Lipogenic and mitochondrial proteins are repressed in *Lmna*^{iADKO} WAT, and *Lmna* KO pmWAT adipocytes but not psWAT adipocytes have reduced respiration. Quantification of immunoblots from Fig. 7A-C for (**A**) psWAT lipid metabolism proteins, (**B**) pmWAT lipid metabolism proteins, and (**C**) pmWAT mitochondrial proteins two-weeks post-tamoxifen (n = 4-5). Oroboros Oxygraph 2k analyses of floated adipocytes from pmWAT two-weeks post-tamoxifen of (**D**) ATP-linked respiration, (**E**) spare capacity, and (**F**) leak. Respiration analyses from psWAT adipocytes of (**G**) baseline respiration, (**H**) maximum respiration, (**I**) ATP-linked respiration, (**J**) spare capacity, and (**K**) leak (n = 6). Mitochondrial DNA quantification for (**L**) psWAT and (**M**) pmWAT two-weeks post-tamoxifen (n = 3). Immunoblot quantification from (**N**) adipocytes and (**O**) SVF mitochondrial dynamic proteins from Fig. 7F (n = 3-5). Data are represented as mean ± SD. *P < 0.05. Statistical analyses were performed using two-way ANOVA with a Bonferroni post-hoc test. 99

Supplemental Figure 2.9. Lipolysis is not increased in *Lmna*^{iADKO} WAT. (A) Circulating fasted and fed glycerol concentrations in male mice post-tamoxifen (n = 4-6). (**B**) Stimulated lipolysis assay following i.p. isoproterenol injection four-weeks post-tamoxifen (n = 9-10). (**C**) Glycerol concentrations from stimulated lipolysis assay normalized to fat mass. (**D**) Heatmap of lipolytic genes from *Lmna*^{iADKO} RNA-seq from pmWAT two-weeks post-tamoxifen. (**E**) Immunoblot of lipolysis protein expression from eWAT two-weeks post-tamoxifen and (**F**) quantification of immunoblot (n = 4-5). 100

Supplemental Figure 2.10. Macrophages and T cells are not activated in *Lmna*^{iADKO} WAT, and *Lmna* KO adipocytes have upregulated expression of pro-inflammatory transcripts. (A) Spectral flow cytometry gating strategy to identify macrophage and T cell populations from psWAT and pmWAT two-weeks post-tamoxifen (n = 4). (**B**) SVC number per depot. (**C**) CD45+ cells percentage. Representative density plot from CD45+ cells for CD64+ and CD11c+ adipose tissue macrophages (ATMs) from (**D**) psWAT and (**E**) pmWAT, with (**F**) quantification of CD64+ ATMs. Density plot from CD64+ cells for CD163+ and

TIM4+ cells from (**G**) psWAT with (**H**) quantification, and from (**I**) pmWAT with (**J**) quantification. Density plot from CD3+ T cells that are CD4+ and CD8+ cells from (**K**) psWAT with (**L**) quantification, and from (**M**) pmWAT with (**N**) quantification. RT-qPCR analyses for inflammatory transcripts from (**O**) psWAT, (**P**) pmWAT, (**Q**) psWAT adipocytes, (**R**) psWAT SVF, (**S**) pmWAT adipocytes, and (**T**) pmWAT SVF (n = 4). (**U**) Immunoblot for cleaved and total caspase 3 in pmWAT post-tamoxifen (n = 3). 101

Supplemental Figure 3.1. FGF21/sTGFBR2 reduces plasma TAG concentrations and increases body temperature in high fat diet-fed mice. Core body temperature over time in HFD-fed female mice housed at (**A**) 22°C, (**B**) 26°C and (**C**) 30°C (n = 6-7). Plasma TAG concentrations at (**D**) four weeks and (**E**) six weeks post-treatment (n = 6-7). (**F**) Daily food intake in mice at different housing temperatures. Statistical analyses were performed using two-way ANOVA, followed by Bonferroni's post-hoc test. 141

Supplemental Figure 3.2. FGF21/sTGFBR2 decreases diaphragm weights and kidney weights in HFD-induced obese mice. Female mice were euthanized ten weeks after FGF21/sTGFBR2 treatment (n = 5-7). Weights of (**A**) brain, (**B**) diaphragm, (**C**) kidneys, (**D**) spleen, (**E**) lungs, (**F**) heart, and (**G**) gastrocnemius muscle. (**H**) Quantification of AAV transduction in liver, psWAT, and BAT. (**I**) Plasma adiponectin immunoblot and (**J**) quantification relative to controls housed at 22°C. Statistical analyses were performed using two-way ANOVA, followed by Bonferroni's post-hoc test. 142

Supplemental Figure 3.3. FGF21/sTGFBR2 decreases tibial trabecular connectivity density and increases cortical perimeter. Female mice were euthanized ten weeks after FGF21/sTGFBR2 transduction (n = 4-7). Tibias were analyzed by nanoCT. (**A**) Cortical perimeter (Ct.Pm). (**B**) Cortical bone mineral density (Bt.BMD). (**C**) Trabecular bone volume fraction (Tb. BV/TV). (**D**) Trabecular thickness (Tb.Th). (**E**) Trabecular separation (Tb.Sp). (**F**) Trabecular number (Tb.N). (**G**) Trabecular connectivity density (Tb.Conn.D). (**H**) Trabecular specific bone surface (Tb.BS/BV). (**I**) Trabecular bone mineral density (Tb.BMD). *P < 0.05. Statistical analyses were performed using two-way ANOVA, followed by Bonferroni's post-hoc test. 143

S**upplemental Figure 3.4. FGF21/sTGFBR2 decreases kidney weights in lipodystrophic mice housed at 30°C.** Female mice were euthanized 12 weeks after transduction with FGF21/sTGFBR2 (n = 4-7). Weights of (**A**) kidneys, (**B**) brain, (**C**) diaphragm, and (**D**) gastrocnemius muscle at euthanasia. (**E**) Immunoblot of plasma adiponectin with (**F**) quantification. (**G**) Fed leptin concentrations at euthanasia. *P < 0.05. Statistical analyses were performed using two-way ANOVA, followed by Bonferroni's post-hoc test. 144

Supplemental Figure 3.5. FGF21/sTGFBR2 does not change complete blood counts in lipodystrophic mice. Blood was taken at euthanasia 12 weeks after transduction with FGF21/sTGFBR2 (n = 4-7). Total cell counts of (**A**) white blood cells, (**B**) neutrophils, (**C**) lymphocytes, (**D**) monocytes, (**E**) eosinophils, and (**F**) basophils. Cellular percentage of (**G**) neutrophils, (**H**) lymphocytes, (**I**) monocytes, (**J**) eosinophils, and (**K**) basophils. (**L**) Red blood cell count. (**M**) Hemoglobin concentrations. (**N**) Hematocrit (HCT). (**O**) Mean corpuscular volume (MCV). (**P**) Mean corpuscular hemoglobin (MCH) amount. (**Q**) Mean corpuscular hemoglobin concentrations. (**R**) Red blood cell distribution width. (**S**) Platelet

count. (**T**) Mean platelet volume. Statistical analyses were performed using two-way ANOVA, followed by Bonferroni's post-hoc test..... 145

Supplemental Figure 3.6. FGF21/sTGFBR2 decreases tibial trabecular connectivity density and cortical bone volume fraction in lipodystrophic mice housed at thermoneutrality. Female mice were euthanized ten weeks after FGF21/sTGFBR2 transduction (n = 4-7). Tibias were analyzed by nanoCT. (**A**) Trabecular bone volume fraction (Tb. BV/TV). (**B**) Trabecular thickness (Tb.Th). (**C**) Trabecular separation (Tb.Sp). (**D**) Trabecular number (Tb.N). (**E**) Trabecular connectivity density (Tb.Conn.D). (**F**) Trabecular specific bone surface (Tb.BS/BV). (**G**) Trabecular bone mineral density (Tb.BMD). (**H**) Cortical thickness (Ct.Th). (**I**) Cortical perimeter (Ct.Pm). (**J**) Cortical area (Ct.Ar). (**K**) Cortical bone mineral density (Ct.BMD). (**L**) Cortical specific bone surface (Ct.BS/BV). Statistical analyses were performed using two-way ANOVA, followed by Bonferroni's post-hoc test. 146

Supplemental Figure 3.7. FGF21 has little effect on organ weights in lipodystrophic mice housed at 22°C. Female mice were euthanized eight weeks after FGF21 treatment (n = 3-15). Weights of (**A**) rpWAT, (**B**) prWAT, (**C**) kidneys, (**D**) diaphragm, (**E**) lungs, (**F**) brain, (**G**) spleen. (**H**) Tibia length. (**I**) Plasma adiponectin immunoblot with (**J**) quantification. Statistical analyses were performed using two-way ANOVA, followed by Bonferroni's post-hoc test. ... 147

Supplemental Figure 4.1. I T10I mice have no change in WAT or organ weights on NC or HFD. Necropsy data of male and female *Lmna* T10I mice at 20 weeks of age on NC at 22°C, including (**A**) body weight, (**B**) body length, (**C**) spleen weights, (**D**) heart weights, (**E**) rpWAT weights, (**F**) prWAT weights, (**G**) BAT weights, and (**H**) gastrocnemius muscle diameter. Male mice were challenged with 60% HFD and housed at 30°C. (**I**) Body weight over time. (**J**) Fasted glucose concentrations at 15-17 weeks of age. Female mice were housed at 30°C and (**K**) body weight and (**L**) fasted glucose at 15-17 weeks of age was measured. (**M**) Serum adiponectin in females at 15-17 weeks of age. Data at euthanasia of 26-week-old T10I male mice of (**N**) spleen, kidneys, heart, gastrocnemius diameter and body length. Data at euthanasia of 26-week-old female T10I mice of (**O**) spleen, kidneys, heart, gastrocnemius diameter and body length. All data represented as mean ± SD. Data were analyzed with two-way ANOVA with a Bonferroni post-hoc test. 186

Supplemental Figure 4.2. Female *Lmna* R482Q mice do not have detectable change in voluntary running capacity or grip strength. At 22 weeks of age, mice were placed into cages with voluntary running wheels, and (**A**) time ran per day, (**B**) distance ran per day, (**C**) average speed, and (**D**) maximum speed were measured. (**E**) Cumulative time ran and (**F**) cumulative distance ran for 30 days. (**G**) Grip strength was measured in mice that were 26 weeks of age. Mice underwent forced treadmill running, and (**H**) run time, (**I**) max speed, and (**J**) distance was measured. All data represented as mean ± SD. Data were analyzed with two-way ANOVA with a Bonferroni post-hoc test. 187

Supplemental Figure 4.3. *Lmna* P485R and K486N mice fed NC have no change in voluntary running capacity. At 32 weeks of age, female mice fed NC at 22°C were placed into cages with voluntary running wheels. (**A**) Time ran per day, (**B**) distance per day, (**C**) average speed and (**D**) max speed were measured in *Lmna* P485R mice. (**E**) Grip strength was

measured in 36-week-old mice. (**F**) Time ran per day, (**G**) distance ran per day, (**H**) average speed, and (**I**) max speed were measured in *Lmna* K486N mice. (**J**) Grip strength was measured in 36-week-old mice. All data represented as mean ± SD. Data were analyzed with two-way ANOVA with a Bonferroni post-hoc test. 188

Supplemental Figure 4.4. *Lmna* N582H mice have reduced WAT weights and increased heart weights. At 16 weeks of age, male and female mice fed NC at 22°C were euthanized. (**A**) Body weight. (**B**) Fed glucose. (**C**) Body length. (**D**) psWAT weight. (**E**) gWAT weight. (**F**) prWAT weight. (**G**) rpWAT weight. (**H**) BAT weight. (**I**) Liver weight. (**J**) Heart weight. (**K**) Kidneys weight. (**L**) Spleen weight. All data represented as mean ± SD. Data were analyzed with two-way ANOVA with a Bonferroni post-hoc test. 189

Supplemental Figure 4.5. I R584H* mice have no change in WAT or organ weights. At 24 weeks of age, male and female *Lmna* R584H* (additional off-target mutations besides R584H) were euthanized. (**A**) Body weight. (**B**) Fed glucose. (**C**) Body length. (**D**) psWAT weight. (**E**) gWAT weight. (**F**) rpWAT weight. (**G**) prWAT weight. (**H**) BAT weight. (**I**) Liver weight. (**J**) Spleen weight. (**K**) Heart weight. (**L**) Gastrocnemius muscle diameter. All data represented as mean ± SD. Data were analyzed with two-way ANOVA with a Bonferroni post-hoc test..... 190

Supplemental Figure 4.6. *Lmna* R584H* male mice fed a HFD for five months housed at 30°C had no change in WAT or organ weights. Male *Lmna* R584H* mice at 28 weeks of age were euthanized. (**A**) Body weight. (**B**) psWAT weight. (**C**) eWAT weight. (**D**) rpWAT weight. (**E**) prWAT weight. (**F**) BAT weight. (**G**) Liver weight. (**H**) Spleen weight. (**I**) Kidney weight. (**J**) Heart weight. (**K**) Gastrocnemius muscle diameter. (**L**) Body length. (**M**) Randomly-fed glucose concentrations. All data represented as mean ± SD. Data were analyzed with two-way ANOVA with a Bonferroni post-hoc test. 191

Supplemental Figure 4.7. *Lmna* R584H* female mice on NC housed at 30°C had no change in WAT or organ weights. Female *Lmna* R584H* mice at 28 weeks of age were euthanized. (**A**) Body weight. (**B**) psWAT weight. (**C**) eWAT weight. (**D**) rpWAT weight. (**E**) prWAT weight. (**F**) BAT weight. (**G**) Liver weight. (**H**) Spleen weight. (**I**) Kidney weight. (**J**) Heart weight. (**K**) Gastrocnemius muscle diameter. (**L**) Body length. (**M**) Random-fed glucose. All data represented as mean ± SD. Data were analyzed with two-way ANOVA with a Bonferroni post-hoc test..... 192

Abstract

Lipodystrophy syndromes are rare diseases characterized by selective loss, redistribution, and dysfunction of adipose tissues. Though seemingly the opposite of obesity, lipodystrophy syndromes are accompanied similar metabolic complications. Studying lipodystrophy provides unique insights into adipose tissue homeostasis and its critical role in whole-body metabolism. The most common form of lipodystrophy is familial partial lipodystrophy 2 (FPLD2), caused by pathogenic variants in *LMNA*, which encodes nuclear proteins lamin A/C. These proteins are essential for nuclear function and structure and control gene expression. However, the role of lamin A/C in adipocyte maintenance remains incompletely understood, and the mechanisms driving FPLD2 are still unclear.

The goal of this dissertation was to uncover molecular mechanisms driving adipocyte loss in FPLD2. We recruited eight families containing 16 individuals with developing or developed FPLD2 and performed bulk and single nuclei transcriptomic analyses of adipose tissue biopsies. These studies revealed decreased expression of genes involved in lipid metabolism and mitochondrial function, alongside increased inflammatory signaling. Similar transcriptional signatures were observed in adipose tissue from tamoxifen-inducible, adipocyte-specific *Lmna* knockout mice at early stages of lipodystrophy development. Moreover, *Lmna*-deficient adipocytes exhibited delipidation, cell shrinkage, and eventual disappearance, accompanied by dysfunctional mitochondrial respiration and ultrastructural abnormalities. Comparable gene expression alterations were also found in *Lmna*-deficient fibroblasts and could be linked to altered chromatin accessibility. Together, these findings highlight the fundamental role of lamin A/C in adipocyte maintenance.

Next, we investigated the therapeutic potential of dual gene therapy using adeno-associated virus (AAV) to deliver FGF21 and sTGFBR2 in a mouse model of lipodystrophy. In obese mice, this treatment improved insulin resistance and hyperlipidemia more effectively at warmer housing temperatures. In lipodystrophic mice fed a high-fat diet, dual gene therapy improved hepatic steatosis but not insulin sensitivity. Notably, FGF21 alone at 22°C improved

both insulin resistance and hepatic steatosis in lipodystrophic mice. Hepatic transcriptomic analyses revealed that lipodystrophic mice had increased hepatic cell proliferation and fibrosis pathways, which were attenuated by FGF21 treatment, along with an increase in mitochondrial metabolism pathways. These results suggest that AAV-mediated gene therapy targeting FGF21 and TGFβ signaling holds promise for improving the metabolic dysfunction caused by lipodystrophy.

Finally, we generated and characterized seven new mouse lines with FPLD2-causing pathogenic variants across *Lmna*. Most lines did not develop lipodystrophy or metabolic dysfunction, apart from mild adipose loss in the P485R and N582H lines. Interestingly, *Lmna* T10I and high-fat diet-fed P485R biallelic mice had reduced voluntary running capacity, despite preserved maximal muscle strength. Indirect calorimetry revealed that *Lmna* T10I and R482Q mice had decreased fat oxidation and lower energy expenditure compared to controls. Transcriptomic analyses of adipose tissue from these variants recapitulated gene expression changes seen in human biopsies and *Lmna* adipocyte-specific knockout mice, including alterations in inflammatory signaling, oxidative phosphorylation, lipid metabolism, and muscle-related pathways. These results demonstrate that even in the absence of overt lipodystrophy, pathogenic *Lmna* variants can impair energy metabolism and physical activity, reflecting subtle but meaningful molecular phenotypes that warrant further investigation.

In summary, this work integrates human, mouse, and *in vitro* models to uncover shared molecular mechanisms driving FPLD2, identify novel therapeutic strategies, and reveal fundamental insights into the role of lamin A/C in adipocyte biology and disease.

Chapter 1 Introduction

1.1 Adipose tissue is a key metabolic organ and contributes to whole-body metabolism

Adipose tissues, colloquially known as "fat," are major regulators of whole-body metabolism and health, contrary to the historic belief that they are simply passive energy storage depots. Adipose tissues contain specialized lipid-handling cells called adipocytes, which store energy in the form of triacylglycerols (TAGs). Beyond lipid storage, adipocytes are insulin-sensitive, secrete endocrine hormones, and actively synthesize and break down lipid[1]. As the rates of obesity, characterized by excess adipose tissue, have doubled since 1990[2], so has metabolic dysfunction, including type 2 diabetes and fatty liver disease. Obesity is also accompanied by increased risk of other diseases like cancer[1]. It is crucial to understand adipose tissue homeostasis and its contribution to whole body metabolism to combat metabolic and other diseases and to improve human health.

Adipose tissue can be classified into multiple categories and are in distinct depots throughout the body. White adipose tissue (WAT) is comprised of adipocytes with a unilocular lipid droplet, which primarily stores energy in the form of TAG and which makes up most of the adipose tissue volume in mammals. However, adipocytes only comprise 25-30% of the total cells in WAT, as WAT contains other cell types including adipose stem and progenitor cells (ASPCs), endothelial cells, and immune cells. WAT is in depots throughout the body, including viscerally in the peritoneal cavity and subcutaneously underneath the skin; smaller depots e.g. within the joints, bone, and dermis also play important metabolic roles. White adipocytes are typically up to 100 μm in diameter and can expand and increase their size (hypertrophy) up to 300 μm under obese conditions, highlighting their adaptive ability to store energy under times of calorie excess. Alternatively, WAT can also expand via increased cell number, called hyperplasia. WAT is a crucial metabolic organ and secretes endocrine hormones like leptin, adiponectin, and resistin, which control processes like food intake, body weight, glucose metabolism, and insulin sensitivity [3–5]. White adipocytes undergo extensive lipid processing to maintain homeostasis, including lipid breakdown during times of energy need via lipolysis, storage of excess energy

(e.g. glucose, amino acids) via *de novo* lipogenesis, breakdown of fatty acids to create energy via β-oxidation, and storage of fatty acids from circulation. Furthermore, WAT can become inflammatory both within adipocytes themselves or via activation of immune cells, and can secrete cytokines like TNFα, IL-6, and IL1β along with other factors like non-coding RNAs and extracellular vesicles to control local and inter-organ metabolism.[6] The multifaceted roles of WAT, including its secretory and endocrine properties, along with its dynamic plasticity, highlight its crucial role in regulating metabolism (**Figure 1.1 A**).

Brown adipose tissue (BAT) contains brown adipocytes with multilocular lipid droplets and a high number of mitochondria. BAT is specialized for non-shivering thermogenesis, especially important for heating small mammals, including human babies. Thermogenesis occurs in BAT because mitochondria in BAT express uncoupling protein 1 (UCP1), which uncouples the proton gradient across the inner mitochondrial membrane to allow energy to be used for heat production instead of ATP. BAT was previously thought to be present in only infants, but has now been shown to be present in human adults; BAT is located in interscapular, cervical, and paravertebral regions[7,8]. Though BAT comprises only a small volume of total adipose tissue in the body, its high metabolic activity is of interest to target obesity and metabolic dysfunction: increasing thermogenesis in BAT improves metabolism and protects against weight gain[9]. Finally, an underappreciated adipose depot, bone marrow adipose tissue (BMAT), accounts for up to 70% of bone marrow volume and about 10% of total adiposity[10]. BMAT accumulates during obesity and type 2 diabetes, but also during states of calorie restriction, and regulates hematopoiesis and bone health[11]. Taken together, adipose tissue across different types and depots has distinct metabolic functions, and imbalances in its amount or function could have catastrophic health effects.

1.2 The paradox of too much versus too little adipose tissue

Energy balance in the body is dictated by energy intake, expenditure, and storage[12]. If energy intake is equivalent to energy expenditure, body weight stays the same. However, if energy intake exceeds energy expenditure, body weight increases, of which can be mostly attributed to adipose tissue expansion and lipid accumulation[13]. This positive energy balance can result in obesity, defined as an excess of adiposity, typically classified as a waist to hip ratio of 0.9 or higher in men, and 0.85 or higher in women[14]. This finely-tuned energy balance is

influenced by many factors including genetics and the environment, and is regulated both peripherally and centrally[15].

In obesity, WAT expands through both hypertrophy and hyperplasia. The adipose tissue expandability hypothesis states that there is a maximum capacity for adipose tissue expansion, and once this limit is reached, adipose tissue can no longer store excess energy, causing lipids to accumulate ectopically in other tissues[16]. This ectopic lipid accumulation in tissues like liver, muscle, and pancreas, which are not equipped to handle lipids, is called lipotoxicity: this leads to cellular dysfunction, insulin resistance, and inflammation[16]. Lipotoxicity is likely driven by certain lipid species, including ceramides and acylated fatty acids, which alter insulin signaling and can cause mitochondrial dysfunction[17]. Clinical consequences of insulin resistance and lipotoxicity include fatty liver disease, hyperlipidemia, cardiovascular disease, type 2 diabetes, and diabetic nephropathy[17] (**Figure 1.1 B**).

On the other hand, there is a class of rare disorders called lipodystrophies, which cause loss, dysfunction, and redistribution of adipose tissues. Lipodystrophies are classified as localized, partial, or generalized, depending on the pattern of fat loss, and can be further characterized as having acquired or familial etiology.[18] Lipodystrophies are seemingly the opposite of obesity, but due to the lack of safe lipid storage in adipose tissues, lipodystrophy syndromes result in the same lipotoxicity and metabolic dysfunction as in obesity (**Figure 1.1 B**). Therefore, lipodystrophy and obesity have a shared reduction in excess energy storage, underscoring the importance of having both functional and healthy adipose tissue to maintain whole-body homeostasis. Though rare, lipodystrophy syndromes can inform us about 1) how adipose tissue is maintained in the body and 2) how adipose tissue contributes to metabolism, which can 3) unlock therapeutic treatments for not just patients with lipodystrophy but also those with obesity and metabolic syndromes.

1.3 Familial partial lipodystrophy 2: prevalence and clinical characteristics

Lipodystrophy syndromes are rare with an estimated clinical prevalence of 1.3 to 4.7 per 1 million people, though recent studies have demonstrated that the genetic prevalence of inherited lipodystrophy-associated pathogenic variants is closer to 1 in 7,000[18–20]. Inherited or familial lipodystrophies, driven by genetic variants causing disease, will be the focus of this dissertation. The most extreme inherited lipodystrophies are called congenital generalized lipodystrophies (CGL), which cause loss of essentially all adipose tissues in the body from birth.

CGL are caused by pathogenic variants in essential lipid metabolism genes like *AGPAT2, BSCL2, CAV1,* or *PTRF*[18]. Patients with CGL have severe insulin resistance, diabetes, and hyperlipidemia, along with other metabolic features like accelerated growth, cardiomyopathy, and muscular dystrophy. Extensive research has been conducted on molecular mechanisms causing adipose loss in different genetic forms of CGL, and has been reviewed in detail elsewhere[18].

A more heterogenous group of inherited lipodystrophies are termed familial partial lipodystrophies (FPLD), which are characterized by varying degrees of adipose tissue loss, which often occur in a depot-specific manner. FPLD is also accompanied by a range of metabolic dysfunctions. FPLD is caused by variants in genes such as *LMNA* (FPLD2), *PPARG* (FPLD3), *PLIN1* (FPLD4), *CIDEC* (FPLD5), and *LIPE* (FPLD6); FPLD1 is polygenic and does not have a known single genetic variant causing disease[18]. *PPARG*, *PLIN1, CIDEC,* and *LIPE* are all involved in adipogenesis or lipid droplet maintenance, so variants in these genes understandably cause impaired adipogenesis or dysfunction of lipid homeostasis in adipocytes. However, FPLD2, the most common type of FPLD, has been investigated molecularly with no clear disease mechanism. We hope to elucidate these mechanisms in our studies.

FPLD2 is characterized by loss of subcutaneous adipose tissue from the trunk, buttocks, and limbs, with expansion of adipose tissue in the face and neck causing a Cushingoid-like appearance, and in the labia majora[20,21] (**Figure 1.2 A**). Visceral adipose tissue can either also be lost or can increase in amount – there is much heterogeneity in clinical presentation (**Figure 1.2 A-C**). Patients also have visible physical signs of insulin resistance like acanthosis nigricans, along with signs of hyperandrogenism in women, reproductive dysfunction including polycystic ovarian syndrome (PCOS), and metabolic dysfunction like hyperlipidemia, non-alcoholic fatty liver disease, and type 2 diabetes[20]. Patients with FPLD2 have a high rate of heart disease, including heart failure and conduction disturbances[20]. Less common phenotypes include atherosclerosis, hypothyroidism, and kidney disease[20]. Due to their lack of adipose tissue, patients have low circulating concentrations of leptin and adiponectin and are hyperphagic[22] (**Figure 1.2 C**). Patients are born with adipose tissue, with subsequent loss of adipose tissue typically occurring around puberty, though adipose tissue loss can occur as young as six and as old as mid-20s[23]. Females have a higher rate of diagnosis due to their more recognizable phenotype compared to males, and typically have more severe metabolic complications relative

to males[24]. FPLD2 is inherited in an autosomal dominant manner, with most patients having heterozygous variants in *LMNA*. Biallelic variants in the *LMNA* gene are associated with a more severe FPLD2 phenotype[22]. Most patients with the classic FPLD2 phenotype harbor heterozygous missense variants within exon 8, p.(R482Q) or p.(R482W). However, variants are found across the *LMNA* gene with varying phenotype severity, which may explain the wide heterogeneity across FPLD2.

Current treatments for FPLD2 are focused on improving the associated metabolic comorbidities. Low fat, low carbohydrate and high protein diets are often suggested, with very-low-calorie diets improving metabolic abnormalities[25]. Metformin is commonly prescribed to control diabetes, with new glucagon-like peptide 1 (GLP1) receptor agonists and other incretin mimetics proving to be effective treatments for metabolic dysfunction associated with FPLD2[26,27]. Creation of an analog of recombinant human leptin, Metreleptin, has been a dramatic breakthrough for patients with FPLD2: this leptin replacement therapy decreases hyperphagia, improves glucose concentrations and HbA1c levels, decreases hepatic lipid accumulation, and lowers hyperlipidemia[28,29]. However, issues with leptin treatment exist, like frequent administration, side effects, and potential development of leptin resistance[30]. New treatments are being explored, including fibroblast growth factor 21 (FGF21) administration which shows promise in treating FPLD2-associated metabolic dysfunction preclinically, decreasing liver fat and improving hyperlipidemia[31,32]. A recent example of personalized gene therapy was able to reverse a genetic variant in different rare disease, which will hopefully be embraced for correction of the *LMNA* genetic variant underlying FPLD2 pathology[33]. Ongoing studies of FPLD2 pathogenesis are necessary to better understand the disease progression in hopes of finding alternative treatments for patients.

1.4 Lamins are regulators of nuclear function and gene expression

Genetic variants in *LMNA* (lamin A/C) cause FPLD2: it is necessary to understand lamin A/C biology to explore molecular mechanisms of disease. Lamins are type V intermediate filament proteins that comprise the nuclear lamina, a meshwork of proteins that line the inner nuclear membrane. Lamins can be separated into A- and B-type lamins with distinct functions in cell differentiation and regulation. A-type lamins are encoded by the *LMNA* gene (**Figure 1.3 A**), and consist of lamin A, lamin C, and two minor isoforms C2 and AΔ10. B-type lamins are encoded either by the *LMNB1* gene (lamin B1) or *LMNB2* (lamin B2, B3). The nuclear lamina

provides mechanical support and structure for the nucleus, senses and adapts to mechanical stressors within the cell, facilitates nuclear transport and signaling, and binds directly to chromatin at areas called lamina-associated domains (LADs) to regulate gene expression[34]. The ubiquitous roles of lamin proteins implicate them in many crucial cellular processes, underscored by their evolutionary conservation with expression of lamin analogs in plants, trypanosomes, and invertebrates[35]. Mouse and human lamin A/C are 96% identical in their amino acid sequence, with differences primarily in the C-terminus tail. B-type lamins are constitutively expressed in most mammalian cells and A-type lamins are expressed in most differentiated cell types, highlighting their differences in cellular function dependent on cell state and maturation[34]. In human adipocytes, lamin A and lamin C expression increases with differentiation, and lamin A is expressed at a higher amount than lamin C; out of the B-type lamins, only lamin B1 is expressed in human white adipocytes[36]. Due to the involvement of A-type lamins in FPLD2, this section will be focused primarily on the processing, binding partners, and function of lamin A/C rather than lamin B.

The *LMNA* gene is alternatively spliced at a site within exon 10 to generate lamin A (646 amino acids) and lamin C (572 amino acids). They are frequently referred to as lamin A/C, but their individual functions are becoming increasingly appreciated[37]. The lamin genes contain a head N-terminal domain, a rod domain, and a C-terminal long carboxy-terminal tail domain. The tail domain contains a nuclear localization signal (NLS), an immunoglobin-like (Ig-like) fold domain, a DNA-binding site, and a CAAX motif for lamin A post-translational processing[38]. Lamin C is translated without any post-translational processing, but lamin A undergoes considerable post-translational processing. Lamin A is first translated as prelamin A, which undergoes multiple stages of processing: 1) farnesylation on the C-terminal cysteine via farnesyltransferase enzyme , 2) cleavage of -AAX residues on C-terminal end via Ras-converting enzyme 1 (RCE1) or zinc metalloproteinase Ste24 homolog (ZMPSTE24), 3) carboxymethlation of C-terminal cysteine by isoprenylcysteine carboxyl methyltransferase (ICMT), and 4) cleavage of the last 15 C-terminal amino acids via ZMPSTE24[38] (**Figure 1.3 A**). Lamins B1 and B2 also undergo farnesylation after translation from the *LMNB1* and *LMNB2* genes, but remain permanently farnesylated at the C-termini and do not undergo steps 2-4 as described[39].

Lamins undergo post-translational modifications (PTM) beyond farnesylation, including phosphorylation. Lamin A has over 70 Ser/Thr phosphorylation sites, along with at least seven

Tyr phosphorylation sites; phosphorylation is crucial for lamin polymer formation, solubility, and targeting to the inner nuclear membrane[40,41]. Phosphorylation of B-type lamins is also crucial for assembly and nuclear organization[41,42]. Lamins also undergo acetylation, modification with small ubiquitin-like modifiers (SUMO) via SUMOylation, methylation, ubiquitination, O-GlcNAcylation (lamin A only), which contribute to localization, stability, and lamin assembly[40,43,44] (**Figure 1.3 B**). The regulation of lamin processing is tightly controlled and essential for normal functions.

Following translation and processing, lamins assemble and organize into 3.5 nm thick filaments; together, the nuclear lamina meshwork is 14-16 nm thick[45,46]. Lamins contain an a-helical coiled-coil domain, which allow for lamin dimer assembly. Dimers then interact longitudinally to form polar head-to-tail polymers[45,47]. These polymers then assemble laterally an anti-parallel, half-staggered manner to build a protofilament. Protofilaments then interact laterally to form filaments. Lamin filament lengths are relatively short, with an average persistent length (the length over which filaments stay straight) of less than 200 nm[46,48]. Lamin filament assemblies are similar between A- and B-type lamins[49]. The stoichiometry of A-type lamins to B-type lamins can vary dependent on cell type and differentiation state[46]. Lamin A and lamin C amounts are generally equal in cells, although this ratio can be found altered in some diseases[50]. The ratio of lamin A:C mRNAs in WAT are 1:0.85, in skeletal and heart muscle are 1:1.31 and 1:1.87 in spleen[51]. Interestingly, lamins have been shown to be organized into separate but interacting perinuclear microdomains, with distinct A- and B-type lamin networks[52]. In mouse embryonic fibroblasts (MEFs) without *Lmna* or *Lmnb1*, the lamina meshwork structure was disrupted, but the lack of just *Lmnb2* had minor effects on lamina structure, highlighting the importance for A-type lamins and lamin B1 in lamina assembly[53]. Both lamin types also exist in the nucleoplasm where they exhibit different functions dependent on localization[54,55].

The extensive roles of lamins were revealed with the use of proteomics to characterize tissue-specific binding partners of lamin A/C to nuclear envelope proteins[56]. These data identified primarily nuclear envelope transmembrane proteins (NETs) as bound to lamin A/C, including the canonical NETs known to bind to lamin A/C like the lamin B receptor (LBR), lamina-associated polypeptide 1/2 (LAP1 and 2), emerin, Sad1 and UNC84 domain-containing proteins 1/2 (SUN1 and 2), in addition to various nucleoporin proteins, along with over 70 novel transmembrane proteins[56] (**Figure 1.3 C**). SUN proteins and proteins with Klarsicht, ANC-1,

Syne Homology (KASH) domains, like nesprin-1, -2, and -4, form a unique complex called the Linker of Nucleoskeleton to Cytoskeleton (LINC) complex, which allows the nuclear envelope and lamins to sense mechanical stresses through the cytoskeleton. The cytoplasmic domains of nesprins can interact with cytoskeletal proteins, including actin and other intermediate filaments. Forces like mechanical changes at the plasma membrane affect mechanosensitive proteins, which then transfer stresses via the cytoskeleton bound to the LINC complex, which then reaches the nucleus[57]. This sophisticated communication system helps control nuclear shape and orientation, regulates centrosome and chromosome localization during cell division, transmits mechanical forces to alter gene expression via altering lamin A/C-LAD interactions, and can help repair DNA in response to damage[58–60]. Finally, lamin A/C associates with nuclear pore complexes (NPCs) via nucleoporins, helps with NPC spatial distribution, and affects active and passive transport across the nuclear membranes[61,62] (**Figure 1.3 C**).

Beyond nuclear transport and mechanosensing, the nuclear lamina binds to chromatin at LADs, first identified using DNA adenine methyltransferase (Dam) identification (DamID) by the Van Steensel lab, which marks regions where lamin B1 binds to DNA by taking advantage of Dam's methyltransferase activity[63]. LADs have a median size of 0.1-1 mb[64]. LADs make up 40% of the genome, are typically gene-poor, and high in di- and trimethaylated histone H3 lysine 9 (H3K9me2, H3K9me3), modifiers of heterochromatin[63]. However, at least 10% of the genes bound to the nuclear lamina are expressed, and there is constant binding and release between the nuclear lamina and chromatin, highlighting its dynamic nature[65,66]. Nuclear lamina association does not always indicate that gene expression is repressed; LADs are structurally heterogenous and may form microloops not bound to lamins, allowing for active transcription[64,67]. LADs can be classified as constitutive, containing structural elements that bind DNA to the nuclear lamina, or variable, which tend to be developmentally regulated and express cell-type specific genes[68]. Furthermore, most LADs that bind to lamin A/C versus lamin B overlap, but substantial differences exist, which is unsurprising considering their often segregated organization[69,70]. Using HeLa cells, the Collas group found that one third of LADs were unique to lamin B, and one fifth were unique to lamin A/C[69]. Beyond the nuclear periphery, lamin A/C can bind to euchromatin in the nuclear interior in a LAP2α-dependent manner: LAP2α is bound to chromatin and exclusively binds lamin A[71,72]. Taken together, lamins have many roles in nuclear structure, function, and regulation of gene expression. It is plausible that a change or loss of

function in lamin A/C, as observed in patients with FPLD2, could lead to catastrophic molecular outcomes and disease pathogenesis for specific cell types.

1.5 Laminopathies: diseases beyond FPLD2 caused by lamin A/C variants

Beyond FPLD2, there is a larger group of diseases caused by variants in the *LMNA* gene, called laminopathies (**Figure 1.4**). These include Hutchinson-Gilford progeria syndrome (HGPS)[73], Emery-Dreifuss muscular dystrophy (EDMD)[74], dilated cardiomyopathy (DCM)[75], mandibuloacral dysplasia type A (MADA)[76], and an axonal peripheral neuropathy called Charcot-Marie-Tooth Disorder Type 2 (CMT2) [77]. Over 600 missense disease-causing *LMNA* variants have been reported in ClinVar[78]. These unique disorders raise multiple questions about lamin A/C and its role in disease: How do global variants in *LMNA* lead to tissue-specific phenotypes? What is it about lamin A/C that can causes a wide variety of diseases, with phenotypes often dependent on where in the gene the pathogenic variant is located? We hope to elucidate some of these answers through study of FPLD2; studying other laminopathies may also give us insights into FPLD2 pathology.

Progeria is characterized by features of premature aging, including stunted growth, loss of adipose tissue, thin and wrinkled skin, hair loss, joint stiffness, and cardiovascular issues, with an average life expectancy of about 15 years. Progeroid symptoms can occur in other types of laminopathies, but the most common progeroid disorder is HGPS, though still extremely rare. The most common pathogenic HGPS variant is in exon 11 at c.1824C > T, which creates a new splicing site, leading to transcription of a truncated prelamin A transcript, which is translated into a protein called progerin; this protein is 50 amino acids shorter than lamin A and retains a C-terminal farnesyl group. Progerin causes cellular catastrophe after incorporation into the nuclear lamina, causing DNA damage and nuclear membrane ruptures[79,80]. Progeroid syndromes can also occur from variants in *ZMPSTE24*, an enzyme crucial in prelamin A post-translational processing[81]. Though progeria syndromes are caused by progerin accumulation rather than a loss/change of lamin A/C function, the mechanisms of disease by which progerin disrupts nuclear health and structure can serve as a strong foundation for study of other laminopathy disease mechanisms.

Multiple pathogenic variants across *LMNA* can lead to EDMD, which causes a progressive wasting and weakness of muscles, specifically in the shoulders, upper arms, and calf muscles[82]. Patients with EDMD have stiff joints and often have cardiac diseases like congestive

heart failure. EDMD-causing variants likely often impair lamin A/C-emerin interactions, along with causing dysfunctional lamina assembly and causing a mislocalization of emerin[83,84]. Furthermore, lamin A/C and emerin interact with LAP1; variants in LAP1 also cause muscular dystrophy, underscoring the importance of the lamin A/C, emerin, and LAP1 interaction in preserving healthy muscle function[85]. Global *LMNA* knockout (KO) mice develop EDMD and die prematurely, providing evidence that a loss of lamin A/C function can lead to muscular dystrophy. Study of these KO mice are confounded by their premature death, which is addressed in detail later[86].

Related to EDMD, variants in *LMNA* can also cause DCM, accounting for six to eight percent of idiopathic DCM[87,88]. DCM is characterized by enlargement of the left ventricle, reduced systolic function, conduction system disease, and/or arrhythmias, typically presenting in early adulthood[89]. DCM can cause sudden cardiac death, even with minimal or no previous systolic dysfunction. Studies deleting *Lmna* in mouse cardiomyocytes *in vivo* led to premature cell death, apoptosis, and fibrosis, and activation of the DNA damage response pathway[90]. Lamin A/C has a key role in muscle homeostasis, seeing as *LMNA* pathogenic variants can cause issues in skeletal and cardiac muscle health.

Variants in the lamin A/C gene cause other ultrarare diseases, including MADA and CMT2. MADA is a complex, multi-system disorder that causes growth retardation, craniofacial abnormalities like mandibular hypoplasia (underdevelopment of lower jaw), skin changes including atrophy and mottled pigmentation, and lipodystrophy[91]. CMT2 is characterized by a reduction in nerve-conduction velocities, loss of large myelinated fibers, and axonal degeneration, which causes muscle weakness and wasting, and foot deformities[77]. Interestingly, relatively few diseases are caused by variants in B-type lamins, although identified *LMNB1* and *LMNB2* variants have been linked to nervous system phenotypes[92]. Taken together, lamin A/C dictates a variety of cellular functions across different tissues, but it is still unclear how variants in *LMNA* lead to a tissue-specific phenotype in laminopathies. Oftentimes, patients with FPLD2 have symptoms of other laminopathies including muscular dystrophy and cardiac abnormalities, so there are shared phenotypes between disease dependent on variant site[93]. Multiple hypotheses exist for the wide range of laminopathy diseases, which will be discussed later in this chapter. Further studies into basic lamin biology and how amino acid changes alter lamin A/C structure and function are required to better understand laminopathies.

1.6 Lamin A/C knockout studies to study fundamental roles of lamins

1.6.1 Lmna KO MEFs

To study mechanisms of adipose tissue loss in FPLD2, and more broadly, laminopathies, we reviewed previous studies about lamin A/C function to understand its most fundamental cellular roles. A commonly used model to study this question are the *Lmna* KO MEFs, isolated from global *Lmna* KO mouse embryos at day 13[86]. An early study of *Lmna* KO MEFs revealed elongated and irregular nuclear shape, NPC clustering, a switch of lamin B1 expression to cluster at one pole of the nuclei, and a loss of heterochromatin localization at the nuclear periphery[86]. Additional studies confirmed that *Lmna* KO MEFs do indeed have nuclear deformities, including nuclear surface irregularity and distortions, which are most dramatic when both lamin A and C are knocked out; lamin C-only and lamin B1-only MEFs had slightly altered nuclear shape and blebbing[94,95]. These nuclear shape abnormalities can be partially attributed to Golgi SUN1 accumulation in *Lmna* KO MEFs, as *Sun1* and *Lmna* double KO MEFs had lessened nuclear defects[96]. Truncated lamin A also accumulated in *Lmna* KO MEFs, which may play a pathologic role[97]. Due to the role of LMNA in nuclear mechanics, nuclear strain and stiffness of nuclei were measured in *Lmna* KO MEFs, revealing that *Lmna* KO but not lamin C-only MEFs had reduced nuclear stiffness, which could be rescued by exogenous expression of prelamin A[94]. When *Lmna* KO MEFs were subjected to biaxial mechanical strain, *Lmna* KO cells had deformed nuclear shape and increased nuclear fragility compared to control cells[98]. By compressing cells to cause mechanical stress, Broers et al. showed that *Lmna* KO MEFs had increased nuclear damage, and that nuclei deformed isotropically (equal in all directions) as compared to control MEFs which deformed anisotropically (perpendicular to long axis)[99]. Taken together, *Lmna* KO MEFs have altered nuclear shape and stiffness, and are more prone to deformities upon mechanostresses.

Due to the close interactions of lamin A/C with the cytoskeleton through the LINC complex, many groups have studied how the cytoskeleton changes upon lamin A/C deficiency. Actin stress fibers and the vimentin network organization were disrupted in *Lmna* KO MEFs, along with a decrease in microtubule attachment number to the nuclear membrane[99]. This was supported in a separate study where *Lmna* KO in MEFs separated the microtubule organizing center from the nuclear envelope, showing disruption of not just number of microtubules but also cellular organization[100]. When *Lmna* KO MEFs were plated on rhodamine fibronectin-coated plates, the authors saw no change in actin amount but did find less organized actin stress fibers,

including the fibers being thinner and less prominent, along with smaller focal adhesions[101]. However, another study found that there were no visual disruptions in the actin cytoskeleton in *Lmna* KO MEFs after staining with phalloidin, though cytoskeletal stiffness was decreased compared to controls[98]. Other functional studies of *Lmna* KO MEFs showed less observed cytoskeleton contractility[101], less cytoskeleton elasticity and viscosity, and reduced migration speed during a wound healing assay[100]. A 2022 study from Vahabikashi et al. used atomic force microscopy to characterize *Lmna* KO MEFs, and confirmed reduced cytoplasmic stiffness[95]. Vahabikashi et al. explored LINC complex integrity and found that *Lmna* KO MEFs have increased mobility of LINC complexes that bind with actin and vimentin compared to control MEFs. The vimentin network around the nucleus was also lost upon *Lmna* KO in MEFs[95]. Therefore, loss of *Lmna* in MEFs decreases cytoskeleton stiffness, disrupts actin and vimentin fiber organization, and cell migration speed, highlighting the role of lamin A/C in cytoskeletal control.

Beyond LINC complexes, others have studied changes in lamin A/C-bound nuclear envelope proteins and chromatin upon *Lmna* KO. A recent preprint utilized cryo-electron tomography to understand the interplay between lamins and chromatin, and observed that upon loss of lamin A/C, nucleosome concentration was decreased in MEFs at the nuclear periphery, which led to many genes switching between a transcriptionally active and inactive chromatin compartment[102]. *Lmna* KO MEFs also had a shift in telomere localization towards the nuclear periphery compared to control MEFs, accompanied by shortened telomeres, increased γH2AX-positive loci (indicative of DNA damage), and decreased telomere repair in *Lmna* KO MEFs[103]. Decreased DNA repair in *Lmna* KO MEFs is proposed to lead to mitochondrial defects by increasing NAD+ consumption[104]. More broadly, Assay for Transposase-Accessible Chromatin sequencing (ATAC-seq) analyses showed large changes in chromatin accessibility at gene regulatory elements both within and outside LADs upon *Lmna* KO in MEFs[104]. Broader analyses of the nuclear envelope in *Lmna* KO MEFs revealed that spatial interactions between NPCs and the nuclear lamina were maintained, indicating that lamin A/C are not required for NPC organization perse, but are likely important for NPC functioning or transport control[105]. Finally, primary *Lmna* KO MEFs have been shown to differentiate more readily into adipocytes than wild-type MEFs, showing effects of *Lmna* KO on lipid synthesis and accumulation, which contradict other *in vitro* studies discussed in the next section[106]. Loss of A-type lamins affects

chromatin positioning and genome stability leading to outcomes like mitochondrial damage and decreased respiration in *Lmna* KO MEFs.

1.6.2 Lamin KO in embryonic stem cells (ESCs), mesenchymal stem cells (MSCs), and other cellular models

Other *in vitro* studies of *Lmna* KO have used ESCs to study changes in chromatin organization, lamina assembly, and effects of lamin deficiency on cell differentiation. Interestingly, ESCs deficient of all lamins were able to proliferate, survive, and differentiate into fibroblast, neural, and cardiac lineages[107]. Study of *Lmnb1* and *Lmnb2* KO mouse ESCs (mESCs) by the Zheng group revealed that functional lamin B1 is required for targeting of lamin A/C into the nuclear lamina[108]. This same study also found that lamin A is required for normal emerin distribution within the nucleus. The Zheng lab went on to study mESCs that had all lamin proteins knocked out, and found that specific LADs were disrupted, and that lamins are crucial for maintaining active and repressive chromatin domains[109]. These studies once again highlight the role of lamins in organizing chromatin and controlling nuclear envelope function.

In similar studies to the Zheng group, independent work showed that haploinsufficiency of lamin A/C did not affect mESC pluripotency marker expression[110]. However, in contrast to the Zheng group, neuronal and myogenic differentiation was impaired in *Lmna* haploinsufficient mESCs[110]. Impaired differentiation has been shown in other lamin A/C-deficient cell types, like *Lmna* knockdown adipocytes differentiated from mESCs, which were not able to accumulate lipid[111]. In mESCs which were directed to differentiate into cardiomyocytes, premature cardiomyocyte differentiation occurred, along with abnormal contractility[112]. These cardiomyocyte defects were driven by major chromatin reorganization, with upregulation of cardiac morphogenesis genes in *Lmna* KO mESCs[112]. Contrary to previous studies mentioned, this study concluded that lamin A/C is crucial for maintaining pluripotency, specifically in cardiomyocyte differentiation[112]. Our lab has also explored effects of *Lmna* deficiency on adipocyte differentiation. We isolated mouse ear MSCs (eMSCs) from mice with floxed *Lmna* alleles ($Lmna^{fl/fl}$) and infected them with an adenovirus expressing GFP as a control or expressing Cre to induce *Lmna* KO. We added an adipocyte differentiation cocktail and saw no impairment of differentiation or lipid droplet accumulation up to day 28 of differentiation[113]. We did see a slight increase in isoproterenol or norepinephrine-stimulated glycerol release in *Lmna* KO adipocytes compared to controls, which may implicate lamin A/C in control of lipid

metabolism in cultured adipocytes. Taken together, the role of lamin A/C in cell differentiation and pluripotency maintenance is still controversial, and likely is regulated in a cell-type specific manner.

Beyond lamin A/C knockout, other groups have used a truncated lamin A mutant with a deleted N-terminus (ΔNLA), which has been shown to disrupt nuclear lamina organization and disrupts the existing lamin network, and also reduces DNA replication[114]. The ΔNLA mutant is thought to act in a dominant negative manner, which may be helpful in studying mechanisms of progerin pathology in HGPS. Cells injected with ΔNLA had disrupted splicing factor distribution and decreased transcription by disrupting RNA polymerase II activity[115]. Studying the pathology of a truncated lamin A has helped reveal knowledge about basic lamin biology and assembly.

1.6.3 Global Lmna KO mouse models

Cell culture models have many advantages, like the ability to use super resolution microscopy and migration assays to study cell biology. However, *in vivo* models using mice and other model organisms are one step closer to studying laminopathies in human patients. Two global *Lmna* knockout models have been created to study the role of lamin A/C *in vivo*: the first in 1999 by deleting *Lmna* exons 8 to part of 11 ($Lmna^{KO}$ mice),[86] and the next in 2011 using gene-trap disruption of the lamin A/C gene ($Lmna^{GTKO}$)[116]. $Lmna^{KO}$ mice had reduced growth rate, development of stiff walking posture and scoliosis, and death by eight weeks of age[86]. Histological analyses revealed muscular dystrophy and atrophy of myocytes, similar to EDMD[86]. $Lmna^{GTKO}$ mice largely showed the same phenotype as $Lmna^{KO}$ mice, including reduced growth and foraging behavior compared to controls, but died earlier, at 16-18 days postpartum (PP)[116]. Before death, $Lmna^{GTKO}$ mice had decreased blood glucose concentrations, hepatic glycogen storage, and increased usage of ketone bodies and free fatty acids[116]. Necropsy analyses of $Lmna^{GTKO}$ mice revealed cardiac hypertrophy and smaller myocyte size, and microarray analysis of ventricular tissue showed decreased gene expression related to fatty acid oxidation, muscle contraction, electron transport chain, and adipogenesis[116]. Skeletal muscles were hypotrophic and had reduced muscle strength at PP15 in KO mice compared to controls. Furthermore, subcutaneous WAT weights were decreased at PP14 in $Lmna^{GTKO}$ mice compared to controls, but gonadal WAT and BAT were unchanged in weights[116]. Taken together, lamin A/C is required globally for normal growth, health, and tissue differentiation.

Additional studies using global *Lmna* KO mice have been performed to better understand tissue-specific abnormalities upon loss of lamin A/C. Study of heterozygous $Lmna^{KO}$ mice, with one functional copy of *Lmna*, were studied in hopes of understanding FPLD2 pathology. At baseline or after challenge with an eight-week high-fat diet (HFD), heterozygous $Lmna^{KO}$ mice did not phenocopy human FPLD2, with presence of only minor metabolic abnormalities and no change in WAT weights[51]. Global deletion of p53 (*Trp53*), a regulator of DNA damage repair in $Lmna^{KO}$ mice did not improve longevity or muscle function, indicating that p53 activation is not a major driver of disease progression in $Lmna^{KO}$ mice[117]. Another study evaluated whether rapamycin would rescue the extreme phenotype of $Lmna^{KO}$ mice, and observed that rapamycin increased their body weight and fat mass,and doubled their truncated lifespan[118]. $Lmna^{KO}$ mice had increased lipolysis in their WAT compared to controls, which may be a contributor to their decreased adiposity; rapamycin treatment reversed this elevated lipolysis[118]. Many of these detailed studies about lamin A/C deficiency are interesting, but confounded by the runted size of $Lmna^{KO}$ mice, which increases the surface area to volume ratio, which alone can cause higher heat loss, increased metabolic rate, and a shorter lifespan[119]. The significance of this runted size is highlighted in the increased survival rate and body weight gain of $Lmna^{KO}$ mice when housed at 30°C instead of 22°C [118]. Therefore, changes in adiposity and muscle function are likely partially due to a primary effect of *Lmna* deficiency but are difficult to interpret when these mice undergo stunted growth and premature death.

Global deletion of lamin A and prelamin A in lamin C-only mice did not cause major disease phenotypes, suggesting that lamin A and prelamin A are dispensable in mice[120]. The same outcome occurred in lamin A-only mice, which did not show any pathology in mice[121]. When *Lmnb1* had an insertional mutation causing lamin B1 dysfunction, mutant mice died at birth, accompanied by abnormal lung development and impaired bone ossification[122]. Taken together, lamin A or lamin C alone are dispensable in mice, but global lamin A/C deletion causes muscular dystrophy, metabolic issues, and premature death. Functional lamin B1 is required for mouse development, underscoring its importance in embryonic and early life. The study of global lamin deficiency in mice have been informative in our understanding of their fundamental role *in vivo*.

1.6.4 Tissue-specific Lmna KO mouse models

With the advent of the Cre-LoxP system, generating tissue-specific knockout mouse models are now relatively easy and quick, allowing for more refined studies of gene/protein function in particular cell types. Multiple tissue-specific *Lmna* KO models have been created to understand the fundamental role of *Lmna* in homeostasis of tissues like heart, liver, and adipose. Sikder et al. created a model to knock out *Lmna* in cardiomyocytes specifically using a tamoxifen-inducible CreERT2 controlled by the *Myh6* promoter ($Lmna^{CMKO}$). In $Lmna^{CMKO}$ mice, fractional shortening and ejection fraction were decreased by four weeks post-tamoxifen, causing severe cardiomyopathy[123]. $Lmna^{CMKO}$ mice had myocyte hypertrophy, collagen deposition, and fibrosis, which was accompanied by breakdown of the nuclear envelope, Golgi swelling, and increased unfolded protein response (UPR)[123]. Perinuclear damage occurring in *Lmna* KO cardiomyocytes was driven by accumulation of autophagic markers, and development of cardiomyopathy was lessed by stimulating autophagy and targeting of endoplasmic reticulum (ER) stress[123]. Therefore, total loss of functional lamin A/C in cardiomyocytes causes nuclear and organelle damage, which leads to cardiomyopathy. These observations provide insight into molecular mechanisms of lamin-related diseases.

The Omary group studied the role of lamin A/C in the liver to investigate whether the hepatic steatosis observed in FPLD2 was solely because the liver serves as a storage depot for fatty acids due to the lack of WAT, or whether there is a primary effect of losing/changing lamin A/C function within hepatocytes themselves. Using Albumin-Cre, the authors knocked out *Lmna* in hepatocytes ($Lmna^{LKO}$) and observed deformed and blebbing hepatocyte nuclei[124]. By 14 weeks of age, male $Lmna^{LKO}$ mice developed liver injury and steatosis on a normal chow diet, with no change in circulating triglyceride concentrations. Challenge with HFD revealed dramatic lipid accumulation in $Lmna^{LKO}$ livers compared to controls, accompanied by liver injury, increased liver weight, and decrease of body weight[124]. Transcriptomic analyses revealed that lipid storage and inflammatory genes were upregulated in $Lmna^{LKO}$ livers. Specifically, STAT1 was upregulated at the RNA and protein level in male $Lmna^{LKO}$ livers, which may contribute to disease pathogenesis. Furthermore, *Lmna* KO hepatocytes had a blunted response to growth hormone signaling in male livers[124]. In summary, lamin A/C is crucial for maintaining hepatocyte nuclear shape, liver health, and modulating growth hormone, lipid metabolism, and inflammatory signaling. Lamin A/C is crucial not only for whole body homeostasis, but also for tissue-specific maintenance documented, to date, for the heart and liver.

Our lab has studied the fundamental role of *Lmna* in adipocytes to understand what goes awry in adipose tissue during FPLD2. We crossed *Lmna*$^{fl/fl}$ mice with Adiponectin-Cre mice to knock out *Lmna* specifically in adipocytes (*Lmna*^{ADKO}), and observed decreased WAT and BAT mass, and increased liver weights by 12 to 14 weeks of age in *Lmna*^{ADKO} mice compared to controls[113]. These changes were driven by a loss of adipocyte number in WAT and BAT, and remaining brown adipocytes had a white adipocyte-like appearance characterized by larger lipid droplets. *Lmna*^{ADKO} mice developed metabolic dysfunction, and had increased blood glucose, insulin, and triacylglycerol concentrations, and decreased adiponectin and leptin concentrations[113]. Surprisingly, considering the global lack of WAT mass, *Lmna*^{ADKO} mice were still glucose tolerant, though they developed insulin resistance and were metabolically inflexible. Challenge of *Lmna*^{ADKO} mice with HFD led to a worsening of metabolic dysfunction. Like patients with FPLD2, *Lmna*^{ADKO} mice developed adipose tissue postnatally, which was subsequently lost coincident with puberty when mice were four to six weeks old. One discrepancy between the *Lmna*^{ADKO} mouse model and patients with FPLD2 is that *Lmna*^{ADKO} mice had increased bone mass and decreased BMAT, whereas patients have decreased bone mass. Taken together, *Lmna*^{ADKO} mice recapitulate many phenotypes observed in patients with FPLD2, including loss of WAT and metabolic dysfunction, and underscores the importance of lamin A/C in adipocyte maintenance.

1.7 Studying disease mechanisms caused by *LMNA* variants

1.7.1 Pathogenic LMNA variants that cause laminopathies: structure and function relationship

Lamin A/C KO models have informed the field about the essential role of lamins, but do not recapitulate the genetic cause of laminopathies, which are usually missense variants that cause a single amino acid change in the *LMNA* gene. Before reviewing how *LMNA* variants disrupt cellular function, we wanted to understand how variants at residues could change lamin A/C protein function. Variants in the *LMNA* C-terminal Ig and tail domain cause multiple laminopathies, including EDMD, DCM, and FPLD2. Analyses of *LMNA* structure revealed that EDMD-causing variants likely destabilize the three dimensional structure of the C-terminus end[125]. Mutated residues that cause FPLD2, including R482Q/W, do not destabilize lamin A/C structure, but the loss of a positive charged amino acid changes its binding partners (**Figure**

1.4)[125]. A study characterized the crystal structure of the R482W variant which may lead to an allosteric effect, causing a conformational change that leads to a new aggregation state[126]. Fragment 411-553 of lamin A/C binds DNA, and variants in this region likely change lamin-DNA interactions which may also play a role in laminopathy pathology[127]. Another study characterized the variant *LMNA* S143F, which causes both progeria and muscular dystrophy in patients[128]. This variant did not change the coiled-coil structure or linear filament creation of lamin A/C. However, this variant did strengthen the X-shaped interaction between lamin filaments, leading to amplification of hydrophobic interactions and uneven rigidity within the nuclear lamina, which led to blebbing and aggregation of lamin filaments[128]. Therefore, *LMNA* missense mutations throughout the gene cause changes in protein conformation that alter interactions between lamin A/C and its nuclear binding partners.

Anderson et al. undertook a more broad approach in systematically analyzing 178 missense variants in *LMNA* across five structural domains which cause different laminopathies, including FPLD2, EDMD, and progeria[129]. The authors expressed these 178 variants in HEK293 and C2C12 myoblasts. They observed that of the variants in the coiled-coil domain (CCD), many of the skeletal and cardiac disease-associated variants formed nuclear aggregates, with few of the lipodystrophy and progeria variants causing aggregates. If *LMNA* mutations were in the Ig domain (IgD), many of the skeletal and lipodystrophy variants formed aggregates, with less of the cardiac and progeria variants forming aggregations. In silico analyses combined with *in vitro* solubility assays revealed that many IgD variants misfold, whether aggregation occurs or not. Anderson et al. showed that 80% of the skeletal and 47% of the cardiac-linked variants cause aggregation, which they propose is due to protein misfolding and faulty protein-protein interactions. A drawback of this study is that the authors overexpressed various *LMNA* variants rather than expressing variants at endogenous levels; overexpression of wild-type and mutated *LMNA* has been shown to inhibit adipocyte differentiation[106]. However, the Anderson et al. study helps further genotype-phenotype relations across laminopathies, and helps correlate variant positioning with disease.

There have been two hypotheses proposed for how *LMNA* variants cause different types of disease: the structural vs. the gene expression model[130]. In the structural model, most of the *LMNA* variants that cause EDMD and DCM are located within the rod domain between exons one and six, (**Figure 1.4**), a region crucial for lamin A/C structure, so some have proposed that

variants in this region alter nuclear integrity and mechanosensing. Alternatively, in the gene expression model, most of the *LMNA* variants that cause FPLD2 are located between exons seven and 12, which likely do not alter lamin structure, but are hypothesized rather to interrupt interaction sites between lamin A/C and chromatin or its other binding partners. Though the mechanisms of laminopathies are likely not this simple, the connections between *LMNA* variant site and alterations in protein function could be an important factor in explaining the tissue-specificity for different laminopathies.

1.7.2 LMNA R482 variants in vitro

Many missense variants across *LMNA* have been studied using cell culture systems. Of the FPLD2-causing variants, mutations at R482 are the most studied, with one of the first articles analyzing effects of R482Q/W on differentiation of mouse 3T3-L1 preadipocytes[106]. Overexpression of either variant and wild type lamin A/C inhibited adipocyte differentiation, with cells unable to undergo *de novo* TAG synthesis, accompanied by decreased expression of *Glut4* and *Pparg2*. Due to similar effects seen with overexpression of wild type and mutated lamin A/C, it is clear that stoichiometry of lamins is important and is a cautionary note to keep in mind for other overexpression studies. Molecular analyses of *LMNA* variants by Lloyd et al. have been carried out in 3T3-L1 cells via a yeast two-hybrid interaction screen, which revealed sterol response element binding protein (SREBP1) as a lamin A/C binding partner[131]. The authors then expressed disease-causing *LMNA* variants in HeLa cells, which resulted in a decreased interaction of R482W lamin A to SREBP1 by 25-45%, and an EDMD variant decreased lamin A-SREBP1 binding by 62%[131]. This change in lamin-SREBP1 interaction may disrupt SREBP1 transcriptional activity potentially explaining differentiation disruptions in adipocytes harboring *LMNA* variants.

Beyond mouse cells, groups have utilized cells from patients with FPLD2 to study FPLD2 disease mechanisms. Using skin fibroblasts isolated from a *LMNA* R482L patient, Capanni et al. showed that prelamin A accumulates in patient fibroblasts in the nucleoplasm and is bound to SREBP1[132]. In contrast to the previously mentioned study by Lloyd et al., this study showed that SREBP1 did not co-precipitate with lamin A/C in patient fibroblasts. Capanni et al. goes on to conclude that prelamin A sequesters SREBP1 at the nuclear periphery, which decreases *Pparg* expression and reduces pre-adipocyte differentiation[132]. Therefore, SREBP1 may be implicated in FPLD2 disease progression, but data about its interaction with prelamin A

vs. lamin A/C are contradicting, and likely depends on cell type used for *in vitro* studies. Prelamin A has also been implicated in human endothelial cells overexpressing *LMNA* R482W, as it accumulates abnormally at the nuclear envelope, inducing endothelial dysfunction, senescence, oxidative stress, and inflammation[133]. These alterations were prevented by targeting of prelamin A to the nucleoplasm, suggesting that prelamin A accumulation at the nuclear periphery is toxic to endothelial cells, a potential explanation of *LMNA* variants having a primary effect in causing cardiovascular dysfunction in patients with FPLD2[133]. Another protein called fragile X-related protein 1 (FXR1P) has been shown to interact with lamin A/C. FXR1P is upregulated and redistributed in *LMNA* R482W FPLD2 patient fibroblasts, and upregulation of FXR1P in healthy adipose stem cells was sufficient to block adipogenesis and stimulate myogenic gene expression[134]. Therefore, various lamin A/C binding partners including SREBP1, prelamin A, and FXRIP may play a role in disrupting adipogenesis and causing cellular dysfunction.

A follow-up study about FXR1P and lamin A/C from the Collas group found that miR-335, a promyogenic and anti-adipogenic miRNA, upregulates *Fxr1* (FXR1P gene) expression[135]. In human adipose stem cells, expression of *LMNA* R482W upregulated miR-355, and decreasing miR-355 back to normal expression levels rescued impaired adipocyte differentiation in R482W cells. Chromatin immunoprecipitation sequencing (ChIP-seq) revealed that lamin A/C is bound to the *MEST/MIR355* locus and maintains a repressive chromatin state, as confirmed by knockdown of *LMNA* in adipose stem cells which led to miR-355 upregulation. In R482W-expressing stem cells undergoing adipogenesis, lamin A/C no longer associated with the *MIR355* promoter, indicating that the *LMNA* R482W variant interferes with the lamin A/C-miR355 interaction. In variant cells, acetylation of two enhancer elements caused *MIR355* overexpression, rather than lamin A/C directly affecting miR355 expression. Therefore, lamin A/C is essential for chromatin rearrangement, specifically in control of miR355 expression, which can affect adipocyte differentiation. This study provides a detailed and mechanistic look into how specific loci and lamin A/C interact, but the exact mechanism *in vivo* by which adipocytes are lost during FPLD2 has still not been elucidated.

Patient skin fibroblasts containing the *LMNA* R482Q/W heterozygous variants had dysmorphic nuclei and a disorganized lamina network, which was not due to an arrest in cell cycle or apoptosis[136]. FPLD2 fibroblasts also had abnormal localization of inner nuclear

membrane proteins like emerin, LAP2b, and nucleoporin Nup153, observed in two separate studies[136,137]. Presence of the *LMNA* R482L variant also caused nuclear blebbing and altered differentiation in human cells[138]. Study of WAT-derived preadipocytes from patients with FPLD2 (R482Q/W) agreed with skin fibroblast studies, as these FPLD2 nuclei also had abnormal emerin localization and nuclear shape deformities, along with prelamin A accumulation at the nuclear envelope[139]. Therefore, *LMNA* R482 variants cause nuclear envelope disorganization *in vitro*.

Furthermore, control WAT stromal vascular cells (SVCs) were treated to induce prelamin A accumulation, and were then transfected with *LMNA* R482Q to mimic FPLD2 patient cells (FPLD2-like): this study revealed that variant cells had a block in autophagic activity, possibly due to dysregulation of p70 S6 kinase, key in mTOR signaling[139]. These FPLD2-like cells also had reduced adipogenic capacity, decreased lipid droplet size, and increased mitochondrial number compared to control cells. In this same study, adipose tissue collected from the parathyroid neck region of patients with FPLD2 was positive for BAT markers PRDM16 and UCP1. Parathyroid FPLD2 SVCs had higher brown and white adipocyte differentiation capacity compared to control cells. Taken together, these *in vitro* studies suggest that autophagy is impaired in white adipocytes with FPLD2-causing *LMNA* variants, and that neck brown preadipocytes from FPLD2 patients may be easily programmed to become white adipocytes, a possible explanation for adipose expansion in the neck in FPLD2[139]. Though this study suggests detailed disease mechanisms, the use of FPLD2-like cells rather than detailed analysis of precursors from FPLD2 patients themselves may be a confounding factor in experimental interpretation. Also, the collection of biopsies to study browning were taken from the parathyroid region, which is known to have features of BAT, but is just a small subset of adipose around the upper neck and face that expands with FPLD2, which has been typically considered to be WAT. Though these studies of adipose browning in FPLD2 are enlightening, it likely only explains a small portion of how the upper neck and face adipose expands.

Other *in vitro* studies surrounding the R482 variant have been performed using inducible pluripotent stem cells (iPSCs). Friesen and Cowan studied iPSCs created from R482W patient skin fibroblasts, and saw no change in pluripotency with *LMNA* variants, similar to *Lmna* KO mESC studies[140]. Following iPSC adipocyte differentiation, *LMNA* R482W adipocytes had decreased adipogenic capacity, reduced adipocyte marker gene expression, and decreased

adiponectin secretion. Consistent with our group's *Lmna* KO eMSC adipocytes, Friesen and Cowan saw increased stimulated lipolytic capacity after isoproterenol stimulation in R482W adipocytes compared to controls. Maximum oxygen consumption and markers of autophagy were also increased in R482W adipocytes. The Stone group has also used *LMNA* variant iPSCs, but programmed by CRISPR/Cas9 gene editing to knock-in the *LMNA* R482W variant[140]. Like Friesen and Cowan, the Stone group observed decreased adipocyte differentiation and lipid droplet accumulation in variant cells compared to controls, along with decreased glucose uptake. However, Seahorse XR analysis demonstrated decreased maximal oxygen consumption, in contrast to Friesen and Cowan. RNA-seq of the R482W variant cells showed a decrease in adipogenic transcripts compared to control cells. Taken together, *LMNA* R482W iPSC studies demonstrate decreased adipogenesis, but are conflicting about mitochondrial function. Nonetheless, this approach is a useful new model of FPLD2 pathogenic variants to study disease mechanisms *in vitro*.

1.7.3 Other LMNA variants in vitro

Much *in vitro* work has been conducted on the *LMNA* R482 variant hotspot, but also at other amino acid residues that cause FPLD2 and other laminopathies. In patients, the *LMNA* R133L variant causes generalized lipoatrophy, diabetes, and focal segmental glomerulosclerosis. When 3T3-L1 cells expressed R133L, their nuclei had disrupted shape, were varied in size, and exhibited membrane blebbing[141]. *LMNA* R133L adipocytes were unable to accumulate lipid upon adipogenic stimulation, and *Pparg, Srebp1,* and *Scd1* transcripts were not induced. Similarly, primary human preadipocytes containing the *LMNA* T528M variant failed to differentiate, had decreased adipogenic gene expression, and accumulated prelamin A[142]. Skin fibroblasts from patients harboring the *LMNA* FPLD2-causing variant R439C had increased nuclear blebbing, but localization of emerin was normal, and prelamin A did not accumulate within variant nuclei[143]. Further studies of the mutant R439C protein showed increased binding between lamin A/C and DNA compared to wild type lamin A/C, and that R439C fibroblasts have increased reactive oxygen species (ROS) production[143]. Finally, other FPLD2-causing variants G465D and K486N reduced SUMOylation on the lamin A tail compared to controls, which likely disrupts SUMO-dependent lamin A/C functions[144]. Therefore, FPLD2-causing variants across *LMNA* reduce adipocyte differentiation *in vitro*, often accompanied by decreased adipogenic gene expression, which may explain part of why patient WAT is unable to be maintained in FPLD2.

Studying effects of *LMNA* variants within other laminopathies may prove to help explain molecular mechanisms of FPLD2. A recent study by Qiu et al. studied a frameshift mutation that causes DCM, *LMNA* A388fs, which when expressed in iPSCs differentiated into cardiomyocytes, caused arrythmias and abnormal Ca^{2+} handling[145]. These variant cardiomyocytes had swollen mitochondria, decreased maximum oxygen consumption, and increased ROS production, driven by accelerated SIRT1 degradation. Furthermore, the elevated ROS led to an upregulation of SUN1, causing nuclear envelope deformation like a previously mentioned model of *Lmna* KO *in vitro*[96,145]. Other DCM variants like *LMNA* L35P, R249Q, and G449V, have been studied using iPSC lines; these cells are able to differentiate into cardiomyocytes normally but have decreased lamin A/C expression, altered nuclear structure, and increased nuclear envelope rupture[146]. In these variant iPSCs, the proposed mechanism of nuclear damage starts with mislocation of lamin A/C, which changes nuclear shape and size, leading to nuclear envelope rupture, potential DNA damage, and eventual cardiomyocyte health decline[146]. Clearly, DCM-causing *LMNA* variants cause dysfunctional mitochondria and nuclear envelope abnormalities, but their role in altering chromatin architecture may also be important in disease pathogenesis. A study from the Jain group introduced *LMNA* T10I and R541C variants into iPSCs and differentiated variant cells into cardiomyocytes. Variant cardiomyocytes had reduced contraction *in vitro,* accompanied by defective nuclear structure and reduced presence of repressive histone mark H3K9me2[147]. ChIP-seq analyses revealed that subsets of LADs were affected with T10I and R541C variants, specifically those with high gene density and lower lamin B1 contact frequency. Altered LADs were close to shared LADs (unaffected LADs in control and variant iPSCs). When these variants were expressed in iPSCs that were differentiated into hepatocytes and adipocytes, the same LAD remodeling was not observed, underscoring the cell-type specificity for chromatin-lamina interaction disruptions dependent on *LMNA* variant[147]. In summary, DCM-causing *LMNA* variants likely lead to disease through cell-wide changes, including alteration of gene expression important for cell fate and identity.

Cell culture studies of primary myoblasts containing EDMD-causing *LMNA* variants like N195K and H222P showed that variant myofibers had decreased contractility, viability, and number of myonuclei, and had increased caspase-3 activity[148]. These functional defects were accompanied by reduced nuclear stability, chromatin protrusions, and nuclear envelope rupture. Myonuclei that had chromatin protrusions also had increased positive gH2AX staining, showing

elevated DNA damage, with *LMNA* N195K-containing cells more prone to DNA damage than H222P cells[148]. These data align with an earlier study of mouse cells overexpressing EDMD variant *LMNA* R453W, in which mutated nuclei had increased intranuclear lamin aggregates and irregular perinuclear lattices[137]. Additionally, patient fibroblasts with this R453W variant had abnormal distribution of both A- and B-type lamins compared to control cells[137]. Expression of EDMD *LMNA* variant R386K in COS7 cells similarly caused lamin A/C nuclear aggregation, with aggregates even forming outside of the nuclear envelope[149]. Beyond EDMD, *LMNA* variants can also cause a more severe form of muscular dystrophy called congenital muscular dystrophy (CMD), which has also been studied *in vitro.* Proteomics profiling of patient myoblasts and myotubes with CMD *LMNA* variants R249W, del.32K, and L380S variants showed that variant cells had increased necroptosis, altered carbohydrate metabolism, and synaptogenesis compared to control cells[150]. Mouse cells with these CMD variants had mislocalized emerin and NETs, which may be contribute to the observed gene and protein expression changes[151]. Taken together, EDMD and CMD-causing *LMNA* variants cause sensitivity to mechanostresses, changes in chromatin and lamina organization, and dysfunctional nuclear envelope protein localization and integrity. These studies of other non-FPLD2 *LMNA* variants may prove to be relevant areas of investigation for study of FPLD2 disease mechanisms.

Much work has been conducted on understanding disease mechanisms of HGPS which are better understood than that of the other laminopathies, especially relative to FPLD2. HGPS fibroblasts with the *LMNA* G608G variant display multiple signs of cellular dysfunction, including abnormally shaped nuclei, increased ROS, and decreased DNA damage repair[152]. These cells also have impaired mitochondrial function, increased cellular senescence, and elevated secretion of proinflammatory cytokines like IL-6 and TNFa[153]. Furthermore, similar to other changes observed upon *Lmna* KO *in vitro*, HGPS patient cells had a subset of phosphorylated lamin A/C binding sites lost across the genome, with new binding of phosphorylated lamin A/C to loci that are typically quiescent; these changes led to upregulation of genes linked to progeria phenotypes[154]. Though the dysfunction observed in HGPS cells are likely due to progerin acting in a dominant-negative manner, it is compelling that disruption of the nuclear lamina in HGPS still shows molecular similarities to other laminopathies studies.

1.7.4 LMNA FPLD2 variants in vivo

To study mechanisms of FPLD2, two groups have made mouse models to study the effect of lamin A/C pathogenic variants *in vivo*. The first was in 2009 by Wojtanik et al., who overexpressed human R482Q lamin A, driven by the aP2 (FABP4) promoter (FPLD mice)[155]. After over 32 weeks of HFD challenge, FPLD mice had lower body weights and less fat mass accumulation compared to control mice, which were not driven by changes in food intake. Epididymal WAT, perirenal WAT, retroperitoneal WAT, and BAT depots were reduced in size in FPLD mice relative to controls when mice were ~1 year old. These phenotypes were not due to the overexpression of lamin A, as the authors also made a wild type lamin A overexpression mouse, which did not have the same lipodystrophy phenotype. FPLD mice had hepatic lipid accumulation, insulin resistance, and reduced thermogenic capacity. Studies on isolated adipocytes or differentiated primary stromal vascular fraction (SVF) showed no change in lipolytic capacity from FPLD mice, but did show defects in adipocyte differentiation and lipid accumulation *in vitro*. Therefore, this FPLD mouse model had a mild lipodystrophy phenotype upon HFD challenge, which was potentially due to a defect in adipogenesis. This study has many caveats, including 1) the need for aged/HFD-challenged mice to observe a lipodystrophy phenotype, 2) use of the aP2 promoter, which is expressed in not just WAT but also macrophages, 3) overexpression of the variant, and 4) the R482Q variant being overexpressed in only lamin A and not both lamin A and C. Caveats aside, this study of *LMNA* variants rather than global or tissue-specific knockouts is helpful for the field in increasing translatability of mouse models and understanding lamin biology *in vivo*.

In 2017, the Worman group created another *LMNA* transgenic mouse model, again overexpressing human lamin A R482Q or wild-type lamin A using the aP2 promoter[156]. Even after HFD challenge, these transgenic mice did not develop lipodystrophy or have changes in circulating lipids, though female R482Q lamin A mice had a trending impairment of glucose tolerance compared to controls. When this R482Q lamin A mouse model was compared to the previous Wojtanik et al. FPLD mouse model, the authors found that the FPLD mice had a 8.5 fold increase in R482Q lamin A expression, whereas the Worman et al. R482Q lamin A mice had a 5 fold increase in expression compared to controls. This discrepancy in lamin A amount may dictate whether lipodystrophic phenotypes occur in mice. Further analysis of the R482Q lamin A mouse WAT showed an increase in extracellular matrix (ECM) and fibrosis deposition, even in the absence of lipodystrophy, suggesting that increased ECM may be an important role in

FPLD2 pathogenesis before WAT loss. Supporting these data, R482Q mouse WAT had increased TGFβ1 signaling, which was confirmed to be upregulated in human subcutaneous FPLD2 WAT. This study helps highlight some of the underlying reasons for phenotyping discrepancies between different mouse models, along with giving light to some potential mechanisms of FPLD2 pathology. This study has many of the same experimental caveats as the Wojtanik et al. study, calling attention to the need for more sophisticated mouse models to study FPLD2.

1.7.5 Other laminopathy-causing LMNA variants in vivo

Animal models have been created with a variety of *LMNA* variants to study disease mechanisms of laminopathies, often focused on recapitulating muscular dystrophy and cardiomyopathies. One model that mimics human striated muscle laminopathies closely is the knock-in *Lmna* H222P mouse, in which homozygous H222P/H222P mice had reduced growth rate compared to controls, a hunched back, and premature death between four to nine months of age, whereas heterozygous H222P/+ mice were healthy[157]. H222P/H222P mice developed DCM and muscular dystrophy but not lipodystrophy. Part of the pathologic phenotype may be driven by increased phospho-Smad2/3 in H222P/H222P myonuclei compared to controls, associated with increased fibrosis through TGFb signaling. Interestingly, male variant mice had an earlier-onset DCM and muscle phenotype compared to females, which may elucidate some sex-differences in laminopathy presentation. Another study of the H222P/H222P mice found that MAPK pathways were upregulated in variant mouse hearts compared to controls, leading to JNK and ERK activation, proposed to be part of DCM pathology[158].

Related was the creation of a mouse model with a-MHC driven expression of M371K lamin A (typically an EMDM-causing mutation), in which variant mice died by two to seven weeks of age and had cardiac lesions, eosinophilia, and fragmentation of cardiomyofibrils[159]. Mice with the homozygous *Lmna* N195K variant also developed DCM and died prematurely, accompanied by disruption of gap junction proteins and disorganized sarcomeres and intercalated disks[160]. DCM variant *Lmna* R541C knocked into mice caused ventricular dilation and reduced systolic functions, accompanied by increased heterochromatin amount, disorganized mitochondrial organization, and reduced oxidative respiration compared to controls[161]. Additionally, the CMD-causing mutation *Lmna* del.32K in mice caused reduced growth, abnormal gait, and premature death by three weeks after birth, with presence of skeletal muscle

and cardiac maturation defects[162]. In livers from *Lmna* del.32K variant mice, expression of SREBP1 and its target genes were reduced, suggesting that mutated lamin A/C may disrupt SREBP1 transcriptional activity. This disruption may have implications for WAT and FPLD2 in that SREBP1 is known to bind to lamin A/C[131]. Finally, another EDMD variant, *Lmna* L530P, has been expressed in mice, which caused progeroid symptoms rather than muscular dystrophy[163]. New studies are now using *Lmna* variant mice, like those with CMD-causing R249W, to try CRISPR/Cas9-mediated gene therapy to correct variants *in vivo*, which can improve survival and health[164]. In summary, many of the EDMD and DCM-causing lamin A/C genetic variants, when expressed in mice, phenocopy many characteristics of human disease, proving to be a valuable tool to study disease mechanisms. Interestingly, these variants seem to cause more severe disease in mice than expression of *LMNA* variants that cause FPLD2, which may highlight functional differences between mouse and human lamin A/C specifically at residues implicated in FPLD2.

Study of HGPS has been advanced by the creation of homozygous *Lmna* G609G/G609G mice, which have clinical features of HGPS, progerin accumulation across different tissues, and nuclear shape abnormalities[165]. These mice also have reduced circulating glucose, insulin, leptin, and IGF-1 concentrations, accompanied by increased growth hormone and adiponectin. Transcriptomic analyses of livers from variant mice revealed upregulation of stress response pathways and decreased expression of fatty acid metabolism, oxidative phosphorylation, and mitochondria biogenesis[165]. The authors utilized antisense oligonucleotides to reduce progerin concentrations, which drastically improved mouse health and extended lifespan. Another knock-in mouse model in which a non-farnesylated progerin protein was created globally also recapitulated human HGPS[166]. Though the phenotype of these discussed HGPS mouse models is severe, their metabolic dysfunction and hepatic transcriptomic changes may prove to be a helpful comparison for FPLD2 study *in vivo*.

Motor and sensory neuropathies, like CMT2, have also been studied using mouse models. The CMT2 *Lmna* R298C variant was knocked into mice, and homozygous variants did not recapitulate peripheral neuropathy signs seen in patients: muscle strength, motor ability, and pain sensitivity were normal in homozygous R298C/R298C mice[167]. Though these knock-in mice were phenotypically normal, analyses at the molecular level revealed an increase in *Pmp22* expression in sciatic nerves of variant mice, and a decrease in *Lmna* transcripts in all tissues

compared to controls. Though the mechanisms leading to these gene changes are yet to be elucidated, this mouse model is an example of a laminopathy mouse model failing to phenocopy human disease. This highlights the physiological differences between mice and humans including tissue size difference, mouse lifespan, and inbred genetics, all of which likely contribute to the lack of disease recapitulation.

As an alternative model for studying laminopathies, Zhang et al. sought to study otitis media (OM), a disease that causes eustachian tube dysfunction and potential hearing loss. Symptoms of OM can accompany HGPS, suggesting that OM may be related to laminopathies. Therefore, the authors studied the *Lmna*^{Dhe} mutation, a spontaneous mutation, *Lmna* L52R, that causes "disheveled hair and ears," small skull formation, hypomineralized bones, and reduced body fat[168]. Further study of the *Lmna*^{Dhe} mice revealed abnormal middle ear anatomy, increased middle ear inflammation, and impaired epithelial cilia compared to control mice[169]. Peritoneal macrophages from *Lmna*^{Dhe} mice had impaired nuclear meshworks, larger nuclear volumes, and signs of macrophage activation, implicating this *Lmna* variant in nuclear dysfunction. Taken together, the *Lmna*^{Dhe} mice exhibit signs of OM pathology, along with other molecular features of laminopathies, which may serve as an alternative model to the other discussed models here.

Beyond mice, Luo et al. generated a primate model of DCM in hopes of understanding disease mechanism to create new targeted drugs for DCM[170]. Transgenic cynomolgus monkeys were generated harboring the *LMNA* c.357-2A>G splice-site variant, which caused a decrease in cardiac function, increased ventricle dilation, and arrythmia. Histologic analyses of cardiac tissue showed that primates with the *LMNA* variant had deformed cardiomyocyte nuclei and increased fibrosis, like that of human DCM patient hearts. Finally, RNA-seq analyses revealed upregulated inflammation and extracellular matrix genes, and downregulated cardiac conduction, respiration, and fatty acid oxidation processes. Using primates to study laminopathies is a helpful improvement for the field not just to simulate not just clinical symptoms, but also to study disease progression over a much longer lifespan than mice.

1.8 Human tissue experiments to study mechanisms of FPLD2

Studies reviewed thus far span cell culture, mouse models, and primates upon lamin A/C knockout or mutation, which have proved to reveal many mechanistic insights of disease pathogenesis. However, working with and analyzing human tissue from patients with disease are still the gold standard. Few studies have been able to collect biopsies from patients with FPLD2,

due to its rarity and patients having vanishingly small amounts of adipose tissue. Comparison of abdominal and thigh subcutaneous adipose tissue between patients with FPLD2 and controls revealed reduced expression of genes like *PPARG2, LPL, RB1, CCND1, GLUT4* in patients with FPLD2[171]. No differences were observed in *SREBP1* expression between patients and controls. Prelamin A expression was also increased in WAT from patients with FPLD2. Electron microscopy analyses revealed that adipocytes in FPLD2 biopsies had heterochromatin defects with a fibrous dense lamina. Therefore, in WAT depots that are lost in patients with FPLD2, remaining adipose tissue has reduced lipid metabolism gene expression and disrupted nuclear shape.

Others have also studied dorsocervical subcutaneous WAT (dsWAT) which typically expands with FPLD2. A study analyzed dsWAT from patients with FPLD2, and saw that patient WAT had heterogenous adipocyte morphology, decreased adipocyte size, and increased fibrosis[172]. The authors saw that SREBP1, UCP1, and prelamin A protein expression was increased and PPARg was decreased in FPLD2 biopsies compared to controls. Electron microscopy analyses revealed increased mitochondria number, so the authors concluded that the dsWAT expanded in patients with FPLD2 is more BAT-like rather than WAT-like. Study of the parathyroid neck WAT showed a similar phenotype, with patient neck WAT having an intermediate BAT phenotype compared to control biopsies[139]. Additionally, another study of dsWAT also showed increased fibrotic tissue deposition and increased *TGFB1* and *CTGF* mRNA expression compared to control biopsies[156]. Taken together, these studies of dsWAT and neck WAT reveal that in FPLD2, areas of WAT expansion have altered adipocyte morphology, increased fibrosis, and may be more BAT-like. These studies help further the field but are limited by a small patient number, along with a wide range of genotypes, sexes, and ages, making it difficult to make large conclusions about phenotypic and molecular changes within WAT.

1.9 New studies to fill in existing knowledge gaps

As outlined in this dissertation chapter, the last three decades have been instrumental in identifying and characterizing FPLD2 and other laminopathies, along with studying basic lamin biology and mechanisms of disease, as summarized in **Figure 1.5**. However, multiple questions remain unanswered about FPLD2, which I aim to study in this dissertation.

1) Building off our lab's previous work[113]: why is lamin A/C required for adipocyte maintenance? How exactly are adipocytes lost when lamin A/C is knocked out?

2) What changes occur in WAT from patients with FPLD2 morphologically and transcriptionally? Can we use insights from biopsy studies to reveal FPLD2 disease mechanisms?

3) Can we identify new treatments to treat the metabolic dysfunction associated with FPLD2? Is gene therapy a viable option for patients to improve health?

4) We need more sophisticated mouse models to study FPLD2 to ask: how do global *Lmna* variants in mice lead to FPLD2 and other laminopathies?

This dissertation will aim to provide answers to the questions above to further our understanding of FPLD2 mechanisms, and more broadly, to improve our fundamental knowledge of lamin biology and adipose tissue.

1.10 Figures and legends

Figure 1.1

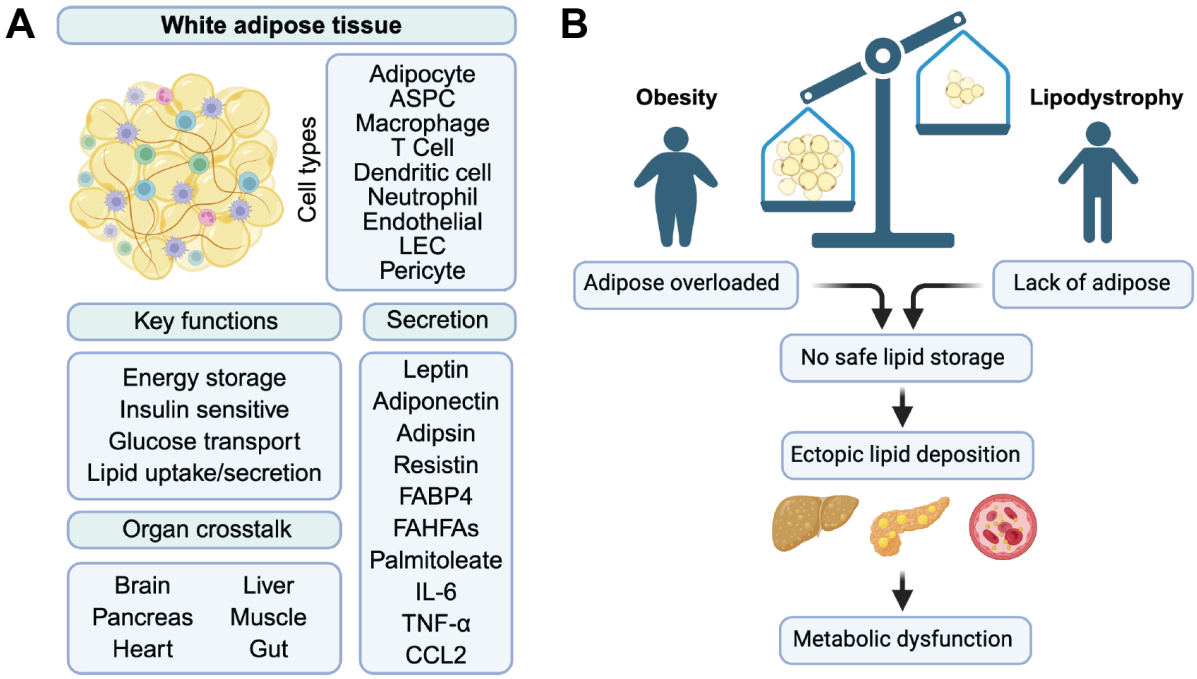


Figure 1.1. Adipose tissue is a key metabolic organ, and obesity and lipodystrophy are caused by an imbalance of adipose tissue amount and impaired function. (**A**) White adipose tissue (WAT) is the most abundant type of adipose tissue in the body, comprised of multiple cell types beyond adipocytes like adipose stem and progenitor cells (ASPCs), immune cells like macrophages and T cells, and endothelial and lymphatic endothelial cells (LECs). WAT has multiple key functions including storing energy in the form of triacylglycerols (TAGs) and orchestrating lipid uptake and breakdown. WAT is also an endocrine organ, and secretes many adipokines like leptin, adiponectin, and adipsin, along with fatty acid binding protein 4 (FABP4) and fatty acid esters of hydroxy fatty acids (FAHFAs). These adipokines and other cytokines (interleukin 6 (IL-6), tumor necrosis factor alpha (TNFα) and C-C motif chemokine ligand 2 (CCL2)) can crosstalk with other organs like the brain, liver, and heart to influence metabolism. (**B**) Obesity is caused by excess adipose tissue, which causes WAT to become overloaded with lipid, unable to expand further, which causes ectopic lipid deposition and metabolic dysfunction. Lipodystrophy, a rare disease that causes a loss of adipose tissue, leads to the same deficiency in a safe lipid storage depot, causing the same metabolic dysfunction as observed in obesity. Figure adapted from Lim et al. 2021.

Figure 1.2

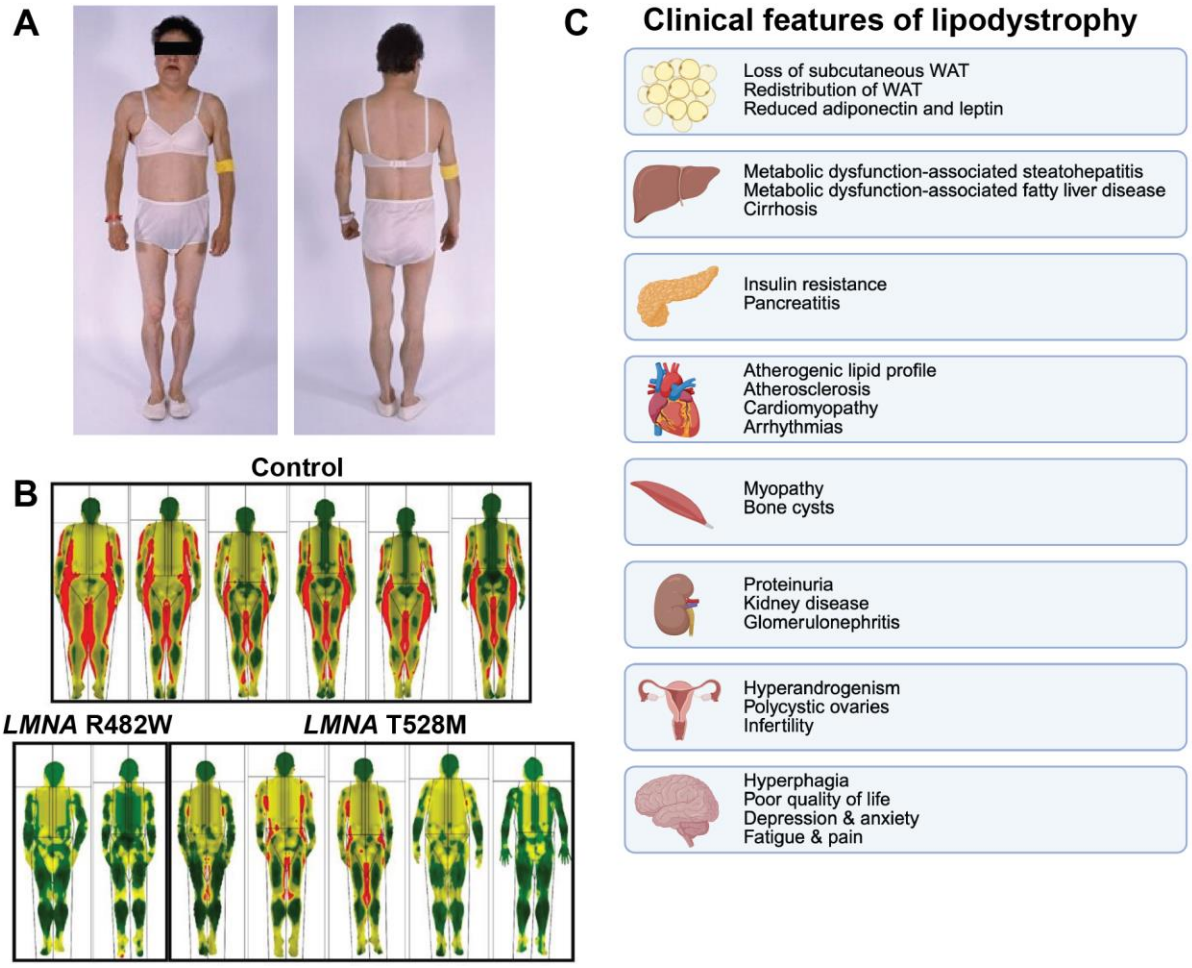


Figure 1.2. Familial partial lipodystrophy 2 (FPLD2) is caused by mutations in LMNA, leading to adipose tissue loss and redistribution and many clinical features, including metabolic dysfunction and cardiac issues. (**A**) Patient with FPLD2 showing pattern of adipose tissue loss and redistribution. Picture from Akinci et al. 2018. (**B**) Dual energy X-ray absorptiometry (DEXA) scans of adipose tissue distribution in control patients or patients with FPLD2 (either harboring *LMNA* R482W or T528M variant. Red = areas of high adipose, yellow = areas of medium adipose, green = areas of low adipose tissue. Data from Araujo-Vilar et al. 2021. (**C**) Clinical features of FPLD2 affecting different peripheral and central organs. Data from Akinci et al. 2018.

.

Figure 1.3

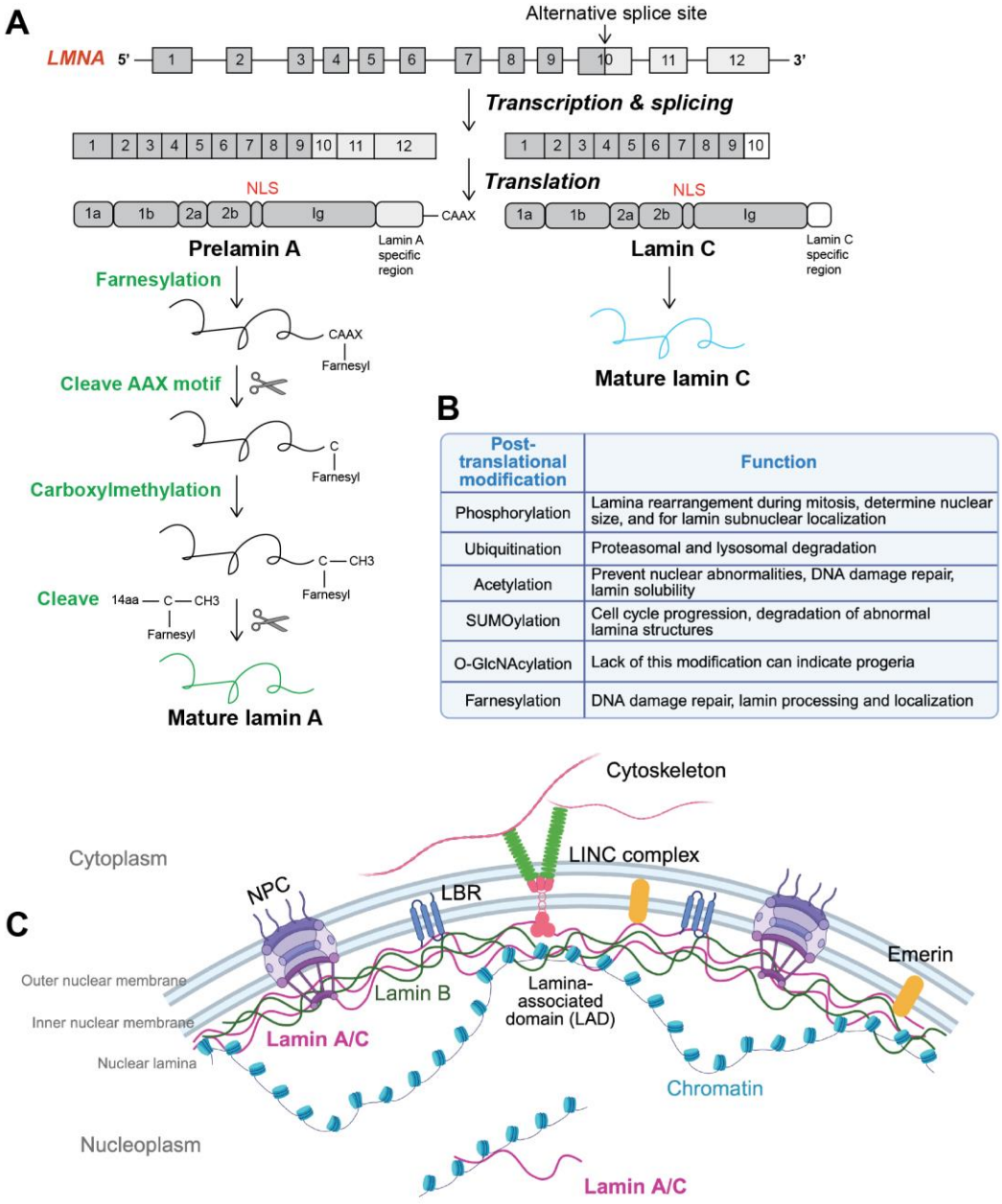


Figure 1.3. Lamin A/C undergoes post-translational processing and modifications to be assembled into the nuclear lamina to influence nuclear stability and structure, and to associate with chromatin to affect gene expression. (**A**) The lamin A/C gene, *LMNA*, encodes both lamin A and lamin C, which are alternatively spliced. Prelamin A, the precursor to mature lamin A, undergoes multiple post-translational processing steps to reach its final form. Alternatively, lamin C is translated as its mature form without post-translational processing. (**B**) Both lamin A and C undergo multiple post-translational modifications including phosphorylation and acetylation to allow for normal function, data from review by Zheng et al. 2022. (**C**) Schematic of lamin A/C within the nucleus as part of the nuclear lamina. Lamin A/C interacts with nuclear pore complexes (NPCs) to control nuclear transport, with other transmembrane proteins like emerin and lamin B receptor (LBR), and indirectly with the cytoskeleton through the Linker of Nucleoskeleton and Cytoskeleton (LINC) complex. Finally, lamin A/C interacts with chromatin at lamina-associated domains (LADs), typically gene-poor regions of heterochromatin. Figure adapted from Gaillard and Reddy 2018.

Figure 1.4

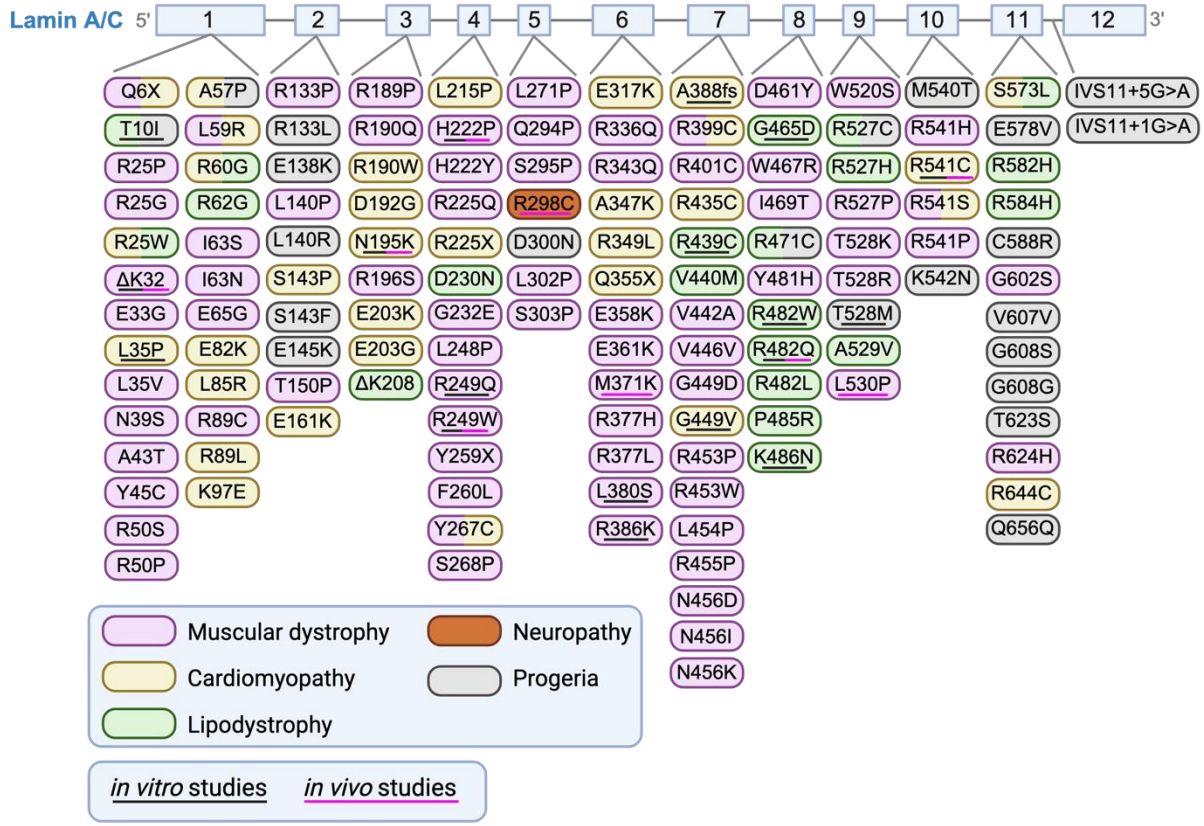


Figure 1.4. Variants throughout LMNA cause a wide spectrum of laminopathy diseases beyond FPLD2. Map of amino acid mutations that cause different diseases in patients, like muscular dystrophy (pink), cardiomyopathy (yellow), lipodystrophy (green), neuropathy (orange), and progeria (gray). Boxes with two colors (e.g. yellow and green) indicate that *LMNA* variant causes both disease phenotypes. Variants with a black underline indicates published *in vitro* studies in the literature, and a magenta underline indicates *in vivo* studies. If variants are underlined with both black and magenta, both *in vitro* and *in vivo* studies are published. Adapted from Mckenna et al. 2013.

Figure 1.5

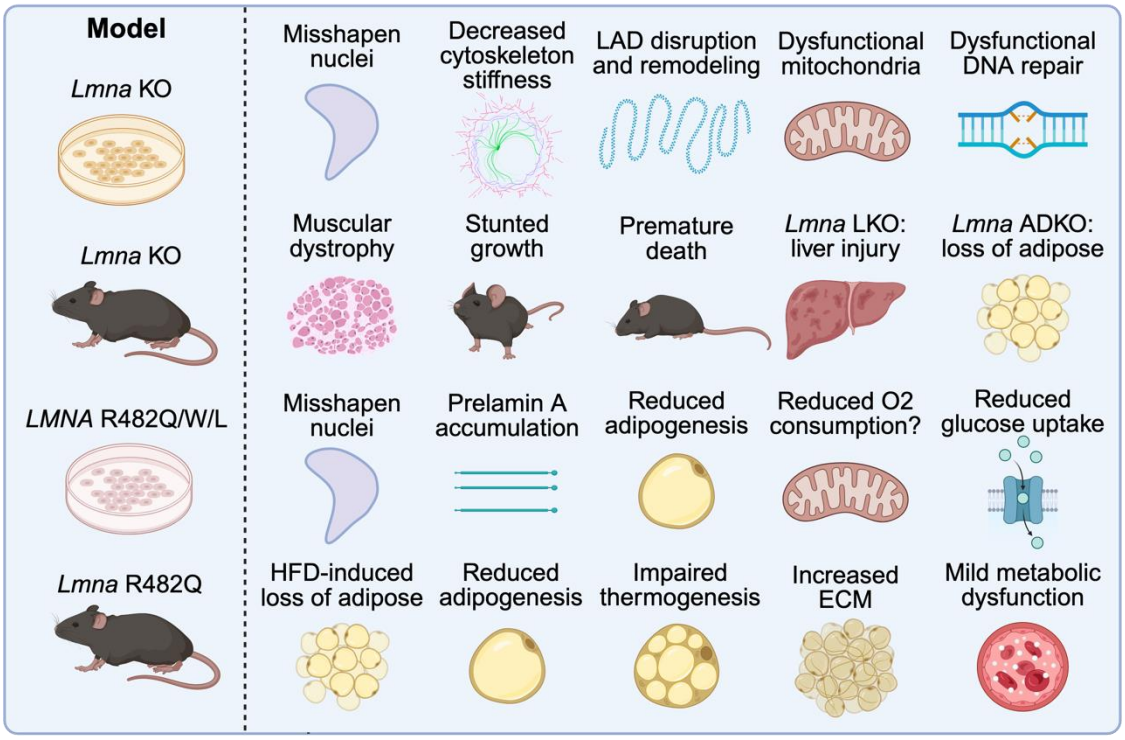


Figure 1.5. Summary of key literature findings about lamin A/C knockout (KO) and variant models. Many studies have explored the effects of *Lmna* KO in culture or *in vivo*, which leads to nuclear abnormalities, dysfunctional mitochondria, and premature death in mice. Variant studies investigating the common R482 residue site for mutations also show nuclear abnormalities *in vitro* along with reduced adipogenic capacity. Mouse models harboring the *Lmna* R482Q variant lose adipose tissue, albeit a mild phenotype, and have increased extracellular matrix (ECM) deposition in WAT.

1.11 References

1. Richard, A. J., *et al*. Adipose Tissue: Physiology to Metabolic Dysfunction. in *Endotext* (eds. Feingold, K. R. et al.) (MDText.com, Inc., South Dartmouth (MA), 2000).
2. World Health Organization. Obesity and overweight. Fact sheet. https://www.who.int/news-room/fact-sheets/detail/obesity-and-overweight.
3. Zhang, Y. *et al.* Positional cloning of the mouse obese gene and its human homologue. *Nature* 372, 425–432 (1994).
4. Scherer, P. E., *et al*. A novel serum protein similar to C1q, produced exclusively in adipocytes. *J. Biol. Chem.* 270, 26746–26749 (1995).
5. Steppan, C. M. *et al.* The hormone resistin links obesity to diabetes. *Nature* 409, 307–312 (2001).
6. Funcke, J.-B. & Scherer, P. E. Beyond adiponectin and leptin: adipose tissue-derived mediators of inter-organ communication. *J. Lipid Res.* 60, 1648–1684 (2019).
7. Nedergaard, J., *et al*. Unexpected evidence for active brown adipose tissue in adult humans. *Am. J. Physiol. Endocrinol. Metab.* 293, E444-452 (2007).
8. Sakers, A., *et al*. Adipose-tissue plasticity in health and disease. *Cell* 185, 419–446 (2022).
9. Harms, M. & Seale, P. Brown and beige fat: development, function and therapeutic potential. *Nat. Med.* 19, 1252–1263 (2013).
10. Suchacki, K. J. *et al.* Bone marrow adipose tissue is a unique adipose subtype with distinct roles in glucose homeostasis. *Nat. Commun.* 11, 3097 (2020).
11. Li, Z. *et al.* Constitutive bone marrow adipocytes suppress local bone formation. *JCI Insight* 7, e160915.
12. Hill, J. O., *et al*. Energy Balance and Obesity. *Circulation* 126, 126–132 (2012).
13. Hill, J. O. & Commerford, R. Physical activity, fat balance, and energy balance. *Int. J. Sport Nutr.* 6, 80–92 (1996).
14. Harris, E. Study: Waist-to-Hip Ratio Might Predict Mortality Better Than BMI. *JAMA* 330, 1515–1516 (2023).
15. Busebee, B., *et al*. Obesity: A Review of Pathophysiology and Classification. *Mayo Clin. Proc.* 98, 1842–1857 (2023).
16. Virtue, S. & Vidal-Puig, A. Adipose tissue expandability, lipotoxicity and the Metabolic Syndrome--an allostatic perspective. *Biochim. Biophys. Acta* 1801, 338–349 (2010).
17. Yazıcı, D., *et al*. Insulin Resistance, Obesity, and Lipotoxicity. in *Obesity and Lipotoxicity* (eds. Engin, A. B. & Engin, A.) 391–430 (Springer International Publishing, Cham, 2024).
18. Lim, K. *et al*. Lipodystrophy: A paradigm for understanding the consequences of 'overloading' adipose tissue. *Phys Rev*. 101, 907-993 (2021).
19. Chiquette, E., *et al*. Estimating the prevalence of generalized and partial lipodystrophy: findings and challenges. *Diabetes Metab. Syndr. Obes. Targets Ther.* 10, 375–383 (2017).
20. Gonzaga-Jauregui, C. *et al.* Clinical and Molecular Prevalence of Lipodystrophy in an Unascertained Large Clinical Care Cohort. *Diabetes* 69, 249–258 (2020).
21. Akinci, B., *et al*. Phenotypic and Genetic Characteristics of Lipodystrophy: Pathophysiology, Metabolic Abnormalities, and Comorbidities. *Curr. Diab. Rep.* 18, 143 (2018).
22. Fernandez-Pombo, A. *et al.* Clinical Spectrum of LMNA-Associated Type 2 Familial Partial Lipodystrophy: A Systematic Review. *Cells* 12, 725 (2023).
23. Patni, N. *et al.* Regional Body Fat Changes and Metabolic Complications in Children With Dunnigan Lipodystrophy-Causing LMNA Variants. *J. Clin. Endocrinol. Metab.* 104, 1099–1108 (2019).

24. Garg, A. Gender differences in the prevalence of metabolic complications in familial partial lipodystrophy (Dunnigan variety). *J. Clin. Endocrinol. Metab.* 85, 1776–1782 (2000).
25. Foss-Freitas, M. C. *et al.* A Very-Low-Calorie Diet Can Cause Remission of Diabetes Mellitus and Hypertriglyceridemia in Familial Partial Lipodystrophy. *Obes. Facts* 17, 103–108 (2023).
26. Meral, R. *et al.* Metabolic Improvements With Tirzepatide in Lipodystrophy: A Novel Option? *Diabetes Care* 48, 756–762 (2025).
27. Foss-Freitas, M. C. *et al.* Efficacy and Safety of Glucagon-Like Peptide 1 Agonists in a Retrospective Study of Patients With Familial Partial Lipodystrophy. *Diabetes Care* 47, 653–659 (2024).
28. Oral, E. A. *et al.* Leptin-replacement therapy for lipodystrophy. *N. Engl. J. Med.* 346, 570–578 (2002).
29. Park, J. Y., *et al*. Long-term efficacy of leptin replacement in patients with Dunnigan-type familial partial lipodystrophy. *Metabolism.* 56, 508–516 (2007).
30. Patni, N. *et al.* Diagnosis, treatment and management of lipodystrophy: the physician perspective on the patient journey. *Orphanet J. Rare Dis.* 19, 263 (2024).
31. Véniant, M. M. *et al.* FGF21 Promotes Metabolic Homeostasis via White Adipose and Leptin in Mice. *PLOS ONE* 7, e40164 (2012).
32. BonDurant, L. D. *et al.* FGF21 Regulates Metabolism Through Adipose-Dependent and -Independent Mechanisms. *Cell Metab.* 25, 935-944.e4 (2017).
33. Musunuru, K. *et al.* Patient-Specific In Vivo Gene Editing to Treat a Rare Genetic Disease. *N. Engl. J. Med.* 12, 2235-2243 (2025).
34. Dittmer, T. A. & Misteli, T. The lamin protein family. *Genome Biol.* 12, 222 (2011).
35. Odell, J. & Lammerding, J. Lamins as structural nuclear elements through evolution. *Curr. Opin. Cell Biol.* 85, 102267 (2023).
36. Lelliott, C. J. *et al.* Lamin Expression in Human Adipose Cells in Relation to Anatomical Site and Differentiation State. *J. Clin. Endocrinol. Metab.* 87, 728–734 (2002).
37. Al-Saaidi, R. & Bross, P. Do lamin A and lamin C have unique roles? *Chromosoma* 124, 1–12 (2015).
38. Tiwari, V., *et al.* The structure and function of lamin A/C: Special focus on cardiomyopathy and therapeutic interventions. *Life Sci.* 341, 122489 (2024).
39. Liu, Q. *et al.* Dynamics of Lamin-A Processing Following Precursor Accumulation. *PLOS ONE* 5, e10874 (2010).
40. Simon, D. N. *et al.* OGT (O-GlcNAc Transferase) Selectively Modifies Multiple Residues Unique to Lamin A. *Cells* 7, 44 (2018).
41. Machowska, M., *et al*. Regulation of lamin properties and functions: does phosphorylation do it all? *Open Biol.* 5, 150094 (2015).
42. Hennekes, H., *et* al. Phosphorylation on protein kinase C sites inhibits nuclear import of lamin B2. *J Cell Biol*. 120, 1293-304 (1993).
43. Zheng, M., *et al*. Post-Translational Modification of Lamins: Mechanisms and Functions. *Front. Cell Dev. Biol.* 10 (2022).
44. Karoutas, A. *et al.* The NSL complex maintains nuclear architecture stability via lamin A/C acetylation. *Nat. Cell Biol.* 21, 1248–1260 (2019).
45. Turgay, Y. & Medalia, O. The structure of lamin filaments in somatic cells as revealed by cryo-electron tomography. *Nucl. Austin Tex* 8, 475–481 (2017).

46. Buxboim, A. *et al.* Scaffold, mechanics and functions of nuclear lamins. *FEBS Lett.* 597, 2791–2805 (2023).
47. Aebi, U., *et al.* The nuclear lamina is a meshwork of intermediate-type filaments. *Nature* 323, 560–564 (1986).
48. Winheim, S. *et al.* Deconstructing the late phase of vimentin assembly by total internal reflection fluorescence microscopy (TIRFM). *PloS One* 6, e19202 (2011).
49. Turgay, Y. *et al.* The molecular architecture of lamins in somatic cells. *Nature* 543, 261–264 (2017).
50. Dubik, N. & Mai, S. Lamin A/C: Function in Normal and Tumor Cells. *Cancers* 12, 3688 (2020).
51. Cutler, D. A., *et al*. Characterization of adiposity and metabolism in Lmna-deficient mice. *Biochem. Biophys. Res. Commun.* 291, 522–527 (2002).
52. Shimi, T. *et al.* The A- and B-type nuclear lamin networks: microdomains involved in chromatin organization and transcription. *Genes Dev.* 22, 3409–3421 (2008).
53. Shimi, T. *et al.* Structural organization of nuclear lamins A, C, B1, and B2 revealed by superresolution microscopy. *Mol. Biol. Cell* 26, 4075–4086 (2015).
54. Bridger, J. M., *et al.* Internal lamin structures within G1 nuclei of human dermal fibroblasts. *J. Cell Sci.* 104 (Pt 2), 297–306 (1993).
55. Hozák, P., *et al*. Lamin proteins form an internal nucleoskeleton as well as a peripheral lamina in human cells. *J. Cell Sci.* 108 (Pt 2), 635–644 (1995).
56. Korfali, N. *et al.* The nuclear envelope proteome differs notably between tissues. *Nucl. Austin Tex* 3, 552–564 (2012).
57. Gundersen, G. G. & Worman, H. J. Nuclear Positioning. *Cell* 152, 1376–1389 (2013).
58. Lei, K. *et al.* Inner Nuclear Envelope Proteins SUN1 and SUN2 Play a Prominent Role in the DNA Damage Response. *Curr. Biol.* 22, 1609–1615 (2012).
59. Chang, W., *et al.* Linker of nucleoskeleton and cytoskeleton (LINC) complex-mediated actin-dependent nuclear positioning orients centrosomes in migrating myoblasts. *Nucleus* 6, 77–88 (2015).
60. Koszul, R., *et al.* Meiotic chromosomes move by linkage to dynamic actin cables with transduction of force through the nuclear envelope. *Cell*. 133, 1188-201 (2008).
61. Guo, Y. & Zheng, Y. Lamins position the nuclear pores and centrosomes by modulating dynein. *Mol. Biol. Cell* 26, 3379–3389 (2015).
62. Scott, N. R. & and Parekh, S. H. A-type lamins involvement in transport and implications in cancer? *Nucleus* 13, 223–237 (2022).
63. Guelen, L. *et al.* Domain organization of human chromosomes revealed by mapping of nuclear lamina interactions. *Nature* 453, 948–951 (2008).
64. Briand, N. & Collas, P. Lamina-associated domains: peripheral matters and internal affairs. *Genome Biol.* 21, 85 (2020).
65. Wu, F. & Yao, J. Identifying Novel Transcriptional and Epigenetic Features of Nuclear Lamina-associated Genes. *Sci. Rep.* 7, 100 (2017).
66. Lund, E. *et al.* Lamin A/C-promoter interactions specify chromatin state-dependent transcription outcomes. *Genome Res.* 23, 1580–1589 (2013).
67. Ikegami, K., *et al*. Caenorhabditis elegans chromosome arms are anchored to the nuclear membrane via discontinuous association with LEM-2. *Genome Biol.* 11, R120 (2010).
68. Meuleman, W. *et al.* Constitutive nuclear lamina-genome interactions are highly conserved and associated with A/T-rich sequence. *Genome Res.* 23, 270–280 (2013).

69. Lund, E. G., *et al*. Distinct features of lamin A-interacting chromatin domains mapped by ChIP-sequencing from sonicated or micrococcal nuclease-digested chromatin. *Nucleus* 6, 30–39 (2015).
70. Lund, E., *et al.* Enriched domain detector: a program for detection of wide genomic enrichment domains robust against local variations. *Nucleic Acids Res.* 42, e92 (2014).
71. Dechat, T. *et al.* Lamina-associated polypeptide 2alpha binds intranuclear A-type lamins. *J. Cell Sci.* 113 Pt 19, 3473–3484 (2000).
72. Gesson, K. *et al.* A-type lamins bind both hetero- and euchromatin, the latter being regulated by lamina-associated polypeptide 2 alpha. *Genome Res.* 26, 462–473 (2016).
73. De Sandre-Giovannoli, A. *et al.* Lamin A Truncation in Hutchinson-Gilford Progeria. *Science* 300, 2055–2055 (2003).
74. Bonne, G. *et al.* Mutations in the gene encoding lamin A/C cause autosomal dominant Emery-Dreifuss muscular dystrophy. *Nat. Genet.* 21, 285–288 (1999).
75. Fatkin, D. *et al.* Missense mutations in the rod domain of the lamin A/C gene as causes of dilated cardiomyopathy and conduction-system disease. *N. Engl. J. Med.* 341, 1715–1724 (1999).
76. Novelli, G. *et al.* Mandibuloacral Dysplasia Is Caused by a Mutation in LMNA-Encoding Lamin A/C. *Am. J. Hum. Genet.* 71, 426–431 (2002).
77. Sandre-Giovannoli, A. D. *et al.* Homozygous Defects in LMNA, Encoding Lamin A/C Nuclear-Envelope Proteins, Cause Autosomal Recessive Axonal Neuropathy in Human (Charcot-Marie-Tooth Disorder Type 2) and Mouse. *Am. J. Hum. Genet.* 70, 726–736 (2002).
78. Worman, H. J. & Bonne, G. "Laminopathies": A wide spectrum of human diseases. *Exp. Cell Res.* 313, 2121–2133 (2007).
79. Kim, P. H. *et al.* Nuclear membrane ruptures underlie the vascular pathology in a mouse model of Hutchinson-Gilford progeria syndrome. *JCI Insight* 6, e151515 (2021).
80. Kim, P. H. *et al.* Progerin forms an abnormal meshwork and has a dominant-negative effect on the nuclear lamina. *Proc. Natl. Acad. Sci.* 121, e2406946121 (2024).
81. Barrowman, J., *et al.* Human ZMPSTE24 disease mutations: residual proteolytic activity correlates with disease severity. *Hum. Mol. Genet.* 21, 4084–4093 (2012).
82. Bonne, G., *et al*. Emery-Dreifuss Muscular Dystrophy. in *GeneReviews®* (eds. Adam, M. P. et al.) (University of Washington, Seattle, Seattle (WA), 1993).
83. Holt, I. *et al.* Effect of pathogenic mis-sense mutations in lamin A on its interaction with emerin in vivo. *J. Cell Sci.* 116, 3027–3035 (2003).
84. Raharjo, W. H., *et al*. Nuclear envelope defects associated with LMNA mutations cause dilated cardiomyopathy and Emery-Dreifuss muscular dystrophy. *J. Cell Sci.* 114, 4447–4457 (2001).
85. Shin, J.-Y. *et al.* Lamina-Associated Polypeptide-1 Interacts with the Muscular Dystrophy Protein Emerin and Is Essential for Skeletal Muscle Maintenance. *Dev. Cell* 26, 591–603 (2013).
86. Sullivan, T. *et al.* Loss of A-type lamin expression compromises nuclear envelope integrity leading to muscular dystrophy. *J. Cell Biol.* 147, 913–920 (1999).
87. Parks, S. B. *et al.* Lamin A/C mutation analysis in a cohort of 324 unrelated patients with idiopathic or familial dilated cardiomyopathy. *Am. Heart J.* 156, 161–169 (2008).
88. Taylor, M. R. G. *et al.* Natural history of dilated cardiomyopathy due to lamin A/C gene mutations. *J. Am. Coll. Cardiol.* 41, 771–780 (2003).
89. Hershberger, R. E. & Jordan, E. LMNA-Related Dilated Cardiomyopathy. in *GeneReviews®* (eds. Adam, M. P. et al.) (University of Washington, Seattle, Seattle (WA), 1993).

90. Cheedipudi, S. M., *et al.* Genetic Ablation of the DNA Damage Response Pathway Attenuates Lamin-Associated Dilated Cardiomyopathy in Mice. *JACC Basic Transl. Sci.* 7, 1232–1245 (2022).
91. Garavelli, L. *et al.* Mandibuloacral dysplasia type A in childhood. *Am. J. Med. Genet. A.* 149A, 2258–2264 (2009).
92. Padiath, Q. S. *et al.* Lamin B1 duplications cause autosomal dominant leukodystrophy. *Nat. Genet.* 38, 1114–1123 (2006).
93. Vantyghem, M. C. *et al.* Patients with familial partial lipodystrophy of the Dunnigan type due to a LMNA R482W mutation show muscular and cardiac abnormalities. *J. Clin. Endocrinol. Metab.* 89, 5337–5346 (2004).
94. Lammerding, J. *et al.* Lamins A and C but Not Lamin B1 Regulate Nuclear Mechanics *. *J. Biol. Chem.* 281, 25768–25780 (2006).
95. Vahabikashi, A. *et al.* Nuclear lamin isoforms differentially contribute to LINC complex-dependent nucleocytoskeletal coupling and whole-cell mechanics. *Proc. Natl. Acad. Sci. U. S. A.* 119, e2121816119 (2022).
96. Chen, C.-Y. *et al.* Accumulation of the Inner Nuclear Envelope Protein Sun1 Is Pathogenic in Progeric and Dystrophic Laminopathies. *Cell* 149, 565–577 (2012).
97. Kim, J. R., *et al*. Revisiting the truncated lamin A produced by a commonly used strain of Lmna knockout mice. *Nucleus* 14, 2262308.
98. Lammerding, J. *et al.* Lamin A/C deficiency causes defective nuclear mechanics and mechanotransduction. *J. Clin. Invest.* 113, 370–378 (2004).
99. Broers, J. L. V. *et al.* Decreased mechanical stiffness in LMNA-/- cells is caused by defective nucleo-cytoskeletal integrity: implications for the development of laminopathies. *Hum. Mol. Genet.* 13, 2567–2580 (2004).
100. Lee, J. S. H. *et al.* Nuclear Lamin A/C Deficiency Induces Defects in Cell Mechanics, Polarization, and Migration. *Biophys. J.* 93, 2542–2552 (2007).
101. van Loosdregt, I. A. E. W. *et al.* Lmna knockout mouse embryonic fibroblasts are less contractile than their wild-type counterparts. *Integr. Biol.* 9, 709–721 (2017).
102. Wang, B. *et al.* The molecular basis of lamin-specific chromatin interactions. 2024.08.05.604734 Preprint at https://doi.org/10.1101/2024.08.05.604734 (2024).
103. Gonzalez-Suarez, I. *et al.* Novel roles for A-type lamins in telomere biology and the DNA damage response pathway. *EMBO J.* 28, 2414–2427 (2009).
104. Maynard, S. *et al.* Lamin A/C impairments cause mitochondrial dysfunction by attenuating PGC1α and the NAMPT-NAD+ pathway. *Nucleic Acids Res.* gkac741 (2022) doi:10.1093/nar/gkac741.
105. Kittisopikul, M. *et al.* Computational analyses reveal spatial relationships between nuclear pore complexes and specific lamins. *J. Cell Biol.* 220, (2021).
106. Boguslavsky, R. L., *et al.* Nuclear lamin A inhibits adipocyte differentiation: implications for Dunnigan-type familial partial lipodystrophy. *Hum. Mol. Genet.* 15, 653–663 (2006).
107. Kim, Y., *et al.* Proliferation and differentiation of mouse embryonic stem cells lacking all lamins. *Cell Res.* 23, 1420–1423 (2013).
108. Guo, Y., *et al*. Concentration-dependent lamin assembly and its roles in the localization of other nuclear proteins. *Mol. Biol. Cell* 25, 1287–1297 (2014).
109. Zheng, X. *et al.* Lamins Organize the Global Three-Dimensional Genome from the Nuclear Periphery. *Mol. Cell* 71, 802-815.e7 (2018).

110. Sehgal, P.,*et al*. Lamin A/C haploinsufficiency modulates the differentiation potential of mouse embryonic stem cells. *PLoS One* 8, e57891 (2013).
111. Zhou, Y. *et al.* Loss of Mature Lamin A/C Triggers a Shift in Intracellular Metabolic Homeostasis via AMPKα Activation. *Cells* 11, 3988 (2022).
112. Wang, Y. *et al.* Lamin A/C-dependent chromatin architecture safeguards naïve pluripotency to prevent aberrant cardiovascular cell fate and function. *Nat. Commun.* 13, 6663 (2022).
113. Corsa, C. A. S. *et al.* Adipocyte-specific deletion of lamin A/C largely models human familial partial lipodystrophy type 2. *Diabetes* (2021) doi:10.2337/db20-1001.
114. Spann, T. P., *et al*. Disruption of nuclear lamin organization alters the distribution of replication factors and inhibits DNA synthesis. *J. Cell Biol.* 136, 1201–1212 (1997).
115. Spann, T. P., *et al*. Alteration of nuclear lamin organization inhibits RNA polymerase II-dependent transcription. *J. Cell Biol.* 156, 603–608 (2002).
116. Kubben, N. *et al.* Post-natal myogenic and adipogenic developmental: defects and metabolic impairment upon loss of A-type lamins. *Nucl. Austin Tex* 2, 195–207 (2011).
117. Kirby, T. J., *et al.* Eliminating elevated p53 signaling fails to rescue skeletal muscle defects or extend survival in lamin A/C-deficient mice. *Cell Death Discov.* 10, 1–14 (2024).
118. Liao, C.-Y. *et al.* Rapamycin Reverses Metabolic Deficits in Lamin A/C-Deficient Mice. *Cell Rep.* 17, 2542–2552 (2016).
119. Reitman, M. L. Of mice and men – environmental temperature, body temperature, and treatment of obesity. *FEBS Lett.* 592, 2098–2107 (2018).
120. Fong, L. G. *et al.* Prelamin A and lamin A appear to be dispensable in the nuclear lamina. *J. Clin. Invest.* 116, 743–752 (2006).
121. Coffinier, C. *et al.* Direct synthesis of lamin A, bypassing prelamin a processing, causes misshapen nuclei in fibroblasts but no detectable pathology in mice. *J. Biol. Chem.* 285, 20818–20826 (2010).
122. Vergnes, L., *et al*. Lamin B1 is required for mouse development and nuclear integrity. *Proc. Natl. Acad. Sci. U. S. A.* 101, 10428–10433 (2004).
123. Sikder, K. *et al.* Perinuclear damage from nuclear envelope deterioration elicits stress responses that contribute to LMNA cardiomyopathy. *Sci. Adv.* 10, eadh0798 (2024).
124. Kwan, R. *et al.* Hepatocyte-Specific Deletion of Mouse Lamin A/C Leads to Male-Selective Steatohepatitis. *Cell. Mol. Gastroenterol. Hepatol.* 4, 365–383 (2017).
125. Krimm, I. *et al.* The Ig-like structure of the C-terminal domain of lamin A/C, mutated in muscular dystrophies, cardiomyopathy, and partial lipodystrophy. *Struct. Lond. Engl. 1993* 10, 811–823 (2002).
126. Magracheva, E., *et al*. Structure of the lamin A/C R482W mutant responsible for dominant familial partial lipodystrophy (FPLD). *Acta Crystallograph. Sect. F Struct. Biol. Cryst. Commun.* 65, 665–670 (2009).
127. Stierlé, V. *et al.* The carboxyl-terminal region common to lamins A and C contains a DNA binding domain. *Biochemistry* 42, 4819–4828 (2003).
128. Ahn, J. *et al.* Crystal structure of progeria mutant S143F lamin A/C reveals increased hydrophobicity driving nuclear deformation. *Commun. Biol.* 5, 267 (2022).
129. Anderson, C. L. *et al.* Most myopathic lamin variants aggregate: a functional genomics approach for assessing variants of uncertain significance. *Npj Genomic Med.* 6, 1–11 (2021).
130. Elzeneini, E. & Wickström, S. Lipodystrophic laminopathy: Lamin A mutation relaxes chromatin architecture to impair adipogenesis. *J. Cell Biol.* 216, jcb.201707090 (2017).

131. Lloyd, D. J., *et al*. A novel interaction between lamin A and SREBP1: implications for partial lipodystrophy and other laminopathies. *Hum. Mol. Genet.* 11, 769–777 (2002).
132. Capanni, C. *et al.* Altered pre-lamin A processing is a common mechanism leading to lipodystrophy. *Hum. Mol. Genet.* 14, 1489–1502 (2005).
133. Bidault, G. *et al.* Lipodystrophy-linked LMNA p.R482W mutation induces clinical early atherosclerosis and in vitro endothelial dysfunction. *Arterioscler. Thromb. Vasc. Biol.* 33, 2162–2171 (2013).
134. Oldenburg, A. R., *et al.* Deregulation of Fragile X-related protein 1 by the lipodystrophic lamin A p.R482W mutation elicits a myogenic gene expression program in preadipocytes. *Hum. Mol. Genet.* 23, 1151–1162 (2014).
135. Oldenburg, A. *et al.* A lipodystrophy-causing lamin A mutant alters conformation and epigenetic regulation of the anti-adipogenic MIR335 locus. *J. Cell Biol.* 216, 2731–2743 (2017).
136. Vigouroux, C. *et al.* Nuclear envelope disorganization in fibroblasts from lipodystrophic patients with heterozygous R482Q/W mutations in the lamin A/C gene. *J. Cell Sci.* 114, 4459–4468 (2001).
137. Favreau, C. *et al.* Expression of lamin A mutated in the carboxyl-terminal tail generates an aberrant nuclear phenotype similar to that observed in cells from patients with Dunnigan-type partial lipodystrophy and Emery-Dreifuss muscular dystrophy. *Exp. Cell Res.* 282, 14–23 (2003).
138. Perepelina, K. *et al.* Lamin A/C mutation associated with lipodystrophy influences adipogenic differentiation of stem cells through interaction with Notch signaling. *Biochem. Cell Biol. Biochim. Biol. Cell.* 96, 342–348 (2018).
139. Pellegrini, C. *et al.* Altered adipocyte differentiation and unbalanced autophagy in type 2 Familial Partial Lipodystrophy: an in vitro and in vivo study of adipose tissue browning. *Exp. Mol. Med.* 51, 1–17 (2019).
140. Friesen, M. & Cowan, C. A. FPLD2 LMNA mutation R482W dysregulates iPSC-derived adipocyte function and lipid metabolism. *Biochem. Biophys. Res. Commun.* 495, 254–260 (2018).
141. Wang, Z. *et al.* A new laminopathy caused by an Arg133/Leu mutation in lamin A/C and the effects thereof on adipocyte differentiation and the transcriptome. *Adipocyte* 8, 280–291 (2019).
142. Araújo-Vilar, D. *et al.* Variable Expressivity and Allelic Heterogeneity in Type 2 Familial Partial Lipodystrophy: The p.(Thr528Met) LMNA Variant. *J. Clin. Med.* 10, (2021).
143. Verstraeten, V. L. R. M. *et al.* The R439C mutation in LMNA causes lamin oligomerization and susceptibility to oxidative stress. *J. Cell. Mol. Med.* 13, 959–971 (2009).
144. Simon, D. N., *et al*. Lamin A tail modification by SUMO1 is disrupted by familial partial lipodystrophy-causing mutations. *Mol. Biol. Cell* 24, 342–350 (2013).
145. Qiu, H. *et al.* Lamin A/C deficiency-mediated ROS elevation contributes to pathogenic phenotypes of dilated cardiomyopathy in iPSC model. *Nat. Commun.* 15, 7000 (2024).
146. Wallace, M. *et al.* Nuclear damage in LMNA mutant iPSC-derived cardiomyocytes is associated with impaired lamin localization to the nuclear envelope. *Mol. Biol. Cell* mbcE21100527 (2023) doi:10.1091/mbc.E21-10-0527.
147. Shah, P. P. *et al.* Pathogenic LMNA variants disrupt cardiac lamina-chromatin interactions and de-repress alternative fate genes. *Cell Stem Cell* 28, 938-954.e9 (2021).
148. Earle, A. J. *et al.* Mutant lamins cause nuclear envelope rupture and DNA damage in skeletal muscle cells. *Nat. Mater.* 19, 464–473 (2020).
149. Sylvius, N. *et al.* Specific contribution of lamin A and lamin C in the development of laminopathies. *Exp. Cell Res.* 314, 2362–2375 (2008).

150. Storey, E. C. *et al.* Proteomic characterization of human LMNA-related congenital muscular dystrophy muscle cells. *Neuromuscul. Disord.* 38, 26–41 (2024).
151. Bertrand, A. T. *et al.* Lamin A/C Assembly Defects in LMNA-Congenital Muscular Dystrophy Is Responsible for the Increased Severity of the Disease Compared with Emery–Dreifuss Muscular Dystrophy. *Cells* 9, 844 (2020).
152. Richards, S. A., *et al*. The accumulation of un-repairable DNA damage in laminopathy progeria fibroblasts is caused by ROS generation and is prevented by treatment with N-acetyl cysteine. *Hum. Mol. Genet.* 20, 3997–4004 (2011).
153. Lamis, A. *et al.* Hutchinson-Gilford Progeria Syndrome: A Literature Review. *Cureus* 14, e28629.
154. Ikegami, K., *et al*. Phosphorylated Lamin A/C in the Nuclear Interior Binds Active Enhancers Associated with Abnormal Transcription in Progeria. *Dev. Cell* 52, 699-713.e11 (2020).
155. Wojtanik, K. M. *et al.* The role of LMNA in adipose: a novel mouse model of lipodystrophy based on the Dunnigan-type familial partial lipodystrophy mutation. *J. Lipid Res.* 50, 1068–1079 (2009).
156. Le Dour, C. *et al.* Extracellular matrix remodeling and transforming growth factor-β signaling abnormalities induced by lamin A/C variants that cause lipodystrophy. *J. Lipid Res.* 58, 151–163 (2017).
157. Arimura, T. *et al.* Mouse model carrying H222P-Lmna mutation develops muscular dystrophy and dilated cardiomyopathy similar to human striated muscle laminopathies. *Hum. Mol. Genet.* 14, 155–169 (2005).
158. Muchir, A. *et al.* Activation of MAPK pathways links LMNA mutations to cardiomyopathy in Emery-Dreifuss muscular dystrophy. *J. Clin. Invest.* 117, 1282–1293 (2007).
159. Wang, Y., *et al*. Pathology and nuclear abnormalities in hearts of transgenic mice expressing M371K lamin A encoded by an LMNA mutation causing Emery-Dreifuss muscular dystrophy. *Hum. Mol. Genet.* 15, 2479–2489 (2006).
160. Mounkes, L. C., *et al*. Expression of an LMNA-N195K variant of A-type lamins results in cardiac conduction defects and death in mice. *Hum. Mol. Genet.* 14, 2167–2180 (2005).
161. Yang, L. *et al.* The LMNA p.R541C mutation causes dilated cardiomyopathy in human and mice. *Int. J. Cardiol.* 363, 149–158 (2022).
162. Bertrand, A. T. *et al.* DelK32-lamin A/C has abnormal location and induces incomplete tissue maturation and severe metabolic defects leading to premature death. *Hum. Mol. Genet.* 21, 1037–1048 (2012).
163. Mounkes, L. C., *et al*. A progeroid syndrome in mice is caused by defects in A-type lamins. *Nature* 423, 298–301 (2003).
164. Gómez-Domínguez, D. *et al.* CRISPR/Cas9-mediated elimination of the LMNA c.745C>G pathogenic mutation enhances survival and cardiac function in LMNA-associated congenital muscular dystrophy. *bioRxiv* (2025).
165. Osorio, F. G. *et al.* Splicing-directed therapy in a new mouse model of human accelerated aging. *Sci. Transl. Med.* 3, 106ra107 (2011).
166. Yang, S. H., *et al*. Progerin elicits disease phenotypes of progeria in mice whether or not it is farnesylated. *J. Clin. Invest.* 118, 3291–3300 (2008).
167. Poitelon, Y. *et al.* Behavioral and Molecular Exploration of the AR-CMT2A Mouse Model LmnaR298C/R298C. *NeuroMolecular Med.* 14, 40–52 (2012).

168. Odgren, P. R. *et al.* Disheveled Hair and Ear (Dhe), a Spontaneous Mouse Lmna Mutation Modeling Human Laminopathies. *PLoS ONE* 5, e9959 (2010).
169. Zhang, Y. *et al.* Pathological Features in the LmnaDhe/+ Mutant Mouse Provide a Novel Model of Human Otitis Media and Laminopathies. *Am. J. Pathol.* 181, 761–774 (2012).
170. Luo, X. *et al.* Primate Model Carrying LMNA Mutation Develops Dilated Cardiomyopathy. *JACC Basic Transl. Sci.* 9, 380–395 (2024).
171. Araújo-Vilar, D. *et al.* Site-dependent differences in both prelamin A and adipogenic genes in subcutaneous adipose tissue of patients with type 2 familial partial lipodystrophy. *J. Med. Genet.* 46, 40–48 (2009).
172. Béréziat, V. *et al.* LMNA mutations induce a non-inflammatory fibrosis and a brown fat-like dystrophy of enlarged cervical adipose tissue. *Am. J. Pathol.* 179, 2443–2453 (2011).

Chapter 2 Bridging Human and Mouse Lipodystrophy: The Requirement of Functional Lamin A/C for Adipocyte Homeostasis

Adapted from: Maung, J. N., Schill, R. L., Nishii, A., Foss de Freitas, M., Obua, B., Nygard, M., Mendez-Casillas, M. D., Gilio, D., Besci, O., Desrosiers, B., Adler, R. E., Gomes, A. D., Mori, H., Uranga, R. M., Li, Z., Hariri, H., Hermsmeyer, I. D. K., Chen, Y., Hoose, K. S., Lewis, K. T., Hetrick, T. A., Lumeng, C. N., Mandrup, S., Oral, E. A., MacDougald, O. A. Mechanisms of adipocyte loss in familial partial lipodystrophy 2. Submitted & awaiting revisions (2025).

2.1 Abstract

Familial partial lipodystrophy 2 (FPLD2) is a rare disease characterized by adipose tissue loss, redistribution, and metabolic dysfunction, caused by pathogenic *LMNA* variants encoding nuclear lamins A/C. The mechanisms driving adipocyte loss remain poorly defined. Here, we recruited eight families with developing or developed FPLD2 and performed clinical, histological, and transcriptomic analyses of subcutaneous adipose tissue biopsies. Single-nucleus and bulk RNA-sequencing revealed suppression of lipid metabolism and mitochondrial pathways, alongside increased inflammation. These signatures were mirrored in tamoxifen-inducible adipocyte-specific *Lmna* knockout mice, in which lamin A/C-deficient adipocytes shrank and disappeared. *Lmna*-deficient fibroblasts shared similar gene expression changes, linked to altered chromatin accessibility, underscoring lamin A/C's regulatory role in lipid metabolism and inflammatory programs. This is the first study to directly compare atrophic and expanding depots in FPLD2, and integrates human, mouse, and *in vitro* models to reveal shared molecular mechanisms, providing new insights into disease progression and potential therapeutic targets.

2.2 Introduction

Adipose tissue is a key metabolic and endocrine organ, and alterations in its quantity or function can lead to severe health consequences. Whilst excess adipose tissue contributes to obesity and its associated metabolic comorbidities, a contrasting group of rare diseases called lipodystrophy syndromes are characterized by adipose tissue loss, redistribution, and dysfunction. Despite its outward contrast to obesity, lipodystrophy results in similar metabolic complications like fatty liver disease, insulin resistance, and cardiovascular disease, due to the absence of safe lipid storage[1,2]. The most common form of lipodystrophy is familial partial lipodystrophy 2 (FPLD2), also known as Dunnigan's disease[3]. Though initially estimated to have a clinical prevalence of ~1 in 1 million[4], more recent studies suggest clinical prevalence of up to ~1 in 20,000, with a genetic prevalence as high as ~1 in 7000[5]. FPLD2 is characterized by the selective loss of subcutaneous adipose tissue from the limbs and trunk, and redistribution to the face and neck, and occasionally visceral depots[1,6,7]. Current treatments for FPLD2 involve diet and lifestyle interventions, management of hyperlipidemia and insulin resistance, and administration of recombinant leptin, which has been shown to improve multiple metabolic complications[8]. However, underlying mechanisms responsible for adipose tissue loss in FPLD2 remain poorly understood. Uncovering these pathways is essential to unlock new therapeutic targets for patients aimed at preventing or restoring adipose tissue in affected individuals.

Pathogenic missense variants in *LMNA*, which encodes the intermediate filament proteins lamin A/C, are the underlying cause of FPLD2[9]. Lamin A/C are a essential structural component of the nuclear lamina, a meshwork of polymerized lamins that forms a scaffold beneath the inner nuclear membrane. The nuclear lamina provides nuclear support, regulates nuclear transport, mediates responses to mechanical stresses, and organizes chromatin by directly interacting with chromatin at lamina-associated domains (LADs)[10–12]. Given these widespread roles, it is not surprising that mutations disrupting lamin A/C can result in profound cellular dysfunction. In FPLD2, the most commonly mutated residue is arginine 482 (R482), which can become R482Q/W/L[13]. This residue lies in a region known to directly bind DNA, so disrupting this site likely leads to widespread transcriptional dysregulation[14–16]. Importantly, pathogenic variants throughout *LMNA* cause not only FPLD2, but a broad class of diseases termed laminopathies, which include various forms of muscular dystrophy, cardiomyopathies, neuropathies, and premature aging syndromes such as progeria. Therefore, study of molecular

mechanisms that drive adipose tissue loss in FPLD2 may reveal truths about lamin biology and unravel how specific *LMNA* variants give rise to complex, tissue-specific disease phenotypes.

To study the fundamental role of lamin A/C in cellular physiology, many groups have studied *Lmna* knockout (KO) mouse embryonic fibroblasts (MEFs). Lamin A/C-deficient MEFs exhibit abnormal nuclear morphology, disrupted nuclear pore complex (NPC) distribution, and reduced nuclear stiffness[17,18]. Mice with global deletion of *Lmna* display muscular dystrophy, stunted growth, and premature death by eight weeks of age, limiting their utility for studying metabolic tissues like adipose[17,19]. Although these mice also exhibit decreased white adipose tissue (WAT), interpretation is confounded by their runted phenotype, making them a suboptimal model for studying mechanisms of lipodystrophy. Beyond KO models, the common FPLD2-causing *LMNA* R482Q/W variant has been overexpressed in 3T3-L1 preadipocytes, where it inhibited adipocyte differentiation, a phenotype also observed with wild type lamin A/C overexpression[20]. This suggests that disruption of lamin A/C stoichiometry alone can perturb adipogenesis, complicating interpretation of overexpression studies. Two groups have generated transgenic mice overexpressing human R482Q lamin A under control of the aP2 (FABP4) promoter. These mice either had no overt lipodystrophy phenotype[21] or had mild adipose loss only 32 weeks on a high-fat diet (HFD)[22]. Analyses of WAT in R482Q lamin A mice revealed an increase in extracellular matrix (ECM) and fibrotic tissue deposition, even in the absence of lipodystrophy, suggesting that *LMNA* variants disrupt adipose ECM organization[21]. However, reliance on overexpression models and the use of the FABP4 promoter, which is also active in macrophages[23], complicates interpretation and underscores the need for improved models to study adipocyte-specific consequences of lamin A/C disruption.

Studies of human WAT in FPLD2 are limited due to the disease's rarity and the scarcity of residual adipose tissue inpatients. One study analyzed abdominal and thigh subcutaneous adipose tissue from patients, which revealed downregulation of lipid metabolism genes and defects in heterochromatin organization in FPLD2 biopsies[24]. Study of dorsocervical subcutaneous adipose tissue, a typical site of fat accumulation in FPLD2, revealed heterogenous adipocyte morphology, increased fibrosis, and features of a brown adipose tissue (BAT)-like phenotype[25]. Increased fibrosis in dorsocervical WAT has also been confirmed by others[21]. These findings suggest complex remodeling of adipose tissue in FPLD2, but the molecular mechanisms underlying these changes remain incompletely defined.

Previously, our group created a constitutive adipocyte-specific *Lmna* KO model (*Lmna*^{ADKO}) that recapitulated key features of FPLD2, including the development and subsequent loss of WAT and metabolic dysfunction[26]. Female *Lmna*^{ADKO} mice exhibited smaller adipocytes, though this was not associated with macrophage infiltration, suggesting cell-autonomous mechanisms. Cell culture studies of *Lmna* KO mesenchymal stem cells revealed no alteration in adipocyte differentiation, but KO adipocytes had increased glycerol release upon β-adrenergic stimulation[26]. Although this model lacks a pathogenic *LMNA* variant, it effectively highlights the essential role of lamin A/C in adipocyte maintenance and function.

In this study, we recruited eight families with confirmed pathogenic *LMNA* variants with either developing or developed FPLD2 and collected subcutaneous biopsies from the abdomen and neck to assess histological and molecular changes in WAT. With 16 patients in total, this represents the largest biopsy cohort for FPLD2 and is the first to profile FPLD2 adipose transcriptomes at single-cell resolution. We also employed a novel tamoxifen-inducible adipocyte-specific *Lmna* KO model (*Lmna*^{iADKO}) to study the dynamics of adipocyte loss upon lamin A/C depletion in adult mice. By integrating findings from human biopsies and our mouse model highlight, we uncovered conserved transcriptional changes, including suppressed lipid metabolism and enhanced inflammatory signaling, which may contribute to adipocyte degeneration in FPLD2. To further explore the fundamental role of lamin A/C in gene regulation, we incorporated chromatin accessibility and transcriptomic data from *Lmna* KO MEFs with gene expression data from *Lmna*^{iADKO} WAT. This analysis revealed that lamin A/C deficiency alters the chromatin accessibility landscape of both lipid metabolism and immune regulatory genes, providing mechanistic insight into the transcriptional rewiring observed in FPLD2. Taken together, our study provides a comprehensive multi-model analysis of FPLD2 pathogenesis, combining human tissue profiling, genetic mouse models, and epigenomic integration to identify key pathways of therapeutic relevance for treatment of FPLD2.

2.3 Results

Patients with FPLD2 have loss of adipose tissue and metabolic dysfunction

To study how pathologic *LMNA* variants drive FPLD2 progression, we recruited eight families into the Longitudinal Evaluation of Adiposity Distribution and Adipocyte Biology in Children with Lipodystrophy (LEAD-ABC) study. Patients were stratified into three groups: Group C, which were unaffected control family members or recruited study subjects, Group A, individuals with a pathologic variant but who have not yet developed extensive symptoms, or Group B, patients with overt, developed FPLD2 (**Figure 2.1 A**). Whole genome sequencing identified five disease-causing *LMNA* variants across the eight family pedigrees (**Figure 2.1 B**). Patients with developing FPLD2 (Group A) still had visible subcutaneous white adipose tissue (WAT) on their limbs and trunk, with no signs of visceral WAT accumulation (**Figure 2.1 C**). In contrast, patients with developed FPLD2 (Group B) showed classical fat redistribution: reduced subcutaneous WAT, increased visceral adiposity, and prominent fat accumulation in the upper neck and face (**Figure 2.1 D**). These regional shifts were further visualized using fat shadow imaging (**Figure 2.1 E; Supplemental Figure 2.1 A**). Quantitative assessment revealed reduced total body fat percentage in both developing and developed FPLD2 groups compared to control patients (**Figure 2.1 F**). Notably, individuals with FPLD2 specifically had reduced leg fat (**Figure 2.1 G**), and patients with developing FPLD2 already had reduced trunk fat percentage (**Figure 2.1 H**), suggesting that trunk fat may be lost early in FPLD2 progression. Liver magnetic resonance imaging (MRI) revealed a trend towards increased hepatic liver accumulation in patients with FPLD2 (**Figure 2.1 I, J**).

We next evaluated metabolic parameters across groups. Patients with developed FPLD2 (Group B) exhibited increased glycated hemoglobin (**Figure 2.1 K**), circulating triglycerides (**Figure 2.1 L**), and non-esterified fatty acids (NEFA) (**Figure 2.1 M**), and increased glucose area under the curve (AUC) post-oral GTT (OGTT) (**Supplemental Figure 2.1 B**), indicating impaired metabolic control. However, no significant differences were observed across groups for Homeostatic Model Assessment of Insulin Resistance (HOMA-IR) (**Figure 2.1 N**), insulin AUC (**Supplemental Figure 2.1 C**), NEFA AUC (**Supplemental Figure 2.1 D**), fasted insulin (**Supplemental Figure 2.1 E**), and the adipose tissue insulin resistance index (Adipo-IR) (**Supplemental Figure 2.1 F**). Circulating levels of leptin (**Figure 2.1 O**) and adiponectin (**Figure 2.1 P**) concentrations were reduced in FPLD2, consistent with WAT loss. Both

fibroblast growth factor 21 (FGF21) (**Figure 2.1 Q**) and growth differentiation factor 15 (GDF15) (**Supplemental Figure 2.1 G**) were increased in patients with FPLD2, which are typically increased with stress or metabolic dysfunction[27]. Clinical characteristics of the cohort are summarized in Table 2.1. Taken together, our patient data highlight patterns of adipose loss during FPLD2 progression, and confirms that patients with FPLD2, but not developing FPLD2, have metabolic dysfunction[1,28].

White adipose tissue (WAT) biopsies from patients with FPLD2 have decreased fatty acid metabolism and increased inflammation gene expression

To study mechanisms of adipose tissue loss, we collected patient subcutaneous WAT biopsies from two locations: the abdomen, which undergoes progressive atrophy, and the dorsocervical (upper neck) region, which expands with FPLD2[1]. Comparison of these two distinct depots allows us to study adipose loss and redistribution during FPLD2 within individual patients. Histological analyses of WAT morphology was performed, alongside Picrosirius Red staining to assess collagen deposition. Abdominal biopsies had a visual increase with areas of fibrosis during FPLD2 progression (**Figure 2.2 A**), but due to variability across the patient cohort and inconsistencies in adipose sampling, we were unable to robustly quantify collagen content. No change in adipocyte size was observed in abdominal samples across disease states (**Figure 2.2 B, C**). A similar pattern was observed in the upper neck depot: of increased fibrosis with FPLD2 progression without a detectable change in adipocyte size (**Figure 2.2 D-F**). Skin biopsies from patients were comparable across disease states (**Supplemental Figure 2.1 G**). Therefore, adipocytes that are remaining in FPLD2 adipose tissue appear morphologically equivalent, at least grossly.

Next, we wanted to study the molecular changes that underlie FPLD2 progression. We combined the abdomen and upper neck biopsies within each patient group and performed bulk RNA-sequencing (RNA-seq) (**Figure 2.2 G**). We combined groups with developing (Group A) and developed FPLD2 (Group B) to analyze broad transcriptomic effects of pathogenic *LMNA* variants within WAT. We performed Gene Set Enrichment Analysis (GSEA) and observed elevated pathways related to inflammation, intermediate filament organization, and muscle-related pathways (**Figure 2.2 G**). Suppressed GSEA pathways were related to mitochondrial function, protein translation, and fatty acid metabolism (**Figure 2.2 H**). Together, these findings

reveal a distinct molecular signature in WAT from patients with pathologic *LMNA* variants, characterized by decreased metabolism and increased inflammation, which may contribute to disease progression.

Single nuclei RNA-sequencing identifies depot differences between upper neck and abdominal patient biopsies

Following our observations, we were interested in understanding 1) depot differences between the abdomen and upper neck biopsies, and 2) what cell types contribute to the bulk transcriptomic changes with FPLD2 (**Figure 2.2 H**). We performed single nuclei RNA-sequencing (snRNA-seq) on patient WAT biopsies and identified seven major cell populations: adipocytes, adipose stem and progenitor cells (ASPC), macrophages, endothelial cells, T cells, pericytes, and lymphatic endothelial cells (LEC) (**Figure 2.3 A**). Other smaller cell populations such as mast cells, natural killer cells, and dendritic cells were detected but grouped into broader categories for downstream analysis. Cell types were identified by their marker genes, e.g. *ADIPOQ* for adipocytes and *PDGFRA* for ASPCs (**Figure 2.3 B**)[29,30].

We first explored depot differences under control conditions, as direct comparisons between the upper neck and abdomen WAT have not been previously made. In control samples, the upper neck depot had a higher proportion of adipocytes, and reduced proportions of LECs, macrophages, and ASPCs compared to abdominal WAT (**Figure 2.3 C**). We next sought to characterize differences in molecular and physiologic cell states between depots under control conditions. Adipocytes subclustered into two distinct clusters: Cluster 1 had high expression of adipogenic pathways, and cluster 2 was characterized by expression of proinflammatory gene sets (**Figure 2.3 D**). However, there was no difference in adipocyte subcluster proportions between depots, indicating that adipocyte identity remains consistent across regions under basal conditions (**Figure 2.3 E**). ASPCs subclustered into four clusters, and in the upper neck, high adipogenic ASPCs were proportionally increased, and proinflammatory and high mTOR signaling ASPCs were decreased, indicating potential for increased adipogenic capacity in ASPCs within the dorsocervical upper neck depot (**Figure 2.3 F, G**).

Within immune cell populations, the lipid-associated macrophages, cluster 3, characterized by high inflammation/fatty acid metabolism, were decreased in the upper neck vs. the abdomen of control patients (**Figure 2.3 H, I**). However, low inflammatory T cells (Cluster

2) were decreased in proportion in the upper neck compared to the abdomen (**Figure 2.3 J, K**). We also observed that high inflammation endothelial cells (Cluster 3) were increased in the upper neck relative to the abdomen (**Supplemental Figure 2.2 A, B**). High myogenesis (Cluster 2) pericytes were decreased (**Supplemental Figure 2.2 C, D**) and high protein translation LECs were decreased (**Supplemental Figure 2.2 E, F**) in the upper neck vs. the abdomen. In summary, in unaffected individuals, the upper neck depot shows no changes in adipocyte subclustering composition, but contains a higher proportion of proadipogenic ASPCs and fewer proinflammatory macrophages.

Adipocytes are reduced in proportion and have decreased fatty acid metabolism and increased inflammatory gene expression in adipose depots of patients with FPLD2

After establishing depot differences in control patients, we next examined how cell type composition changes across disease states using our snRNA-seq dataset. We generated UMAP plots combining both depots across our three patient groups (**Figure 2.4 A**), as well as stratified UMAPs by genotype (**Supplemental Figure 2.3 A**) and sex (**Supplemental Figure 2.3 B**). In the abdominal depot, we observed a decreased proportion of adipocytes in patients with developing and developed FPLD2 (**Figure 2.4 B, C**), consistent with WAT atrophy in this region in FPLD2. Interestingly, LECs increased in proportion during development of FPLD2 (**Figure 2.4 B**), but then had a trending decrease in proportion in patients as disease progressed (**Figure 2.4 C**). Macrophages and pericytes were increased in proportion of abdominal cells in patient groups with FPLD2 (**Figure 2.4 C**). In the upper neck, we observed that adipocytes were decreased in proportion in patients with developing FPLD2, which was not further changed with FPLD2 (**Figure 2.4 D, E**). Like the abdomen, upper neck biopsies had an increase in LECs in biopsies from patients with developing FPLD2, which ultimately became a decrease in LEC proportion in patients with developed FPLD2, suggesting that LECs may play an important role in FPLD2 progression (**Figure 2.4 D, E**).

We previously established differences in upper neck vs. abdomen proportions in control patients (**Figure 2.3 C**) but wanted to explore how these depots differed with pathogenic *LMNA* variants. Interestingly, depot differences during FPLD2 progression reflected those observed in control patients, including decreased LEC and macrophage proportions and increased adipocyte proportion with both developing and developed FPLD2 (**Figure 2.4 F, G**). Furthermore, in

patients with developing FPLD2, we observed decreased ASPC proportions in the upper neck, and in FPLD2, pericytes were decreased in the upper neck (**Figure 2.4 G**). Therefore, many of the observed changes between the upper neck and the abdomen WAT depots are part of fundamental biology, as they are preserved across patients with and without FPLD2.

After characterizing changes in cell-type proportions, we next studied how cell identities change with FPLD2. GSEA of adipocytes from both depots in developing or FPLD2 states revealed patterns of decreased lipid synthesis and metabolism compared to controls, accompanied by increased extracellular matrix (ECM) and inflammation (**Figure 2.4 H**). These data align closely with results from bulk RNA-seq of WAT from patients with FPLD2, which also showed suppression of fatty acid metabolism and increased inflammation (**Figure 2.4 G, H**). In subcluster analyses, we found no differences in composition of adipocyte subclusters with disease state (**Figure 2.4 I**). These data suggest that on a pseudobulk level, remaining adipocytes in patient WAT have dysfunctional fatty acid metabolism, but proportions of proadipogenic (Cluster 1) vs. proinflammatory (Cluster 2) adipocytes are unchanged.

ASPCs from patients with developing or developed FPLD2 had decreased oxidative phosphorylation and ribosomal genes, and an increase in lipid metabolism (**Figure 2.4 J**). Subcluster analyses revealed that proadipogenic ASPCs (Cluster 2) were increased in developing and FPLD2 disease states, and proinflammatory ASPCs (Cluster 3) were decreased in proportion (**Figure 2.4 K**). These findings suggest that ASPCs within WAT of patients with FPLD2 may respond to loss of adipocytes by shifting to a high adipogenic state. Macrophages from patients with developing and developed FPLD2 were less inflammatory and had decreased lipid metabolism when analyzed at the pseudobulk level (**Figure 2.4 L**). However, proinflammatory and high lipid metabolism macrophages (Cluster 3) were increased in proportion with FPLD2 (**Figure 2.4 M**). This discrepancy suggests that although there may be a small population of lipid-associated macrophages that increase with disease, on a population level, macrophages become less inflammatory overall with FPLD2.

Endothelial cells had decreased lipid metabolism and increased growth factor signaling with FPLD2 progression (**Supplemental Figure 2.3 C**) accompanied by a rise in the high EMT signaling endothelial cells (**Supplemental Figure 2.3 D**). T cells showed reduced activation in FPLD2 overall (**Supplemental Figure 2.3 E**), with subcluster analysis revealing a shift towards a less inflammatory phenotype (Cluster 2) in FPLD2 (**Supplemental Figure 2.3 F**). Pericytes

from patients with patients with developing or developed FPLD2 displayed downregulation of adipogenesis and oxidative phosphorylation pathway (**Supplemental Figure 2.3 G**), but subcluster proportions remained unchanged across disease states (**Supplemental Figure 2.3 H**). LECs had reduced expression of genes related to inflammation, translation, and oxidative phosphorylation in FPLD2 (**Supplemental Figure 2.3 I**), reflected by the decrease in high translation LECs proportion (Cluster 2) with developed FPLD2 (**Supplemental Figure 2.3 J**). Collectively, these snRNA-seq analyses reveal widespread shifts in cellular identity during FPLD2 progression: adipocytes show impaired fatty acid metabolism, ASPCs adopt a more adipogenic state, and macrophages exhibit features of lipid scavenging.

Cell proportions change with FPLD2 progression in a depot-specific manner

Building upon the cell identity changes observed with FPLD2 progression (**Figure 2.4**; **Supplemental Figure 2.3**), we next examined how these signatures differ across depots with disease. In patients with FPLD2, proinflammatory adipocytes were increased in the upper neck relative to the abdomen (**Supplemental Figure 2.4 A**). We observed an increase in proadipogenic ASPCs in the upper neck, specifically in biopsies from patients with developing FPLD2 (**Supplemental Figure 2.4 B**), which may explain the eventual expansion of upper neck WAT in with disease. Interestingly, lipid-associated macrophages were reduced in the upper neck relative to the abdomen in FPLD2, suggesting that abdominal macrophages adopt a more inflammatory phenotype (**Supplemental Figure 2.4 C**). A higher proportion of proinflammatory endothelial cells was present in the upper neck in developing and developed FPLD2 compared to the abdomen (**Supplemental Figure 2.4 D**). Proinflammatory T cells were similarly increased in the upper neck relative to the abdomen in developing FPLD2, potentially contributing to the proinflammatory environment of upper neck WAT (**Supplemental Figure 2.4 E**). In contrast, pericyte identity remained unchanged between depots with *LMNA* variants (**Supplemental Figure 2.4 F**), and proadipogenic LECs (**Supplemental Figure 2.4 G**) were increased in the upper neck relative to the abdomen in the developing disease state. Together, these data highlight depot-specific alterations in cellular subpopulations during FPLD2 progression. Compared to abdominal WAT, upper neck WAT is enriched for proinflammatory adipocytes and endothelial cells and has a decreased proportion of lipid activated macrophages. These depot-specific shifts

in cell identity and function likely contribute to the contrasting patterns of fat loss and redistribution in FPLD2.

Inducible lamin A/C knockout in adipocytes causes lipodystrophy but not metabolic dysfunction

Our bulk RNA-seq and snRNA-seq data from patients with FPLD2 revealed a broad downregulation of metabolic pathways and upregulation of inflammatory signaling, linked to pathogenic *LMNA* variants causing changes in adipocyte characteristics (**Figure 2.4 H**). To further investigate roles of lamin A/C in adipocyte maintenance, we created a tamoxifen-inducible adipocyte-specific *Lmna* knockout mouse (*Lmna*^{iADKO}), building on our previously published constitutive Adiponectin-Cre *Lmna* knockout model[26]. This inducible system enables targeted *Lmna* deletion in adult mice, avoiding confounding effects of puberty and allowing temporal control of *Lmna* knockout. Tamoxifen was administered intraperitoneally for five consecutive days to *Lmna*$^{fl/fl}$ and *Lmna*^{iADKO} mice (**Figure 2.5 A**). By two weeks post-tamoxifen, *Lmna*^{iADKO} mice exhibited reduced fat mass (**Figure 2.5 B**) without changes in body weight (**Supplemental Figure 2.5 A**) or lean mass (**Supplemental Figure 2.5 B**). Weights of posterior subcutaneous white adipose tissue (psWAT) and epididymal white adipose tissue (eWAT) were decreased at two- and four- weeks post-tamoxifen (**Figure 2.5 C, D**), though partially recovered by 16 weeks post-tamoxifen in *Lmna*^{iADKO} mice (**Figure 2.5 C, D**). Retroperitoneal white adipose tissue (rpWAT) was also decreased at two weeks post-tamoxifen, while perirenal white adipose tissue (prWAT), brown adipose tissue (BAT), and liver weights remained unchanged (**Supplemental Figure 2.5 C**). No sex-specific differences in WAT loss were observed, (**Supplemental Figure 2.5 D**), and both sexes were used throughout these mouse studies. Histological analyses showed no overt morphological changes in *Lmna*^{iADKO} WAT two- or eight-weeks post-tamoxifen (**Figure 2.5 E; Supplemental Figure 2.5 E**) or in liver tissue (**Supplemental Figure 2.5 E**). However, by eight weeks post-tamoxifen, *Lmna*^{iADKO} mice displayed slight whitening of BAT and partial loss of regulated bone marrow adipose tissue (rBMAT) and constitutive bone marrow adipose tissue (cBMAT) (**Supplemental Figure 2.5 E**). Circulating adiponectin levels were reduced at four weeks post-tamoxifen (**Figure 2.5 F; Supplemental Figure 2.5 F**), but no impairments in insulin sensitivity or glucose tolerance were observed at six- or 12 weeks post-tamoxifen in *Lmna*^{iADKO} mice compared to controls (**Figure**

2.5 G, H; Supplemental Figure 2.5 G, H). In summary, *Lmna*^{iADKO} mice exhibit early-onset adipose tissue loss following tamoxifen-induced *Lmna* deletion, with partial recovery over time and no development of metabolic dysfunction.

Lamin A/C-deficient adipocytes shrink, become misshapen, and disappear from WAT

To understand the fate of *Lmna* knockout adipocytes, we used the mTmG fluorescent reporter system[31], in which all cells express membrane-targeted tdTomato until Cre-mediated recombination triggers a switch to membrane-targeted GFP (**Figure 2.5 J**). We crossed this reporter line with *Adipoq*-Cre^{ERT2} mice and either the unmodified *Lmna* gene (*Lmna*^{CTRL} mTmG) or *Lmna*$^{fl/fl}$ (*Lmna*^{iADKO} mTmG) backgrounds. This allowed us to track *Lmna* knockout adipocytes *in vivo* by following GFP expression. Live tissue confocal imaging of WAT two weeks post-tamoxifen revealed widespread GFP+ adipocytes in psWAT and eWAT, confirming efficient recombination. At this early timepoint, GFP+ adipocytes in *Lmna*^{iADKO} and *Lmna*^{CTRL} mTmG mice were comparable in size and morphology (**Figure 2.5 J, K, M, N**). By six weeks post-tamoxifen, however, *Lmna*^{iADKO} GFP+ adipocytes had signs of degeneration, including shrinkage, irregular shape, and membrane budding, whereas GFP+ adipocytes in control WAT remained intact (**Figure 2.5 J, M**). Notably, the number of GFP+ adipocytes in *Lmna*^{iADKO} declined over time, coinciding with an increase in tdTomato+ adipocytes, suggesting compensatory adipogenesis by non-recombined precursors (**Figure 2.5 J, L, M, O**). By 16 weeks post-tamoxifen, few GFP+ adipocytes remained in *Lmna*^{iADKO} WAT, and tdTomato+ adipocytes predominated in psWAT and eWAT (**Figure 2.5 J, L, M, N**).

To test whether GFP+ *Lmna* knockout adipocytes might de-differentiate into stromal vascular cells (SVCs), we examined WAT in another imaging experiment, in which we saw some small GFP+ cells in psWAT and eWAT of *Lmna*^{iADKO} mTmG mice six weeks post-tamoxifen (**Supplemental Figure 2.6 A, B**), which were no longer detectable by 16 weeks post-tamoxifen (**Figure 2.5 J, M**). These data suggest that *Lmna* knockout adipocytes do not shrink and persist as SVCs. Flow cytometry confirmed that GFP+ SVCs in *Lmna*^{iADKO} mTmG WAT were not elevated versus controls; in fact, control WAT had more GFP+ SVCs than *Lmna*^{iADKO} tissue (**Supplemental Figure 2.6 C, D**). Together, these data indicate that *Lmna* knockout adipocytes undergo progressive atrophy, loss of lipid content and structure, and eventual

clearance from tissue. These data supports a critical role for lamin A/C in the maintenance and survival of mature adipocytes.

Lmna^{iADKO} WAT has a similar molecular pattern as WAT from patients with FPLD2: increased inflammation and decreased fatty acid metabolism

To investigate the molecular mechanisms underlying adipocyte shrinkage and loss (**Figure 2.5 J, M**), we performed bulk RNA-seq and proteomics on parametrial white adipose tissue (pmWAT) from *Lmna*^{iADKO} and *Lmna*$^{fl/fl}$ mice two weeks post-tamoxifen, prior to obvious changes in adipocyte morphology. GSEA of both datasets revealed substantial overlap in dysregulated pathways (**Figure 2.6 A**). Notably, immune-related processes such as myeloid activation and antigen binding were upregulated at the transcript and protein level in *Lmna*^{iADKO} WAT, whereas pathways related to oxidative phosphorylation and fatty acid biosynthesis were consistently downregulated (**Figure 2.6 B**). Additional proteome-specific changes in *Lmna*^{iADKO} WAT included elevated cell death signatures and suppression of muscle-associated pathways (**Figure 2.6 C**). Following our pathway analyses, we found repression of lipogenic and triacylglycerol (TAG) synthesis genes (**Figure 2.6 D**), as well as downregulation of mitochondrial genes (**Figure 2.6 E**). Concurrently, proinflammatory genes (**Figure 2.6 F**) and cell death genes (**Figure 2.6 G**) were upregulated, indicating a shift towards inflammation and cellular deterioration.

To contextualize these findings, we compared our *Lmna*^{iADKO} RNA-seq data with transcriptomic data from psWAT of female four-week-old *Lmna*^{ADKO} mice, in which *Lmna* is constitutively knocked out with Adiponectin-Cre[26]. Integration of GSEA results from both models revealed strong concordance, including increased inflammation and decreased mitochondrial and lipid metabolism pathways (**Supplemental Figure 2.7 A, B**). *Lmna*^{iADKO} WAT had broader suppression of metabolism pathways including polysaccharide and pyruvate metabolism (**Supplemental Figure 2.7 C**), whereas *Lmna*^{ADKO} WAT had a pronounced activation of fibrosis and collagen-related gene programs (**Supplemental Figure 2.7 D**). This integrative analysis underscores a conserved role for lamin A/C in maintaining adipocyte transcriptional homeostasis.

Lastly, we integrated the GSEA from our *Lmna*^{iADKO} WAT with our human bulk RNA-seq data from patients with FPLD2 (**Figure 2.6 I**). This revealed significant overlap in enriched

pathways, including increased inflammation and downregulated mitochondrial and lipid metabolism pathways (**Figure 2.6 J**). Together, these transcriptomic and proteomic analyses highlight fundamental key disruptions in adipocytes following *Lmna* deletion, mirroring key features of FPLD2 pathology, reinforcing the essential role of functional lamin A/C in adipose tissue homeostasis.

Lipogenic and mitochondrial protein expression is lower in *Lmna*^{iADKO} WAT, accompanied by decreased respiration and altered mitochondrial structure

To assess functional consequences of the molecular differences observed in our datasets, we evaluated protein expression and mitochondrial function in *Lmna*^{iADKO} WAT. In *Lmna*^{iADKO} psWAT, which showed no change in WAT mass two-weeks post-tamoxifen (**Figure 2.5 C**), we found no difference in protein expression of adipogenic transcription factors PPARg and C/EBPa. However, expression of the lipogenic transcription factor carbohydrate response element binding protein (ChREBP) was reduced, along with key lipogenic enzymes such as acetyl co-A carboxylase (ACC), fatty acid synthase (FASN), and sterol co-A desaturase 1 (SCD1) (**Figure 2.7 A; Supplemental Figure 2.8 A**). Similar patterns of protein expression were observed in *Lmna*^{iADKO} eWAT, with reduced expression of ChREBP and lipogenic enzymes (**Figure 2.7 B; Supplemental Figure 2.8 B**). Interestingly, PPARg expression was increased in *Lmna*^{iADKO} eWAT, potentially reflecting a compensatory response, as this depot was slightly decreased in mass two weeks post-tamoxifen (**Figure 2.5 D**). Given the well-established link between lipid metabolism and mitochondrial function[32,33], and the suppression of mitochondrial pathways observed in both human and mouse RNA-seq datasets, we next examined mitochondrial protein expression. We observed a decrease in oxidative phosphorylation (OXPHOS) complex expression in *Lmna*^{iADKO} eWAT (**Figure 2.7 C; Supplemental Figure 2.8 C**), which led us to explore functional changes in mitochondrial respiration.

Using Oroboros Oxygraph-2k high-resolution respirometry on floated adipocytes from pmWAT two weeks post-tamoxifen, we observed that *Lmna*^{iADKO} adipocytes had decreased baseline (**Figure 2.7 D**), maximal (**Figure 2.7 E**), and ATP-linked (**Supplemental Figure 2.8 D**) respiration, along with reduced spare respiratory capacity (**Supplemental Figure 2.8 E**) and proton leak (**Supplemental Figure 2.8 F**). In contrast, *Lmna* KO adipocytes isolated from

psWAT at the same time point did not exhibit changes in mitochondrial respiration (**Supplemental Figure 2.8 G-K**), suggesting that reductions in lipid metabolism proteins (**Figure 2.7 A**) may precede overt mitochondrial dysfunction following *Lmna* deletion in adipocytes. Mitochondrial DNA content remained unchanged in both psWAT (**Supplemental Figure 2.8 L**) or pmWAT, regardless of genotype (**Supplemental Figure 2.8 M**). Further analyses of floated adipocytes from *Lmna*^{iADKO} WAT two-weeks post-tamoxifen showed decreased OXPHOS proteins and revealed reduced expression of several key regulators of mitochondrial biogenesis and dynamics, including PGC1a, MFN2, OPA1 and VDAC1 (**Figure 2.7 F, Supplemental Figure 2.8 N, O**). Expression of the outer mitochondrial membrane marker TOM20 was unchanged, suggesting that mitochondrial number is not significantly altered in *Lmna*^{iADKO} adipocytes compared to controls (**Figure 2.7 F, Supplemental Figure 2.8 N, O**). Due to the decrease in fission and fusion protein expression in *Lmna*^{iADKO} WAT, we next explored changes in mitochondrial distribution and localization. We imaged primary adipocytes at two weeks post-tamoxifen and observed evenly distributed mitochondria across the adipocytes, with many concentrated in the perinuclear region, as previously shown[34]. However, in *Lmna*^{iADKO} adipocytes, we observed irregular mitochondrial distribution, with clustering and aggregations, a potential sign of cell damage which has been observed in MFN2 KO cells[35].

To investigate potential structural abnormalities, we performed transmission electron microscopy (TEM) on *Lmna*^{iADKO} and *Lmna*$^{fl/fl}$ eWAT two weeks post-tamoxifen. We first assessed nuclear morphology and saw no obvious changes in nuclear shape or nuclear lamina integrity in *Lmna*^{iADKO} WAT (**Figure 2.7 H**). We did see potential changes in condensed heterochromatin, particularly within the nuclear interior and periphery, suggesting altered chromatin organization. Examination of lipid droplets revealed an increased number of small lipid droplet associated with the large unilocular lipid droplet in *Lmna*^{iADKO} adipocytes. These small lipid droplets had many small mitochondria surrounding them, suggesting either active lipd synthesis, droplet fission, or budding (**Figure 2.7 H**). Furthermore, close analyses of mitochondria in *Lmna*^{iADKO} WAT revealed pronounced mitochondrial abnormalities, with mitochondria exhibiting disorganized cristae and swollen morphology (**Figure 2.7 H**), consistent with impaired mitochondrial function observed at the molecular and functional levels. In summary, *Lmna* deletion in adipocytes leads to defects in mitochondrial respiration, suppressed expression of mitochondrial regulatory proteins, and structural abnormalities, including

disorganized cristae and increased small lipid droplet formation. Together, these features may contribute to the progressive decline and eventual loss of *Lmna* KO adipocytes.

Adipocyte loss is not driven by increased adipocyte lipolysis

Following our TEM observations of increased small lipid droplets in *Lmna*^{iADKO} adipocytes, we investigated whether enhanced lipolysis might cause adipocyte delipidation and loss *in vivo*. First, we measured circulating glycerol concentrations under fed and fasted conditions at multiple timepoints post-tamoxifen. By four weeks post-tamoxifen, *Lmna*^{iADKO} mice exhibited reduced circulating glycerol concentrations, which continued to decline at later timepoints post-tamoxifen (**Supplemental Figure 2.9 A**). These findings suggest that basal lipolysis is not increased during adipose tissue loss. To assess stimulated lipolysis, we administered isoproterenol, a β-adrenergic agonist, at four weeks post-tamoxifen, when *Lmna*^{iADKO} mice are actively losing WAT. Whereas *Lmna*^{iADKO} mice had showed reduced glycerol concentrations post-isoproterenol compared to controls (**Supplemental Figure 2.9 B**), this difference was attributable to reduced fat mass. When glycerol concentrations were normalized to fat mass, no difference in stimulated lipolytic capacity was observed (**Supplemental Figure 2.9 C**). Analyses of bulk RNA-seq data from *Lmna*^{iADKO} pmWAT revealed a broad downregulation of lipolytic genes at two weeks post-tamoxifen, suggesting that adipocytes are likely suppressing lipolytic programs to preserve lipid stores (**Supplemental Figure 2.9 D**). However, we did not observe a suppression of lipolysis-associated proteins in *Lmna*^{iADKO} WAT (**Supplemental Figure 2.9 E, F**). These results indicate that lipolysis is not increased in *Lmna*^{iADKO} WAT, at least by our measures, and suggest that adipocytes delipidate and are lost through alternative, lipolysis-independent mechanisms.

***Lmna*-deficient adipocytes have upregulated expression of proinflammatory genes**

In our bulk human and mouse datasets, we consistently observed increased inflammatory gene expression in WAT when lamin A/C is knocked out or mutated. Analysis of snRNA-seq data from patients with FPLD2 could inform where this immune signature is coming from, but at a bulk level, macrophages exhibited a less inflammatory signature in disease, whereas T cells displayed increased proinflammatory gene expression (**Figure 2.4 L, Supplemental Fig 2.3 E**). To investigate which immune cells might contribute to the proinflammatory signature in

Lmna^{iADKO} WAT, we performed spectral flow cytometry to assess macrophage and T cell populations in *Lmna*^{iADKO} psWAT and pmWAT two weeks post-tamoxifen (gating strategy in **Supplemental Figure 2.10 A**). We detected no difference in the total number of SVCs or CD45+ immune cells between genotypes or depots (**Supplemental Figure 2.10 B, C**). Likewise, the number of adipose-tissue macrophages (ATMs; CD64+) and their expression of CD11c (marker of M1-like macrophages) were unchanged in *Lmna*^{iADKO} WAT (**Supplemental Figure 2.10 D-F**). We further evaluated macrophage subtypes and found no difference in the proportions of TIM4+ (tissue-resident) or CD163+ (M2-like) macrophages between groups in either depot (**Supplemental Figure 2.10 G-J**). Similarly, analysis of T cells (CD3+) showed no significant differences in helper CD4+ or cytotoxic CD8+ T cells regardless of genotype or depot (**Supplemental Figure 2.10 K-N**). Taken together, based on classical surface markers, neither macrophages nor T cells exhibit a proinflammatory shift in *Lmna*^{iADKO} WAT.

Given the absence of overt immune cell activation, we next evaluated whether *Lmna* KO adipocytes themselves may be contributing to the proinflammatory gene signature. Reverse transcriptase quantitative PCR (RT-qPCR) revealed modest, non-significant in multiple proinflammatory transcripts in *Lmna*^{iADKO} WAT (**Supplemental Figure 2.10 O, P**). When we isolated adipocytes and SVF from both depots, we found that *Lmna* KO adipocytes in psWAT showed increased expression of *Il6, Il10*, *Nlrp3*, *Il1b*, and *Tnfa* (**Supplemental Figure 2.10 Q**), while the corresponding SVF showed increased *Il1b* only (**Supplemental Figure 2.10 R**). A similar pattern was observed in pmWAT, where *Lmna* KO adipocytes had increased *Il10*, *IL1b*, and a non-significant trend towards higher expression of *Il6* and *Tnfa* (**Supplemental Figure 2.10 S**); the SVF showed increased *Il10* and *Tnfa* (**Supplemental Figure 2.10 T**). Therefore, these data suggest that elevated proinflammatory transcripts in *Lmna*^{iADKO} WAT are primarily driven by inflammation in *Lmna* KO adipocytes through a cell-autonomous mechanism, potentially via the NLRP3 inflammasome, with minor contributions from other SVF cells.

Finally, we assessed classical apoptosis in *Lmna*^{iADKO} WAT by examining cleaved caspase-3 expression. Although our mTmG imaging revealed shrunken adipocytes with intact membranes (**Figure 2.5 J, M**), consistent with an apoptotic process, we did not detect cleaved caspase-3 protein at two, four, or six weeks post-tamoxifen (**Supplemental Figure 2.10 U**). While some cell death-related transcripts were upregulated in our bulk RNA-seq of *Lmna*^{iADKO} WAT (**Figure 2.6 G**), the signal may be diluted due to the sparse and asynchronous nature of

adipocyte loss across the tissue (**Figure 2.5 J, M**). Thus, although we hypothesize that *Lmna* KO adipocytes undergo delipidation, shrinkage, and ultimately cell death, the precise mechanism underlying this process is still unknown.

Fundamental role of lamin A/C in regulating lipid metabolism and inflammatory gene expression across cell types

Thus far, we have observed consistent gene expression changes in both models of *Lmna* deficiency in mouse adipocytes and WAT from human patients with pathogenic *LMNA* variants, including suppression of lipid metabolism pathways and upregulation of inflammation. To determine whether these molecular alternations are specific to lamin A/C-induced lipodystrophy, or indicative of a broader regulatory role for lamin A/C, we analyzed publicly available microarray and Assay for Transposase-Accessible Chromatin sequencing (ATAC-seq) datasets from *Lmna* KO mouse embryonic fibroblasts (MEFs). Notably, these *Lmna* KO MEFs exhibit impaired mitochondrial respiration and irregular mitochondrial localization, similar to our observations in *Lmna* KO adipocytes[36,37]. To explore shared regulatory signatures, we integrated RNA-seq data from *Lmna*^{iADKO} WAT with gene expression and ATAC-seq data from *Lmna* KO MEFs (**Figure 2.8 A**). We then performed GSEA to identify coordinated changes in transcription and chromatin accessibility upon lamin A/C deficiency (**Figure 2.8 B**). This revealed broad dysregulation of lipid metabolism pathways, including lipid transport and lipid biosynthesis, across both gene expression and chromatin states (**Figure 2.8 B**). We next analyzed overlapping leading edge genes from relevant lipid-related pathways and found a subset of genes were similarly dysregulated in *Lmna*^{iADKO} WAT and *Lmna* KO MEFs and correlated with changes in chromatin accessibility (**Figure 2.8 C**). Among these, *Acsl4*, *Acsl6*, *Rbp1* and *Scl27a3* are known to play important roles in adipocyte homeostasis, suggesting that lamin A/C may directly regulate these genes at the chromatin level across different cell types. We then extended these analyses to genes involved inflammation. We found that regulation of inflammatory response was altered across both gene expression and chromatin accessibility in *Lmna* KO MEFs and adipocytes (**Figure 2.8 D**). Overlapping leading edge genes included *Il1rl1*, *Il33*, and *Cd44*, all of which regulate inflammation in adipose tissue (**Figure 2.8 E)**. Together, these findings indicate that loss of lamin A/C leads to coordinated changes in lipid metabolism and inflammatory genes across distinct models, and many of these changes can be linked to

alternations in chromatin accessibility. Therefore, this suggests a possible conserved role for lamin A/C in maintaining metabolic and immune gene programs.

We next analyzed the significant ATAC-seq peaks from the control and *Lmna* KO MEFs, to determine how they were distributed across different annotated chromatin features[38]. We did not observe differences in the proportion of peaks falling within specific chromatin annotations between control and KO MEFs (**Figure 2.8 F**), suggesting that loss of *Lmna* does not selectively alter accessibility in particular chromatin contexts. This is consistent with the ubiquitous binding of lamin A/C to 30-40% of the genome[39].

Although the distribution of chromatin features remained unchanged, we asked whether altered transcription factor accessibility may underlie changes in gene expression observed in *Lmna* KO MEFs. To explore this, we performed motif enrichment analysis to evaluate transcription factor binding motifs that were overrepresented in accessible chromatin regions, particularly near differentially expressed genes. To do this, we stratified *Lmna* KO MEF microarray data into four bins based on their log2fold change, from most downregulated to most upregulated (**Figure 2.8 G**). Motif enrichment analysis revealed that KLF family motifs were enriched near the most downregulated genes, while motifs for HNF1A/B, HOX family transcription factors, and immediate early genes such as FOS and JUN were enriched near the most upregulated genes (**Figure 2.8 G**). These findings suggest that altered activity of specific transcription factors like KLFs and FOS/JUN may play a key role in regulating *Lmna*-dependent gene expression programs.

The enrichment of KLF family motifs was particularly notable, given their well-established roles in lipid metabolism, inflammation, and adipose tissue biology[40]. To investigate further, we examined ATAC-seq signal tracks at the *Klf4* and *Klf13* loci, both of which showed significant changes in chromatin accessibility. We identified three putative enhancer regions near *Klf4* that became more accessible following *Lmna* KO (log2fold change = -1.48) (**Figure 2.8 H**). As *Klf4* is a key regulator of adipocyte differentiation, reduced expression or activity could impair adipocyte function and tissue homeostasis[41]. Similarly, *Klf13* was surrounded by several putative enhancers that exhibited both gains and losses in accessibility, with an overall downregulation of expression (log2fold change of -2.04) (**Figure 2.8 I**). Given that *Klf13* has been implicated in suppressing inflammatory responses, its downregulation may contribute to the heightened inflammation observed in *Lmna* KO models[42]. Together, these findings suggest that

loss of lamin A/C disrupts enhancer accessibility at loci of lipid- and inflammation-related transcription factors, contributing to adipocyte dysfunction.

2.4 Discussion

In this study, we investigated mechanisms underlying lipodystrophy using human, mouse, and cell culture models to better understand the progression and pathogenesis of FPLD2. We first analyzed patients with developing and developed FPLD2 and found, as expected, a decrease in body fat percentage compared to healthy controls[7]. Notably, no prior studies focused on the "developing" state of FPLD2, during which patients harbor pathogenic *LMNA* variants but exhibit few clinical symptoms. We found that even before the overt onset of adipose tissue loss and metabolic dysfunction, patients with developing FPLD2 have a reduction in total body fat, and, specifically, trunk fat percentage. Assessment of metabolic parameters revealed that only patients with developed FPLD2 had elevated HbA1c, hyperlipidemia, and increased circulating FGF2, indicating that systemic metabolic dysfunction emerges later, in conjunction with severe adipose loss. It is important to note that the severity of metabolic syndrome in both FPLD2 patient groups may be underestimated in our cohort, as many patients were taking metformin and lipid-lowering agents.

We also performed histological analyses of WAT from patients with FPLD2. Interestingly, adipocytes size was unaltered in both abdominal and upper neck depots, with no significant differences between patient groups. These data are supported by our mouse studies, where we tracked the fate of *Lmna*-deficient adipocytes. At two weeks post-tamoxifen, a comparable analog to our developing patient group, we saw no change in adipocyte size in $Lmna^{iADKO}$ WAT (**Figure 2.5 K, N**). However, just a few weeks later, many adipocytes appeared shrunken and misshapen and were subsequently lost. In the response to this loss, we observed new compensatory adipogenesis, as indicated by the increase in tdTomato+ adipocytes (**Figure 2.5 L, O**). While we are unable to directly track adipocyte fate in human WAT biopsies, these mTmG mouse experiments suggest that adipocytes lacking functional lamin A/C undergo turnover and can be partially replaced. Importantly, this regeneration is incomplete: after the loss of *Lmna* KO adipocytes, we observed only a partial rescue of adipose tissue mass (**Figure 2.5 C, D**), indicated impaired or exhausted adipogenesis in the remaining precursor pool. There may be a unique inability for abdominal subcutaneous WAT to replenish itself in the context of *LMNA* variants. We propose that precursors with *LMNA* variants can undergo the first round of adipogenesis during gestation and early life. However, given the ~10 year half-life of adipocytes, once mature adipocytes naturally turnover, new adipocytes are unable to regenerate and maintain

adipose tissue mass[43]. This model aligns with the clinical onset of FPLD2, which typically emerges around puberty, coinciding with the timing of adipocyte renewal.

The similarity in results between our diverse datasets, including bulk RNA-seq from human FPLD2 subcutaneous WAT, proteomics and bulk RNA-seq from *Lmna*^{iADKO} pmWAT, and bulk RNA-seq from *Lmna*^{ADKO} psWAT was particularly striking. We observed a consistent suppression in lipid metabolism and adipogenesis genes, many of them related to *de novo* lipogenesis, triacylglycerol synthesis, and glyceroneogenesis. Notably, SCD1 was essentially undetectable in *Lmna*^{iADKO} WAT (**Figure 2.7 A, B**), suggesting that impaired lipid synthesis contributes to adipocyte loss when lamin A/C is disrupted. Our human snRNA-seq data from patient WAT revealed that this suppression of lipid metabolic gene expression is most prominent in adipocytes, but is also evident in macrophages, pericytes, and endothelial cells. We also detected decreased expression of ChREBP in *Lmna*^{iADKO} WAT two weeks post-tamoxifen, a key regulator of lipogenesis in adipocytes[44]. Prior work showed that adipocyte-specific ChREBP KO leads to reduced pmWAT but not sWAT in 16-week-old mice[44]; potentially explaining the susceptibility of gWAT to be lost before psWAT in our *Lmna*^{iADKO} mice (**Figure 2.5 C, D; Supplemental Figure 2.5 D**). Although SREBP1 protein levels were unchanged in *Lmna*^{iADKO} WAT, the downregulation of its transcriptional targets at the mRNA and protein levels suggests impaired transcriptional activity (**Figure 2.6 D; 2.7 A, B**). SREBP1 has an increasingly appreciated contribution to lipogenesis in WAT[45], and has been shown to directly interact with lamin A, with FPLD2-causing *LMNA* variants disrupting the interaction between lamin A and SREBP1[46]. Mice with constitutively active SREBP1 in adipose tissue exhibited lipodystrophy and metabolic dysfunction, driven by reduced adipogenic gene programs, further implicating SREBP1 with impaired WAT function[47]. Additionally, *Scd1* KO in cultured adipocytes causes autophagic cell death, highlighting the importance of intact lipogenesis for adipocyte homeostasis[48].

Another conserved feature across our human and mouse datasets was impaired mitochondrial gene expression and function. In patient WAT with *LMNA* variants, our snRNA-seq data showed reduced oxidative phosphorylation signatures in all cell types. Similar findings have been reported in *Lmna* KO MEFs (e.g. reduced mitochondrial respiration, clumped mitochondrial distribution)[36], hearts from *Lmna* KO mice (e.g. decreased OXPHOS protein levels and cristae number)[49] and *LMNA* R482W inducible pluripotent stem cells (iPSCs) (e.g.

reduced oxygen consumption)[50]. While it remains unclear whether impaired mitochondrial function precedes or follows suppression of lipid metabolism, our data suggest that lipogenic defects occur first: in *Lmna*^{iADKO} psWAT, lipogenic enzymes are downregulated before disruption of oxygen consumption in *Lmna* KO adipocytes (**Figure 2.7 A; Supplemental Figure 2.8 G-K**).

We have consistently observed upregulation of inflammatory pathways across our models. However, our flow cytometry and snRNA-seq analyses did not reveal increased activation of macrophages or an increase in proinflammatory T cells. Instead, RT-qPCR analyses indicated that *Lmna* KO adipocytes had increased expression of immune-related genes, suggesting inflammation originates within the adipocytes themselves. These findings were supported by patient snRNA-seq data, which showed upregulation of IL6/JAK/STAT3 signaling and IL2/STAT5 signaling in adipocytes (**Figure 2.4 H; Supplemental Figure 2.10 Q, S**). The trigger for inflammation in our studies remains unclear. It may be a direct consequence of lamin A/C disruption, as supported by proinflammatory signatures in *Lmna* KO MEFs (**Figure 2.8 D, E**), or it might be secondary to impaired lipogenesis and/or mitochondrial dysfunction. Supporting the latter, ChREBP adipocyte-specific KO WAT had increased ATM infiltration, suggesting that impairing *de novo* lipogenesis in adipocytes triggers immune cell recruitment[44]. In human WAT biopsies, increased inflammation was associated with decreased lipogenic marker expression[51]. Furthermore, haploinsufficiency of *Crif1* in adipocytes, a mitochondrial translation factor, triggered proinflammatory cytokine secretion and macrophage infiltration[52].

Our snRNA-seq dataset provided insights into the cellular contributors to bulk transcriptional changes and disease progression in FPLD2. In both abdominal and upper neck depots, we observed an increased proportion of LECs in patients with developing FPLD2, which declined once FPLD2 had progressed (**Figure 2.4 B-E**). While LECs are known to regulate lymphatic, paracrine, and immune signaling in WAT, they have not been previously been implicated in lipodystrophy. Our data suggest that changes in LEC abundance may reflect a compensatory response to adipocyte loss or contribute directly to tissue remodeling. Furthermore, we observed that adipogenic ASPCs increase in both developing and developed FPLD2 WAT biopsies, suggesting that ASPCs are attempting to undergo differentiation to restore WAT mass. Prior studies have shown that pathogenic *LMNA* variants can impair adipogenesis *in vitro*, consistent with our observation that ASPCs upregulate their adipogenic

gene expression but are unable to compensate sufficiently[20,25,53,54]. Finally, though we did not see a global proinflammatory phenotype in macrophages with FPLD2 (**Figure 2.4 L**), we did see a shift in the proportion of lipid-associated macrophages in both developing and FPLD2 states (**Figure 2.4 M**). Other models of lipodystrophy have shown an increase in proinflammatory recruited macrophages in WAT[55]; but our findings suggest a more subtle shift towards lipid-scavenging phenotypes in response to adipocyte loss in FPLD2.

Our study provides the first direct comparison between atrophic (abdominal) and hypertrophic (upper neck) adipose depots in FPLD2. We found that adipocyte were transcriptionally similar between depots, but stromal cells differed: ASPCs were more proadipogenic in the neck, macrophages more proinflammatory in the abdomen, pericytes more proadipogenic in the abdomen, and endothelial cells more inflammatory in the upper neck. These cell-type-specific shifts may contribute to depot-selective fat loss or gain. Although prior studies of the neck depot reported increased fibrosis and decreased adipocyte size[56], we did not observe an increase in fibrosis or adipocyte size differences in this depot with FPLD2. However, our snRNA-seq analyses revealed distinct signatures between depots with FPLD2 development, including increased of proinflammatory adipocytes and endothelial cells, and decreased proportion of proinflammatory macrophages and mitotic ASPCs (**Supplemental Figure 2.4 A-D**). These insights into fundamental depot differences and shifts in cellular proportions with FPLD2 elucidate how WAT remodeling occurs with disease progression.

Finally, we investigated the chromatin basis of transcriptional dysregulation upon lamin A/C disturbance. Lamin A/C deletion regulates changes in chromatin accessibility both within and outside LADs in KO MEFs[36]. Another study of total lamin KO in mouse embryonic stem cells revealed a disruption in a subset of LADs and drastic switches of chromatin between active and repressive states[57]. Our data extend these observations: we found overlap in gene expression changes between *Lmna*^{iADKO} WAT and *Lmna* KO MEFs (**Figure 2.8**), including suppression of lipid metabolism genes and activation of inflammatory pathways, which may be driven by changes in enhancer accessibility of transcription factors upon *Lmna* KO. However, the overall overlap was limited, this is likely due to differences in cell type, tissue complexity, and the known cell type specificity of lamin A/C's genomic interactions[58]. Nonetheless, our findings support a model in which lamin A/C disruption impairs chromatin organization in a manner that

broadly dysregulates lipid metabolism, mitochondrial function, and inflammation across multiple cell types.

Despite these insights, our study has multiple limitations. Our human cohort spans a wide age range and uses both sexes, which may introduce variability. Furthermore, due to adipocyte fragility, we pursued snRNA-seq instead of single cell RNA-seq (scRNA-seq), which limits detection of cytoplasmic transcripts. In mice, our use of an adipocyte-specific *Lmna* KO mouse model does not fully model human FPLD2; future studies should utilize knock-in mouse models to study effects of pathogenic *LMNA* variants in WAT. In summary, we show that lamin A/C is essential for ensuring adipocyte homeostasis and survival, and maintains adipocyte lipid metabolism and mitochondrial function, and its disruption leads to inflammation, adipocyte shrinkage, and eventual cell loss. These findings uncover fundamental pathways linking lamin A/C dysfunction to lipodystrophy and provide a new framework for future therapeutic interventions.

2.5 Materials and methods

Human participants

Patients carrying pathogenic LMNA variants (R482Q, n = 6; R482W, n = 4; R582L, n = 2; R584H, n = 2; R582C, n = 1; R582C, n = 1) and their unaffected relatives were enrolled in this prospective, longitudinal observational study. Participants were classified into three groups: Group A were young individuals (ages 15–23 years) with LMNA variants who were developing signs of lipodystrophy but with visually residual adipose depots in areas destined to be lost, Group B were affected adult relatives (ages 39-63 years) with overt partial lipodystrophy, and displaying full phenotype with complete loss of fat from extremities, gluteal regions and78ut8 ryyt56ycgx subcutaneous abdominal wall and Group C were unaffected relatives (parents, siblings, or cousins aged 23–58 years) as negative controls.

Physical examinations included anthropometric measurements (height, weight, waist and hip circumferences, as well as blood pressure, pulse rate, and full physical exam. Fasting blood samples (≥10 hours) were collected for measurement of plasma glucose, insulin, HbA1c, C-peptide, adipokines including leptin and adiponectin, triglycerides, HDL and LDL cholesterol, liver enzymes (ALT, AST, GGT), kidney function markers (BUN and creatinine), C-reactive protein (CRP), as well as other inflammatory markers: fibroblast growth factor 21 (FGF-21, pg/mL), interferon gamma (IFNγ), interleukin-6 (IL-6), monocyte chemoattractant protein-1 (MCP-1), tumor necrosis factor-alpha (TNFα), soluble tumor necrosis factor receptor I (sTNFRI) and soluble tumor necrosis factor receptor II (sTNFRII).

A five-hour oral glucose tolerance test (OGTT) using 75 grams glucose was performed with blood sampling every 30 minutes to assess glucose, insulin, non-esterified fatty acids (NEFA), and C-peptide. Indices of insulin resistance, including HOMA-IR and ADIPO-IR, were calculated from fasting values. Body composition was assessed using two complementary methods. MRI-based fat quantification was conducted using a 3 Tesla scanner (Philips Healthcare) using a custom in-house MatLab program to analyze fat mass from the images. Whole-body composition, including fat and lean mass, was also measured using dual-energy X-ray absorptiometry (DEXA; GE Lunar Prodigy, model PA +41744). Hepatic fat quantification was performed on a 3 Tesla clinical MRI system (Philips Healthcare) using the vendor-provided, torso phased-array surface coil positioned on the abdomen. Additionally, breath-hold, single-

shot, turbo-spin-echo sequences for localization were obtained, and fat were quantified using two image-based and one spectroscopy-based technique as previously published[59]. The study was approved by the University of Michigan Institutional Review Board (IRB: HUM#00174659) and all participants provided written informed consent.

Bulk RNA-sequencing from human or mouse WAT

For human tissue, RNA was isolated from 150-200 mg of human adipose tissue and processed via the RNeasy Lipid Tissue Mini Kit (74804, Qiagen) according to manufacturer's instructions. For mouse tissue, total RNA was isolated and purified from mouse WAT using RNA STAT-60 (CS-110, amsbio) according to the manufacturer's instructions. After DNAse treatment, samples were subjected to quality control, library preparation, and strand-specific mRNA sequencing (Beijing Genomics Institute, China). Over twenty million reads were obtained using a paired-end 100 bp module on DNBSEQ platform. FastQC (v.0.12.1) was used to check the quality of the raw read data. Alignment was conducted using STAR (version 2.7.11a), using UCSC mm39 as the reference genome sequence. A second quality control was performed post-alignment using FastQC to ensure that only high-quality data were used for gene expression quantitation and differential expression analyses. Differential expression analysis was conducted using DESeq2. Plots were generated using variations or alternative representations of native DESeq2 plotting functions, ggplot2, plotly, and other packages within the R environment. Pathway analyses were conducted on ranked lists of log2 fold change using Gene Set Enrichment Analysis (GSEA) software v4.3.3 and the Broad Institute Molecular Signature Database (MSigDB). Output from DESeq2 analyses was used to generate lists of genes ranked by the metric -log10 p-value $*$ log2 fold change. The resulting lists were run through pre-ranked GSEA using the Molecular Signatures Database v2024.1.Mm (M5: ontology gene sets). Enriched pathways were defined by an FDR < 0.05. Normalized enrichment score (NES) is the primary metric from GSEA for evaluating the magnitude of differentially expressed pathways. The ggplot2 package in R was used to further visualize enriched pathways.

Remove unwanted variation (RUV)-seq analysis on human WAT

To reduce the impact of both known and unknown confounding factors in the human samples, we incorporated known covariates into the DESeq2 model and accounted for hidden sources of

variation using the RUVseq latent variable method[60]. The analysis followed a multi-step approach: (1) An initial differential expression (DE) analysis was conducted using DESeq2, with RIN and fasting insulin included as known covariates. Genes that were not significantly different between conditions (p-value > 0.5) in this analysis were considered stable and used as empirical control genes in the RUVg function from RUVseq to estimate latent factors representing unmodeled variability. (2) These latent variables were then added to the DESeq2 model as additional covariates (alongside RIN and fasting insulin, where applicable) for a second round of DE analysis. The number of latent factors was chosen based on optimal separation of conditions and minimal distortion in relative log expression (RLE) plots. The final list of differentially expressed genes for each cell type was generated by applying a 5% false discovery rate (FDR) threshold to the output of the second DESeq2 run.

Single nuclei RNA-sequencing from human adipose tissue

Nuclei were isolated from 150-250 mg of tissue, which was minced in 1 mL of nuclear extraction buffer (130-128-024, Miltenyi) and transferred into GentleMACS tubes. The h_tumor_01 protocol was run on the GentleMACS three times. Then, tubes were placed on ice for 10 minutes. The homogenate was then passed through a 70 μM filter and washed with 3 mL of nuclei extraction buffer. Samples were centrifuged at 500 x g for 10 minutes at 4°C. Supernatant was removed, and nuclear pellet was resuspended in 2 mL 1% BSA in PBS. Samples were then filtered using a 30 μM filter and rinsed with 2 mL 1% BSA in PBS Samples were centrifuged at 500 x g for 10 minutes at 4°C. Pellets were resuspended in 500 μL 1% BSA in PBS and filtered once more through a pre-wet 20 μM filter. Filters were washed with 500 μL 1% BSA in PBS. Samples were centrifuged at 500 x g for 10 minutes at 4°C, supernatant removed, and nuclear pellet resuspended in 50 μL 1% BSA in PBS. Nuclei were then counted at the University of Michigan Advanced Genomics Core using a Logos cell counter. Probes were hybridized, samples were pooled and processed according to manufacturer instructions for 10X Genomics Chromium Fixed RNA Profiling Reagent Kits for Multiplexed Samples (PN 1000568). Final library quality was assessed using the LabChip GXII HT (PerkinElmer) and libraries were quantified by Qubit (ThermoFisher). Pooled libraries were subjected to paired-end sequencing according to the manufacturer's protocol (Illumina NovaSeq XPlus). BCL Convert Software (Illumina) was used to generate de- multiplexed Fastq files, and the CellRanger

Pipeline (10X Genomics) was used to align reads and generate count matrices. Seurat v5.1.0 was used for filtering low-quality cells and genes, expression normalization, dimensional reduction, clustering, visualization of gene expression, and differential expression analysis. Cells were filtered if they had <1000 UMIs, had <500 detected genes, had >5% of transcripts corresponding to mitochondria-encoded genes, and had log10 Genes Per UMI < 0.80. Genes were filtered if they were detected in <10 cells. The SCTransform function in Seurat was used to perform normalization and variance stabilization of the scRNA-seq datasets, while regarding mitochondria mapping percentage as a covariate. To integrate and correct for batch effects across samples, Harmony was applied to the SCTransformed data using RunHarmony. The resulting Harmony embeddings were used for downstream dimensional reduction and clustering. 30 principal components were used in clustering and UMAP analysis. Clustering was done by a shared nearest neighbor (SNN) modularity optimization-based clustering algorithm. The visualization of the clusters was performed using UMAPs. The clusters were annotated to cell types by known marker genes of cell types and the top differentially expressed genes in the cluster. Pathway analysis was conducted as described above in the bulk RNA-seq analysis section.

Quantification of human adipocyte size and fibrosis

Human adipose tissue sections were stained with hematoxylin & eosin and analyzed using the Aivia AI-based image analysis software (Leica Microsystems). Pixel Classifier profiles were trained to identify adipocytes. After optimization, adipocytes were counted, and area was quantified with Aivia's Recipe Console tool. At least 100 adipocytes were quantified per patient, with a median of 553 adipocytes measured per patient.

Animals

Lmna$^{fl/fl}$ mice had loxP sites flanking exons 10 and 11 of the *Lmna* allele.[61] Adipoq-CreERT2 mice (025124) and mTmG mice (007576) were from the Jackson Laboratory. Control animals were *Lmna*$^{fl/fl}$ and *Lmna*^{iADKO} mice were *Lmna*$^{fl/fl}$ *Adipoq*-Cre$^{ERT2+/-}$. Animals described as *Lmna*^{CTRL} mTmG were *Adipoq*-Cre$^{ERT2+/-}$ mTmG$^{+/-}$, and *Lmna*^{iADKO} mTmG mice were *Lmna*$^{fl/fl}$ *Adipoq*-Cre$^{ERT2+/-}$ mTmG$^{+/-}$. Unless otherwise noted, mice at 12-14 weeks of age were intraperitoneally injected with tamoxifen (50 mg/kg; 13258, Cayman Chemical) in sterile corn

oil for five consecutive days to induce recombination followed by a 10-day washout. Mice were euthanized by inhaled isoflurane overdose and death was assured via cervical dislocation or bilateral pneumothorax. Fat and lean mass was measured in live animals with an EchoMRI-100H (EchoMRI LLC). Animals were group housed under standard conditions (22°C, 30-60% humidity) with a 12-hr light:dark cycle and free access to water and chow. All animal studies were performed in compliance with policies of the University of Michigan Institutional Animal Care and Use Committee (protocol no. PRO00011544). Daily care of mice was overseen by the Unit for Laboratory Animal Medicine at the University of Michigan.

Glucose and insulin tolerance tests

For glucose tolerance tests, mice were fasted overnight (16 hours) and administered an intraperitoneal injection of glucose in water (1 mg/kg body weight). For insulin tolerance tests, mice were fasted 4 hours and administered an intraperitoneal injection of insulin in saline (0.75 U insulin/kg body weight) (Eli Lilly). Blood was collected from the tail vein, and glucose concentrations were monitored using a glucometer and blood glucose strips (Bayer AG).

mTmG imaging and analyses

Tissues were collected from mice and placed in light-protected tubes with cold PBS on ice before imaging. Whole mount tissues were imaged in an imaging chamber in 1x PBS with an inverted confocal microscope (Nikon A1si) and 20x oil objective. mTmG images were analyzed using Fiji and the Cell Counter plugin to count red (tdTomato+) and green (GFP+) adipocytes. At least 300 adipocytes were counted over four to seven images per individual mouse.

Lipolysis measurements *in vivo*

Mice were bled in fed or fasted (~12-16 hours) states at baseline and after injection with tamoxifen. Blood was collected from the tail vein, allowed to coagulate on ice for 2 hours, and was centrifuged at 2000 x g for 20 minutes at 4°C to collect serum. For stimulated lipolysis, mice were administered an intraperitoneal injection of saline (control) or 10 mg isoproterenol/kg body weight to stimulate lipolysis. Blood was collected at baseline, and 30 and 60 minutes after injection, and serum isolated as described. Serum glycerol concentrations were measured via colorimetric assay (F6428, Sigma-Aldrich).

Serum measurements

Blood was collected from tail vein or at sacrifice via inferior vena cava and was allowed to coagulate on ice for 2 hours. After centrifugation at 2000 x g for 20 minutes at 4°C, serum was collected and stored at -80°C. ELISA was used to measure circulating concentrations of leptin (900-K76K, Invitrogen), and triacylglycerols were measured via colorimetric assay (10010303, Cayman Chemical). Serum adiponectin concentrations were measured via immunoblot.

Mouse and human histology

After collection, adipose tissue, skin, and/or liver were fixed for 72 hours in 10% neutral-buffered formalin at 4°C. Tissues were rinsed with PBS and dehydrated in a graded series of ethanol washes, processed, paraffin-embedded through the University of Michigan Orthopedic Research Laboratory Histology Core facility, and sectioned at 5 μM thickness. Sections were stained with hematoxylin & eosin as previously described[62] or with Picrosirius Red according to manufacturer protocol (24901, Polysciences). Sections were imaged using an inverted Zeiss microscope with a 20x objective.

Immunoblot analyses

Immunoblot analyses were performed as previously described.[63]

Adipocyte fractionation for immunoblot and recombination analyses

WAT depots were excised from mice, minced with scissors, and digested with 533.3 U/mL collagenase type I (LS004197, Worthington). Digestion was done in Krebs-Ringer-HEPES (KRH) buffer, pH 7.4 containing 1 g/L glucose and 500 nm adenosine for 30 minutes at 37°C shaking horizontally at 100 rpm. Adipocytes were separated from the stromal vascular fraction by filtering through 300 μm filters and centrifuging at 100 x g for 7 minutes. Floating adipocytes were transferred to 5 mL tubes and washed 3 times with KRH buffer by removing the infranatant from beneath the adipocyte layer with a 5 mL syringe and 21G needle. The stromal vascular fraction (SVF) was pelleted by centrifugation at 500 x g for 7 minutes and washing 3 times with KRH buffer. Adipocyte and SVF fractions were then lysed for either protein or DNA collection.

Adipocyte fractionation for respirometry analyses

Adipocyte fractionation was done as described above, except that collagenase digestion was done in Hank's Balanced Salt Solution (HBSS) (14025-092, Gibco). Adipocyte fractions were washed 3 times with STE-BSA buffer (250 mM sucrose, 5 mM Tris, 2 mM EGTA, 4% fatty acid free BSA, pH 7.4). After isolation, adipocyte metabolism was analyzed with an Oroboros-2k.

Respirometry of adipocytes

Oxygen consumption of adipocytes was measured with high-resolution respirometry using an Oxygraph-2k (OROBOROS Instruments, Innsbruck, Austria). Floated adipocytes (40 µL) from pmWAT were pipetted into 2 mL mitochondrial respiration medium buffer (MIR05) with the stirrer set to 750 rpm. The following respiratory parameters were measured: basal respiration (5 mM pyruvate, 1 mM malate, 5 mM succinate), proton leak respiration (1 µM oligomycin), and maximal respiration (1 µM FCCP steps until no further increase in oxygen consumption was observed). Non-mitochondrial oxygen consumption (2.5 µM antimycin A) was subtracted from the other respiratory states. ATP-linked respiration was calculated by subtracting leak respiration from baseline, and spare capacity was calculated by subtracting baseline from maximal respiration.

DNA content of adipocyte suspensions was quantified by quantitative PCR targeting genomic DNA using primers for glucagon. Samples were diluted 1:5 in digestion buffer (50 mM KCl, 0.45% NP-40, 0.45% Tween-20, 0.2 mg/mL Proteinase K) and incubated at 65°C for 1 hour at 1000 rpm. Proteinase K was inactivated at 65°C for 10 minutes, and 2.25 volumes phenol:chloroform:isoamyl alcohol were added. Samples were centrifuged at 16000 x g for 10 minutes, and the aqueous phase was collected and used for qPCR (StepOnePlus System, Applied Biosystems) using qPCRBIO SyGreen Mix (PB20.12-01, Innovative Solutions). DNA concentrations were determined by comparing samples with a mouse genomic DNA standard dilution series of known concentration.

PCR for recombination

Genomic DNA was isolated from floated adipocytes by boiling samples at 95°C in 100 µL 50 mM NaOH for 1 hour and neutralized by adding 50 µL 1M Tris-HCl pH 7.4. PCR was performed for the floxed and knockout band using a 3-primer system as previously published[26]

(fwd 1: 5'-CCAGCTTACAGAGCACCGAGCT-3'; fwd 2: 5'-TCCTTGCAGTCCCTCTTGCATC-3'; rev: 5'-AGGCACCATTGTCACAGGGTC-3').

Quantitative RT-PCR

M-MLV Reverse Transcriptase (Invitrogen, Carlsbad, CA, USA) was used to transcribe 1 μg RNA to cDNA. DNA was amplified with qPCRBIO SyGreen Mix (Innovative Solutions, Beverly Hills, MI, USA) and detected with a StepOnePlus System (Applied Biosystems, Foster City, CA, USA). All primers were validated with cDNA titration curves prior to use; qPCR product specificities were confirmed by melting curve analysis and gel electrophoresis. Gene expression was calculated using a cDNA titration curve within each plate and normalized to the geomean of reference genes *Tbp, Gapdh,* and *Hprt*, and calculated as mRNA transcript change relative to control samples.

Quantification of mitochondrial DNA

DNA was isolated from floated adipocytes using the Wizard Genomic DNA Purification Kit (A1120, Promega). DNA amount was quantified using a NanoDrop spectrophotometer. DNA was amplified using RT-qPCR with primers identifying nuclear genes *Gcg* and *Hbb*, or mitochondrial-encoded genes *Mt-Cyb* and *Mt-Cox1-Tms1*.

MitoTracker staining of primary adipocytes and imaging

Primary adipocytes were isolated using the protocol for respirometry analyses. Adipocytes were then stained in PBS with BODIPY 493/503 for 30 minutes (D3922, Invitrogen), Hoechst 33342 for 10 minutes (62249, ThermoFisher), and MitoTracker Deep Red FM for 30 minutes (M22426, Invitrogen) and washed with PBS twice. Adipocytes were imaged using an inverted spinning disk confocal (Nikon W1-SoRa).

Flow cytometry analysis of SVF for delipidated adipocytes

SVCs were isolated from psWAT and eWAT as described above from Adipoq-CreERT2$^{+/-}$ mTmG$^{+/-}$ or *Lmna*$^{fl/fl}$ Adipoq-CreERT2$^{+/-}$ mTmG$^{+/-}$ mice. Cells were kept on ice in the dark, stained with propidium iodide (P1304MP, Invitrogen) and immediately brought to the flow cytometer (5-Laser Cytek Aurora Spectral Analyzer with autofluorescence subtraction) for

analysis of fluorescence (GFP vs. tdTomato positive) in SVF cells. Single stained ear mesenchymal stem cells and unstained SVF were used as controls.

Flow cytometry analysis of SVF for inflammation

PmWAT and psWAT depots were collected and weighed. For isolation of SVF, minced WAT was digested with 1 mg/ml collagenase (Type II, C2-BIOC, Sigma–Aldrich) in HBSS (-/-) (14175095, Invitrogen), and tissues were incubated at 37°C for 30 minutes with constant shaking. Cell suspensions were passed through a 100 μm filter and centrifuged at 500 x g for 10 minutes at 4°C to separate floating adipocytes from pelleted SVF. For flow cytometry, SVF were incubated in 0.5 ml red blood cell lysis buffer (155mM NH_4Cl, 10mM $KHCO_3$, 0.1mM EDTA, 1N HCl) for 5 minutes at room temperature and resuspended in PBS/0.5% BSA prior to incubation in Fc Block (anti-CD16/32) for 5 minutes on ice. For extracellular staining (30 minutes), cells were incubated at 4°C with antibodies to CD45, CD64, CD11c, TIM4, and CD163 for ATMs and to CD3, CD4, and CD8 for T cells. The following antibodies were used: anti-CD45 (clone 30-F11), anti-CD64 (X54-5/7.1), anti-cd11c (N418), anti-CD163 (S15949F), anti-TIMD4 (RMT4-54), anti-cd3 (145-2C11), anti-cd4 (RM4-5) and anti-cd8 (53-6.7). Stained cells were washed twice with FACS buffer and fixed in 2% paraformaldehyde. After separation with a Cytek Aurora flow cytometer, data were analyzed using manual compensation and FlowJo software.

Transmission electron microscopy of mouse WAT

Mice were anesthetized and pmWAT immediately dissected, cut into 1 mm^3 pieces and placed into 2.5% glutaraldehyde, 2% formaldehyde in 0.1M sodium cacodylate buffer (CB) at 4°C for 2 hours. Samples were washed 3 times with 0.1 M CB for 15 minutes. Then samples were placed into 1.5% potassium hexacyanidoferrate(II) + 2% osmium tetroxide in 0.1 M CB for 1 hour. Samples were then washed 3 times with 0.1 M CB for 5 minutes and washed 3 times with 0.1 M acetate buffer (AB) for 5 minutes. Samples were placed into 2% uranyl acetate in 0.1 M AB for 1 hour. Samples were washed twice with 0.1 M AB for 5 minutes and washed with deionized water for 5 minutes. After a dehydrated series of 30, 50, 70, 80, 90, 95, and 100% ethanol for 15 minutes each at 4°C, samples were placed in acetone for 15 minutes at 4°C, 2:1 acetone:resin for 1.5 hours, 1:1 for 3 hours, and 1:2 for 16 hours. Samples were embedded in 100% resin under

vacuum for 48 hours, and resin polymerized at 70°C for 24 hours. Sections of 70 μm were imaged on a JOEL JEM-1400 Plus LaB6 transmission electron microscope.

Tandem mass tag proteomics from mouse adipose tissue

Protein digestion and TMT labeling and liquid chromatography-mass spectrometry analysis was performed as previously described.[64] Data were analyzed with Proteome Discoverer (v2.4; ThermoFisher). MS2 spectra were searched against SwissProt mouse protein database (#55336 entries, Mus musculus ALL_UniProtKB 2021_03.fasta, downloaded on 08/06/2021) using the following search parameters: MS1 and MS2 tolerance were set to 10 ppm and 0.6 Da, respectively; carbamidomethylation of cysteines (57.02146 Da) and TMT labeling of lysine and N-termini of peptides (229.16293 Da) were considered static modifications; oxidation of methionine (15.9949 Da) and deamidation of asparagine and glutamine (0.98401 Da) were considered variable. Identified proteins and peptides were filtered to retain only those that passed ≤1% FDR threshold. Quantitation was performed using high-quality MS3 spectra (Average signal-to-noise ratio of 10 and <50% isolation interference).

Public data analysis from *Lmna* KO MEFs

Raw ATAC-seq data were mined from GEO accession GSE120389 and processed using the best practice nf-core atac-seq pipeline (v2.1.1)[65] with default configurations. Microarray data were downloaded from GEO accession GSE124467 and preprocessed as described in its original publication[36].

ATAC-seq analysis and integration with expression data

Differential accessibility analysis was performed using DiffBind (v3.12.0)[66]. Briefly, a consensus peakset was generated, and read counting was done using dba.count() with bUseSummarizeOverlaps=TRUE. TMM and background-aware normalization was carried out with dba.normalize() . Enhancer-to-gene assignments were predicted using rGREAT (v2.6.0)[67] with default parameters. Chromatin state annotations for LMNA wild-type (WT) and knockout (KO) peaksets were quantified by intersecting peaksets with the full-stack 100-segment ChromHMM model from Vu and Ernst 2023[38]. Chromatin state distributions were visualized using grouped percentage bar plots. Genes and enhancers with concurrent changes in chromatin

accessibility and gene expression were stratified into eight directionality-based clusters (e.g., increased accessibility with increased expression). Gene Ontology enrichment analysis was conducted and visualized using clusterProfiler (v4.12.6)[68]. For transcription factor motif analysis, peaks were ranked and binned by $\log_2$ fold change, and motif enrichment was assessed using monaLisa (v1.15.0)[69] with PWMs from JASPAR2020. Motifs with $|\log_2$ enrichment$| > 2$ and $-\log_{10}$ adjusted p-value > 4 were considered significant. ATAC-seq tracks and enhancer-to-gene connections were visualized using pyGenomeTracks (v3.9.0)[70].

Statistics

All data was presented as mean ± SD. Two-way ANOVA with Bonferroni's post-hoc test was performed for human matched case-control comparisons and mouse data with two variables presented in the study. One-way ANOVA with Bonferroni's post-hoc test was used for human comparisons across disease states. Student's t test was used when comparing mouse data between two genotypes. The area under the curve (AUC) for lipid and glycemic parameters was calculated using the linear trapezoidal method based on time-course plots of the measured values. All analyses were conducted using GraphPad Prism version 10. For statistical comparisons, $p < 0.05$ was considered significant.

Primers for quantitative RT-PCR

Gene name	Forward primer (5'-3')	Reverse primer (5'-3')
Gcg	AGGGCCATCTCAGAACC	GCTATTGGAAAGCCTCTTGC
Hbb	GAAGCGATTCTAGGGAGCAG	GGAGCAGCGATTCTGAGTAGA
Mt-Cyb	CATTTATTATCGCGGCCCTA	TGTTGGGTTGTTTGATCCTG
Mt-Cox1-Tms1	GCCTTTCAGGAATACCACGA	CCAATTTTAGGGGGTTCGAT
Gapdh	ATGTTCCAGTATGACTCCACTCACG	GAAGACACCAGTAGACTCCACGACA
Hprt	TCATTATGCCGAGGATTTGGA	GCACACAGAGGGCCACAAT
Tbp	ACCTTATGCTCAGGGCTTGG	GCCGTAAGGCATCATTGGAC
Scd1	GATAGAGCAAGTCCCCGCTG	CCTGCATTAACCCCCTTCAC
Adipoq	CATTCCGGGACTCTACTACTTCT	GAGGCCTGGTCCACATTCTT
Il6	CCAGAGATACAAAGAAATGAT	ACTCCAGAAGACCAGAGGAAAT
Il10	GAGGCGCTGTCATCGATTT	CACCTTGGTCTTGGAGCTTATT
Saa3	CGCAGCACGAGCAGCAGGAT	TGGCTGTCAACTCCCAGG
Tgfb1	TTGCTTCAGCTCCACAGAGA	TGGTTGTAGAGGGCAAGGAC
Ccl2	CTTCTGGGCCTGCTGTTCA	CCAGCCTACTCATTGGGATCA
Nos2	AATCTTGGAGCGAGTTGTGG	CAGGAAGTAGGTGAGGGCTTG
Nlrp3	CCGTCTACGTCTTCTTCCTTTC	CGCAGATCACAGTCCTCAAATA
Il1b	GAGGACATGAGCACCTTCTTT	GCCTGTAGTGCAGTTGTCTAA
Casp1	GGCCCCAGGCAAGCCAAATCT	CAGTCCTGGAAATGTGCCATC
Tnfa	CATCTTCTCAAAATTCGAGTGACAA	TGGGAGTAGACAAGGTACAACCC

Antibodies for immunoblot

Antibody Name	Manufacturer	Catalog #
Adiponectin	Sigma-Aldrich	A6354
Albumin	ThermoFisher	PA5-27707
SREBP1	ThermoFisher	PA1-337
ChREBP	Novus Bio	NB400-135
ACC	Cell Signaling	3662
FASN	Abcam	ab22759
SCD1	Cell Signaling	2438
Laminin	Novus Bio	NB300-144
PPARγ	Millipore Sigma	MAB3872
LMNA	Cell Signaling	4777
C/EBPα	Cell Signaling	8178
ACAA2	Abcam	ab128911
OXPHOS Rodent Antibody Cocktail	Abcam	ab110413
HADHB	Novus Bio	NBP1-54750
CPT1α	Abcam	ab128568
Pyruvate dehydrogenase	Cell Signaling	3205
Mitochondrial Dynamics Sampler Kit	Cell Signaling	74792
VDAC1	Abcam	ab15895
PDGFRβ	Proteintech	13449-1-AP
PGC1α	Abcam	ab191838
β-actin	Cell Signaling	4970
Cleaved caspase 3	Cell Signaling	9664
Total caspase 3	Cell Signaling	9662

Antibodies for flow cytometry

Marker	Fluorophore	Isotype	Clone	Product Info	Laser
CD45	Efluor 450	Mouse / IgG1, kappa	30-F11	ebio 45-0451-80	405
CD64	PE	Mouse (NOD/Lt) IgG1, κ	X54-5/7.1	BD pharmingen 558455	561
CD11c	APC-Cy7	Armenian Hamster IgG1, λ2	N418	Biolegend 117334	640
Tim4	PerCP-efluor 710	Mouse / IgG1, kappa	RMT4-54	Thermofisher 46-5866-82	488
CD163	PECy7	Rat / IgG2a, kappa	S15949F	Biolengend 156707	561
CD11b	BV711	Rat IgG2b, κ	M1/70	Biolegend 101242	405
CD3	APC	Armenian hamster / IgG	145-2C11	eBioscience 17-0031-82	640
CD4	BV650	Rat IgG2b, κ	RM4-5	Biolegend 100555	405
CD8	FITC	Rat / IgG2a, kappa	53-6.7	eBioscience 11-0081-85	488

2.6 Figures and legends

Figure 2.1

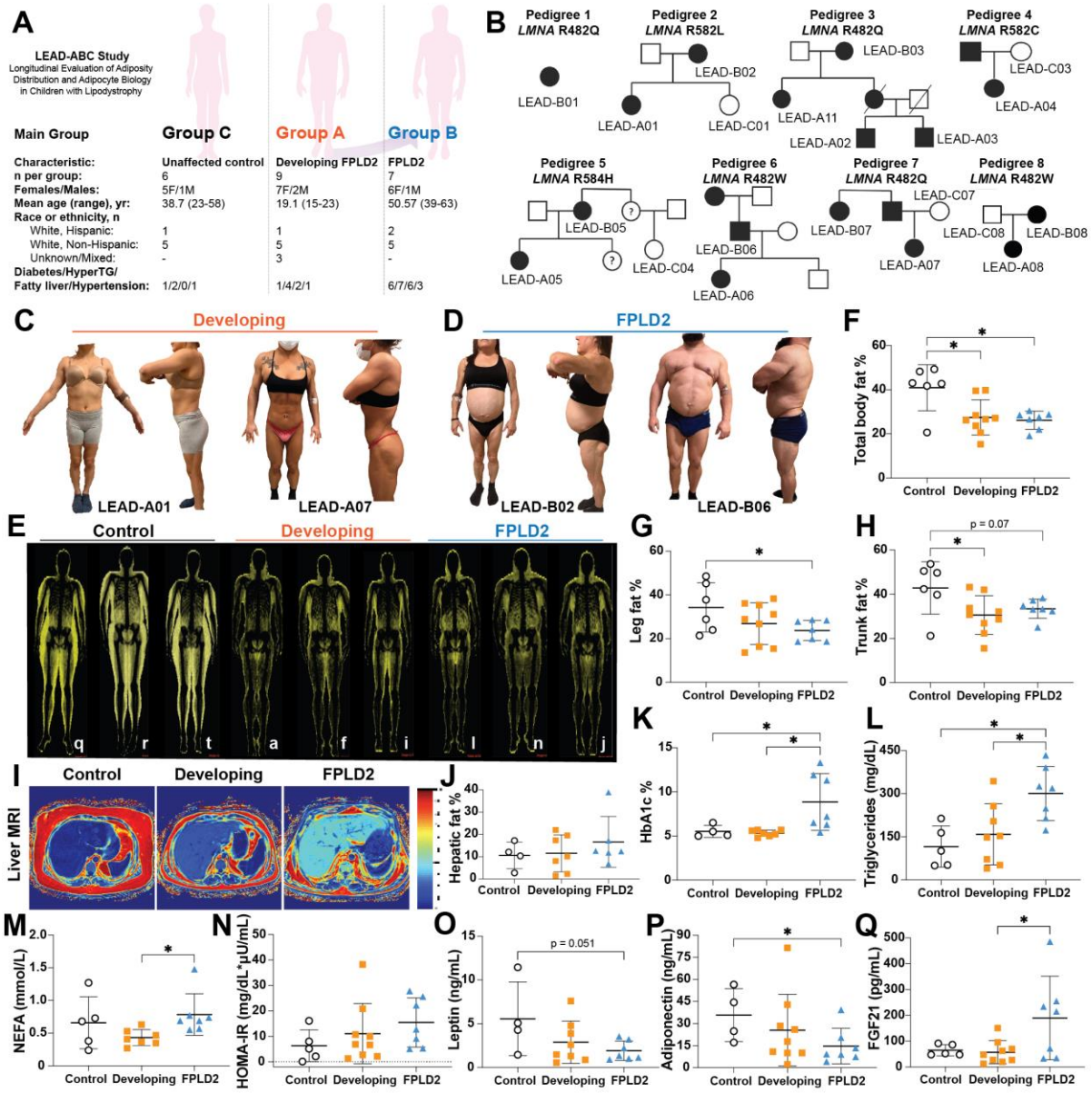


Figure 2.1. **Clinical, metabolic, and molecular characterization of individuals with familial partial lipodystrophy type 2 (FPLD2).** (**A**) Study design and patient groups. Groups include unaffected family members (Control, Group C, n = 6), genetically affected but clinically unaffected individuals (Developing, Group B, n = 9), and patients with FPLD2 (FPLD2, Group A, n = 7). (**B**) Pedigrees from multiple families with FPLD2. Filled symbols represent affected individuals, open symbols indicate unaffected individuals, question marks denote unknown phenotypic status. (**C**) Images of patients with developing FPLD2 with early signs of fat redistribution. (**D**) Images of patients with FPLD2 phenotypes with peripheral lipoatrophy and upper trunk fat accumulation. (**E**) Whole body fat shadows. Quantification of fat mass percentage in (**F**) total body, (**G**) leg, and (**H**) trunk. (**I**) Magnetic resonance imaging (MRI)-based hepatic fat fraction maps with (**J**) quantification. (**K**) Hemoglobin A1c percentages. (**L**) Triglyceride concentrations. (**M**) Non-esterified fatty acid (NEFA) concentrations. (**N**) Homeostatic Model Assessment for Insulin Resistance (HOMA-IR) scores. (**O**) Leptin concentrations. (**P**) Adiponectin concentrations. (**Q**) Fibroblast growth factor 21 (FGF21) concentrations. Data are represented as mean ± SD. *P < 0.05. Statistical analyses were performed using one-way ANOVA, followed by Bonferroni's post-hoc test

Figure 2.2

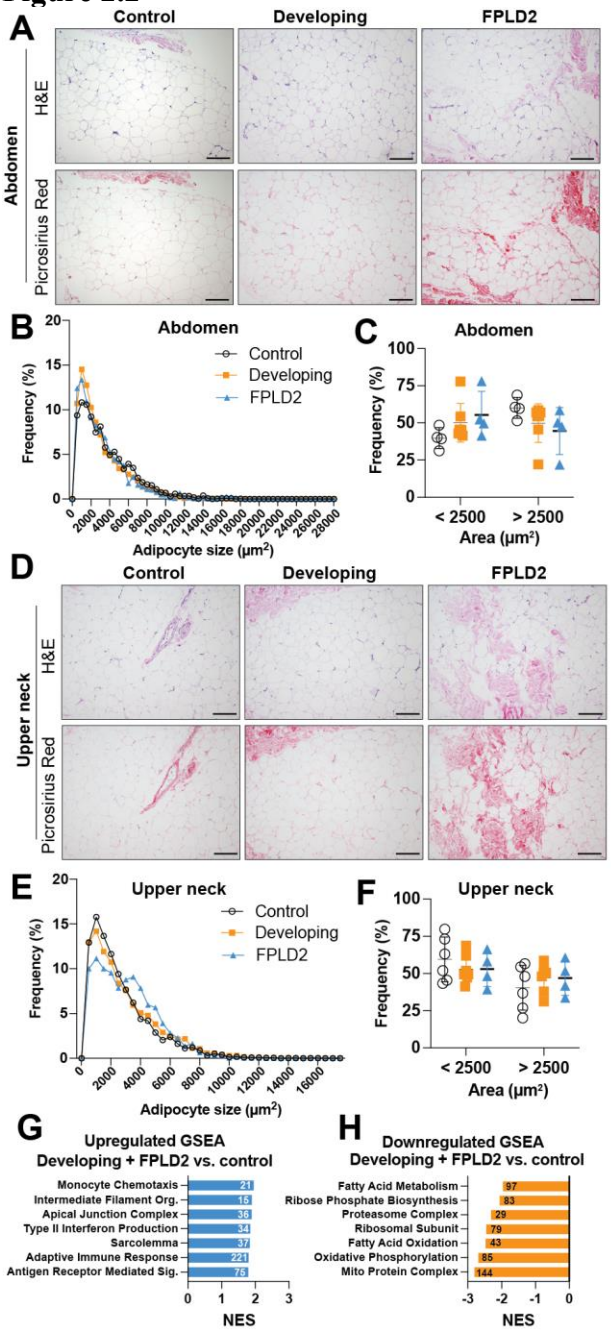
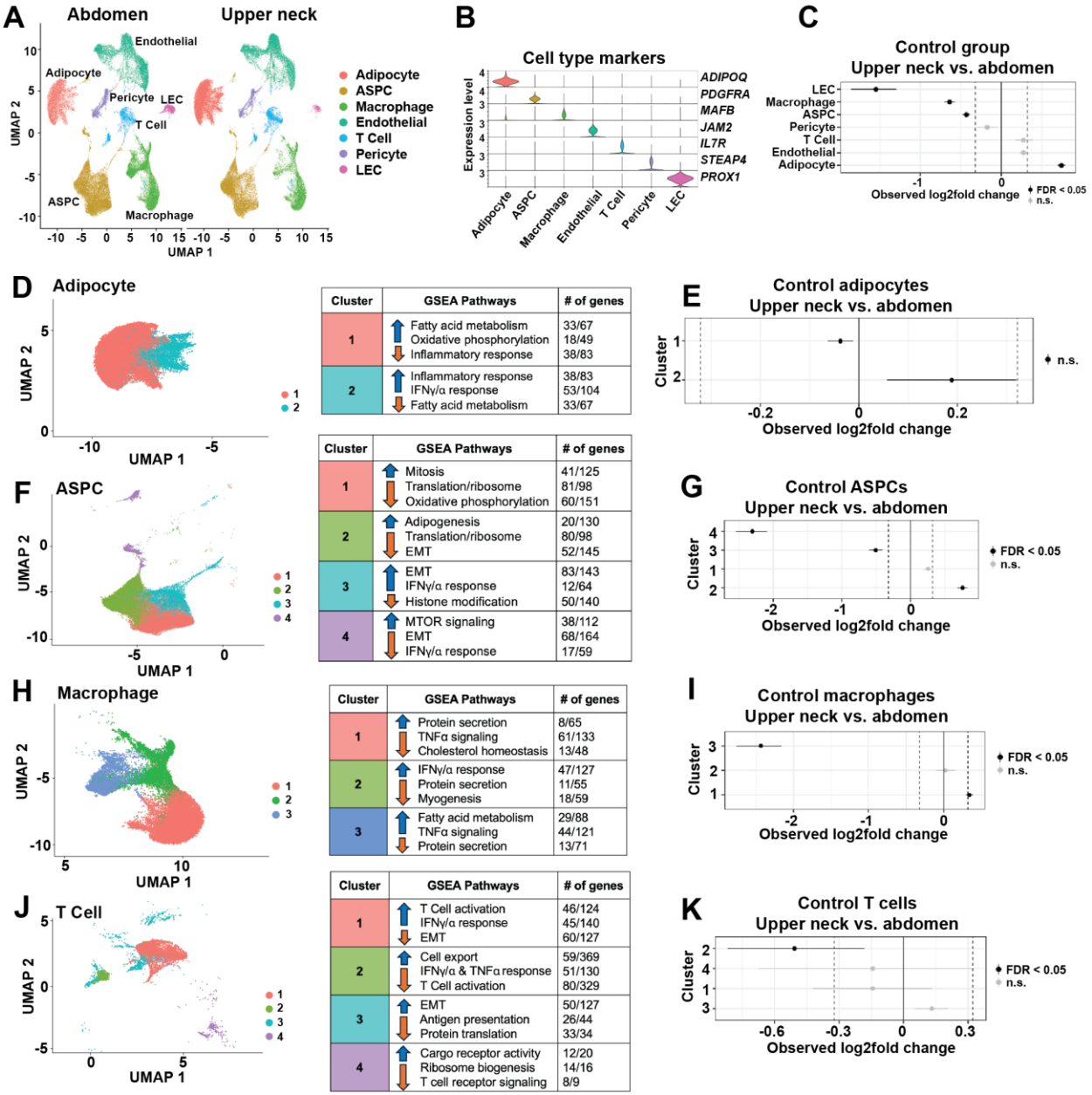


Figure 2.2. Biopsies from patients with FPLD2 have no change in adipocyte size, but bulk RNA-sequencing suggests decreased metabolism and increased inflammation in patient adipose tissue. (**A**) Representative adipose tissue histological images and Picrosirius Red-stained tissue for collagens from biopsies across patient groups in abdominal biopsies. (**B**) Frequency distribution of adipocyte size and (**C**) frequency of adipocytes less or greater than 2500 μm^2 from abdominal biopsies. (**D**) Histological images and Picrosirius Red analyses on upper neck biopsies. (**E**) Frequency distribution of adipocyte size and (**F**) frequency of adipocytes less or greater than 2500 μm^2 from upper neck biopsies. Bulk RNA-sequencing on patient biopsies. Biopsies from Group A and B were combined to compare to Group C. n = 4-5 samples (upper neck and abdomen combined) per group. Gene set enrichment analysis (GSEA) identified (**G**) up and (**H**) downregulated pathways with normalized enrichment scores (NES). Data are represented as mean ± SD. *P < 0.05. Statistical analyses were performed using two-way ANOVA, followed by Bonferroni's post-hoc test.

Figure 2.3



Cluster	GSEA Pathways	# of genes
1	↑ Fatty acid metabolism ↑ Oxidative phosphorylation ↓ Inflammatory response	33/67 18/49 38/83
2	↑ Inflammatory response ↑ IFNγ/α response ↓ Fatty acid metabolism	38/83 53/104 33/67

Cluster	GSEA Pathways	# of genes
1	↑ Mitosis ↓ Translation/ribosome ↓ Oxidative phosphorylation	41/125 81/98 60/151
2	↑ Adipogenesis ↓ Translation/ribosome ↓ EMT	20/130 80/98 52/145
3	↑ EMT ↑ IFNγ/α response ↓ Histone modification	83/143 12/64 50/140
4	↑ MTOR signaling ↑ EMT ↓ IFNγ/α response	38/112 68/164 17/59

Cluster	GSEA Pathways	# of genes
1	↑ Protein secretion ↓ TNFα signaling ↓ Cholesterol homeostasis	8/65 61/133 13/48
2	↑ IFNγ/α response ↓ Protein secretion ↓ Myogenesis	47/127 11/55 18/59
3	↑ Fatty acid metabolism ↑ TNFα signaling ↓ Protein secretion	29/88 44/121 13/71

Cluster	GSEA Pathways	# of genes
1	↑ T Cell activation ↑ IFNγ/α response ↓ EMT	46/124 45/140 60/127
2	↑ Cell export ↑ IFNγ/α & TNFα response ↓ T Cell activation	59/369 51/130 80/329
3	↑ EMT ↑ Antigen presentation ↓ Protein translation	50/127 26/44 33/34
4	↑ Cargo receptor activity ↑ Ribosome biogenesis ↓ T cell receptor signaling	12/20 14/16 8/9

Figure 2.3. Single nuclei RNA-sequencing identifies changes in cell proportions and subclustering analyses between subcutaneous abdomen and upper neck adipose tissue in unaffected patients. (**A**) Uniform Manifold Approximation and Projection (UMAP) of abdomen and upper neck biopsies across all patient groups (A, B and C); ASPC = adipose stem and progenitor cells, LEC = lymphatic endothelial cells. (**B**) Marker genes for each cell population. (**C**) Permutation tests to identify changes in cell proportions in the upper neck relative to the abdominal biopsies from control patients (Group C); changes were statistically significant if the log2fold change was less or greater than 0.32, and the false discovery rate (FDR) was less than 0.05. (**D**)Adipocyte subclusters and corresponding GSEA pathways. (**E**) Adipocyte subclusters changes between the upper neck and abdomen in control patients. (**F**) ASPC subclusters with GSEA pathways. (**G**) ASPC subcluster changes in the upper neck relative to abdomen. (**H**) Macrophage subclusters with GSEA pathways. (**I**) Subcluster changes in macrophages in upper neck relative to abdomen. (**J**) T cell subclusters with GSEA pathways. (**K**) Subcluster changes in T cells in upper neck relative to abdomen.

Figure 2.4

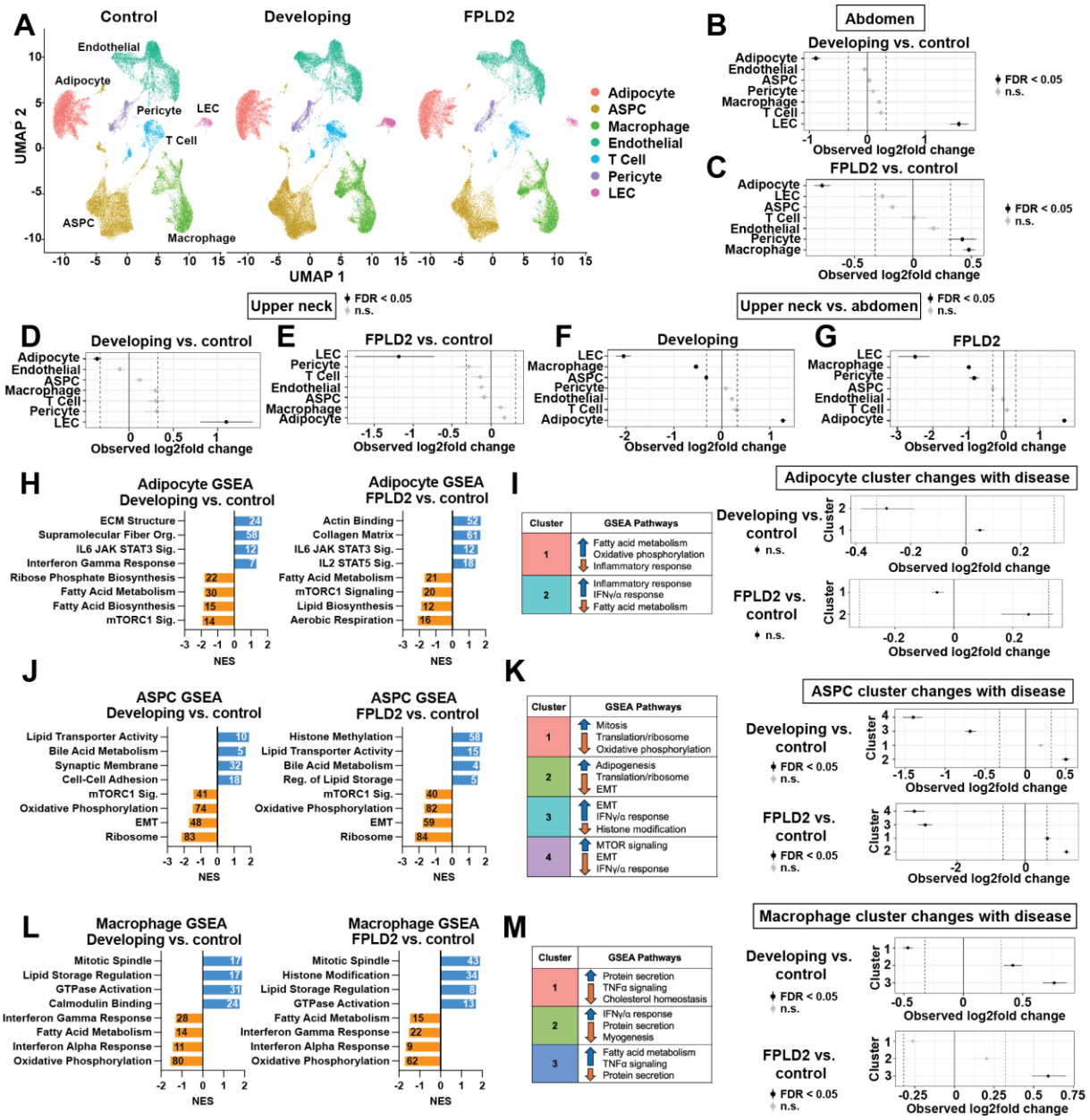


Figure 2.4. Single nuclei RNA-sequencing identifies changes in cell proportions and identity with progression of FPLD2. (**A**) UMAP of combined upper neck and abdomen biopsies across disease states; cell type markers are the same as in Figure 3. Permutation tests identified changes in cell proportion from abdominal biopsies from patients with (**B**) developing FPLD2 and (**C**) FPLD2 relative to control, and from upper neck biopsies in (**D**) developing FPLD2 and (**E**) FPLD2 relative to control. Cell proportion changes in the upper neck relative to abdomen were identified in (**F**) developing and (**G**) FPLD2 disease states. (**H**) All adipocytes from developing or FPLD2 biopsies were analyzed via GSEA and compared to controls to identify population-level changes in cell identity. Sig = signaling; Org = organization. (**I**) Adipocyte subcluster analyses with corresponding GSEA pathways (same as in Figure 3) and subcluster changes with disease. (**J**) ASPC GSEA in developing or FPLD2 biopsies relative to controls. (**K**) ASPC subcluster changes with disease. (**L**) Macrophage GSEA in developing or FPLD2 biopsies relative to controls. (**M**) Macrophage subcluster changes with disease.

Figure 2.5

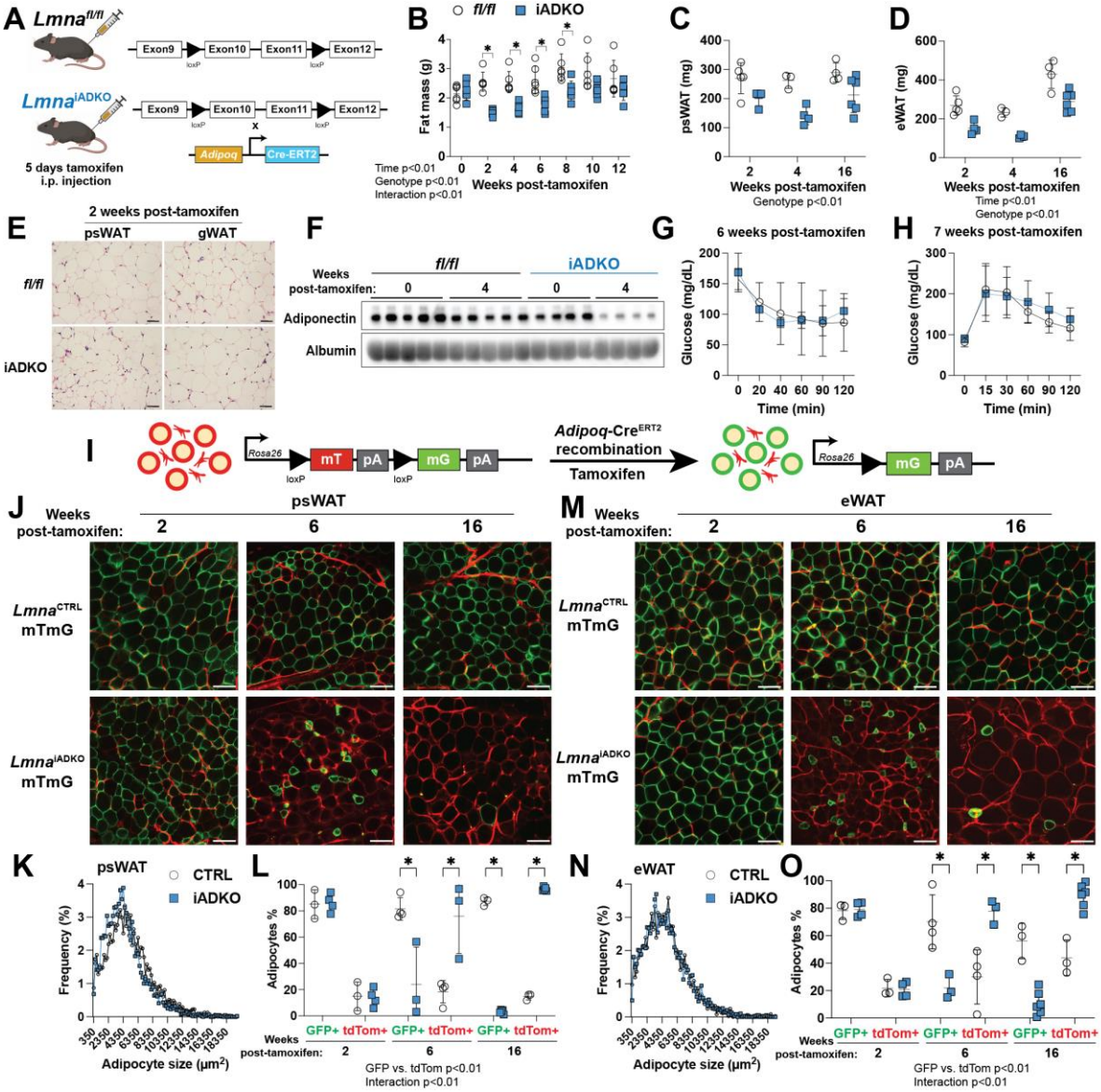


Figure 2.5. Tamoxifen-inducible adipocyte-specific *Lmna* knockout causes transient adipose tissue loss, and *Lmna*-deficient adipocytes shrink and disappear. All data from male mice besides histology from female mice. (**A**) Gene schematic of *Lmna*$^{fl/fl}$ control mice and *Lmna*^{iADKO} inducible *Lmna* adipocyte-specific knockout mice. Adult mice were administered tamoxifen intraperitoneally (i.p.) for five consecutive days to induce recombination. (**B**) Fat mass after tamoxifen administration (n = 6). (**C**) Posterior subcutaneous white adipose tissue (psWAT) weights and (**D**) epididymal white adipose tissue (eWAT) weights at two-, four-, and 16-weeks post-tamoxifen (n = 3-6). (**E**) Representative histology of psWAT and gonadal WAT (gWAT) two weeks post-tamoxifen. Scale bar = 40 μm. (**F**) Insulin tolerance test (ITT) six weeks post-tamoxifen (n = 6). (**G**) Glucose tolerance test (GTT) seven weeks post-tamoxifen (n = 6). (**H**) Serum adiponectin immunoblot at zero- and four-weeks post-tamoxifen (n = 4-5). (**I**) Schematic of mTmG reporter system induced by tamoxifen-mediated Cre activity. (**J**) Representative fresh confocal micrographs of psWAT and (**K**) quantification of psWAT adipocyte size at two-weeks post-tamoxifen (n = 3-4). (**L**) Quantification of psWAT GFP+ or tdTomato+ adipocytes. (**M**) Confocal micrographs of eWAT and (**N**) quantification of eWAT adipocyte size at two weeks post-tamoxifen. (**O**) Quantification of eWAT GFP+ or tdTomato+ adipocytes. Data are represented as mean ± SD. *P < 0.05. Statistical analyses were performed using two-way ANOVA, followed by Bonferroni's post-hoc test.

Figure 2.6

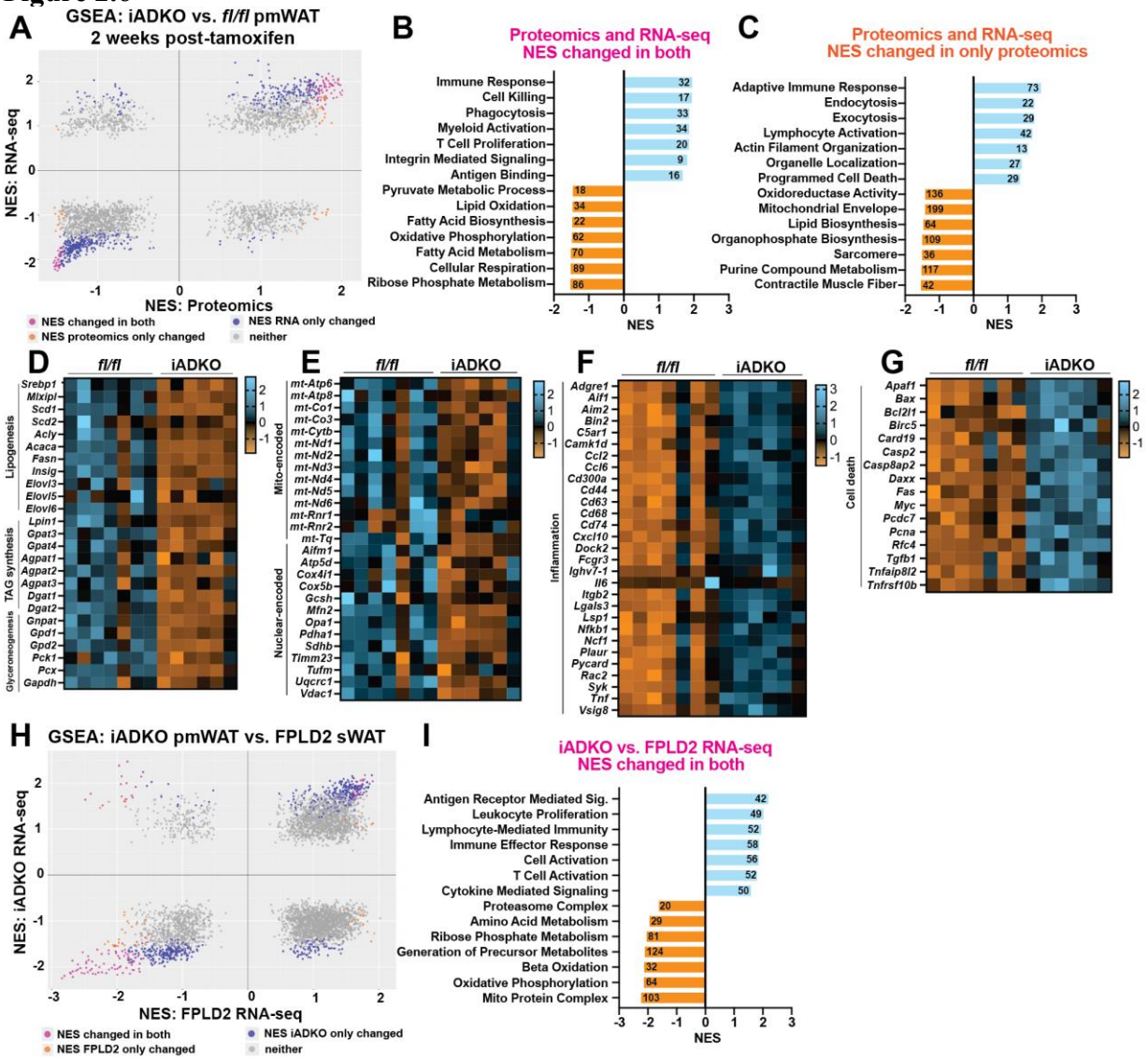


Figure 2.6. Bulk RNA-sequencing and proteomics of *Lmna*^{iADKO} WAT reveals increased inflammation and reduced fatty acid metabolism and mitochondrial pathways, similar to human FPLD2 biopsies. *Lmna*^{iADKO} and *Lmna*$^{fl/fl}$ parametrial white adipose tissue (pmWAT) two-weeks post-tamoxifen was used for RNA-sequencing (n = 6-7) and proteomics (n = 5). (**A**) Integrative GSEA on bulk RNA-sequencing (RNA-seq) and proteomics. Pink dots symbolize that NES were significantly changed in both RNA-seq and proteomics datasets, orange dots = NES only changed in proteomics, blue = NES only changed in RNA-seq. (**B**) Highlighted GSEA pathways changed in both proteomics and RNA-seq. Numbers on bars represent number of overlapping genes driving pathways. (**C**) Highlighted GSEA pathways changed in proteomics only. Heatmaps showing selected changes in genes driving (**D**) lipid biosynthesis, (**E**) mitochondrial function, (**F**) inflammation, and (**G**) cell death. (**H**) Integrative GSEA of *Lmna*^{iADKO} pmWAT bulk RNA-seq compared to FPLD2 bulk RNA-seq (Figure 2). (**I**) Highlighted GSEA pathways changed in both mouse and human RNA-seq datasets.

Figure 2.7

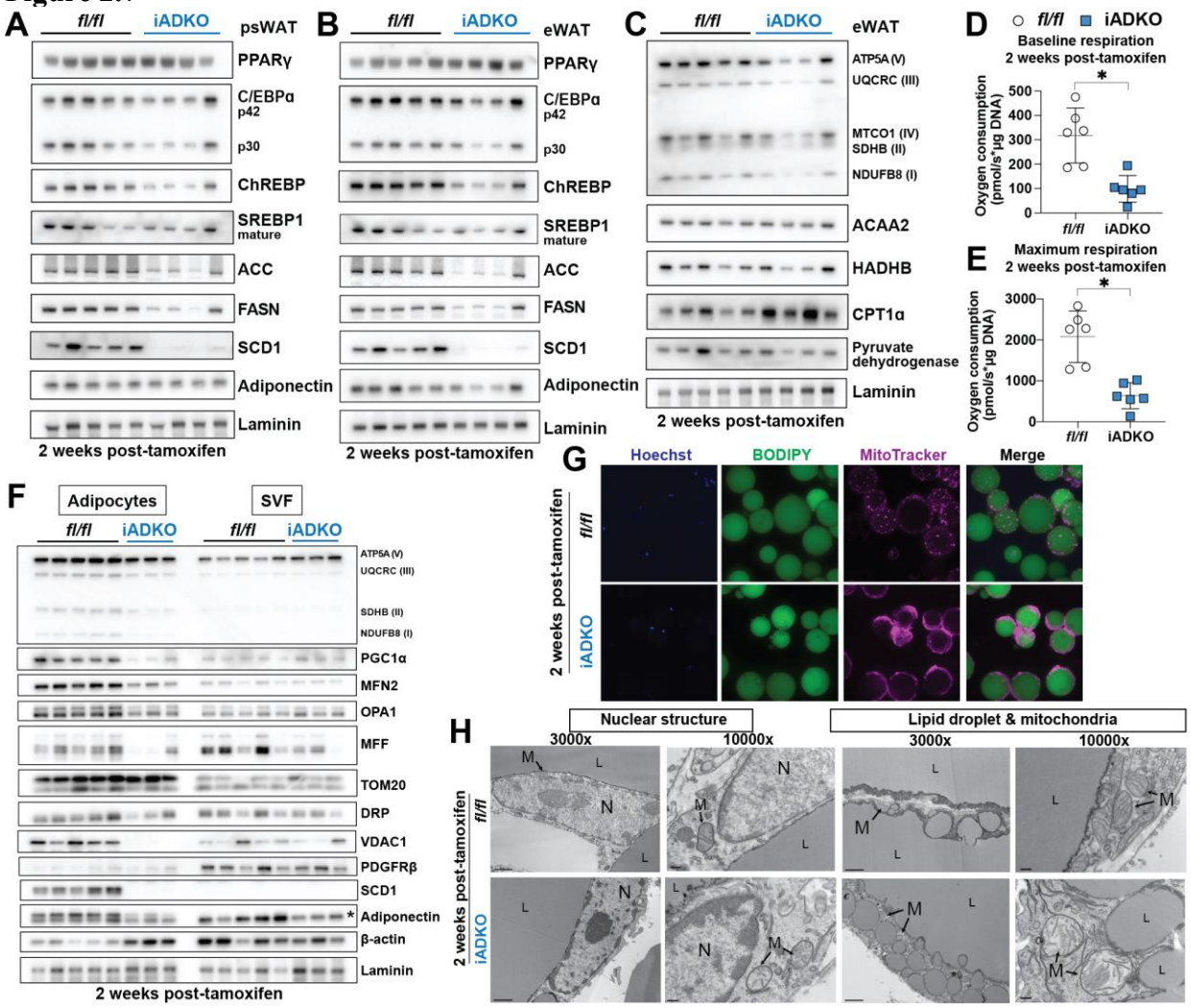


Figure 2.7. *Lmna*^{iADKO} adipocytes have reduced oxygen consumption and dysfunctional mitochondrial dynamics and structure. Immunoblot analyses two-weeks post-tamoxifen of lipid metabolism and lipogenesis proteins in (**A**) psWAT and (**B**) eWAT (n = 4-5). (**C**) Immunoblot of mitochondrial proteins in eWAT two-weeks post-tamoxifen (n = 4-5). Oroboros Oxygraph-2k analyses of (**D**) baseline and (**E**) maximum respiration in floated adipocytes from pmWAT two-weeks post-tamoxifen (n = 6). (**F**) Immunoblot of mitochondrial function and dynamics proteins in floated adipocytes and stromal vascular fraction (SVF) from pmWAT two-weeks post-tamoxifen (n = 3-5). * indicates non-specific band. (**G**) Confocal micrographs of floated adipocytes from pmWAT stained for nuclei (Hoechst), lipid (BODIPY), and mitochondria (MitoTracker Red) and (**H**) Transmission electron micrographs of eWAT two-weeks post-tamoxifen. Scale bar = 1 µM for 3000x; 200 nm for 10000x magnification images. Data are represented as mean ± SD. *P < 0.05. Statistical analyses were performed using Student's t-test.

Figure 2.8

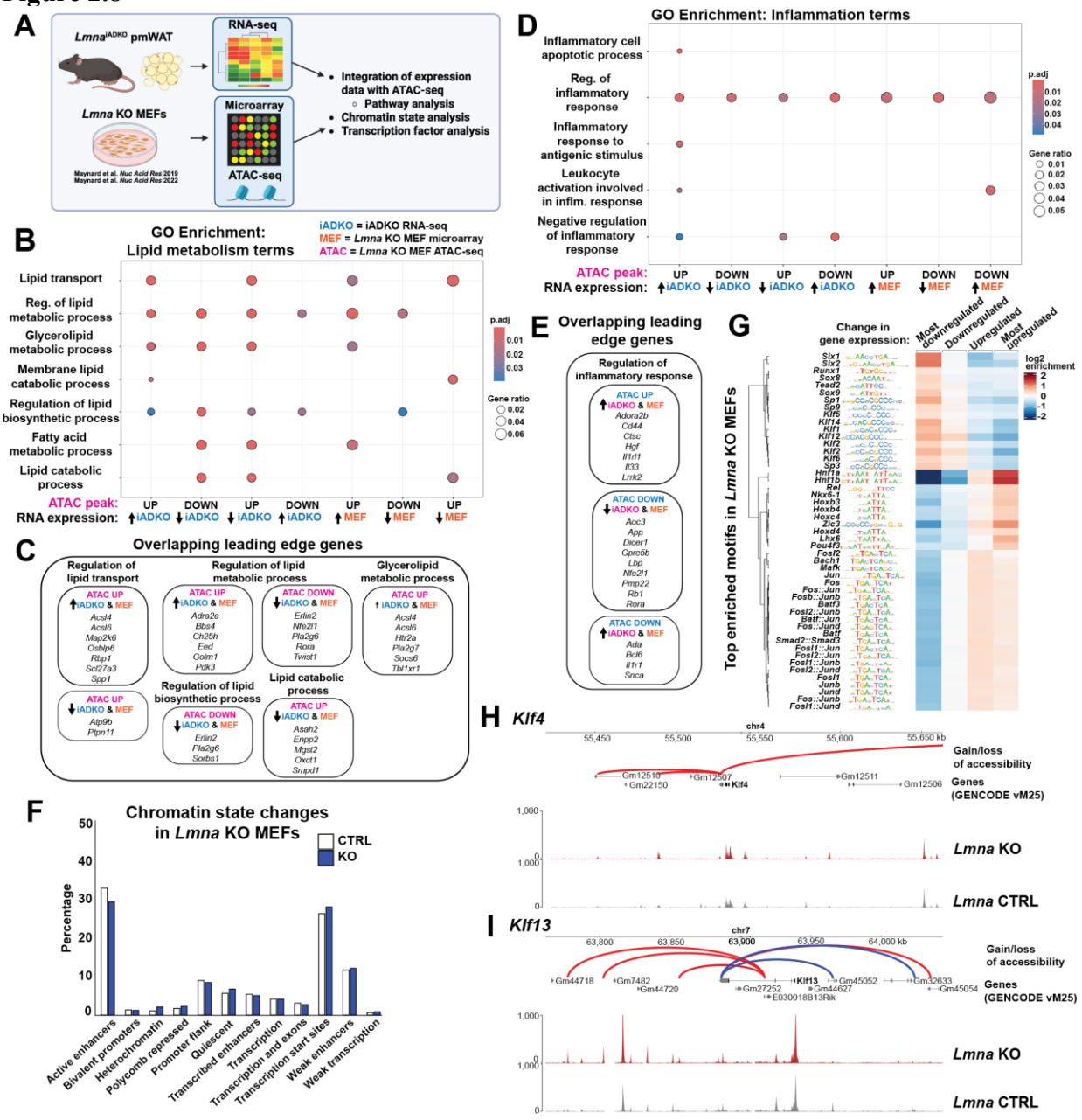
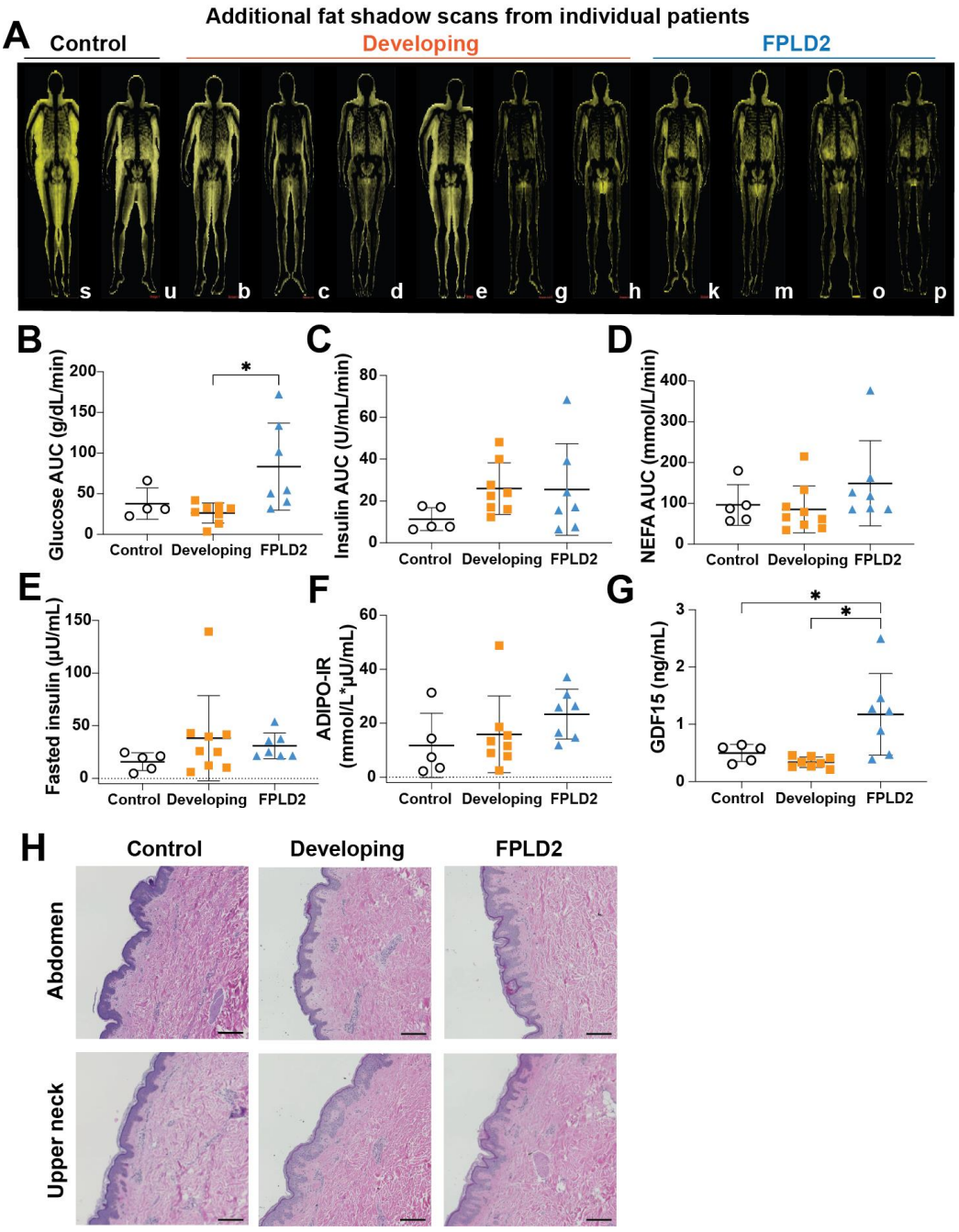
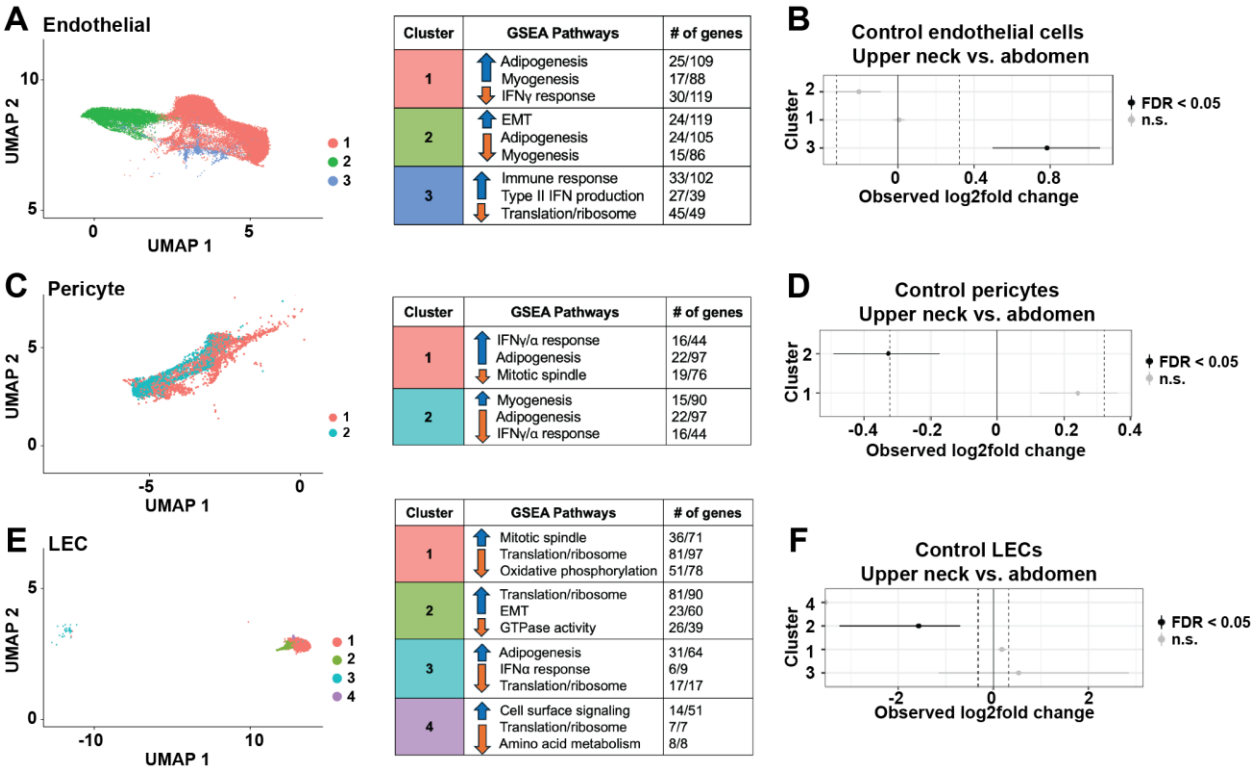


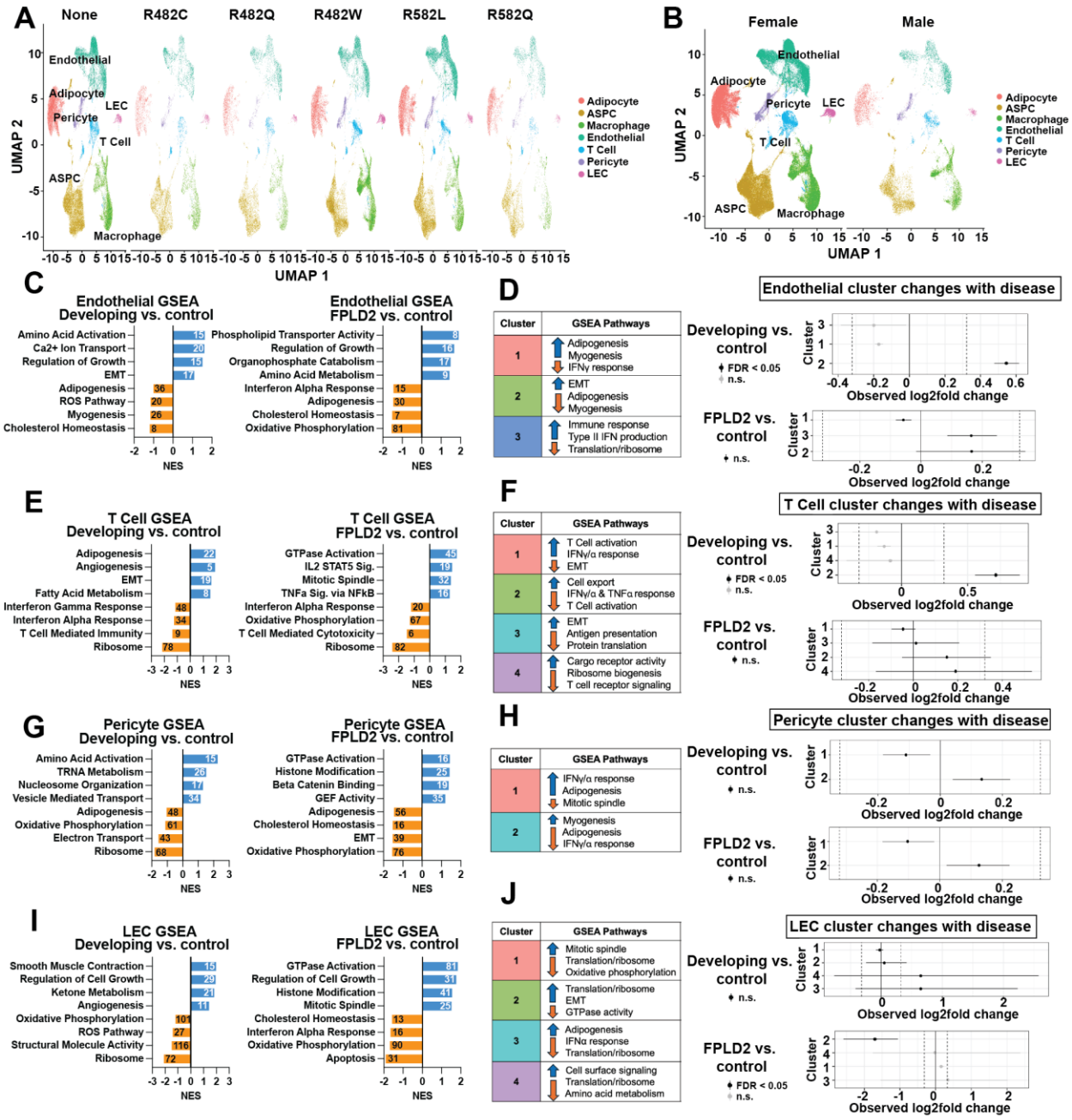
Figure 2.8. ***Lmna*** **KO mouse embryonic fibroblasts (MEFs) and adipocytes have shared patterns of altered gene expression, correlated with changes in chromatin accessibility. (A)** Schematic of dataset integration between *Lmna*^{iADKO} pmWAT RNA-seq and *Lmna* KO MEFs microarray and Assay for Transposase-Accessible Chromatin (ATAC)-seq. Overlapping changed genes in RNA-seq of *Lmna*^{iADKO} WAT (iADKO), *Lmna* KO MEF microarray (MEF) and *Lmna* KO MEF ATAC-seq (ATAC) were identified, and GSEA was ran to identify changes in (**B**) lipid metabolism Gene Ontology (GO) terms with their corresponding (**C**) overlapping leading edge genes, along with (**D**) inflammatory GO terms with (**E**) corresponding overlapping leading edge genes. (**F**) Distribution of chromatin features represented by percentage of overall chromatin composition compared between *Lmna* control (CTRL) and KO MEF ATAC-seq. (**G**) Enriched motifs in *Lmna* KO MEFs, stratified into four bins based on microarray gene expression changes, from most downregulated to most upregulated. (**H**) ATAC-seq signal tracks and visualization of significantly enriched regions and their predicted target genes. Red lines represent enhancers with a positive fold change upon *Lmna* KO, and blue lines are negative.



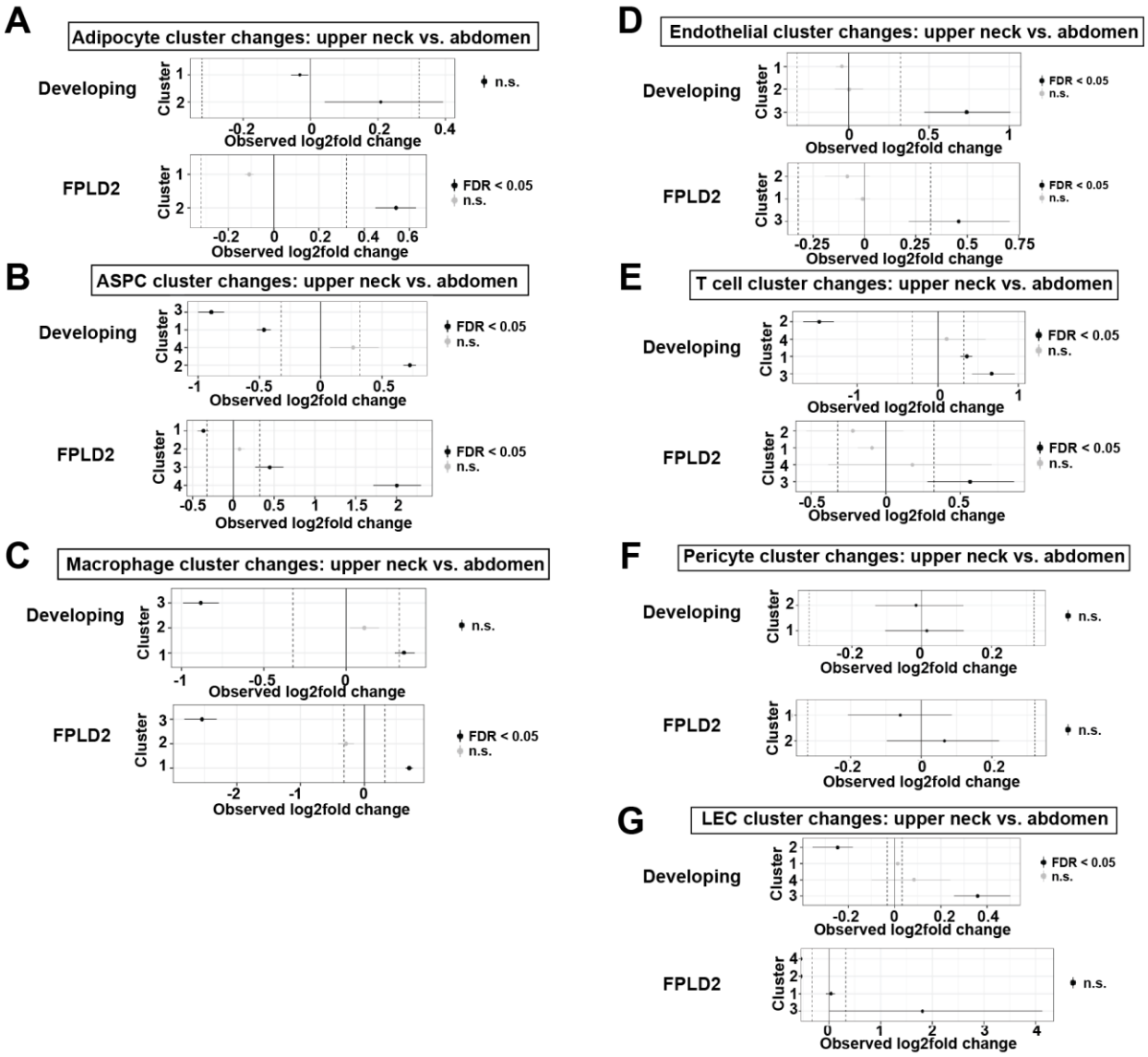
Supplemental Figure 2.1. Patients with FPLD2 have impaired glucose tolerance and increased GDF15 concentrations with otherwise comparable clinical characteristics to controls. (**A**) Additional fat shadow scans from all patients. (**B**) Area under the curve (AUC) from an oral glucose tolerance test (OGTT). (**C**) Insulin AUC during OGTT. (**D**) NEFA AUC during OGTT. (**E**) Fasted insulin concentrations. (**F**) Adipose tissue insulin resistance index (ADIPO-IR). (**G**) Growth differentiation factor 15 (GDF15) concentrations. (**H**) Histological images of skin from subcutaneous adipose tissue biopsies. Scale bar = 50 mm.



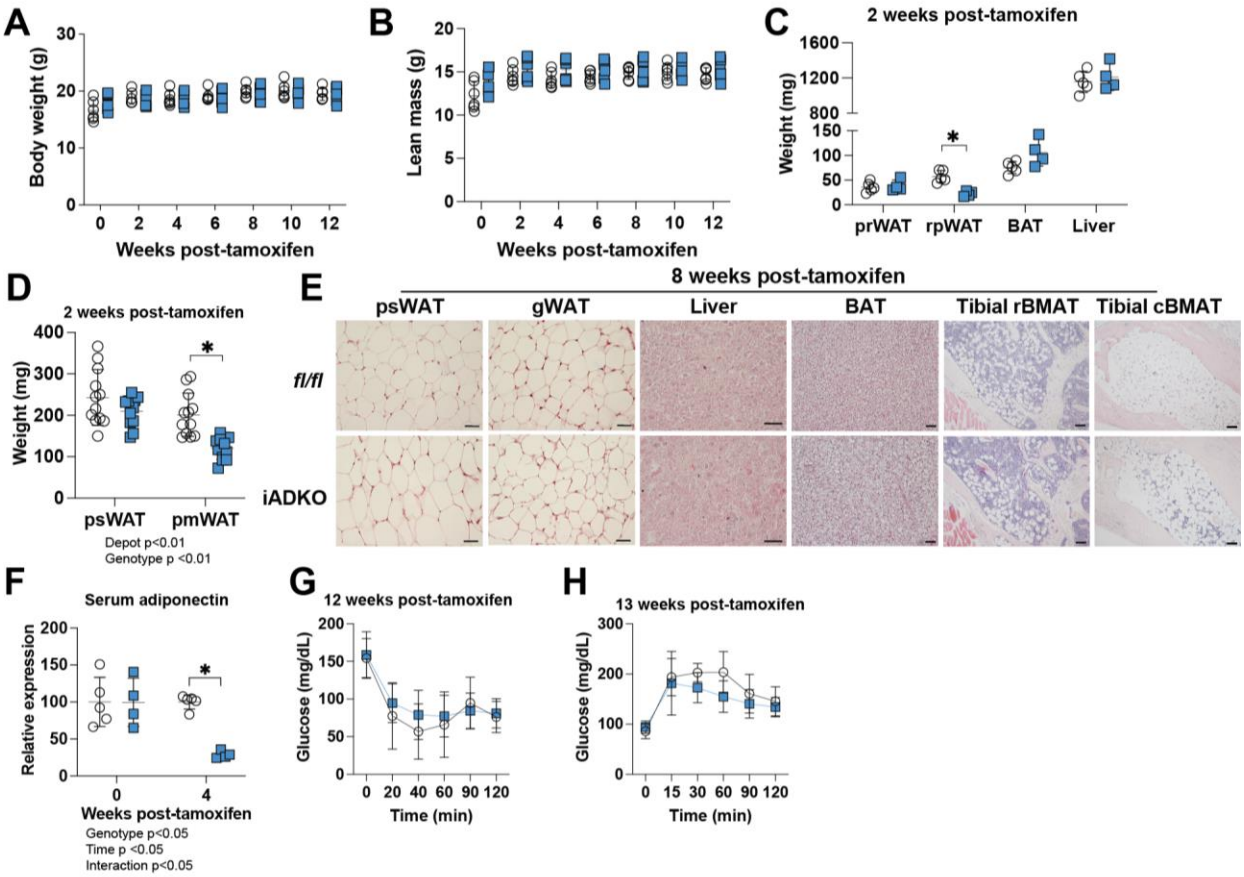
Supplemental Figure 2.2. Single nuclei RNA-sequencing identifies changes in cell proportions and clusters in upper neck and abdominal subcutaneous adipose tissue biopsies from control patients. (**A**) Endothelial subclusters with all disease states and biopsy location combined and their GSEA pathways. (**B**) Endothelial subcluster changes in the upper neck relative to abdomen in control biopsies. (**C**) Pericyte subclusters with GSEA pathways. (**D**) Subcluster changes in pericytes in the upper neck versus the abdomen. (**E**) LEC subclusters with GSEA pathways. (**F**) Subcluster changes in LECs in the upper neck relative to the abdomen.



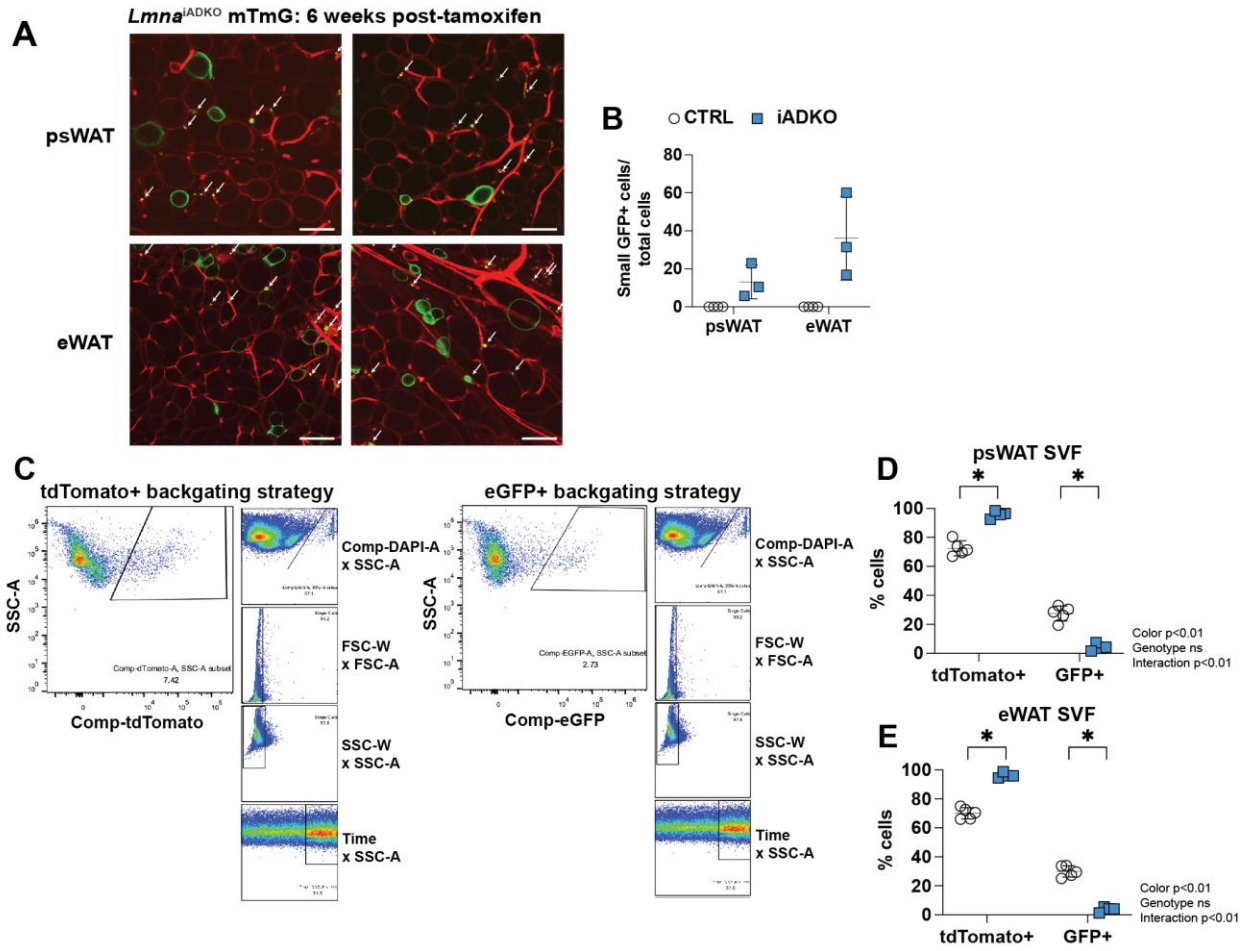
Supplemental Figure 2.3. Single nuclei analyses reveal cell proportion changes and identity with disease state. (**A**) UMAP projection of combined upper neck and abdomen biopsies from patients with different *LMNA* variants, or separated by (**B**) female and male individuals. (**C**) All endothelial cells from developing or FPLD2 biopsies were analyzed via GSEA and compared to controls to identify population-level changes in cell identity. (**D**) Endothelial subclusters with corresponding GSEA pathways and subcluster changes with disease. (**E**) T cell GSEA in developing or FPLD2 biopsies relative to controls. (**F**) T cell subcluster changes with disease. (**G**) Pericyte GSEA in developing or FPLD2 biopsies relative to controls. (**H**) Pericyte subcluster changes with disease. (**I**) LEC GSEA in developing or FPLD2 biopsies. (**J**) LEC subcluster changes with disease.



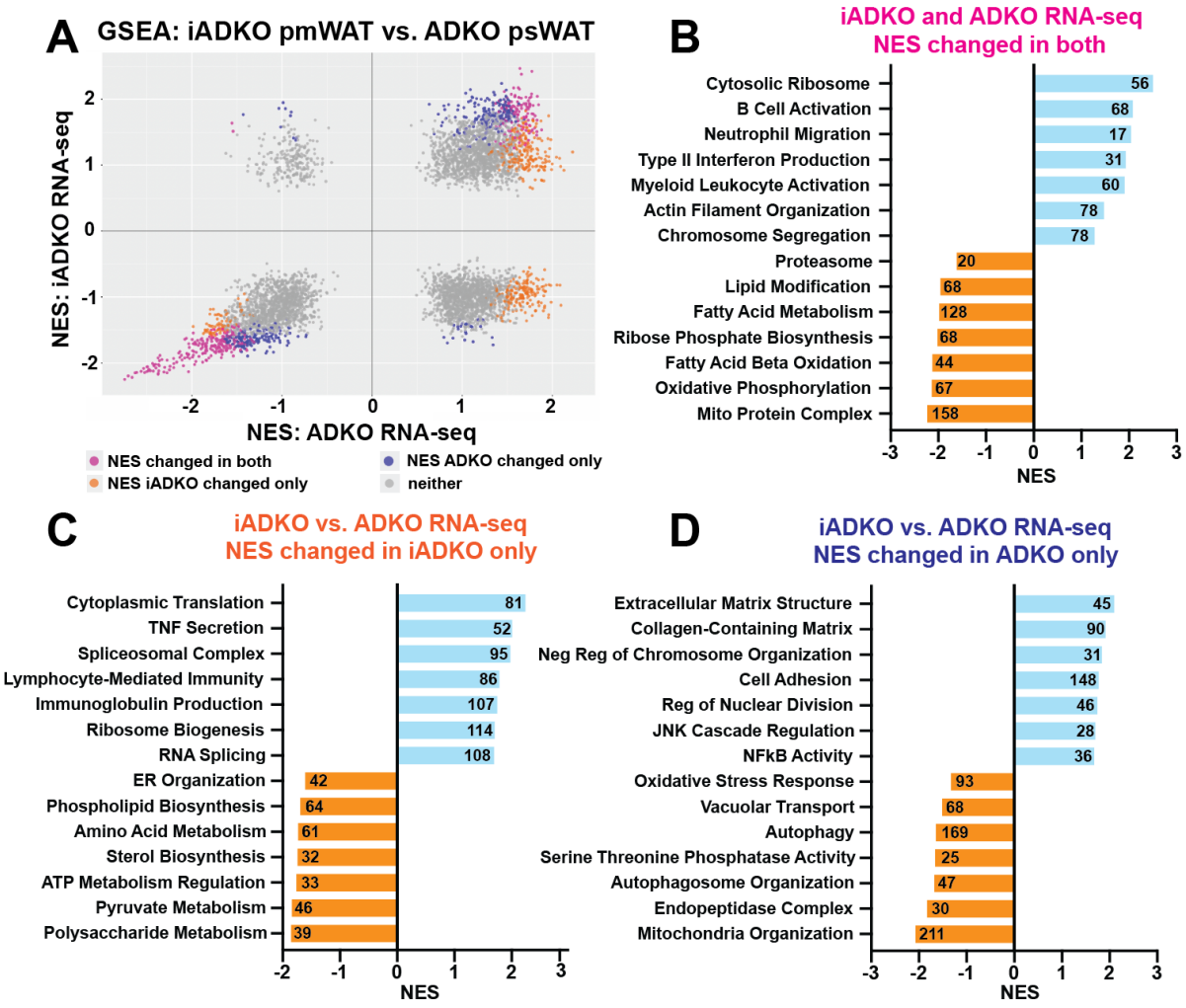
Supplemental Figure 2.4. Subcluster analyses reveal depot-specific shifts in cellular identity. Subcluster changes in the upper neck relative to the abdomen in biopsies from patients with developing and developed FPLD2 in (**A**) adipocytes, (**B**) ASPC, (**C**) macrophages, (**D**) endothelial cells, (**E**) T cells, (**F**) pericytes, and (**G**) LECs.



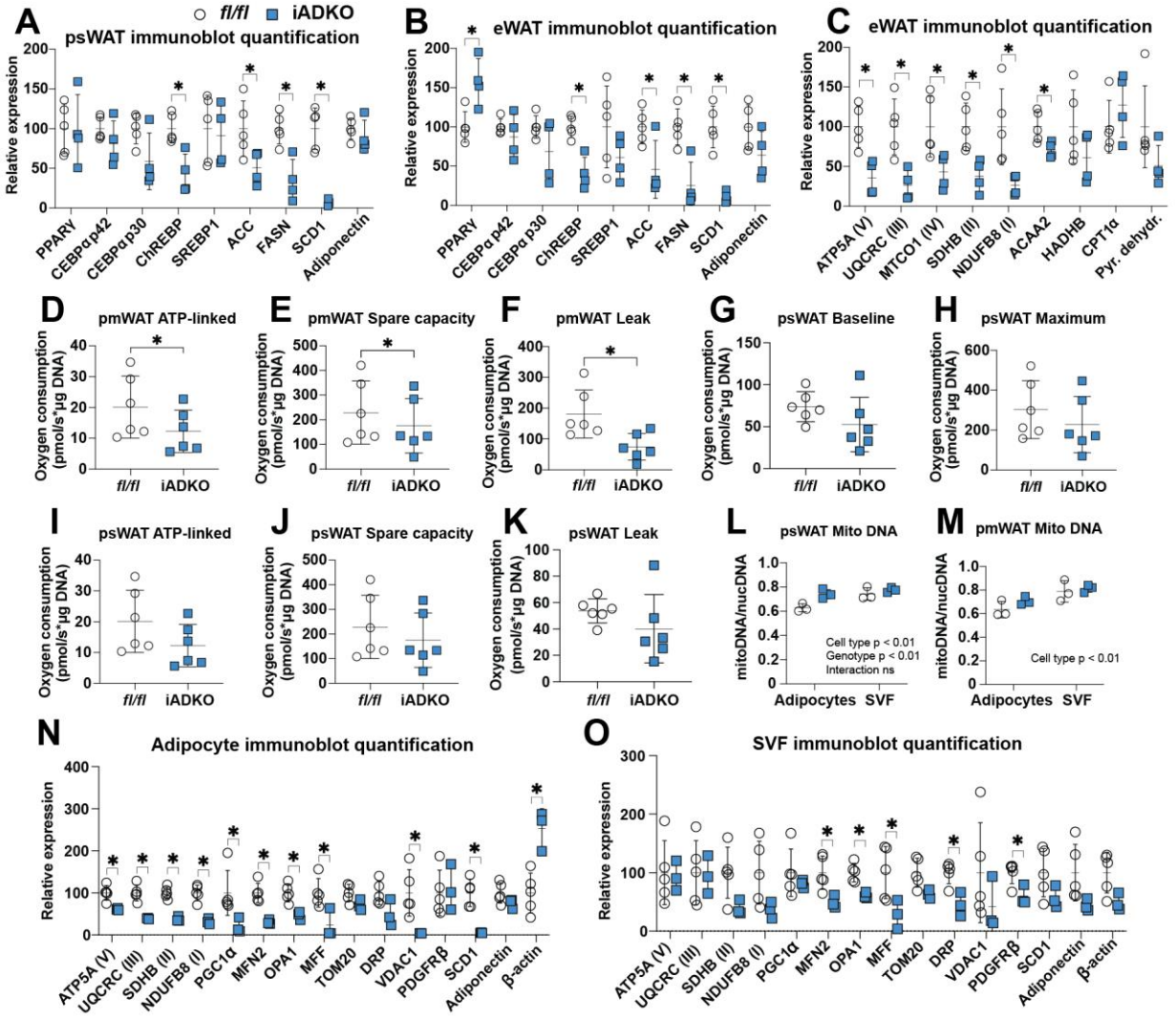
Supplemental Figure 2.5. *Lmna*^{iADKO} mice do not have changes in body weight, lean mass, or develop metabolic dysfunction. All data from male mice except histology from female mice in D. (**A**) Body weight and (**B**) lean mass post-tamoxifen over time (n = 6). (**C**) Weights of perirenal white adipose tissue (prWAT), retroperitoneal white adipose tissue (rpWAT), brown adipose tissue (BAT), and liver two-weeks post-tamoxifen (n = 6). (**D**) psWAT and pmWAT weights of female mice two-weeks post-tamoxifen (n = 12). (**E**) Histology of psWAT, gWAT, liver, BAT, and tibial regulated bone marrow adipose tissue (rBMAT) and constitutive bone marrow adipose tissue (cBMAT). (**F**) Quantification of serum adiponectin immunoblot four-weeks post-tamoxifen (n = 4-5). (**G**) Insulin tolerance test 12 weeks post-tamoxifen (n = 6). (**H**) Glucose tolerance test 13 weeks post-tamoxifen (n = 6). Data are represented as mean ± SD. *P < 0.05. Statistical analyses were performed using two-way ANOVA with a Bonferroni post-hoc test.



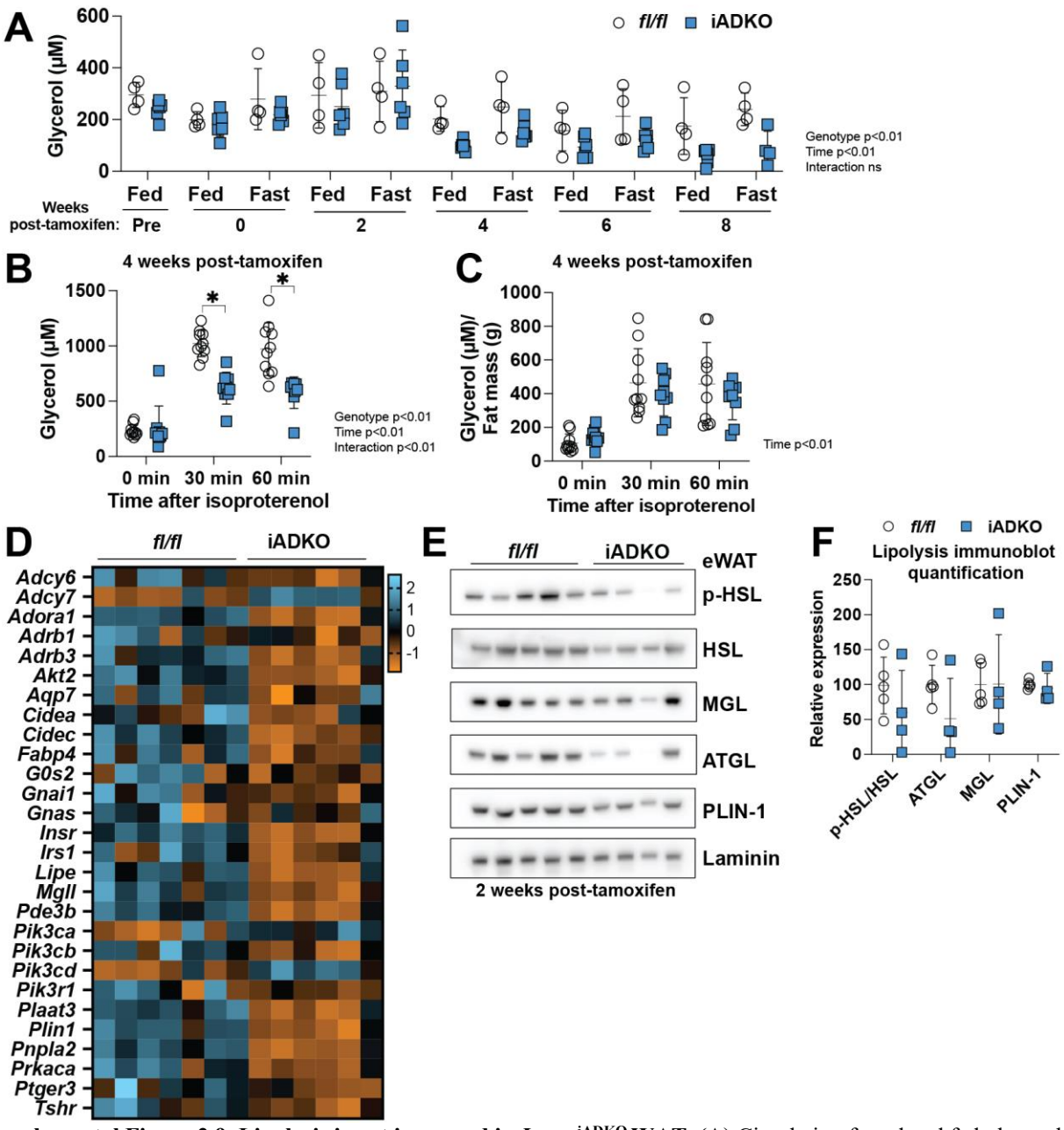
Supplemental Figure 2.6. *Lmna* knockout adipocytes do not de-differentiate and reside in adipose tissue after adipocyte shrinkage. All data from male mice. (**A**) Fresh confocal micrographs of small GFP-positive cells only present in *Lmna*^{iADKO} mTmG psWAT and eWAT six-weeks post-tamoxifen with (**B**) quantification. Scale bar = 100 µm. (**C**) Backgating strategy to identify tdTomato+ and GFP+ stromal vascular cells (SVC) in *Lmna*^{iADKO} mTmG WAT six-weeks post-tamoxifen. Flow cytometry analyses of tdTomato+ and GFP+ SVCs in (**D**) psWAT and (**E**) eWAT.



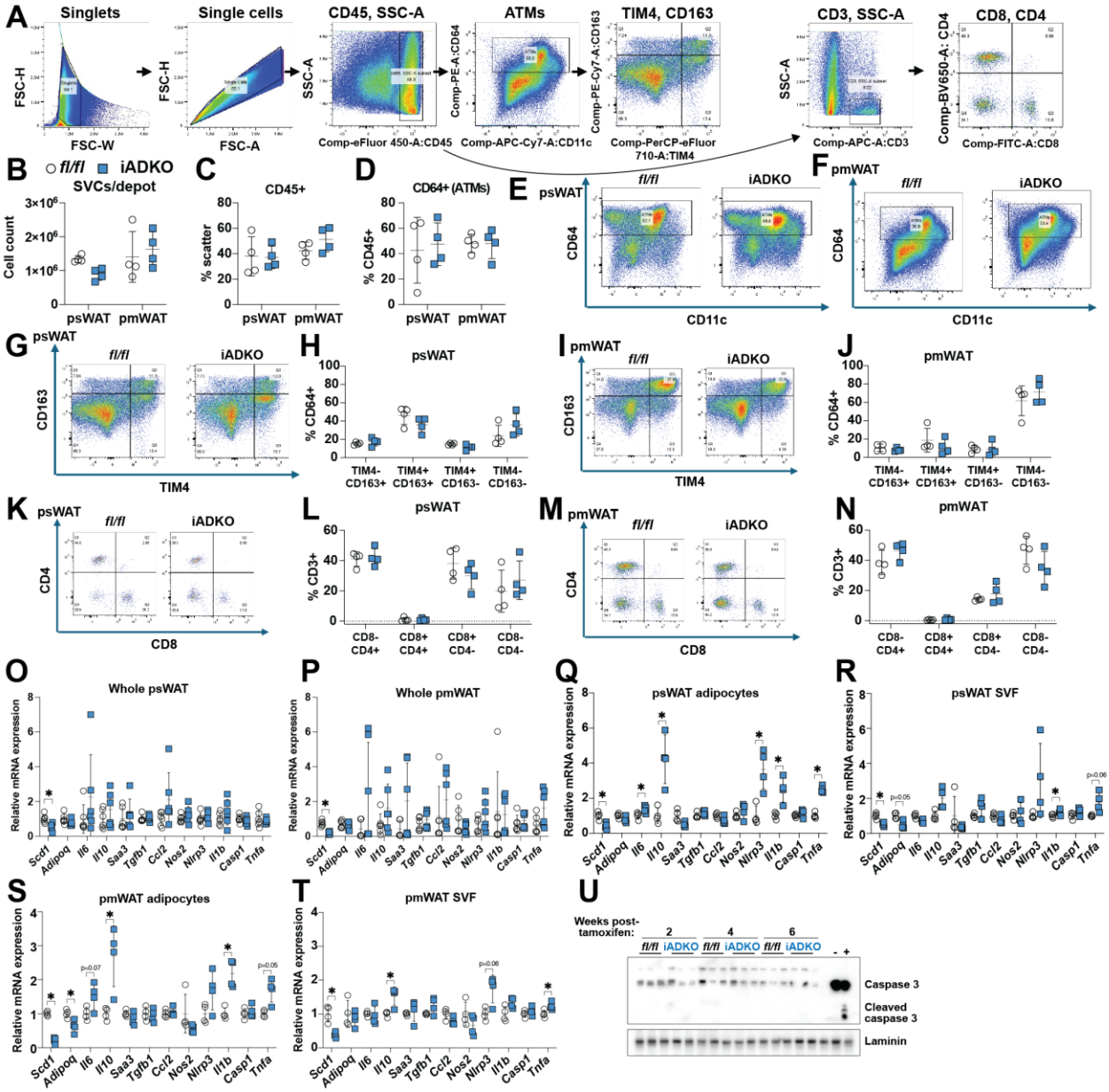
Supplemental Figure 2.7. Integrative RNA-seq analyses of *Lmna*^{iADKO} compared to *Lmna*^{ADKO} WAT reveals conserved patterns of gene expression across *Lmna* knockout models and depots. (**A**) Integrative GSEA comparison of RNA-seq *Lmna*^{iADKO} pmWAT two-weeks post-tamoxifen compared to *Lmna*^{ADKO} psWAT from four-week-old female mice (n= 5-6). Pink dots symbolize that NES were significantly changed in both RNA-seq and proteomics datasets, orange dots = NES only changed in proteomics, blue = NES only changed in RNA-seq. (**B**) Overlapping GSEA pathways in both *Lmna*^{iADKO} and *Lmna*^{ADKO} RNA-seq. Numbers on bars represent number of overlapping genes driving pathways. GSEA pathways changed in only (**C**) *Lmna*^{iADKO} or (**D**) *Lmna*^{ADKO} WAT.



Supplemental Figure 2.8. Lipogenic and mitochondrial proteins are repressed in *Lmna*^{iADKO} WAT, and *Lmna* KO pmWAT adipocytes but not psWAT adipocytes have reduced respiration. Quantification of immunoblots from Fig. 7A-C for (**A**) psWAT lipid metabolism proteins, (**B**) pmWAT lipid metabolism proteins, and (**C**) pmWAT mitochondrial proteins two-weeks post-tamoxifen (n = 4-5). Oroboros Oxygraph 2k analyses of floated adipocytes from pmWAT two-weeks post-tamoxifen of (**D**) ATP-linked respiration, (**E**) spare capacity, and (**F**) leak. Respiration analyses from psWAT adipocytes of (**G**) baseline respiration, (**H**) maximum respiration, (**I**) ATP-linked respiration, (**J**) spare capacity, and (**K**) leak (n = 6). Mitochondrial DNA quantification for (**L**) psWAT and (**M**) pmWAT two-weeks post-tamoxifen (n = 3). Immunoblot quantification from (**N**) adipocytes and (**O**) SVF mitochondrial dynamic proteins from Fig. 7F (n = 3-5). Data are represented as mean ± SD. *P < 0.05. Statistical analyses were performed using two-way ANOVA with a Bonferroni post-hoc test.



Supplemental Figure 2.9. Lipolysis is not increased in *Lmna*^{iADKO} WAT. (A) Circulating fasted and fed glycerol concentrations in male mice post-tamoxifen (n = 4-6). (**B**) Stimulated lipolysis assay following i.p. isoproterenol injection four-weeks post-tamoxifen (n = 9-10). (**C**) Glycerol concentrations from stimulated lipolysis assay normalized to fat mass. (**D**) Heatmap of lipolytic genes from *Lmna*^{iADKO} RNA-seq from pmWAT two-weeks post-tamoxifen. (**E**) Immunoblot of lipolysis protein expression from eWAT two-weeks post-tamoxifen and (**F**) quantification of immunoblot (n = 4-5).



Supplemental Figure 2.10. Macrophages and T cells are not activated in *Lmna*^{iADKO} WAT, and *Lmna* KO adipocytes have upregulated expression of pro-inflammatory transcripts. (**A**) Spectral flow cytometry gating strategy to identify macrophage and T cell populations from psWAT and pmWAT two-weeks post-tamoxifen (n = 4). (**B**) SVC number per depot. (**C**) CD45+ cells percentage. Representative density plot from CD45+ cells for CD64+ and CD11c+ adipose tissue macrophages (ATMs) from (**D**) psWAT and (**E**) pmWAT, with (**F**) quantification of CD64+ ATMs. Density plot from CD64+ cells for CD163+ and TIM4+ cells from (**G**) psWAT with (**H**) quantification, and from (**I**) pmWAT with (**J**) quantification. Density plot from CD3+ T cells that are CD4+ and CD8+ cells from (**K**) psWAT with (**L**) quantification, and from (**M**) pmWAT with (**N**) quantification. RT-qPCR analyses for inflammatory transcripts from (**O**) psWAT, (**P**) pmWAT, (**Q**) psWAT adipocytes, (**R**) psWAT SVF, (**S**) pmWAT adipocytes, and (**T**) pmWAT SVF (n = 4). (**U**) Immunoblot for cleaved and total caspase 3 in pmWAT post-tamoxifen (n = 3).

Table 2.1 Clinical, biochemical, and body composition parameters from patients with FPLD (FPLD), genetically affected but clinically unaffected individuals (Developing FPLD), and nonaffected individuals (Control). Data are expressed as mean ± SD.

Parameter	Control	Developing FPLD2	FPLD2	p-value
Weight	90 ± 5.5	78 ± 6.4	81 ± 6.4	0.4
BMI	31 ± 2.0	27 ± 1.7	29 ± 2.0	0.5
Waist Circumference	99 ± 6.2	87 ± 4.1	94 ± 2.3	0.2
Hip Circumference	107 ± 6.0	93 ± 4.6	98 ± 3	0.2
W/H ratio	0.9 ± 0.02	0.9 ± 0.01	0.9 ± 0.01	0.3
Fasting glucose (mg/dL)	129 ± 40	111 ± 12	221 ± 59	0.5
Fasting insulin (μU/mL)	16 ± 1.3	38 ± 13	31 ± 4.3	0.3
HbA1c (%)	7 ± 1.0	6 ± 0.5 [a]	9 ± 1.1 *	0.01
Triglycerides (mg/dL)	116 ± 26	159 ± 33 [a]	301 ± 33 **	0.007
Total Cholesterol (mg/dL)	184 ± 13	166 ± 16	188 ± 12	0.4
HDL-cholesterol (mg/dL)	45 ± 4.0	38 ± 3	34 ± 3	0.1
LDL-cholesterol (mg/dL)	127 ± 9	111 ± 17	107 ± 10	0.4
AST (IU/L)	22 ± 1.3	25 ± 2.4	27 ± 2.3	0.5
ALT (IU/L)	22 ± 3.4	27 ± 3.4	36 ± 5.7	0.1
GGT (IU/L)	18 ± 3.5	19 ± 2.6	28 ± 4.3	0.08
C-reactive Protein (mg/L)	10 ± 4.6	2.1 ± 0.9	3.6 ± 1.6	0.3
Fasting FFA (mmol/L)	0.6 ± 0.1	0.5 ± 0.1 [a]	0.8 ± 0.1	0.09
Fasting C-Peptide (ng/mL)	2.3 ± 0.3	3.4 ± 0.8	3 ± 0.5	0.6
HOMA-IR	6 ± 2.2	11 ± 3.7	15 ± 3.4	0.3
ADIPO-IR	12 ± 4.3	16 ± 4.4	23 ± 3.2	0.2
Glucose AUC	51564 ± 12771	33731 ± 7923 [a]	83468 ± 18724	0.01
Insulin AUC	11317 ± 2012	46184 ± 19437	25525 ± 7669	0.2
Triglyceride AUC	39900 ± 10087	45220 ± 9449 [c]	94001 ± 12078	0.03
C-Peptide AUC	1807 ± 430	2990 ± 542	2435 ± 476	0.5
FFA AUC	96 ± 18	85 ± 18	149 ± 36	0.2
Leptin (pg/mL)	5562 ± 1491	3807 ± 1130	1905 ± 383 [&]	0.03
Adiponectin (pg/μL)	35735 ± 6360	25526 ± 7638	14724 ± 4209 *	0.09
FGF-21 (pg/mL)	152 ± 67	57 ± 14 [c]	190 ± 56	0.03
GDF-15 (pg/mL)	498 ± 55	371 ± 41 [b]	1174 ± 249 *	0.001
MCP-1 (pg/mL)	492 ± 94	572 ± 76	657 ± 45	0.7
IL-6 (pg/mL)	3.3 ± 0.5	0.9 ± 0.3 [s]	5.0 ± 3.1	0.03
TNFα (pg/mL)	167 ± 102	16 ± 3	72 ± 44	0.1
Control vs FPLD2: *p-value=0.04; **p-value=0.01; [&] p-value=0.03				
Developing FPLD2 vs FPLD2: [a] p-value= 0.01; [b] p-value=0.004; [c] p-value=0.04				
Control vs Developing FPLD: [s] p-value=0.04				

Abbreviations: BMI, body mass index; HbA1c, hemoglobin A1c; HDL, high-density lipoprotein; LDL, low-density lipoprotein, ALT: alanine aminotransferase, AST: aspartate aminotransferase, GGT: gamma-glutamyl transferase, NEFA: Non-esterified fatty acids, HOMA-IR: Homeostatic Model Assessment for Insulin Resistance; ADIPO-IR: Adipose Tissue Insulin Resistance Index, AUC: area under the curve, FGF: fibroblast growth factor, GDF: growth differentiation factor, MCP: monocyte chemoattractant protein, IL: interleukin, TNF: tumor necrosis factor.

2.7 References

1. Akinci, B., *et al*. *Lipodystrophy Syndromes: Presentation and Treatment*. *Endotext [Internet]* (MDText.com, Inc., 2018).
2. Lim, K. *et al.* Lipodystrophy: A paradigm for understanding the consequences of 'overloading' adipose tissue. *Phys. Rev.* **101**:907-993 (2021).
3. Dunnigan, M. G., *et al.* Familial lipoatrophic diabetes with dominant transmission. A new syndrome. *Q. J. Med.* **43**, 33–48 (1974).
4. Chiquette, E., *et al*. Estimating the prevalence of generalized and partial lipodystrophy: findings and challenges. *Diabetes Metab. Syndr. Obes. Targets Ther.* **10**, 375–383 (2017).
5. Gonzaga-Jauregui, C. *et al.* Clinical and Molecular Prevalence of Lipodystrophy in an Unascertained Large Clinical Care Cohort. *Diabetes* **69**, 249–258 (2020).
6. Akinci, B. *et al.* Clinical presentations, metabolic abnormalities and end-organ complications in patients with familial partial lipodystrophy. *Metab. Clin. Exp.* **72**, 109–119 (2017).
7. Besci, O. *et al.* Deciphering the Clinical Presentations in LMNA-related Lipodystrophy: Report of 115 Cases and a Systematic Review. *J. Clin. Endocrinol. Metab.* **109**, e1204–e1224 (2024).
8. Oral, E. A. *et al.* Leptin-replacement therapy for lipodystrophy. *N. Engl. J. Med.* **346**, 570–578 (2002).
9. Shackleton, S. *et al.* LMNA, encoding lamin A/C, is mutated in partial lipodystrophy. *Nat. Genet.* **24**, 153–156 (2000).
10. Aebi, U., *et al*. The nuclear lamina is a meshwork of intermediate-type filaments. *Nature* **323**, 560–564 (1986).
11. Karoutas, A. & Akhtar, A. Functional mechanisms and abnormalities of the nuclear lamina. *Nat. Cell Biol.* **23**, 116–126 (2021).
12. van Steensel, B. & Belmont, A. S. Lamina-Associated Domains: Links with Chromosome Architecture, Heterochromatin, and Gene Repression. *Cell* **169**, 780–791 (2017).
13. Cao, H. & Hegele, R. A. Nuclear lamin A/C R482Q mutation in Canadian kindreds with Dunnigan-type familial partial lipodystrophy. *Hum. Mol. Genet.* **9**, 109–112 (2000).
14. Stierlé, V. *et al.* The carboxyl-terminal region common to lamins A and C contains a DNA binding domain. *Biochemistry* **42**, 4819–4828 (2003).
15. Rajendran, V., *et al*. In silico investigation of molecular mechanism of laminopathy caused by a point mutation (R482W) in lamin A/C protein. *Amino Acids* **43**, 603–615 (2012).
16. Magracheva, E., *et al.* Structure of the lamin A/C R482W mutant responsible for dominant familial partial lipodystrophy (FPLD). *Acta Crystallograph. Sect. F Struct. Biol. Cryst. Commun.* **65**, 665–670 (2009).
17. Sullivan, T. *et al.* Loss of A-type lamin expression compromises nuclear envelope integrity leading to muscular dystrophy. *J. Cell Biol.* **147**, 913–920 (1999).
18. Lammerding, J. *et al.* Lamins A and C but Not Lamin B1 Regulate Nuclear Mechanics *. *J. Biol. Chem.* **281**, 25768–25780 (2006).
19. Kubben, N. *et al.* Post-natal myogenic and adipogenic developmental: defects and metabolic impairment upon loss of A-type lamins. *Nucl. Austin Tex* **2**, 195–207 (2011).
20. Boguslavsky, R. L., *et al*. Nuclear lamin A inhibits adipocyte differentiation: implications for Dunnigan-type familial partial lipodystrophy. *Hum. Mol. Genet.* **15**, 653–663 (2006).

21. Le Dour, C. *et al.* Extracellular matrix remodeling and transforming growth factor-β signaling abnormalities induced by lamin A/C variants that cause lipodystrophy. *J. Lipid Res.* **58**, 151–163 (2017).
22. Wojtanik, K. M. *et al.* The role of LMNA in adipose: a novel mouse model of lipodystrophy based on the Dunnigan-type familial partial lipodystrophy mutation. *J. Lipid Res.* **50**, 1068–1079 (2009).
23. Makowski, L., *et al*. The fatty acid-binding protein, aP2, coordinates macrophage cholesterol trafficking and inflammatory activity. Macrophage expression of aP2 impacts peroxisome proliferator-activated receptor gamma and IkappaB kinase activities. *J. Biol. Chem.* **280**, 12888–12895 (2005).
24. Araújo-Vilar, D. *et al.* Site-dependent differences in both prelamin A and adipogenic genes in subcutaneous adipose tissue of patients with type 2 familial partial lipodystrophy. *J. Med. Genet.* **46**, 40–48 (2009).
25. Pellegrini, C. *et al.* Altered adipocyte differentiation and unbalanced autophagy in type 2 Familial Partial Lipodystrophy: an in vitro and in vivo study of adipose tissue browning. *Exp. Mol. Med.* **51**, 1–17 (2019).
26. Corsa, C. A. S. *et al.* Adipocyte-specific deletion of lamin A/C largely models human familial partial lipodystrophy type 2. *Diabetes* (2021) doi:10.2337/db20-1001.
27. Keipert, S. & Ost, M. Stress-induced FGF21 and GDF15 in obesity and obesity resistance. *Trends Endocrinol. Metab. TEM* **32**, 904–915 (2021).
28. Meral, R. *et al.* Metabolic Improvements With Tirzepatide in Lipodystrophy: A Novel Option? *Diabetes Care* **48**, 756–762 (2025).
29. Strieder-Barboza, C. *et al.* Single-nuclei Transcriptome of Human AT Reveals Metabolically Distinct Depot-Specific Adipose Progenitor Subpopulations. 2022.06.29.496888 Preprint at https://doi.org/10.1101/2022.06.29.496888 (2022).
30. Emont, M. P. *et al.* A single-cell atlas of human and mouse white adipose tissue. *Nature* **603**, 926–933 (2022).
31. Muzumdar, M. D., *et al*. A global double-fluorescent Cre reporter mouse. *Genes. N. Y. N 2000* **45**, 593–605 (2007).
32. Song, H. *et al.* The regulatory role of adipocyte mitochondrial homeostasis in metabolism-related diseases. *Front. Physiol.* **14**, (2023).
33. Lee, J. H. *et al.* The Role of Adipose Tissue Mitochondria: Regulation of Mitochondrial Function for the Treatment of Metabolic Diseases. *Int. J. Mol. Sci.* **20**, 4924 (2019).
34. Wilson-Fritch, L. *et al.* Mitochondrial remodeling in adipose tissue associated with obesity and treatment with rosiglitazone. *J. Clin. Invest.* **114**, 1281–1289 (2004).
35. Franco, A., *et al*. Mitochondria Clumping vs. Mitochondria Fusion in CMT2A Diseases. *Life* **12**, 2110 (2022).
36. Maynard, S. *et al.* Lamin A/C impairments cause mitochondrial dysfunction by attenuating PGC1α and the NAMPT-NAD+ pathway. *Nucleic Acids Res.* gkac741 (2022) doi:10.1093/nar/gkac741.
37. Maynard, S. *et al.* Lamin A/C promotes DNA base excision repair. *Nucleic Acids Res.* **47**, 11709–11728 (2019).
38. Vu, H. & Ernst, J. Universal chromatin state annotation of the mouse genome. *Genome Biol.* **24**, 153 (2023).
39. Briand, N. & Collas, P. Lamina-associated domains: peripheral matters and internal affairs. *Genome Biol.* **21**, 85 (2020).

40. García-Niño, W. R. & Zazueta, C. New insights of Krüppel-like transcription factors in adipogenesis and the role of their regulatory neighbors. *Life Sci.* **265**, 118763 (2021).
41. Birsoy, K., *et al*. Transcriptional Regulation of Adipogenesis by KLF4. *Cell Metab.* **7**, 339–347 (2008).
42. Yang, S. *et al.* Sp1-like protein KLF13 acts as a negative feedback regulator of TGF-β signaling and fibrosis. *Cell Rep.* **42**, 112367 (2023).
43. Spalding, K. L. *et al.* Dynamics of fat cell turnover in humans. *Nature* **453**, 783–787 (2008).
44. Vijayakumar, A. *et al.* Absence of Carbohydrate Response Element Binding Protein in Adipocytes Causes Systemic Insulin Resistance and Impairs Glucose Transport. *Cell Rep.* **21**, 1021–1035 (2017).
45. Crewe, C., *et al.* SREBP-regulated adipocyte lipogenesis is dependent on substrate availability and redox modulation of mTORC1. *JCI Insight* **4**, (2019).
46. Lloyd, D. J., *et al*. A novel interaction between lamin A and SREBP1: implications for partial lipodystrophy and other laminopathies. *Hum. Mol. Genet.* **11**, 769–777 (2002).
47. Shimomura, I. *et al.* Insulin resistance and diabetes mellitus in transgenic mice expressing nuclear SREBP-1c in adipose tissue: model for congenital generalized lipodystrophy. *Genes Dev.* **12**, 3182–3194 (1998).
48. Mori, H., *et al.* Scd1 and monounsaturated lipids are required for autophagy and survival of adipocytes. *Mol. Metab.* **83**, 101916 (2024).
49. Du, Z. *et al.* SIRT1 Ameliorates Lamin A/C Deficiency-Induced Cardiac Dysfunction by Promoting Mitochondrial Bioenergetics. *JACC Basic Transl. Sci.* **9**, 1211–1230 (2024).
50. Borrego Alvarez, A. *et al.* 1470-P: Modeling Familial Partial Lipodystrophy Type 2 (LMNAp.R482W) Utilizing iPSC-Derived Adipocytes. *Diabetes* **73**, 1470-P (2024).
51. Poulain-Godefroy, O., *et al*. Inflammation is associated with a decrease of lipogenic factors in omental fat in women. *Am. J. Physiol. Regul. Integr. Comp. Physiol.* **295**, R1-7 (2008).
52. Ryu, M. J. *et al.* Crif1 deficiency reduces adipose OXPHOS capacity and triggers inflammation and insulin resistance in mice. *PLoS Genet.* **9**, e1003356 (2013).
53. Friesen, M. & Cowan, C. A. FPLD2 LMNA mutation R482W dysregulates iPSC-derived adipocyte function and lipid metabolism. *Biochem. Biophys. Res. Commun.* **495**, 254–260 (2018).
54. Elzeneini, E. & Wickström, S. Lipodystrophic laminopathy: Lamin A mutation relaxes chromatin architecture to impair adipogenesis. *J. Cell Biol.* **216**, jcb.201707090 (2017).
55. Herrero, L., *et al.* Inflammation and adipose tissue macrophages in lipodystrophic mice. *Proc. Natl. Acad. Sci.* **107**, 240–245 (2010).
56. Béréziat, V. *et al.* LMNA mutations induce a non-inflammatory fibrosis and a brown fat-like dystrophy of enlarged cervical adipose tissue. *Am. J. Pathol.* **179**, 2443–2453 (2011).
57. Zheng, X. *et al.* Lamins Organize the Global Three-Dimensional Genome from the Nuclear Periphery. *Mol. Cell* **71**, 802-815.e7 (2018).
58. Shah, P. P. *et al.* Pathogenic LMNA variants disrupt cardiac lamina-chromatin interactions and de-repress alternative fate genes. *Cell Stem Cell* **28**, 938-954.e9 (2021).
59. Meral, R. *et al.* 'Fat Shadows' From DXA for the Qualitative Assessment of Lipodystrophy: When a Picture Is Worth a Thousand Numbers. *Diabetes Care* **41**, 2255–2258 (2018).
60. Risso, D., *et al*. Normalization of RNA-seq data using factor analysis of control genes or samples. *Nat. Biotechnol.* **32**, 896–902 (2014).

61. Wang, A. S., *et al*. Tissue specific loss of A-type lamins in the gastrointestinal epithelium can enhance polyp size. *Differ. Res. Biol. Divers.* **89**, 11–21 (2015).
62. Parlee, S. D., *et al*. Quantifying size and number of adipocytes in adipose tissue. *Methods Enzymol.* **537**, 93–122 (2014).
63. Bagchi, D. P. *et al.* Wnt/β-catenin signaling regulates adipose tissue lipogenesis and adipocyte-specific loss is rigorously defended by neighboring stromal-vascular cells. *Mol. Metab.* **42**, 101078 (2020).
64. Tank, E. M. *et al.* Abnormal RNA stability in amyotrophic lateral sclerosis. *Nat. Commun.* **9**, 2845 (2018).
65. Ewels, P. A. *et al.* The nf-core framework for community-curated bioinformatics pipelines. *Nat. Biotechnol.* **38**, 276–278 (2020).
66. Stark, R. & Brown, G. DiffBind: Differential binding analysis of ChIP-Seq peak data.
67. rGREAT: an R/bioconductor package for functional enrichment on genomic regions | Bioinformatics | Oxford Academic. https://academic-oup-com.proxy.lib.umich.edu/bioinformatics/article/39/1/btac745/6832038.
68. Yu, G., *et al*. clusterProfiler: an R package for comparing biological themes among gene clusters. *Omics J. Integr. Biol.* **16**, 284–287 (2012).
69. Machlab, D. *et al.* monaLisa: an R/Bioconductor package for identifying regulatory motifs. *Bioinforma. Oxf. Engl.* **38**, 2624–2625 (2022).
70. Lopez-Delisle, L. *et al.* pyGenomeTracks: reproducible plots for multivariate genomic datasets. *Bioinformatics* **37**, 422–423 (2021).

Chapter 3 Effects of FGF21, Soluble TGFβR2, and Environmental Temperature on Metabolic Dysfunction in Lipodystrophic Mice

Adapted from: Maung J. N.*, Chen, Y.*, Hoose, K. S., Adler, R. E., Hariri, H., Dickson, M. J., Hetrick, T. A., Ferguson, G. A., Schill, R. L., Mori, H., Uranga, R. M., Lewis, K. T., Hermsmeyer, I. D. K., Gilio, D., de Solis, C., Toliver, A., Davidsohn, N., Oral, E. A., MacDougald, O. A. Effects of FGF21, soluble TGFβR2, and environmental temperature on metabolic dysfunction in lipodystrophic mice. *JCI Insight*. 2025. Online ahead of print.
**indicates co-first authorship*

3.1 Abstract

Metabolic health is influenced by adipose tissue, and obesity and lipodystrophy are characterized by inflammation and metabolic dysfunction. Whereas obesity and lipodystrophy treatments involve pharmacological approaches and lifestyle changes, these therapies require long-term, repeated dosing, and are not successful for all patients. Gene therapy with targets such as FGF21 and sTGFBR2 provides an alternative approach, specifically in lipodystrophy. Preclinical experiments in mice housed at 22°C are confounded by a mild cold stress not generally experienced by humans, which can negatively affect translation of metabolic therapeutics. In this study, we investigated effects of FGF21/sTGFBR2 combination gene therapy on obese and lipodystrophic mice, and how housing temperature influences therapeutic efficacy. In obese mice, FGF21/sTGFBR2 improved insulin resistance and hyperlipidemia more dramatically at warmer temperatures. In lipodystrophic mice on a high fat diet, combination therapy required adipose tissue to improve insulin resistance at 30°C, whereas FGF21 alone improved insulin resistance at 22°C. Transcriptomic analyses revealed that lipodystrophic mice had upregulated hepatic cell proliferation and fibrosis pathways, and that FGF21 promoted hepatic metabolism. Thus, metabolic dysfunction caused by lipodystrophy is improved by targeting FGF21 and TGFB signaling, but effectiveness in preclinical models may be dependent upon environmental temperature and presence of adipose tissue.

3.2 Introduction

Metabolic health is largely dictated by the amount, location, and function of adipose tissues. Obesity is a medical condition characterized by an excessive accumulation of body fat, and often is estimated clinically with waist-to-hip ratio and other measurements[1]. It has become a global health concern, with prevalence rates of obesity rising steadily - current estimates are that >600 million adult individuals have obesity[2]. Obesity is linked to a range of metabolic dysfunctions, including insulin resistance, hypertension, dyslipidemia, and an increased risk of type 2 diabetes, heart disease, and certain cancers[3]. At the other extreme, lipodystrophy syndromes are rare, heterogeneous disorders characterized by partial or complete loss of adipose tissues[4]. Whereas clinical prevalence of lipodystrophy is about 1 in 20,000 individuals, its genetic prevalence may be as high as 1 in 7,000[5,6]. With a paucity of adipose tissue in which to store excess energy, lipids instead accumulate ectopically in tissues such as liver, muscle, and pancreas, resulting in metabolic dysfunctions similar to those seen in obesity, including insulin resistance, dyslipidemia, and fatty liver disease[7].

Current treatments for both obesity and lipodystrophy often include pharmacological approaches in addition to lifestyle modifications. For obesity, drugs such as GLP-1 receptor agonists promote satiety, reduce appetite, and enhance insulin secretion to stimulate weight loss, metabolic improvements, and reduce cardiovascular disease[8–11]. However, these drugs can also have side effects, including gastrointestinal perturbations and hypotension[12]. Patients with lipodystrophy often have low concentrations of leptin in circulation, and leptin replacement therapy is used to manage metabolic dysfunctions associated with leptin deficiency and hyperphagia[13–15]. Recombinant leptin therapy helps improve insulin sensitivity, reduce circulating triglyceride concentrations, and decrease liver volume in patients with lipodystrophy; however, leptin therapy does not adequately address all the metabolic perturbations for reasons that are incompletely understood[13]. Treatment of metabolic dysfunctions associated with both obesity and lipodystrophy is typically long-term, with some therapies potentially being lifelong. Leptin replacement therapy requires daily subcutaneous injections, whereas GLP-1 receptor agonists are administered at least once weekly. Novel therapies with an extended duration of action and reduced frequency of administration are crucial for improving patient compliance and outcomes, in addition to providing alternative therapies for patients in which current treatments are ineffective or too expensive. Gene therapy, which offers the potential for sustained

therapeutic effects, represents a promising approach for providing long-term treatment solutions specifically for lipodystrophy[16].

In recent years, two new proteins delivered via gene therapy have shown potential for treatment of metabolic dysfunction. First, fibroblast growth factor 21 (FGF21) is an endocrine factor, produced and secreted primarily by the liver, that acts at numerous sites such as adipose tissues and bone to regulate energy balance, glucose and lipid metabolism, and insulin sensitivity[17,18]. Second, soluble transforming growth factor (TGF)-β receptor 2 (sTGFBR2) binds to TGFB1 ligands and prevents their interaction with cell surface receptors, thus repressing physiological processes such as immune response, tissue repair, fibrosis, and cell growth[19,20]. Studies have shown that FGF21 gene therapy reduces body weight, adipose tissue hypertrophy and inflammation, hepatic steatosis, and improves insulin sensitivity, with sustained effects present for over one year in obese mice[21,22]. In mice fed a high fat diet (HFD), combined gene therapy with FGF21 and sTGFBR2 effectively mitigated four age-related diseases: obesity, type 2 diabetes, heart failure, and renal failure[23]. Potential of these factors to improve metabolic dysfunction in lipodystrophic mice has also been explored. Although metabolic benefits of FGF21 were dependent on presence of adipose tissue in aP2-SREBP1c lipodystrophic mice, an FGF21 analog improved insulin sensitivity and adipocyte gene expression in seipin-deficient lipodystrophic mice[24,25]. In contrast, inhibition of TGFB signaling more effectively alleviated abnormal glucose and lipid metabolism in aP2-SREBP1c lipodystrophic mice than in obese mice[26]. Taken together, combination gene therapy of FGF21 and sTGFBR2 has the potential to improve metabolic conditions associated with lipodystrophy.

It is important to note that FGF21 and sTGFBR2 therapies have been tested in mice housed at ~22°C, a temperature comfortable for humans, but which is below the murine thermoneutral zone of ~30°C[27]. Humans typically live within thermoneutral temperatures due to thermostats controlling room temperature, and ease of adjusting warmth with clothing[27]. Mice undergo non-shivering thermogenesis at standard housing temperatures, resulting in elevated energy expenditure, altered metabolic profiles, and increased food intake and physical activity (28, 29). Mice housed at thermoneutrality also have improved immune response, lower heart rate, and decreased bone mineral density[27,30]. Variations in housing temperatures can lead to differences in baseline physiology and treatment efficacies; a previous study found that the degree of weight loss after treatments like GLP-1 and FGF21 in mice varied based on housing

temperatures, and that drug efficacy could not be predicted based on housing temperature[31]. These data underscore the importance of testing preclinical treatments at a variety of housing temperatures to uncover therapeutic effects that might otherwise be missed. In our study, we investigated effects of housing temperatures of 22°C, 26°C, and 30°C with or without gene therapy administration. The intermediate temperature of 26°C was chosen because many universities utilize 26°C housing rooms as an intermediate between ambient temperature and mouse thermoneutrality, and some strains of mice can have a lower thermoneutral point closer to 26°C, with some researchers affirming that 30°C is too warm for mouse studies[32]. Overall, mice prefer to live at environmental temperatures between 26°C and 29°C, even if that is not their physiological thermoneutral point[33].

In the present investigation, our overarching goal was to explore the potential of FGF21/sTGFBR2 gene therapy in improving lipodystrophy-associated metabolic dysfunction. First, to evaluate the best experimental conditions for these studies, we tested effects of three different housing temperatures on efficacy of FGF21/sTGFBR2 gene therapy in obese mice. Then, we evaluated whether FGF21 alone or FGF21/sTGFBR2 combination therapy improved metabolic dysfunction associated with lipodystrophy in an adipocyte-specific *Lmna* knockout mouse model ($Lmna^{ADKO}$)[34]. We were particularly interested in effects of gene therapy on insulin resistance, hepatic steatosis, and bone mass, as these variables have been shown to be altered with FGF21 treatment. In diet-induced obese mice, we found that FGF21/sTGFBR2 had greater improvements to insulin sensitivity and hyperlipidemia at warmer temperatures (i.e. 26°C and 30°C). Furthermore, we found that FGF21/sTGFBR2 gene therapy was dependent on adipose tissue to improve insulin resistance in lipodystrophic mice housed at 30°C, but FGF21 alone improved insulin resistance in lipodystrophic mice at 22°C. FGF21/sTGFBR2 or FGF21 alone was sufficient to reduce hepatic steatosis in lipodystrophic mice, and dual FGF21/sTGFBR2 therapy reduced cortical bone volume fraction. RNA-sequencing revealed that livers of lipodystrophic mice had increased expression of pathways associated with cell proliferation and fibrosis, and that FGF21 increased pathways associated with hepatic mitochondrial metabolism and protein translation. Taken together, these experiments suggest that targeting FGF21 and TGFB1 may have utility for treatment of metabolic dysfunction associated with lipodystrophy, and that murine housing temperature is an important variable to consider when studying therapeutic metabolic endpoints.

3.3 Results

FGF21/sTGFBR2 combination therapy reduces body weight, improves insulin sensitivity, and reduces plasma triacylglycerol (TAG) in HFD-fed mice, with greater effects at 26°C and 30°C than at 22°C.

To investigate impacts of environmental temperature on metabolic effects of FGF21/sTGFBR2 in obese mice, eight-week-old female C57BL/6J mice were housed at 22°C, 26°C, or 30°C, and maintained on a 60% HFD for eight weeks. Mice were then administered vehicle, or AAVs expressing FGF21 and sTGFBR2 (**Figure 3.1 A**). FGF21/sTGFBR2 viral transduction elevated circulating FGF21 and sTGFBR2 for the duration of the experiment for all environmental temperatures (**Figure 3.1 B, C**). Supraphysiological concentrations of FGF21/sTGFBR2 reduced body weights, with greatest effects observed in mice housed at 26°C or 30°C (**Figure 3.1 D-F**). Core body temperature was increased by FGF21/sTGFBR2 therapy in all three housing conditions (**Supplemental Figure 3.1 A-C**). Insulin tolerance tests conducted six weeks after transduction with AAV revealed improved insulin sensitivity across all housing temperatures (**Figure 3.1 G-I**). Furthermore, plasma TAG concentrations were reduced at 26°C and 30°C at four, six (**Supplemental Figure 3.1 D, E**), and eight weeks post-treatment (**Figure 3.1 J**). Daily food intake was reduced in mice housed at higher temperatures, as reported previously (**Supplemental Figure 3.1 F**)[35]. These data indicate that FGF21/sTGFBR2 universally blocks diet-induced obesity; however, because circulating TAG is increased at higher environmental temperatures, improvements to hyperlipidemia with FGF21/sTGFBR2 are more striking at thermoneutrality.

FGF21/sTGFBR2 decreases adiposity, plasma TAG concentrations, and plasma insulin concentrations more effectively at 26°C and 30°C.

Ten weeks of FGF21/sTGFBR2 combination therapy blocked the weight gain observed in vehicle-administered controls, with larger differences observed in mice housed at 26°C or 30°C (**Figure 3.2 A**). Posterior subcutaneous white adipose tissue (psWAT) weight was decreased in transduced mice across all housing temperatures (**Figure 3.2 B**). Brown adipose tissue (BAT) weights were also lower in mice treated with FGF21/sTGFBR2, with substantial changes at 30°C, in part because thermoneutrality increased BAT weight in controls (**Figure 3.2 C**). Due to the decrease in weights of BAT with treatment, we performed histological analyses to

investigate potential changes in BAT whitening. BAT was more whitened in mice housed at warmer temperatures and FGF21/sTGFBR2 restored a BAT-like phenotype with the most improvement at 30°C (**Figure 3.2 D**). FGF21/sTGFBR2 slightly decreased diaphragm, kidney and gastrocnemius weights but did not change weights of other organs including brain, spleen, lungs and heart (**Supplemental Figure 3.2 A-G**). To understand what tissues were most transduced with AAV, we performed a quantitative PCR to recognize a unique AAV DNA sequence in liver, psWAT and BAT. All tissues were transduced with AAV after treatment, but liver had the highest amount of transduction compared to psWAT and BAT, with increased expression at 30°C (**Supplemental Figure 3.2 H**). Differences were not observed in fed plasma glucose concentrations (**Figure 3.2 E**). However, plasma TAG and insulin concentrations were decreased by FGF21/sTGFBR2, particularly at 26°C and 30°C (**Figure 3.2 F, G**). Plasma adiponectin concentrations were not changed by treatment but decreased at higher housing temperatures (**Supplemental Figure 3.2 I, J**). Tibial cortical bone variables were influenced by housing temperature - thermoneutrality increased cortical thickness, area, and perimeter, and decreased cortical bone volume fraction and mineral density (**Figure 3.2 H-J; Supplemental Figure 3.3 A, B**). FGF21/sTGFBR2 increased cortical thickness (**Figure 3.2 H**) and perimeter (**Supplemental Figure 3.3 A**) mostly at 26°C, and cortical area (**Figure 3.2 I**) was elevated at all temperatures, with largest induction by FGF21/sTGFBR2 at 26°C. Whereas trabecular bone parameters were mostly unchanged with treatment, trabecular connectivity density was decreased with FGF21/sTGFBR2 at warmer temperatures (**Supplemental Figure 3.3 C-I**). Taken together, these data suggest that elevated concentrations of FGF21/sTGFBR2 decrease diet-induced adiposity, improve metabolic dysfunction associated with obesity, and increase certain cortical bone variables, particularly when mice are at warmer environmental temperatures.

FGF21/sTGFBR2 decreases liver weights and liver TAG concentrations in HFD-fed mice, with greater effects at 26°C and 30°C.

Elevated circulating concentrations of FGF21/sTGFBR2 reduced liver weights, with greatest effects occurring in mice housed at 26°C or 30°C (**Figure 3.3 A**). Hepatic TAG content increased at warmer temperatures, which made suppression of hepatic lipid by FGF21/sTGFBR2 at 30°C more striking (**Figure 3.3 B**). Furthermore, histology of liver tissue showed an

accumulation of lipid droplets in obese mice, with elevated steatosis observed more at 26°C and 30°C. FGF21/sTGFBR2 treatment partially alleviated effects of HFD as number and size of hepatic lipid droplets were decreased across all temperatures (**Figure 3.3 C**). We observed minimal collagen deposition in obese mice as visualized by Picrosirius Red - this is likely due to an inadequate length of HFD [36]. This collagen deposition was not substantially altered by FGF21/sTGFBR2 (**Figure 3.3 D**). These data suggest that FGF21/sTGFBR2 treatment is more effective in combatting hepatic steatosis in obese mice at higher environmental temperatures.

FGF21/sTGFBR2 requires adipose tissue to increase insulin sensitivity in HFD-fed mice at thermoneutrality.

Obesity and lipodystrophy exhibit overlapping metabolic dysfunctions, including insulin resistance and hepatic steatosis[2,4,5]. To investigate whether metabolic improvements observed in obese mice with FGF21/sTGFBR2 are also observed with lipodystrophy, we studied *Lmna*^{ADKO} lipodystrophic mice in which lamin A/C (*Lmna*) are knocked out of adipocytes. Our previous findings suggest that FGF21/sTGFBR2 treatment is more effective in obese mice at warmer temperatures; thus, for this experiment we housed female control and lipodystrophic mice at thermoneutrality (30°C). We further challenged their metabolic state by feeding a 60% HFD for four weeks. Mice were then administered vehicle or AAVs expressing FGF21 and sTGFBR2 (**Figure 3.4 A**). At 12 weeks after treatment, concentrations of FGF21 and sTGFBR2 were elevated in control and lipodystrophic mice (**Figure 3.4 B, C**). Lipodystrophic mice had an increase in endogenous FGF21 and had a disproportionate increase in plasma FGF21 compared to controls (**Figure 3.4 B**). Body weight, fat mass, and lean mass were decreased 12 weeks after transduction in both genotypes (**Figure 3.4 D-F**). Plasma TAG and glucose concentrations were lowered four weeks after treatment in fasted control and lipodystrophic mice (**Figure 3.4 G, H**). Whereas FGF21/sTGFBR2 increased insulin sensitivity in controls, this dual therapy did not alter insulin sensitivity in lipodystrophic mice (**Figure 3.4 I**). These data indicate that whilst FGF21/sTGFBR2 alters body composition and reduces circulating TAG and glucose similarly in control and lipodystrophic mice, adipose tissue is required for FGF21/sTGFBR2 to improve insulin resistance at thermoneutrality.

FGF21/sTGFBR2 decreases adiposity and partially improves metabolic dysfunction in control and lipodystrophic mice at thermoneutrality.

Mice were euthanized 12 weeks after transduction (**Figure 3.4 A**), and FGF21/sTGFBR2 reduced body weights in control and *Lmna*^{ADKO} mice (**Figure 3.5 A**). Adipose tissue weights in control mice decreased after FGF21/sTGFBR2 treatment (**Figure 3.5 B-D**). Although lipodystrophic mice had exceedingly low amounts of psWAT, parametrial white adipose tissue (pmWAT), and BAT, adiposity was decreased further by FGF21/sTGFBR2 (**Figure 3.5 B-D**). Whereas spleen and heart weights were increased in lipodystrophic mice, FGF21/sTGFBR2 did not alter spleen or heart weights in either genotype (**Figure 3.5 E, F**). Kidney weights were decreased after FGF21/sTGFBR2 therapy (**Supplemental Figure 3.4 A**) but there were no changes in diaphragm or gastrocnemius weights regardless of genotype or treatment although a decrease in brain weight was observed with genotype (**Supplemental Figure 3.4 B-D**). Changes were also not observed with treatment or genotype in hematopoiesis at euthanasia as assessed by circulating populations of red blood cells, white blood cell populations, or platelets (**Supplemental Figure 3.5**). Differences were also not observed in fed plasma glucose concentrations at euthanasia (**Figure 3.5 G**). Plasma TAG concentrations were elevated by lipodystrophy, but FGF21/sTGFBR2 did not decrease TAG concentrations in fed lipodystrophic mice 12 weeks post-treatment (**Figure 3.5 H**). Furthermore, plasma insulin concentrations were also higher in lipodystrophic mice compared to controls in vehicle-treated groups, and FGF21/sTGFBR2 decreased circulating insulin in both genotypes (**Figure 3.5 I**). Lipodystrophic mice had no detectable circulating adiponectin, and FGF21/sTGFBR2 did not alter adiponectin expression in both genotypes (**Supplemental Figure 3.4 E, F**). Similar to the pattern of adiponectin expression, lipodystrophic mice did not have detectable plasma leptin, and the treatment only decreased leptin concentrations in control mice (**Supplemental Figure 3.4 G**). We also analyzed bone variables and found that FGF21/sTGFBR2 did not affect trabecular or cortical characteristics (**Supplemental Figure 6**) except for causing a decrease in trabecular connectivity density (**Supplemental Figure 3.6 E**) and cortical bone volume fraction (**Supplemental Figure 3.6 L**). We next analyzed regulated and constitutive bone marrow adipose tissues (rBMAT, cBMAT, respectively[37]) and observed that rBMAT in the proximal tibia was depleted in lipodystrophic mice compared to controls (**Figure 3.5 J, K**), as observed previously[34]. FGF21/sTGFBR2 decreased volume of rBMAT in obese control mice and the very

low amounts of rBMAT in lipodystrophic mice were not altered further by combination therapy (**Figure 3.5 J, K**). In obese control mice, cBMAT located in the distal tibia was not altered by FGF21/sTGFBR2 therapy (**Figure 3.5 J, L**). In lipodystrophic mice, constitutive BMAT was essentially undetectable by osmium-nanoCT in control and FGF21/sTGFBR2 groups (**Figure 3.5 J, L**). In summary, at thermoneutrality FGF21/sTGFBR2 more effectively improves metabolic parameters in HFD-fed obese mice than in HFD-fed mice with lipodystrophy, and FGF21/sTGFBR2 decreases quantity of rBMAT only in mice with diet-induced obesity.

FGF21/sTGFBR2 treatment reduces liver weight, total hepatic TAG amount, and liver collagen deposition in lipodystrophic mice housed at 30°C.

Lmna^{ADKO} mice had greater liver weights than control mice regardless of treatment, but FGF21/sTGFBR2 reduced liver weights in both control and *Lmna*^{ADKO} mice (**Figure 3.6 A**). Hepatic TAG content was significantly elevated in lipodystrophic mice relative to controls (**Figure 3.6 B**). However, transduction with FGF21/sTGFBR2 did not reduce TAG amount normalized to protein content in either genotype (**Figure 3.6 B**). Notably, a reduction in total hepatic TAG content after normalization to liver weight was observed in control and lipodystrophic mice at 30°C (**Figure 3.6 C**). Histology of liver tissue showed a decrease in the number of lipid droplets with FGF21/sTGFBR2 treatment in control mice but not in lipodystrophic mice (**Figure 3.6 D**). Furthermore, liver collagen deposition, visualized by Picrosirius Red staining, was higher in lipodystrophic mice, and this hepatic fibrosis was visually and quantitatively reduced following transduction with FGF21/sTGFBR2 in both genotypes (**Figure 3.6 E, F**). In summary, FGF21/sTGFBR2 reduced liver weights, hepatic TAG amount and liver fibrosis in lipodystrophic mice housed at 30°C.

FGF21 improves insulin sensitivity of lipodystrophic mice housed at 22°C.

Previous studies have tested multiple therapeutic combinations with FGF21 or just FGF21 alone, and have found that FGF21 alone is sufficient to improve insulin sensitivity and reduce obesity in HFD-fed mice[23]. We were particularly interested in effects of FGF21 alone because multiple studies reported that FGF21 alone as a gene therapy slows aging-related functional decline and improves metabolic dysfunction, and is safe in larger animals, including dogs and non-human primates[22,38,39]. In lipodystrophic mice housed at 30°C, FGF21/sTGFBR2

decreased body weight and liver TAG, but did not improve insulin sensitivity. To determine if insulin sensitivity of *Lmna*^{ADKO} mice is influenced by FGF21 treatment at standard environmental temperature, we housed control and lipodystrophic mice at 22°C and fed them a HFD for four weeks before FGF21 administration (**Figure 3.7 A**). Similar to our previous findings at 30°C, lipodystrophic *Lmna*^{ADKO} mice had higher circulating concentrations of endogenous FGF21 at 22°C and a disproportionate increase in plasma FGF21 after transduction compared to controls (**Figure 3.7 B**). Whereas lipodystrophic mice had reduced body weight and fat mass at 22°C, elevated concentrations of FGF21 did not decrease body weight or fat mass further in these mice (**Figure 3. 7 C, D**). However, lean mass was decreased in control and lipodystrophic mice after FGF21 administration (**Figure 3.7 E**). Glucose and insulin tolerance tests conducted seven to eight weeks after transduction with FGF21 revealed improved glucose and insulin sensitivity in control and *Lmna*^{ADKO} mice at 22°C (**Figure 3.7 F, G**). To investigate whether FGF21 influences energy expenditure in lipodystrophic mice, we performed indirect calorimetry on a subset of *Lmna*^{ADKO} mice. FGF21 treatment in lipodystrophic mice did not alter energy expenditure, fat oxidation, and distance traveled during light and dark cycles (**Figure 3.7 H-J**). These data suggest that adipose tissue is not required for FGF21 to improve insulin sensitivity in mice housed at 22°C.

FGF21 does not improve hyperlipidemia or hyperinsulinemia of lipodystrophic mice housed at 22°C.

Mice from Figure 7 were analyzed after euthanasia. Eight weeks after FGF21 transduction at 22°C reduced body weights but not weights of psWAT, pmWAT, retroperitoneal WAT (rpWAT) or perirenal WAT (prWAT) in control or lipodystrophic mice (**Figure 3.8 A-C; Supplemental Figure 3.7 A, B**). As expected, all these variables including BAT were reduced in *Lmna*^{ADKO} mice regardless of treatment. Although FGF21 reduced BAT weights in controls, treatment had little effect on BAT in lipodystrophic mice (**Figure 3.8 D**). Although lipodystrophic mice had greater spleen and heart weights and smaller tibia lengths than controls, there were no changes in weights of heart, kidney, diaphragm, lungs, brain, spleen or tibia lengths after FGF21 treatment regardless of genotype (**Figure 3.8 E; Supplemental Figure 3.7 C-H**). Circulating TAG and insulin concentrations were elevated in *Lmna*^{ADKO} mice, but FGF21 did not alter concentrations of glucose, TAG or insulin in control or *Lmna*^{ADKO} mice at 22°C

(**Figure 3.8 F-H**). Both adiponectin and leptin were undetectable in lipodystrophic mice, and the treatment did not affect amounts of either adipokine regardless of genotype (**Figure 3.8 I; Supplemental Figure 3.7 I, J**). Taken together, these data suggest that FGF21 does not alter adiposity or improve metabolic dysfunction of lipodystrophic mice housed at 22°C.

FGF21 treatment alone reduces liver weight, total hepatic TAG, and liver collagen deposition in lipodystrophic mice housed at 22°C.

Lmna^{ADKO} mice had greater liver weights than control mice, and FGF21 administration reduced liver weights in control and *Lmna*^{ADKO} mice when housed at 22°C (**Figure 3.9 A**). Hepatic TAG content was higher in lipodystrophic mice than controls, but it was not reduced by FGF21 transduction (**Figure 3.9 B**). Similar to our experiment at 30°C, a decrease in total hepatic TAG was observed in lipodystrophic mice at 22°C when normalized to total liver weight (**Figure 3.9 C**). Histology of liver tissue showed that number and size of lipid droplets were substantially greater in lipodystrophic mice compared to controls (**Figure 3.9 D**). However, FGF21 did not visually reduce lipid droplet accumulation in controls and lipodystrophic mice (**Figure 3.9 D**). Liver collagen stained by Picrosirius Red was higher in lipodystrophic mice than control mice at 22°C, and this hepatic fibrosis was reduced visually and quantitatively by FGF21 treatment (**Figure 3.9 E, F**). These data suggest that, as observed in Figure 6 for dual treatment at 30°C, FGF21 administration reduces liver weights, hepatic TAG amount, and collagen deposition in lipodystrophic mice housed at 22°C.

Bulk RNA-sequencing analyses of livers reveal that FGF21 decreases hepatic cell proliferation and fibrosis in lipodystrophic mice housed at 22°C.

To investigate hepatic molecular changes that occur with lipodystrophy and FGF21 treatment, bulk RNA-sequencing analyses were performed, and data were analyzed using Gene Set Enrichment Analysis (GSEA) to identify transcriptomic patterns (**Figure 3.10 A**). First, we were interested in how lipodystrophy affects the hepatic transcriptome. Lipodystrophic mouse livers had upregulation of cell proliferation and fibrosis, with increased regulation of the G2M checkpoint, spindle assembly, DNA replication, and fibroblast proliferation (**Figure 3.10 B, C**). In addition to increased hepatic steatosis, this signature may partially explain the large increase in liver weights at baseline in lipodystrophic mice. Furthermore, cholesterol homeostasis and

sterol biosynthesis were increased, supporting the observed increased hepatic steatosis. Immune response was mixed in lipodystrophic mice compared to controls when treated with vehicle: interferon alpha and beta responses were downregulated, but macrophage migration and TNFα signaling were increased. Protein translation was also downregulated in lipodystrophic mice regardless of treatment.

Next, the impact of FGF21 was examined. FGF21 transduction led to an upregulation of immune response pathways, such as increased leukocyte migration in control mice and enhanced interferon alpha and gamma responses in *Lmna*^{ADKO} mice (**Figure 3.10 D, E**). Mitochondrial activity was also upregulated in both genotypes after FGF21 treatment, as evidenced by increased expression in gene sets related to oxidative phosphorylation, the electron transport chain, and mitochondrial translation (**Figure 3.10 D, E**). Additionally, FGF21 promoted protein translation and metabolic processes in livers of control and lipodystrophic mice, including amino acid metabolism and sterol biosynthesis (**Figure 3.10 D, E**). Several pathways were downregulated following FGF21 transduction in control mice, including Notch signaling and organelle assembly (**Figure 3.10 D**). In contrast, in lipodystrophic mice, FGF21 transduction led to downregulation of cell proliferation and fibrosis, with a decrease in the regulation of G2M checkpoint, mitotic spindle, DNA replication, and E2F target pathways (**Figure 3.10 E**). In summary, FGF21 treatment increases hepatic immune response, mitochondrial activity, and lipid metabolism across genotypes. The reduction by FGF21 of liver weights and fibrosis in lipodystrophic mice can be explained, in part, by decreased cell proliferation and fibrosis pathways.

3.4 Discussion

Given the unmet clinical need for patients with *LMNA*-induced lipodystrophy, we designed this study to explore the impact of a novel treatment using viral mediated delivery of FGF21 and sTGFBR2 in a preclinical model of *LMNA*-induced lipodystrophy created in our lab. To understand the impact of this novel therapy, we also simultaneously treated obese mice. Both the obesity and lipodystrophy groups were housed at different environmental temperatures to ensure that metabolic dysfunction was uncovered in both disease states. First, we found that in HFD-induced obesity, warmer environmental housing temperatures improved effectiveness of FGF21/sTGFBR2 in decreasing body weight, improving insulin resistance, reducing plasma TAG, and decreasing hepatic steatosis. Part of this greater efficacy at warmer housing temperatures was due to elevated baseline metabolic dysfunction in mice housed at 26°C and 30°C, as reflected in body weight, circulating TAG, and liver TAG in vehicle-treated mice. This finding is consistent with previous literature showing decreased energy expenditure, and increased weight gain, glucose intolerance, and hyperlipidemia in mice housed at 30°C[27,40,41]. FGF21 administration to HFD-induced obese mice caused similar decreases in weight loss at 22°C and 30°C[31]. This study[31] differed in design from ours in that we used female mice rather than male, and we used an AAV to continuously deliver mouse FGF21/sTGFBR2, whereas they used human FGF21 administered twice-daily subcutaneously for three weeks. The previous study[31] did find that FGF21-treated mice housed at 22°C had higher energy expenditure than mice housed at 30°C, which we did not explore in our study. Although prior work suggested effects of human FGF21 on mice were independent of environmental temperature[31], our results suggest that with FGF21/sTGFBR2 administration to obese mice, housing temperatures of 26°C or 30°C may be better than 22°C to detect metabolic effects and to mimic human thermoneutral conditions.

We also characterized on HFD-fed lipodystrophic mice the effects of FGF21/sTGFBR2 combination therapy at 30°C, or FGF21 alone at 22°C. Gene therapy did not restore normal adipose tissue function in lipodystrophic mice as measured by adiponectin and leptin secretion in circulation, perhaps due to the exceedingly low remaining adipocyte amount. We observed that FGF21/sTGFBR2 treatment in control and lipodystrophic *Lmna*^{ADKO} mice housed at thermoneutrality reduced circulating TAG and glucose four weeks post-transduction but did not improve insulin resistance in lipodystrophic mice. However, FGF21 administration alone at 22°C

did improve insulin resistance in *Lmna*^{ADKO} mice, but not other metabolic parameters, suggesting that FGF21 potentially interacts with non-shivering thermogenesis mechanisms to improve insulin sensitivity in these mice[42]. The interplay between temperature and BAT may explain why metabolic improvements are observed under certain conditions. In our studies of obese mice, we saw that FGF21/sTGFBR2 treatment restored a BAT-like phenotype at warmer temperatures, which is a likely contributor to the observed metabolic improvements. However, lipodystrophic mice have reduced BAT, and we only see an improvement in metabolism in treated lipodystrophic mice housed at 22°C, highlighting the possibility of functional BAT, or thermogenic WAT in lipodystrophic mice housed at 22°C vs. 30°C. Support for this idea comes from investigation of global *Bscl2* (seipin) knockout mice. In this model of lipodystrophy, an FGF21 analog, LY2405319, improved insulin sensitivity in young mice housed at 22°C[25]. In contrast, but similar to our findings at 30°C, adipose tissue was required for FGF21 to reduce circulating insulin concentrations in aP2-nSREBP1c lipodystrophic mice fed a normal chow diet, which was proposed to result from impaired FGF21 signaling in lipodystrophic adipose tissue [24]. This study differed from ours in a number of respects. In addition to the genetic modification causing the lipodystrophy, *nSREBP1c* overexpression versus *Lmna*-deficiency, aP2 (i.e. *Fabp4*) drives *Cre* expression more broadly than *Adipoq*, including in adipose tissue macrophages[43], providing one possible reason that the phenotype of aP2-nSREBP1c mice is more extreme than *Lmna*^{ADKO} mice[44]. Expression of nuclear SREBP1c from the aP2 locus caused perinatal distension of the abdomen, interscapular humps, and impaired growth, with some pups dying prior to weaning. As adults, the mice have severe hepatic steatosis and hyperinsulinemia[44]. Another factor that may have influenced differences between studies is background mouse strain. aP2-nSREBP1c mice are on a FVB background[45], which have ~60 genetic variants that directly affect protein structure or mRNA stability, and provide resistance to diet-induced obesity, whereas *Lmna*^{ADKO} mice are on a C57Bl/6J background, which also has genetic variants that affect protein function but which increase susceptibility to diet-induced obesity[46,47]. These studies suggest that in addition to environmental temperature, other variables including the genetic basis for lipodystrophy, background strain, and diet may influence metabolic benefits of FGF21.

The necessity for functional adipose tissue to mediate effects of FGF21 are also illustrated by observations that insulin sensitivity did not improve after FGF21 administration in HFD-

induced obese mice with an adipocyte-specific knockout of the coreceptor for FGF signaling, β-Klotho[48]. This raises the possibility that *Lmna*^{ADKO} lipodystrophic mice, when housed at 30°C, could have a defect in FGF21 signaling in adipose tissue, which may explain the increased insulin sensitivity. FGF21 signaling in non-adipose organs may also contribute to improvements in insulin sensitivity in lipodystrophic mice at 22°C, especially signaling in liver and muscle. Consistent with this notion, expression of *Fgfr2* and *Fgfr4* is decreased in vehicle-treated *Lmna*^{ADKO} livers relative to controls, suggestive of a FGF21 signaling defect. Our study does differ from previous studies of FGF21 in lipodystrophy in that 1) AAV gene therapy was used to administer FGF21, 2) our model of lipodystrophy used an *Adipoq*-Cre driver to knock out *Lmna,* which is expressed specifically in adipocytes and marrow adipogenic lineage progenitors[49], 3) *Lmna*^{ADKO} mice were on a C57BL/6J background whereas aP2-nSREBP1c were on a FVB background, 4) *Lmna*^{ADKO} mice were on a HFD, and 5) we investigated effects at 22°C and 30°C housing temperatures. Taken together, in our model of *Lmna*^{ADKO} lipodystrophy, adipose tissue is required to mediate metabolic improvements after FGF21 administration at housing temperatures of 30°C, but not 22°C, which adds to the complex and at times contradictory literature on metabolic improvements with FGF21 treatment of preclinical models of lipodystrophy.

We observed widespread transcriptomic changes in response to lipodystrophy in this study, with 1953 differentially-expressed genes between vehicle-treated lipodystrophic and control livers, and 888 genes that differed between FGF21-treated lipodystrophic and control livers. Livers from lipodystrophic mice had increased GSEA pathway expression related to cell proliferation and fibrosis, and decreased protein translation, and multiple changes in opposing directions related to immune response and metabolism. To our knowledge, this is the first RNA-seq dataset to profile differences in the liver transcriptome in a mouse model of partial lipodystrophy, in which effects on the liver are likely secondary to metabolic dysfunction resulting from loss of adipose tissue. Interestingly, FGF21 had minor effects on hepatic gene expression, with 42 differentially-expressed genes between FGF21 and vehicle control livers, and only five genes differentially-expressed between FGF21 and vehicle lipodystrophic livers. When analyzed with GSEA, FGF21 treatment increased sterol biosynthesis, cholesterol homeostasis, and triacylglycerol metabolism pathways, which was similar to previously published hepatic RNA sequencing of acute FGF21 treatment in diet-induced obese mice [50]. Transcriptomic analyses of adipose tissue after FGF21 treatment in non-human primates also had similar changes to our hepatic RNA-seq dataset,

including increased oxidative phosphorylation, mitochondria, and lipid synthesis pathways[38]. FGF21 is known to induce hepatic expression of PGC1α and its downstream genes, which aligns with our observed increase in mitochondrial gene expression[51]. Future investigations of how FGF21 alters fibrosis, protein translation, and cell proliferation in lipodystrophic and control livers could explain the observed decrease in liver size but not hepatic steatosis.

The effects of FGF21 on bone mass and BMAT have been controversial. Early reports suggested that elevated FGF21 as a result of transgenesis, AAV delivery, or injection of recombinant protein in male mice all resulted in loss of bone mass and bone mineral density and increased BMAT, with elevated bone and decreased BMAT observed in *Fgf21* knockout mice[52,53]. Subsequent investigation, however, found that in male diet-induced obese mice, human FGF21 administration did not affect bone loss or BMAT, similar to our results with FGF21/sTGFBR2 combination therapy for trabecular and cortical bone in HFD-fed mice at 22°C[54]. Human FGF21 also did not change bone mass in obese non-human primates[55]. An aging study from the Scherer lab with overexpression of FGF21 from adipocytes found that 1.7 years of elevated circulating FGF21 did not influence bone characteristics such as tibial length, or trabecular and cortical bone mineral density[39].

In our experiments, FGF21/sTGFBR2 administration increased cortical area and thickness only at warmer housing temperatures. We also observed a depletion of tibial rBMAT and cBMAT in HFD-fed *Lmna*^{ADKO} mice housed at 30°C, but did not see changes in bone mass, contrary to the mild increase in cortical bone observed previously in female lipodystrophic *Lmna*^{ADKO} mice at 22°C[34]. In contrast, loss of marrow adiposity due to expression of diphtheria antigen increased trabecular and cortical bone mass in both sexes[56]. Taken together, these data suggest that the mechanism of BMAT loss, in addition to diet and housing temperature, greatly influences whether bone mass is altered. Furthermore, we found that in female diet-induced obese mice housed at 30°C, FGF21/sTGFBR2 treatment decreased amount of tibial rBMAT, contrary to previous findings that showed no change in femoral rBMAT with FGF21 treatment in male diet-induced obese mice at 22°C[54]. Therefore, effects of FGF21 treatment on BMAT are at least partially dependent on housing temperature of mice, and could be further confounded by rBMAT location, sex of mice, and HFD duration.

We administered lipodystrophic mice with a dual FGF21/sTGFBR2 treatment, or with FGF21 alone. Differential improvements in insulin sensitivity and lipid metabolism were likely

due to the two housing temperatures evaluated, since room temperature (22°C) versus thermoneutrality (30°C) is known to have a profound effect on the transcriptome of adipose and other tissues[57]. FGF21 likely mediates most of the metabolic effects observed due to its known role in liver, adipose, and metabolic homeostasis; FGF21 alone vs. dual FGF21/sTGFBR2 cause the same degree of weight loss in obese mice[23]. However, the added effect of sTGFBR2 cannot be ignored, especially in targeting liver fibrosis in lipodystrophy and in stopping progression of heart failure[23]. Future investigations are required to confirm whether sTGFBR2 contributes substantially to improvements to metabolic dysfunction and hepatic steatosis in lipodystrophic mice at different housing temperatures. Another group used a dual gene therapy of human adiponectin and leptin in *ob/ob* mice, which improved metabolic dysfunction, highlighting the potential of this therapeutic approach[58]. Furthermore, the McIlroy and Rochford groups have restored human BSCL2 expression in global *Bscl2* KO mice via AAV, which improved lipodystrophy-associated metabolic issues, an exciting application of gene therapy in lipodystrophy[59,60].

A limitation of our study is that we only used female mice in our models of obesity and lipodystrophy. It has been shown that effects of FGF21 on energy balance, liver TAG, signaling in WAT, and adiponectin secretion in diet-induced obese mice are sex dependent[50]. Thus, future studies are necessary to determine whether FGF21 alone or dual FGF21/sTGFBR2 have different metabolic improvement effects in lipodystrophic male mice. Another limitation is that the utilized lipodystrophic mouse model is a genetic knockout model rather than a missense variant model, which is the genetic basis of disease in patients with lipodystrophy. In conclusion, this study demonstrated that 1) FGF21/sTGFBR2 dual treatment improves metabolic dysfunction more at warmer housing temperatures, 2) FGF21/sTGFBR2 slightly improves metabolic dysfunction in lipodystrophic mice housed at 30°C but not insulin resistance, and 3) FGF21 alone improves metabolic dysfunction in lipodystrophic *Lmna*^{ADKO} mice housed at 22°C and decreases liver weight and fibrosis through effects on the hepatic transcriptome. This investigation contributes to our understanding of gene therapy for obesity and lipodystrophy, and it highlights the importance of environmental housing temperature in determining treatment efficacy in preclinical models of metabolic disease.

3.5 Materials and methods

Sex as a biological variable

All mice used in this study were females. Lipodystrophy is more commonly diagnosed in females, and the lipodystrophic mice used in this study have a more severe metabolic phenotype in females[34]. Other mouse models of lipodystrophy also have a sexual dimorphic effect on metabolic dysfunction, with both AZIP mice and global *Bscl2* KO female mice having worsened metabolic parameters compared to males[61,62]. It is unknown whether lipodystrophic male mice would have the same effects of FGF21 or FGF21/sTGFBR2 treatment at different environmental temperatures, which is a limitation of this study, and should be evaluated in the future. It has been previously shown that obese male mice benefit metabolically from FGF21/sTGFBR2 administration at a housing temperature of 22°C.

Animals

C57BL/6J (000664) and *Adipoq*-Cre mice (028020) mice were from the Jackson Laboratory. *Lmna*$^{FL/FL}$ mice had loxP sites flanking exons 10 and 11 of the *Lmna* allele[63]. Animals described as control were *Lmna*$^{Fl/Fl}$ *Adipoq*-Cre^{-} and *Lmna*^{ADKO} were *Lmna*$^{Fl/Fl}$ *Adipoq*-Cre^{+}. Control and *Lmna*^{ADKO} mice were 12-14 weeks old at the start of experiments. C57BL/6J mice were 8 weeks old at the start of experiments. Female mice were analyzed throughout these studies. Mice were euthanized by inhaled isoflurane overdose and death was assured via cervical dislocation or bilateral pneumothorax, and adipose depots were dissected as previously described[64]. Animals were group housed at 22°C, 26°C, and 30°C at a relative humidity of 30-50% with a 12-hr light:dark cycle and free access to water and food. Mice were fed *ad libitum* 60% high fat diet (D12492, Research Diets) and food was changed twice per week. Temperature sensors were implanted intraperitoneally, and core body temperatures measured with an external scanner. Fat and lean mass was measured in live animals with an EchoMRI-100H (EchoMRI LLC). Daily care of mice was overseen by the Unit for Laboratory Animal Medicine at the University of Michigan.

AAV administration

AAV8 vectors were synthesized as previously described, with mouse versions of FGF21 and sTGFBR2 expressed[23]. AAV-FGF21/sTGFBR2 or vehicle (PBS pH 7.4 + 0.001% F-68 Pluronic) were delivered via retroorbital injections. In the temperature efficacy experiments, mice were dosed at 5 X 10^{11} vg per mouse in 50 µL; in the lipodystrophy experiments, mice were dosed at the same concentration but in 100 µL to reduce technical error. All mice were randomized based on weight for each experiment.

Glucose and insulin tolerance tests

For glucose tolerance tests, mice were fasted overnight (12-16 hours) and administered an intraperitoneal injection of glucose in water (1 mg/kg body weight). For insulin tolerance tests, mice were fasted 4 hours and administered an intraperitoneal injection of insulin in saline (0.75 U insulin/kg body weight; Eli Lilly). Blood was collected from the tail vein, and glucose concentrations were monitored using a glucometer and Contour Next blood glucose strips (Bayer AG).

Serum measurements

Blood was collected from tail vein or at euthanasia via inferior vena cava and was allowed to coagulate on ice for 2 hours. Mice were fasted at bleeds for four hours unless otherwise stated in the figure legend. After centrifugation at 2000 x g for 20 minutes at 4°C, serum was collected and stored at -80°C. ELISA was used to measure circulating concentrations of leptin (900-K76K, Invitrogen), insulin (90080, Crystal Chem), murine FGF21 (MF2100, R&D), and murine sTGFBR2 (ab277719, Abcam). TAG were measured via colorimetric assay (10010303, Cayman Chemical). Serum adiponectin was measured via immunoblot.

Complete blood count

Blood was collected at euthanasia and stored in EDTA-coated tubes. Blood was analyzed by University of Michigan's Unit for Laboratory Animal Medicine Pathology Core using a Heska Element HT5 Veterinary Hematology Analyzer.

Liver TAG

Liver TAG was measured via colorimetric assay according to manufacturer protocol (10010303, Cayman Chemical). Briefly, liver pieces were weighed and minced into small pieces on ice. Minced tissue was homogenized in 2 mL of NP40 substitute assay reagent containing protease inhibitors, centrifuged at 10,000 x g for 10 minutes at 4°C, and supernatant was transferred to another tube. Samples were then loaded into a 96-well plate along with TAG standards and an enzyme mixture to result in a coupled enzymatic reaction system to measure glycerol, which was measured at 530-550 nm using a plate reader. For normalization, protein concentrations were determined from liver supernatants via bicinchoninic acid assay (23225, Thermo Scientific).

Mouse liver and BAT histology

After collection, tissues were fixed for 72 hours in 10% neutral-buffered formalin at 4°C. Tissues were rinsed with PBS and dehydrated in a graded series of ethanol washes, processed, paraffin-embedded through the University of Michigan Orthopedic Research Laboratory Histology Core facility, and sectioned at 5 μm thickness. Sections were stained with hematoxylin and eosin as previously described [65] or with Picrosirius Red according to manufacturer protocol (24901, Polysciences). Sections were imaged using an inverted Zeiss microscope with a 20x objective.

Picrosirius Red quantification

Picrosirius Red-stained liver sections were analyzed using the Aivia AI-based image analysis software (Leica Microsystems, Inc.). With the guidance of the Michigan Diabetes Research Center Microscopy and Image Analysis Core, Pixel Classifier profiles in Aivia were trained to segment collagen fibers from normal liver tissue. Once the pixel training was optimal, area of Picrosirius-positive staining were quantified from the images with Aivia's Recipe Console tool. At least three sections per mouse were counted and averaged.

Quantitative PCR for AAV transduction

DNA was isolated from psWAT, BAT, and liver using the Qiagen Puregene Kit (158026). DNA concentrations were normalized to 30 ng/μL, and primers targeting the WPRE (FW: 5'-CTTCCCGTATGGCTTTCATTTT-3', RV: 5'-GCCGTGGCAAGAACTAACCA-3') were used to amplify DNA with qPCRBIO SyGreen Mix (Innovative Solutions), detected with a StepOnePlus System (Applied Biosystems). All primers were validated with DNA titration

curves prior to use; qPCR product specificities were confirmed by melting curve analysis. Gene expression was calculated using a DNA titration curve within each plate and normalized to reference gene *Hprt* (FW: 5'-TCATTATGCCGAGGATTTGGA-3', RV: 5'-GCACACAGAGGGCCACAAT-3') and calculated as change relative to control samples.

Liver RNA-sequencing

Mouse livers were powdered at -80°C on dry ice and 50 mg was homogenized in 1 mL RNA STAT-60 (CS110, AMSBIO) on ice. Samples were spun at 12000 x g for 10 minutes at 4°C to pellet tissue debris. The clear supernatant was pipetted into a new tube, and 200 μL of chloroform was added to the tube, and inverted. The samples were spun at 12000 x g for 10 minutes at 4°C, and the aqueous supernatant was moved to a new tube. Isopropanol was added in equal volume to precipitate RNA overnight at -20°C. Tubes were spun at 12000 x g for 10 minutes at 4°C to isolate precipitated RNA, and supernatant was removed. RNA pellet was washed with 75% ethanol 3 times. After a final spin at 12000 x g for 10 minutes at 4°C, the ethanol wash was removed, and the RNA pellet was air-dried for 3 minutes. RNA was resuspended in DEPC-treated water and quantified via Nanodrop spectrophotometer.

Samples were sequenced by the University of Michigan Advanced Genomics Core, with libraries constructed and subsequently subjected to 150 paired-end cycles on the NovaSeq-6000 platform (Illumina). Data were pre-filtered to remove genes with 0 counts in all samples. Differential gene expression analysis was performed using DESeq2[66], using a negative binomial generalized linear model (thresholds: linear fold change >1.5 or <-1.5, Benjamini-Hochberg FDR (Padj) <0.05). Annotation data from ENSEMBL 102 was used, and genes were additionally annotated with Entrez GeneIDs and text descriptions. Functional analysis, including candidate pathways activated or inhibited in comparison(s) and GO-term enrichments [67], was performed using GSEA[68].

Bone static histomorphometry

Tibias of 7-month-old female and male mice were dissected and fixed in 10% formalin (Thermo Fisher Scientific) for 24 hours at 4°C, dehydrated with graded concentrations of ethanol, and processed for nanoCT scanning. For tibial trabecular parameters, a region of interest (ROI) was

defined starting at 0.75 mm proximal to the growth plate of femurs and extending 2 mm in the direction of the diaphysis where trabeculae were no longer visible. For tibial cortical parameters, ROI was defined starting at 0.25 mm above the tibia/fibula junction landmark. A region of 0.5 mm in height at midshaft was analyzed.). The data analysis and images were generated using Dragonfly software (3D), version 2024 (Comet Technologies Canada Inc., Montreal, Canada).

Bone marrow adipose tissue quantification by osmium staining

Tibias of 7-month-old female mice were stained with osmium tetroxide for marrow fat analysis as previously described[69]. Intact tibias were fixed in 10% formalin for 24 hours at 4°C (Thermo Fisher Scientific) and processed for decalcification in 14% EDTA, pH 7.4, for 14 days. Samples were then transferred to Sorensen's phosphate buffer pH (7.2) in 1.5 mL microtubes. All subsequent steps were performed in the fume hood. Tibias were stained in 1% osmium tetroxide solution (Electron Microscopy Services, Hatfield, PA, USA) and incubated for 48 hours at RT on a rotating wheel. Stained tibias were then washed with Sorensen's buffer twice for 3 hours and then overnight. Stained tibias were embedded in 1% agarose and processed for scanning. Quantification of marrow adipose tissue volume included the ROIs starting at the growth plate to the tibia/fibula junction (proximal) and tibia/fibula junction to the distal end of the bone (distal). The data analysis and images were generated using Dragonfly software (3D), version 2024 (Comet Technologies Canada Inc., Montreal, Canada).

NanoCT analysis

For nanoCT, tibias were immobilized inside a plastic fixture and scanned using a nanotom M nanoCT (Phoenix x-ray, Waygate Technologies USA, LP; Skaneateles, New York). The X-ray tube was powered to 80 kV and 400 µA, utilized a diamond coated tungsten target, a 0.381mm Aluminum filter, and was set to a spot size of 0. Imaging was done at either 10 µm or 8 µm voxel size using an exposure time of 500 ms; 3 frames averaged and 1 skipped for each rotation. The sample stage rotated through 360 degrees and collected 1000 images per scan. Image acquisition and reconstruction of raw data were performed using Datos|x 2 version 2.6.1 (Phoenix x-ray, Waygate Technologies USA, LP; Skaneateles, New York).

Indirect calorimetry

Mice were housed individually and continuously fed a 60% HFD for three days, and then the mice were placed into an indirect calorimetry system (Promethion Core, Sable Systems International), and their O_2 consumption and CO_2 production, in-cage activities, food and water intake were measured at room temperature (22°C, 41% humidity) for three days (12-12 hours 5:00PM~5:00AM) dark-light cycles). All animals were continuously maintained on the 60% HFD diet throughout the experiment and had free access to food and water. Oxygen consumption (VO_2), carbon dioxide production (VCO_2), spontaneous motor activity was measured using the Promethion System, an integrated open-circuit calorimeter equipped with an optical beam activity monitoring device. The Promethion system features high precision sensors measuring food, water intake & body weight in real time. The system was routinely calibrated each time before the experiment using a standard gas (20.5% O_2 and 0.5% CO_2 in N_2). VO_2 and VCO_2 in each cage were sampled sequentially for 30 seconds in five-minute intervals and the motor activity was recorded every second in X, Y, and Z dimensions. The air flow rate through the chambers was adjusted at the level to keep the oxygen differential around 0.3% at resting conditions. Respiratory exchange ratio (RER) was calculated as VCO_2 / VO_2. Total energy expenditure, carbohydrate oxidation, and fatty acid oxidation were calculated respectively based on the values of VO_2, VCO_2, without the estimation of protein breakdown (which is usually estimated from urinary nitrogen excretion)[70–76].

Statistics

All data was presented as mean ± SD unless noted in the figure legend. Two-way ANOVA with Bonferroni's post-hoc test was performed for all data presented in the study. All analyses were conducted using GraphPad Prism version 10. For statistical comparisons, $p < 0.05$ was considered significant.

Study approval

All animal studies were performed in compliance with policies of the University of Michigan Institutional Animal Care and Use Committee (Protocol PRO00011544).

Data availability

Liver RNA-sequencing data are available through NCBI GEO with accession no. GSE294358.

3.6 Figures and legends

Figure 3.1

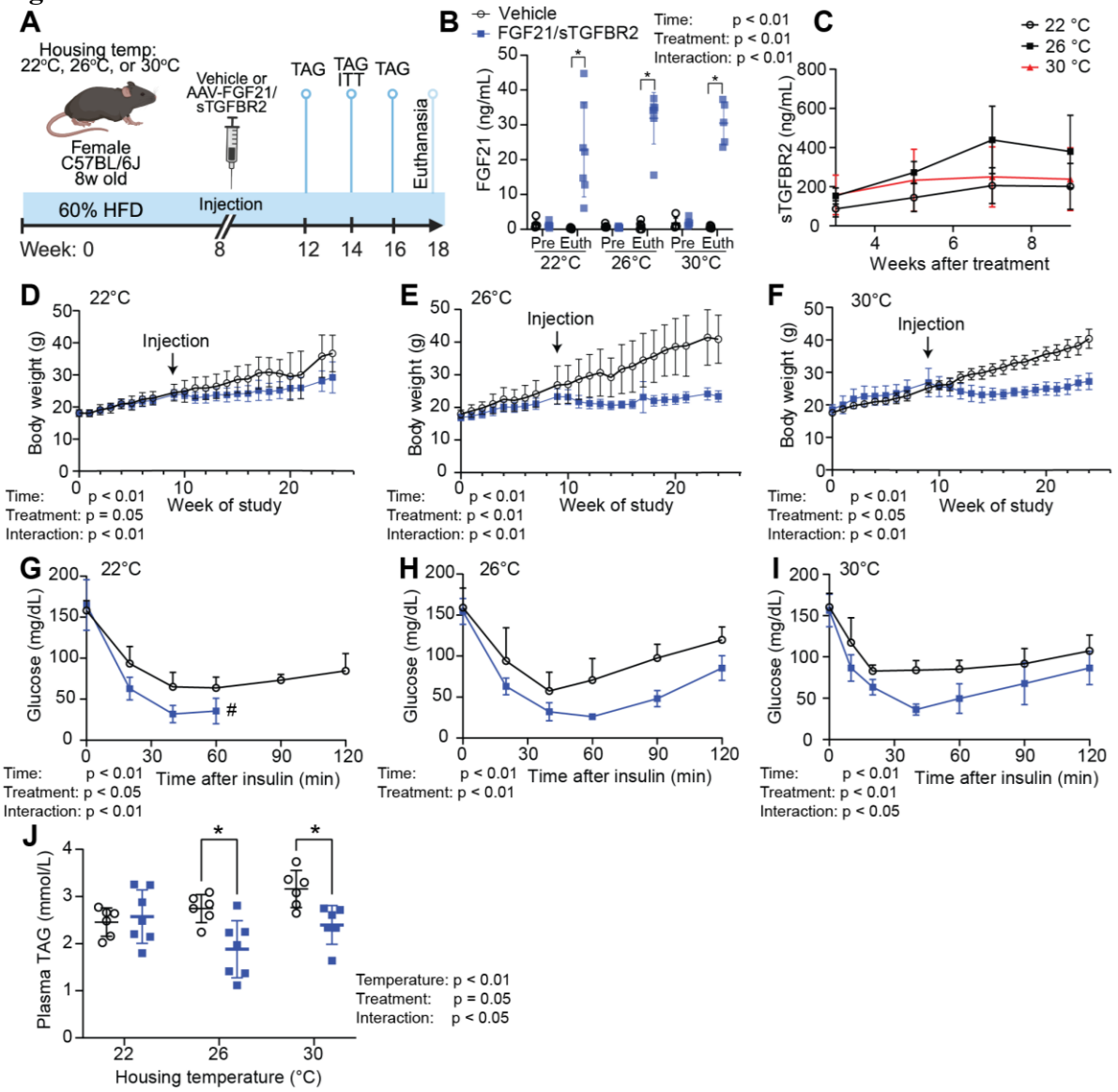


Figure 3.1. FGF21/sTGFBR2 reduces body weight, improves insulin sensitivity, and reduces plasma TAG in high fat diet-fed mice, with greatest effects in mice housed at 26°C and 30°C. (**A**) Schematic illustration of housing conditions and experimental timeline. (**B**) Concentrations of FGF21 in plasma pre-transduction (Pre) and at euthanasia (Euth). (**C**) Concentrations of sTGFBR2 in plasma 3, 5, 7, and 9 weeks after transduction. Body weight over time in 60% HFD-fed female mice housed at (**D**) 22°C, (**E**) 26°C, or (**F**) 30°C (n = 6-7). Insulin tolerance tests (0.75 U/kg) in mice housed at (**G**) 22°C, (**H**) 26°C, or (**I**) 30°C (n = 6-7), data presented as mean ± SEM. #Mice in (E) were given intraperitoneal glucose because their blood glucose concentrations dropped below 30 mg/dL. (**J**) Plasma TAG concentrations eight weeks post-treatment in mice housed at 22°C, 26°C, or 30°C (n = 6-7). *P < 0.05. Statistical analyses were performed using two-way ANOVA, followed by Bonferroni's post-hoc test.

Figure 3.2

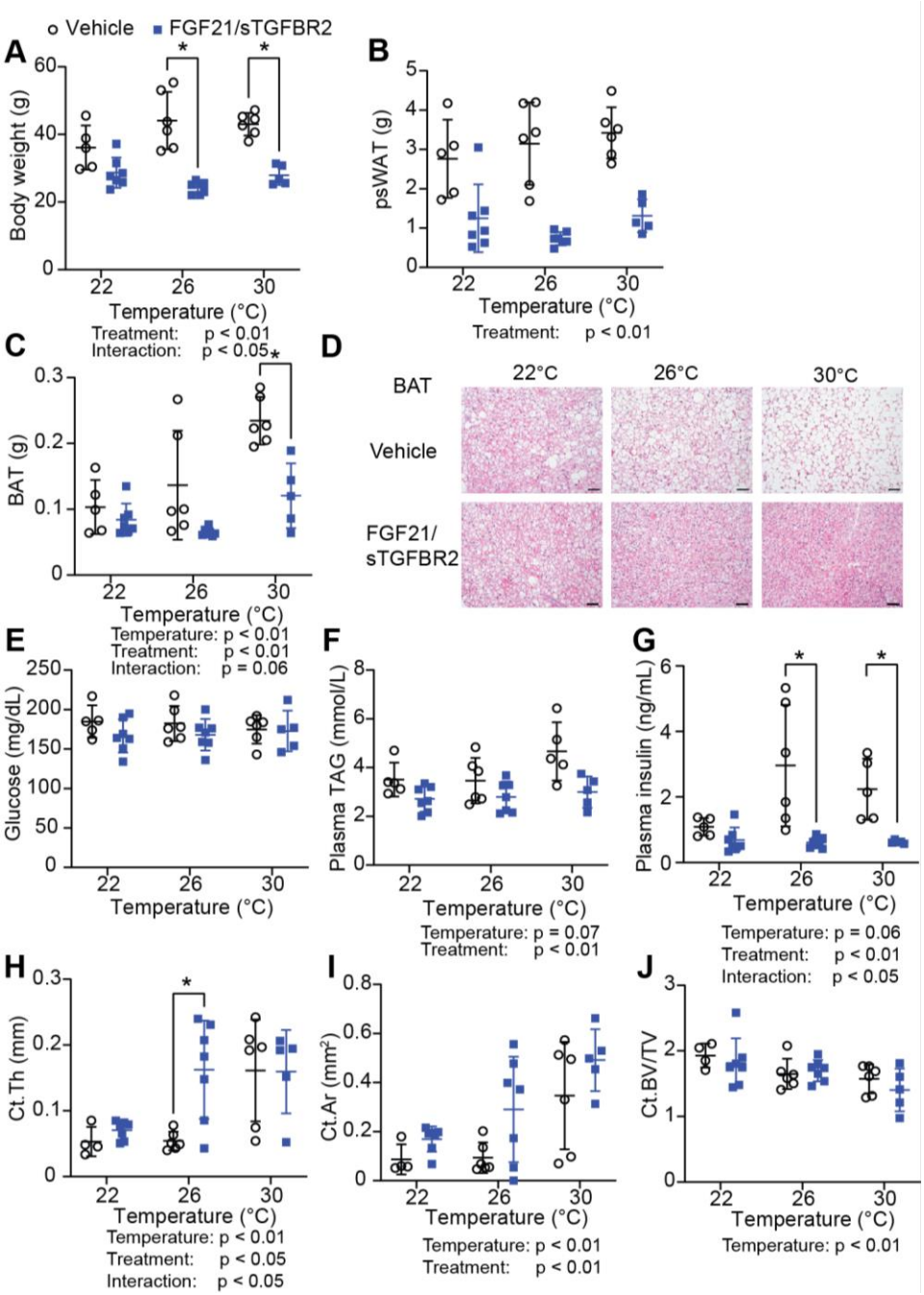


Figure 3.2. FGF21/sTGFBR2 decreases adiposity and plasma insulin concentrations, with highest efficacy at housing temperatures of 26°C and 30°C. Female mice were euthanized ten weeks after transduction with FGF21/sTGFBR2 (n = 5-7). (**A**) Body weight of mice transduced with FGF21/sTGFBR2 at euthanasia. (**B**) Posterior subcutaneous white adipose tissue (psWAT) and (**C**) brown adipose tissue (BAT) weights. (**D**) Representative histological images of mouse BAT stained with H&E. Scale bar = 50 µm. Fed (**E**) blood glucose concentrations, (**F**) plasma TAG and (**G**) insulin concentrations prior to euthanasia. Tibial (**H**) cortical thickness (Ct.Th), (**I**) cortical area (Ct.Ar), and (**J**) cortical bone volume fraction (Ct.BV/TV) analyzed via nanoCT. *P < 0.05. Statistical analyses were performed using two-way ANOVA, followed by Bonferroni's post-hoc test.

Figure 3.3

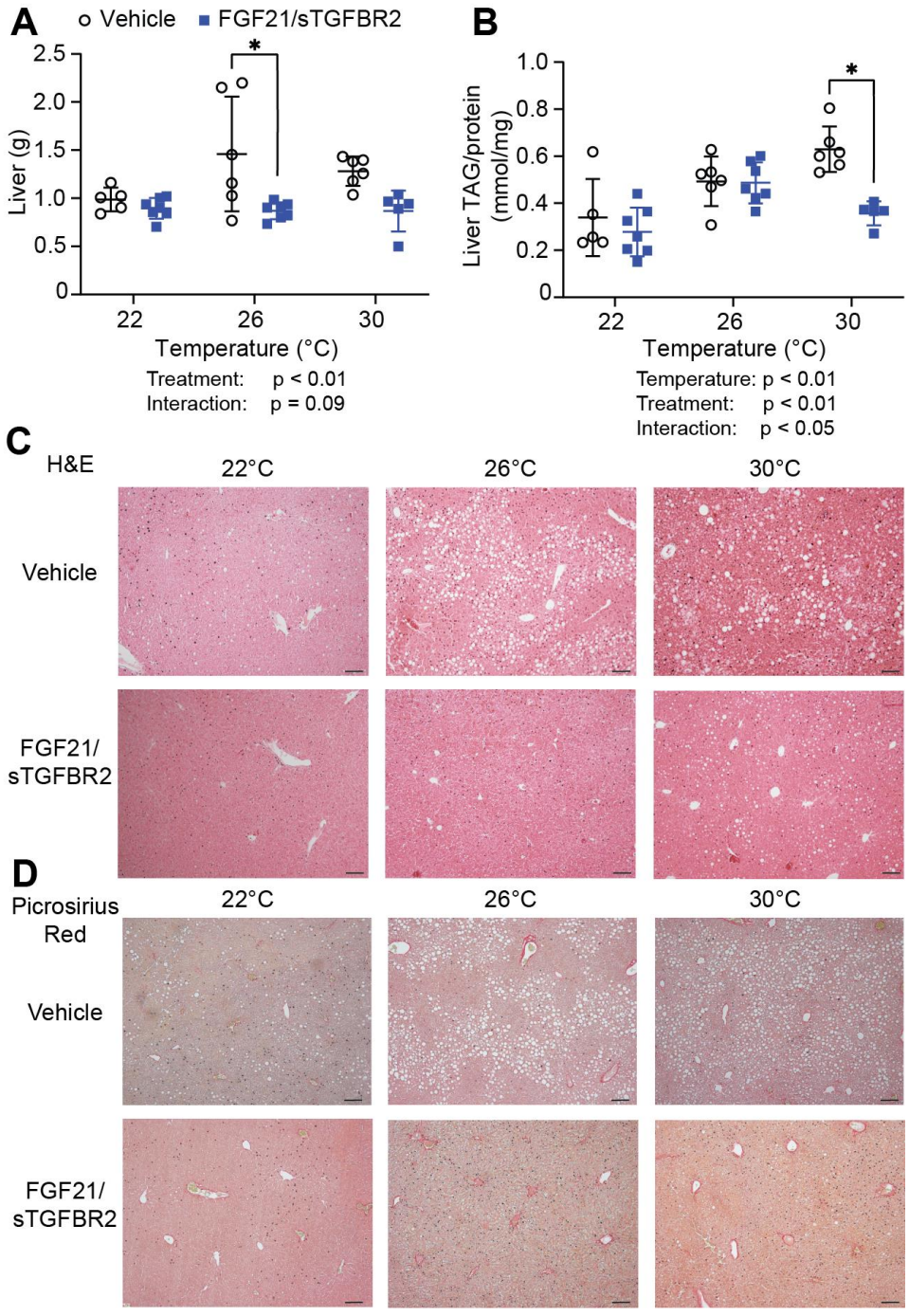


Figure 3.3. FGF21/sTGFBR2 decreases liver weights and hepatic steatosis, with highest efficacy at housing temperatures of 26°C and 30°C. (**A**) Liver weights in vehicle and FGF21/sTGFBR2 treated mice at all housing temperatures ten weeks after transduction (n = 6-7). (**B**) Liver TAG concentration normalized to protein amount (n = 6-7). (**C**) Representative histological images of mouse livers stained with H&E. Scale bar = 50 µm. (**D**) Representative images of mouse livers stained with Picrosirius Red to identify collagen. Scale bar = 50 µm. *P < 0.05. Statistical analyses were performed using two-way ANOVA, followed by Bonferroni's post-hoc test.

Figure 3.4

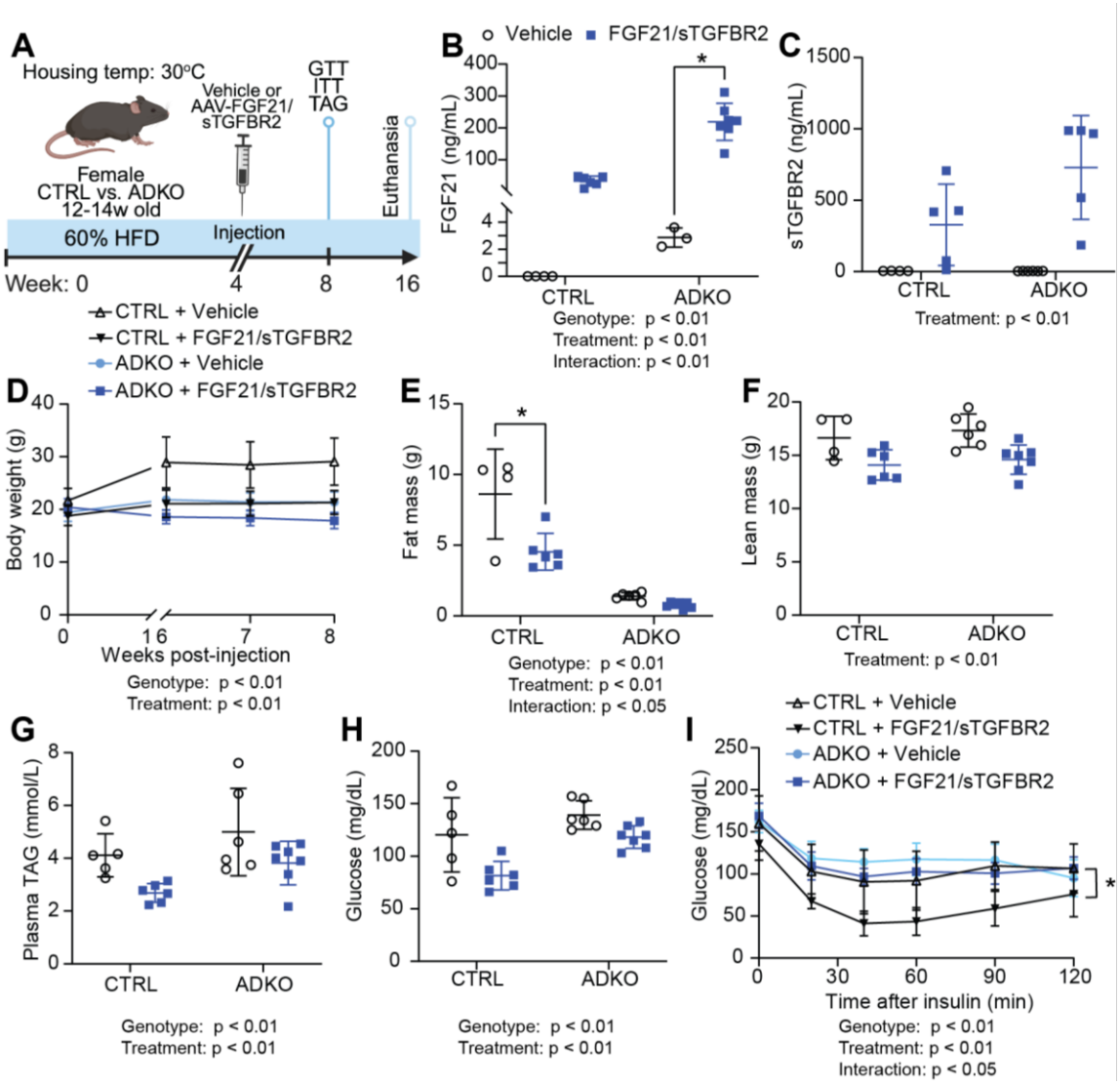


Figure 3.4. Adipose tissue is required for FGF21/sTGFBR2 to mediate metabolic improvements at thermoneutrality. (**A**) Schematic illustration of housing conditions and experimental timeline; *Lmna*$^{Fl/Fl}$ = control mice and *Lmna*^{ADKO} = lipodystrophic mice. Plasma (**B**) FGF21 and (**C**) sTGFBR2 concentrations in mice 12 weeks after transduction (n = 4-7). (**D**) Body weight in vehicle and FGF21/sTGFBR2 mice four weeks after transduction (n = 5-7). (**E**) Fat and (**F**) lean mass measured by EchoMRI four weeks post-transduction (n = 4-7). (**G**) Plasma TAG, and (**H**) blood glucose concentrations four weeks post-treatment (n = 5-7). (**I**) Insulin tolerance tests (0.75 U/kg; n = 5-7), data presented as mean ± SEM. *P < 0.05. Statistical analyses were performed using two-way ANOVA, followed by Bonferroni's post-hoc test.

Figure 3.5

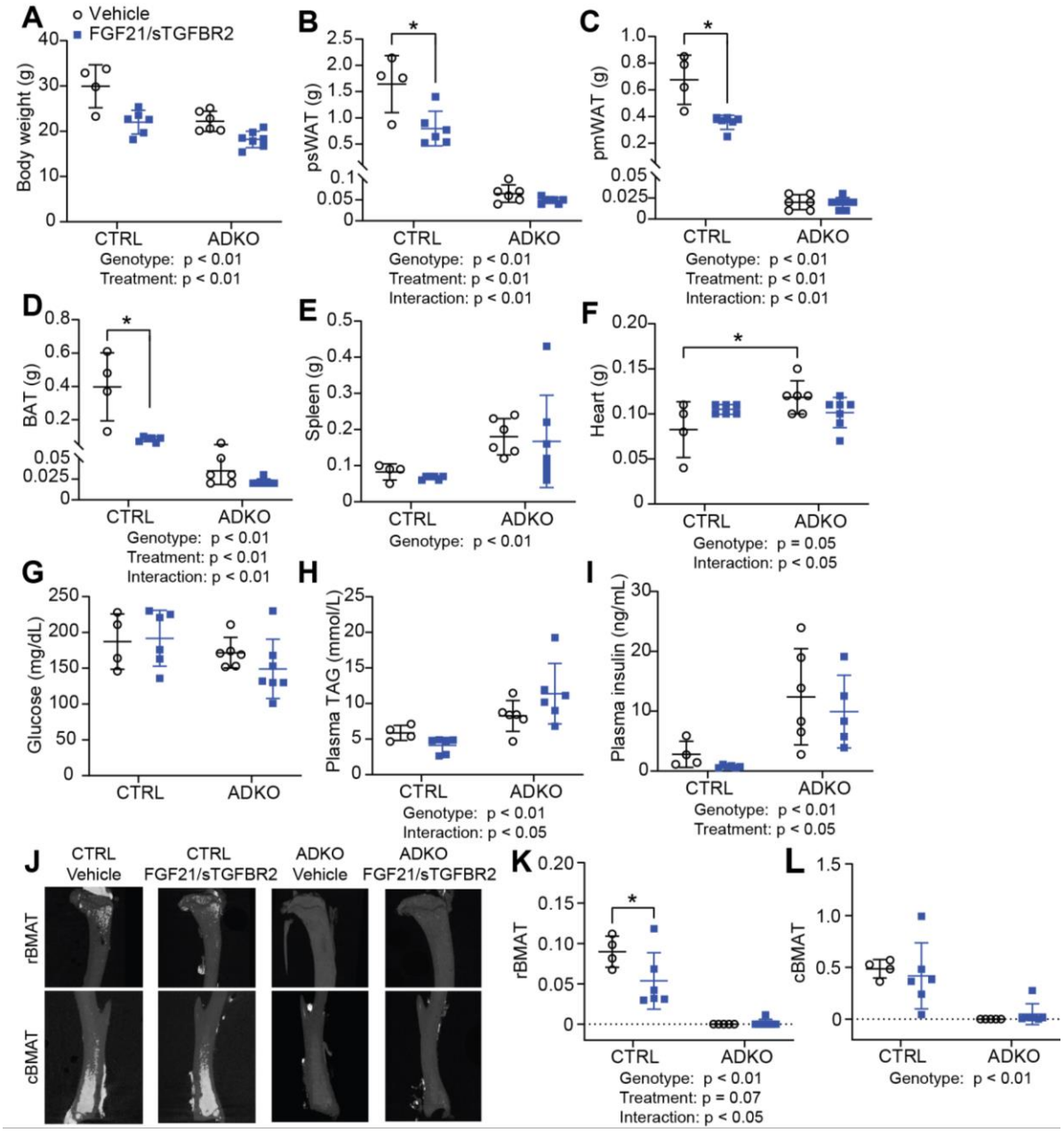


Figure 3.5. FGF21/sTGFBR2 does not improve metabolic dysfunction of lipodystrophic mice housed at thermoneutrality. Female mice were euthanized 12 weeks after FGF21/sTGFBR2 transduction (n = 4-7). (**A**) Body weight, (**B**) psWAT, (**C**) parametrial white adipose tissue (pmWAT), (**D**) BAT, (**E**) spleen, and (**F**) heart weights in mice at euthanasia. Fed (**G**) blood glucose, (**H**) plasma TAG, and (**I**) plasma insulin concentrations prior to euthanasia. (**J**) Representative tibial osmium-nanoCT images. (**K**) rBMAT normalized to marrow volume. (**L**) cBMAT normalized to marrow volume. *P < 0.05. Statistical analyses were performed using two-way ANOVA, followed by Bonferroni's post-hoc test.

Figure 3.6

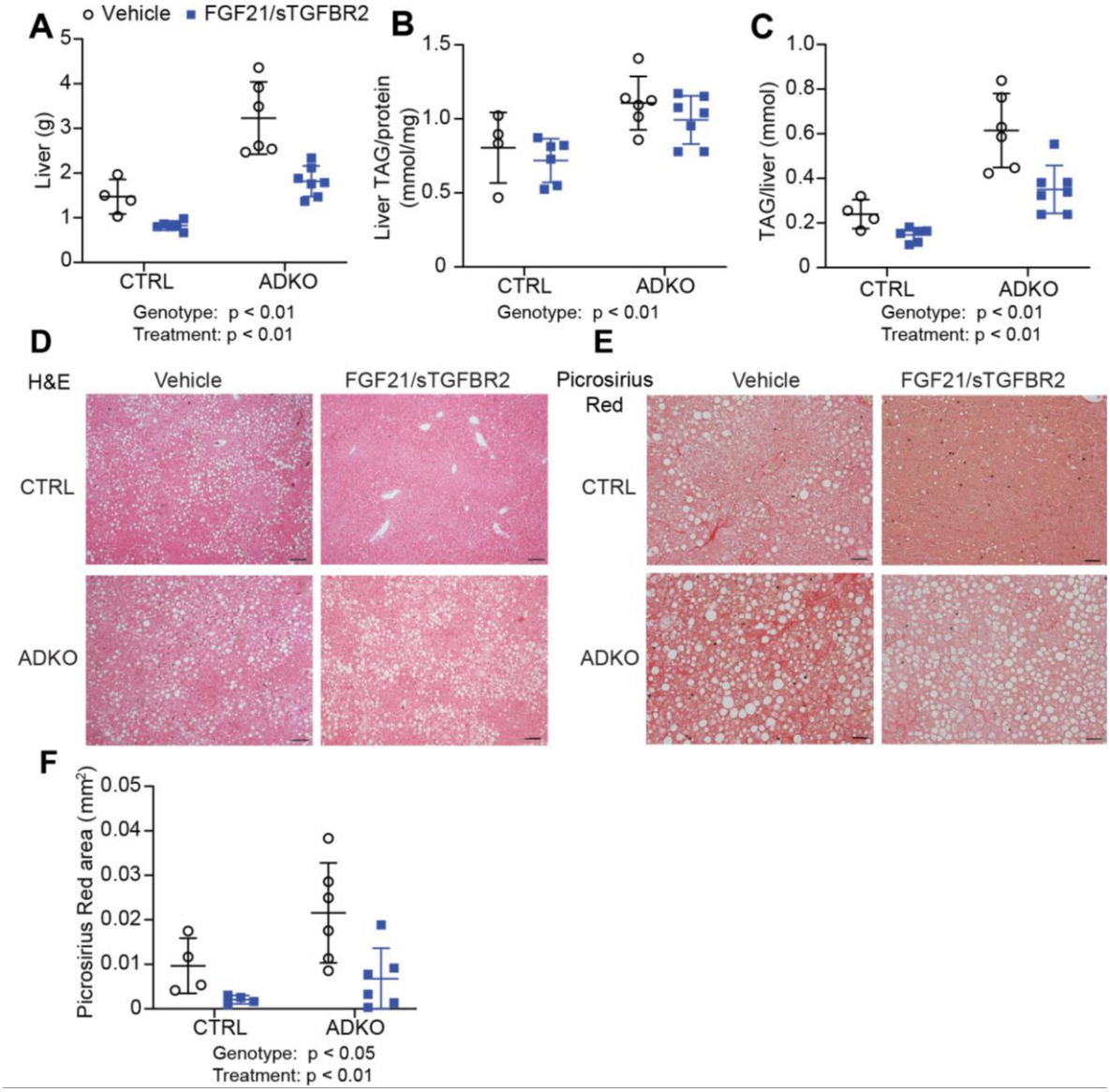


Figure 3.6. FGF21/sTGFBR2 reduces liver weight, total hepatic TAG, and liver collagen deposition in lipodystrophic mice housed at 30°C. Female mice were euthanized 12 weeks after FGF21/sTGFBR2 transduction (n = 4-7). (**A**) Liver weights at euthanasia. (**B**) Liver TAG normalized to protein content. (**C**) TAG amount normalized to total liver weight. (**D**) Representative histological images of mouse livers stained with H&E. Scale bar = 50 µm. (**E**) Representative images of mouse livers stained with Picrosirius Red for collagen. Scale bar = 50 µm. (**F**) Machine learning quantification of area stained by Picrosirius Red in the liver. *P < 0.05. Statistical analyses were performed using two-way ANOVA, followed by Bonferroni's post-hoc test.

Figure 3.7

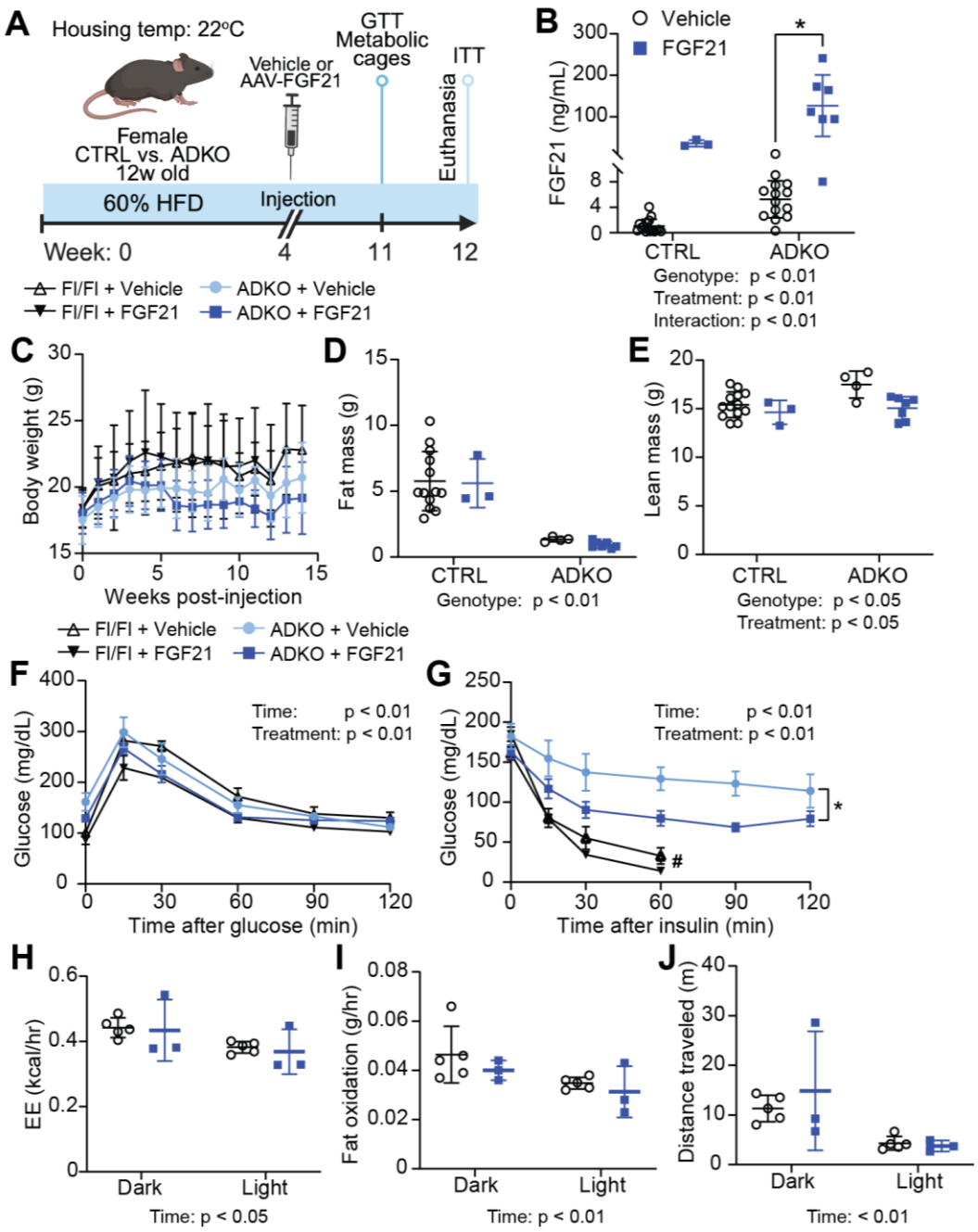


Figure 3.7. FGF21 improves insulin sensitivity of lipodystrophic mice housed at 22°C. (A) Schematic illustration of housing conditions and experimental timeline. (**B**) Plasma FGF21 concentrations eight weeks post-transduction (n = 3-16). (**C**) Body weight, (**D**) fat mass, and (**E**) lean mass measured by EchoMRI seven weeks post-transduction (n = 3-13). (**F**) Glucose tolerance test (1 mg/kg; n = 3-13), data presented as mean ± SEM. (**G**) Insulin tolerance test (0.75U/kg; n = 3-13), data presented as mean ± SEM. #Mice in (G) received intraperitoneal glucose because their blood glucose dropped below 30 mg/dL. Indirect calorimetry was measured for three days using the Promethion System. (**H**) Energy expenditure (EE) averaged during dark or light cycles, (**I**) fat oxidation averaged during the first four hours of dark or light cycles, and (**J**) distance traveled averaged during dark or light cycles. *P < 0.05. Statistical analyses were performed using two-way ANOVA, followed by Bonferroni's post-hoc test.

Figure 3.8

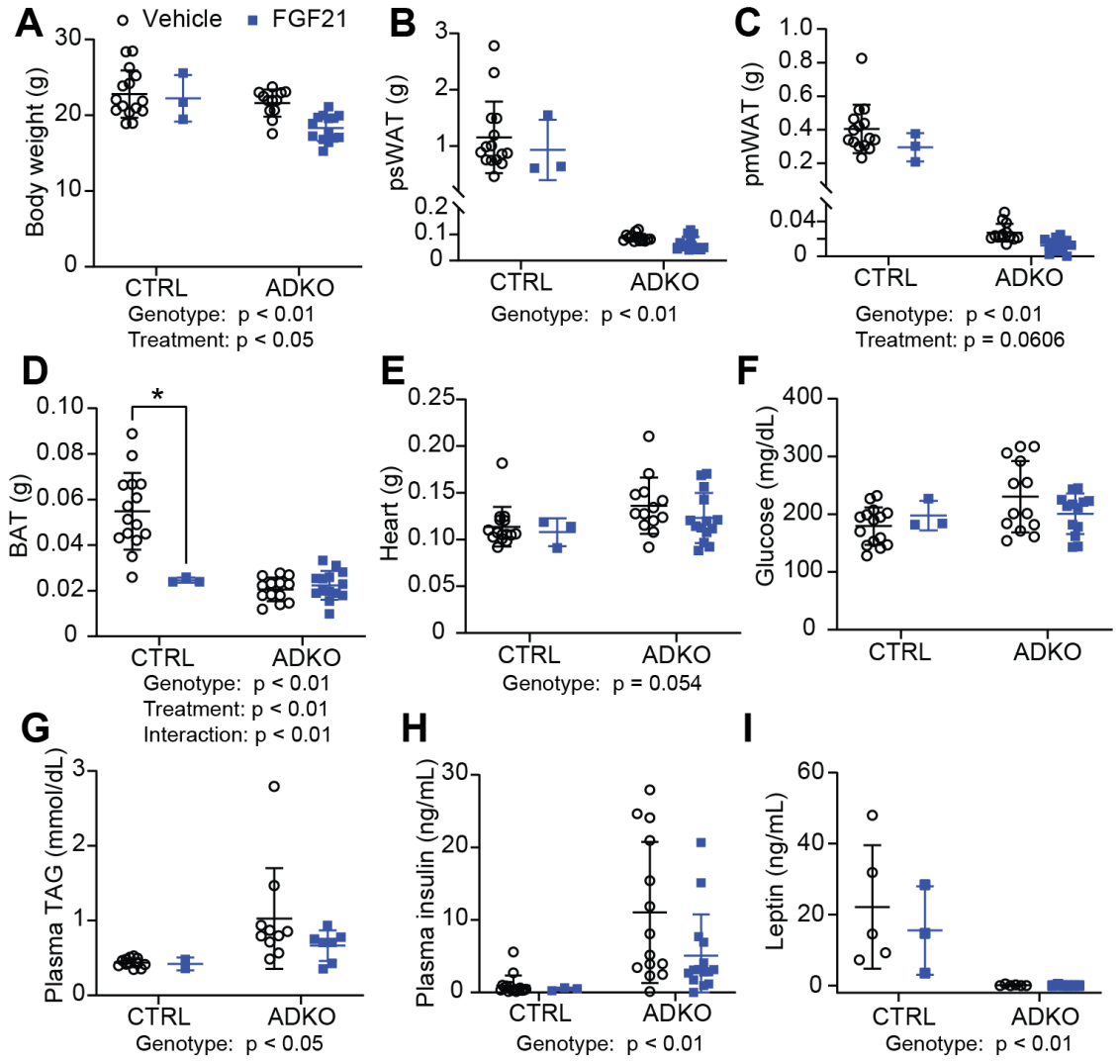


Figure 3.8. FGF21 does not improve metabolic dysfunction of lipodystrophic mice housed at 22°C. Female mice were euthanized eight weeks after FGF21 administration (n = 3-15). (**A**) Body weights, (**B**) psWAT, (**C**) pmWAT, (**D**) BAT, and (**E**) heart weights at euthanasia. Fed (**F**) blood glucose, (**G**) plasma TAG, (**H**) plasma insulin, and (**I**) plasma leptin concentrations prior to euthanasia. *P < 0.05. Statistical analyses were performed using two-way ANOVA, followed by Bonferroni's post-hoc test.

Figure 3.9

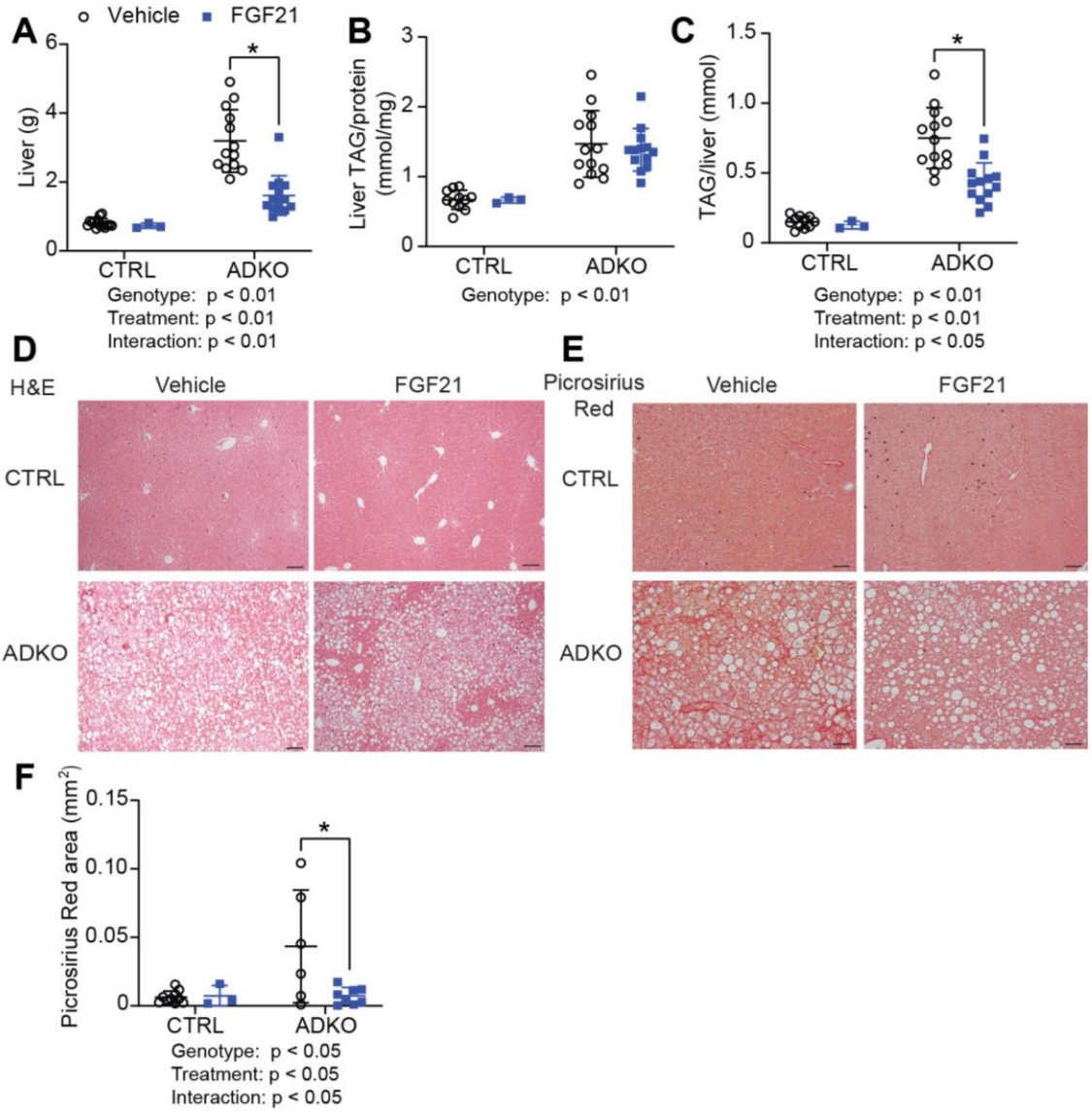


Figure 3.9. FGF21 reduces liver weight, total hepatic TAG content, and liver collagen deposition in lipodystrophic mice housed at 22°C. Female mice were euthanized eight weeks after FGF21 administration (n = 3-15). (**A**) Liver weights at euthanasia. (**B**) Liver TAG normalized to protein content. (**C**) Total liver TAG normalized to liver weights. (**D**) Representative histological images of H&E-stained mouse livers. Scale bar = 50 μm. (**E**) Representative images of mouse livers stained with Picrosirius Red for collagen. Scale bar = 50 μm. (**F**) Machine learning quantification of area stained by Picrosirius Red in the liver. *P < 0.05. Statistical analyses were performed using two-way ANOVA, followed by Bonferroni's post-hoc test.

Figure 3.10

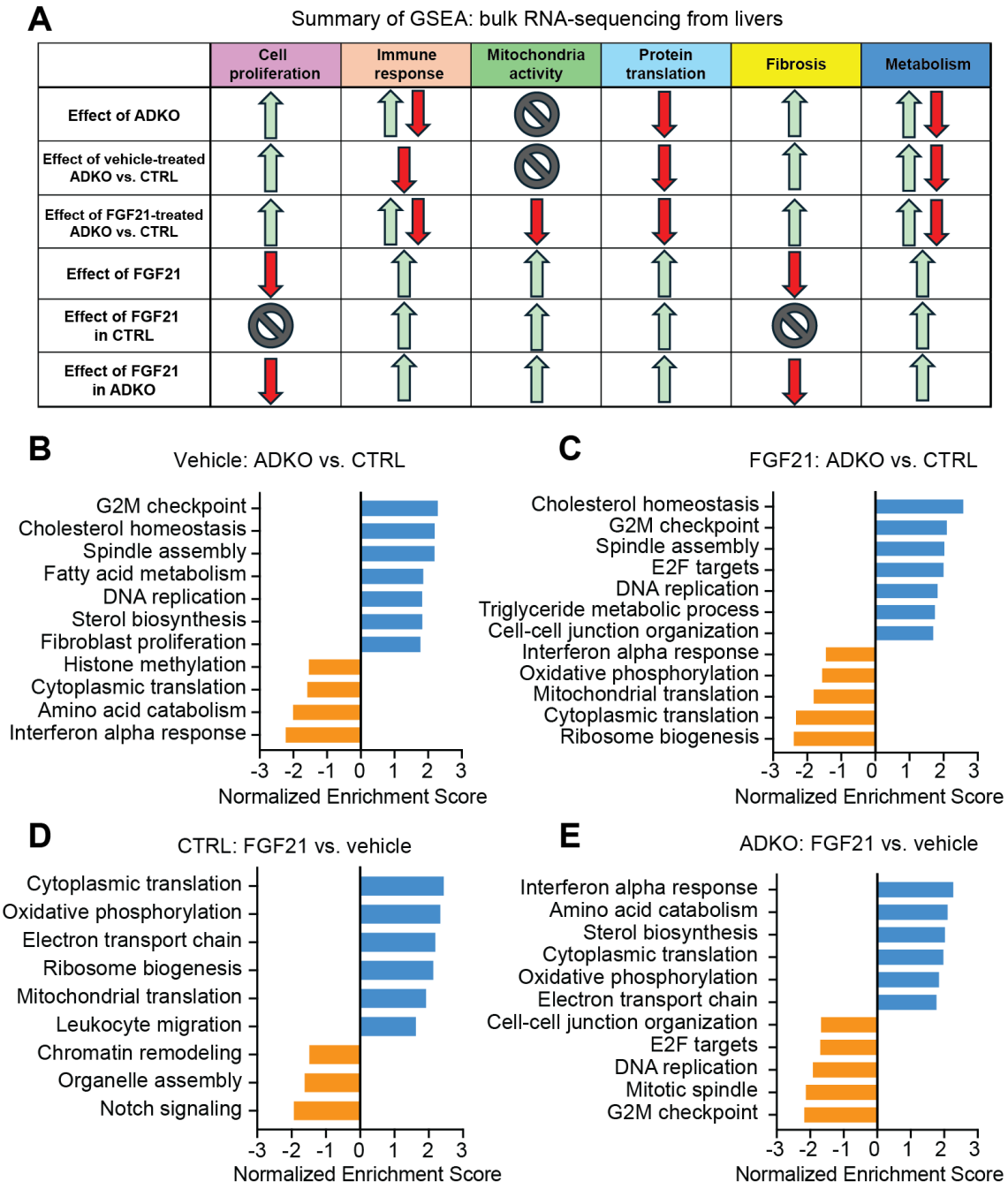
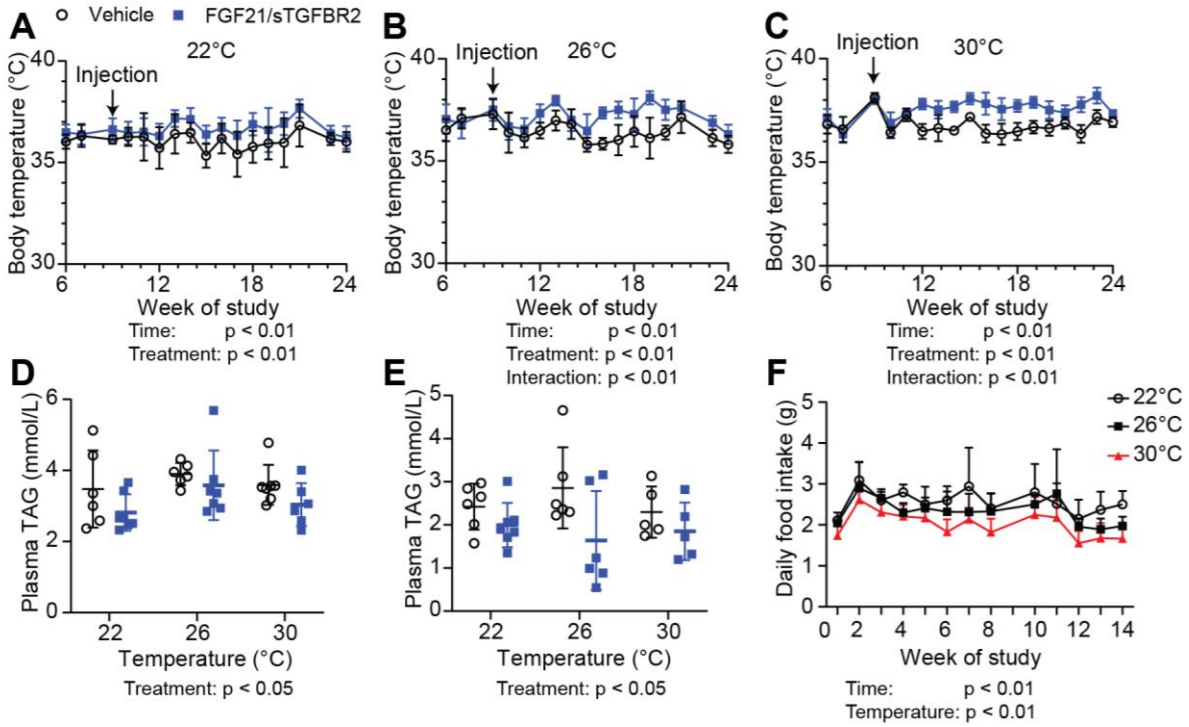
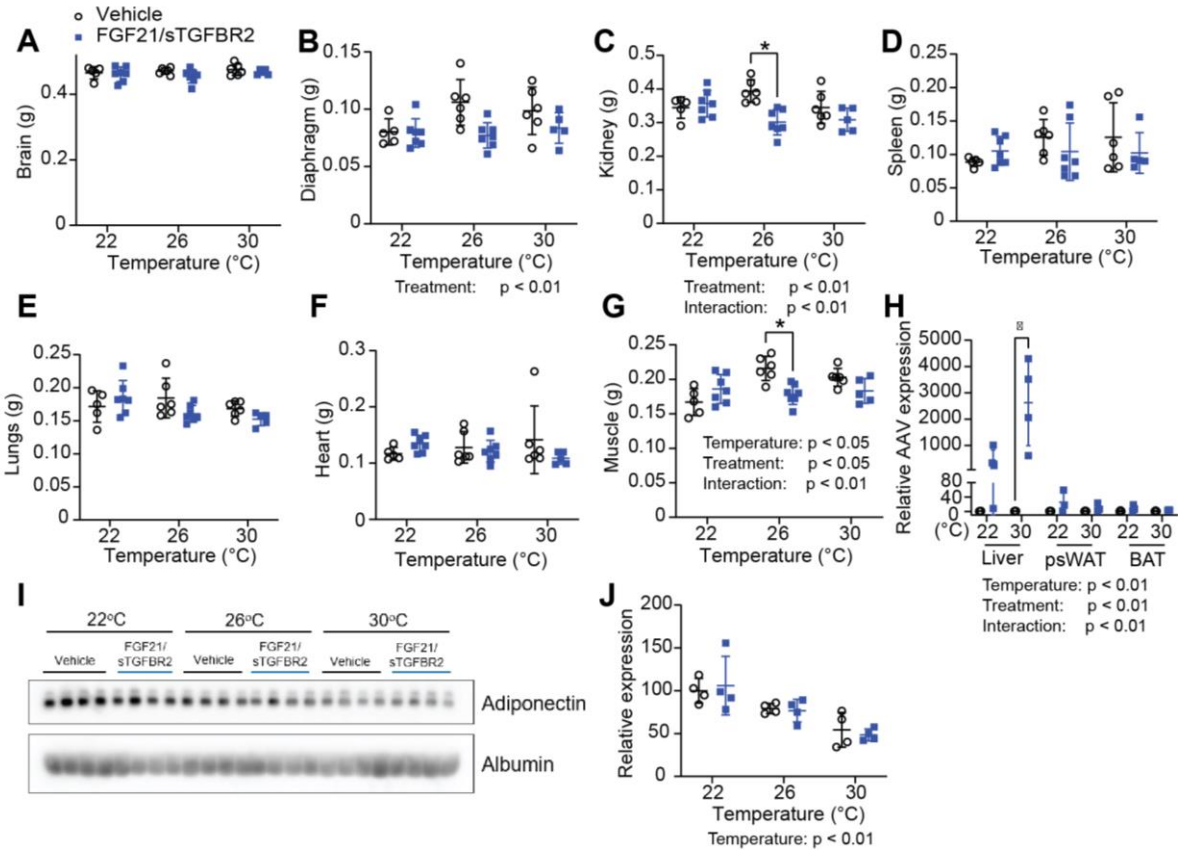


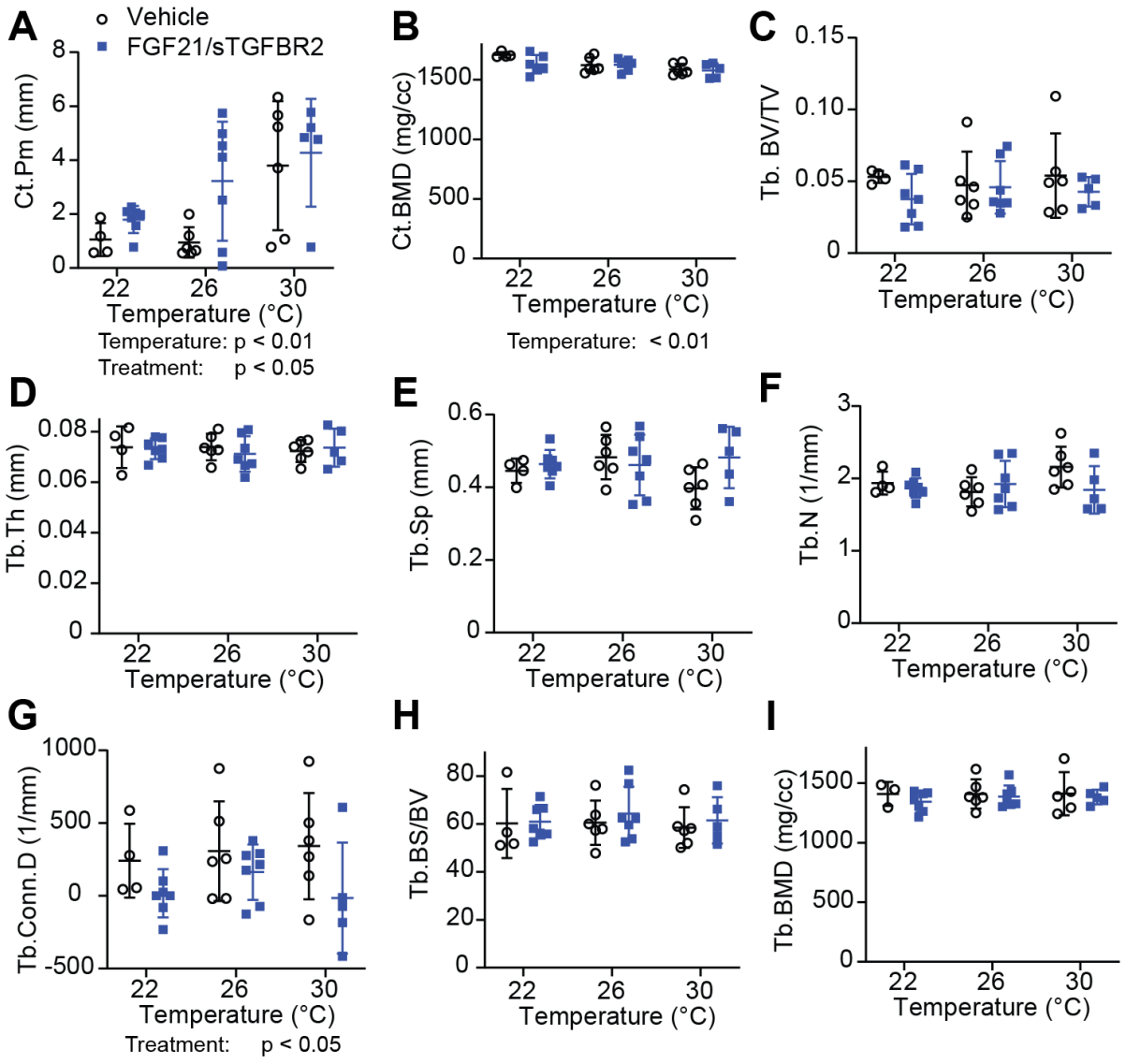
Figure 3.10. RNA-sequencing analyses of livers reveal that livers from lipodystrophic mice have increased cell proliferation and increased fibrosis, and that FGF21 treatment increases mitochondrial and translation pathways. (**A**) Summary of key GSEA pathways in hepatic mRNA of CTRL vs. ADKO mice eight weeks after treatment with FGF21 or vehicle. (**B**) GSEA pathways changed in CTRL mice dependent on treatment, padj<0.05. (**C**) GSEA pathways changed in ADKO mice dependent on treatment, padj<0.05. (**D**) GSEA pathways changed in vehicle-treated mice dependent on genotype, padj<0.05. (**E**) GSEA pathways changed in FGF21-treated mice dependent on genotype, padj<0.05.



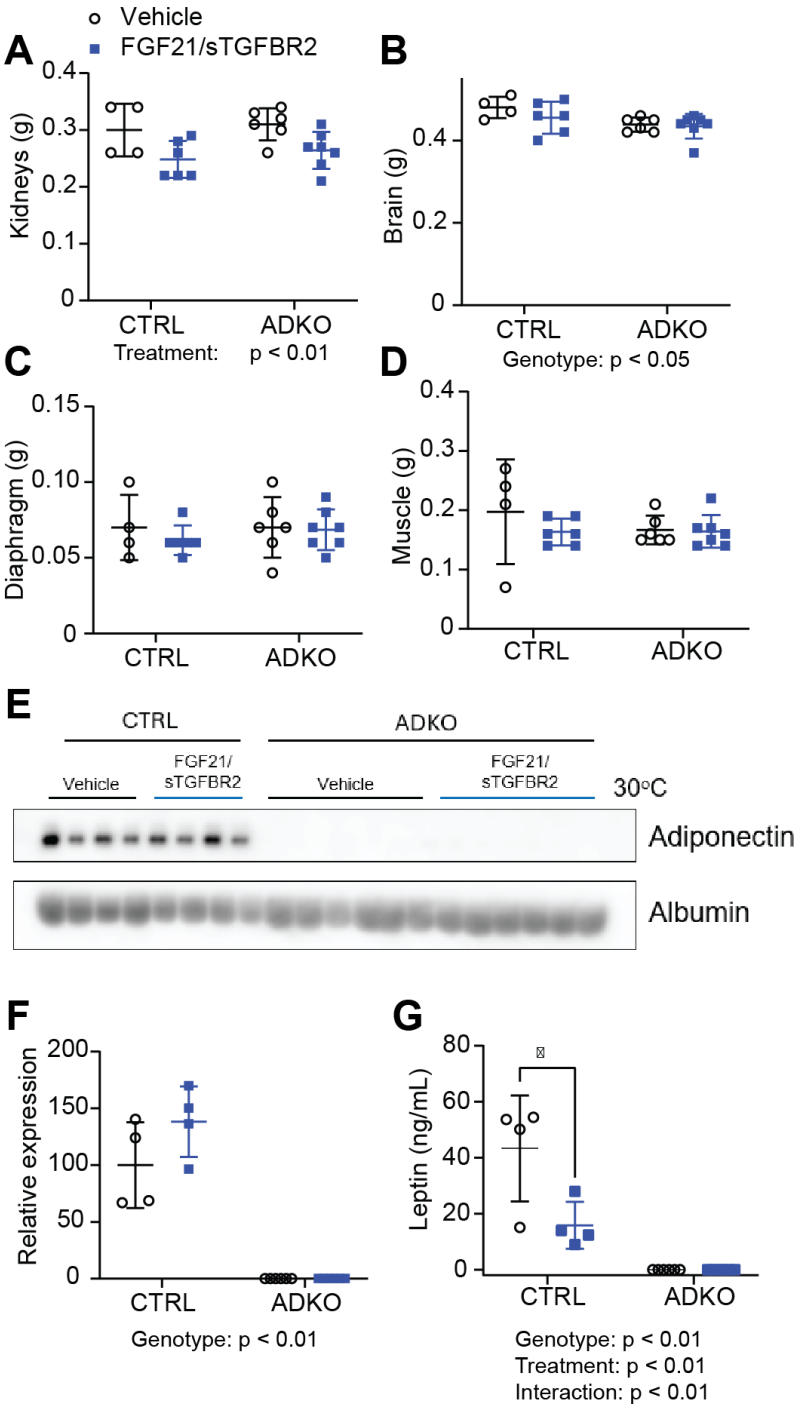
Supplemental Figure 3.1. FGF21/sTGFBR2 reduces plasma TAG concentrations and increases body temperature in high fat diet-fed mice. Core body temperature over time in HFD-fed female mice housed at (**A**) 22°C, (**B**) 26°C and (**C**) 30°C (n = 6-7). Plasma TAG concentrations at (**D**) four weeks and (**E**) six weeks post-treatment (n = 6-7). (**F**) Daily food intake in mice at different housing temperatures. Statistical analyses were performed using two-way ANOVA, followed by Bonferroni's post-hoc test.



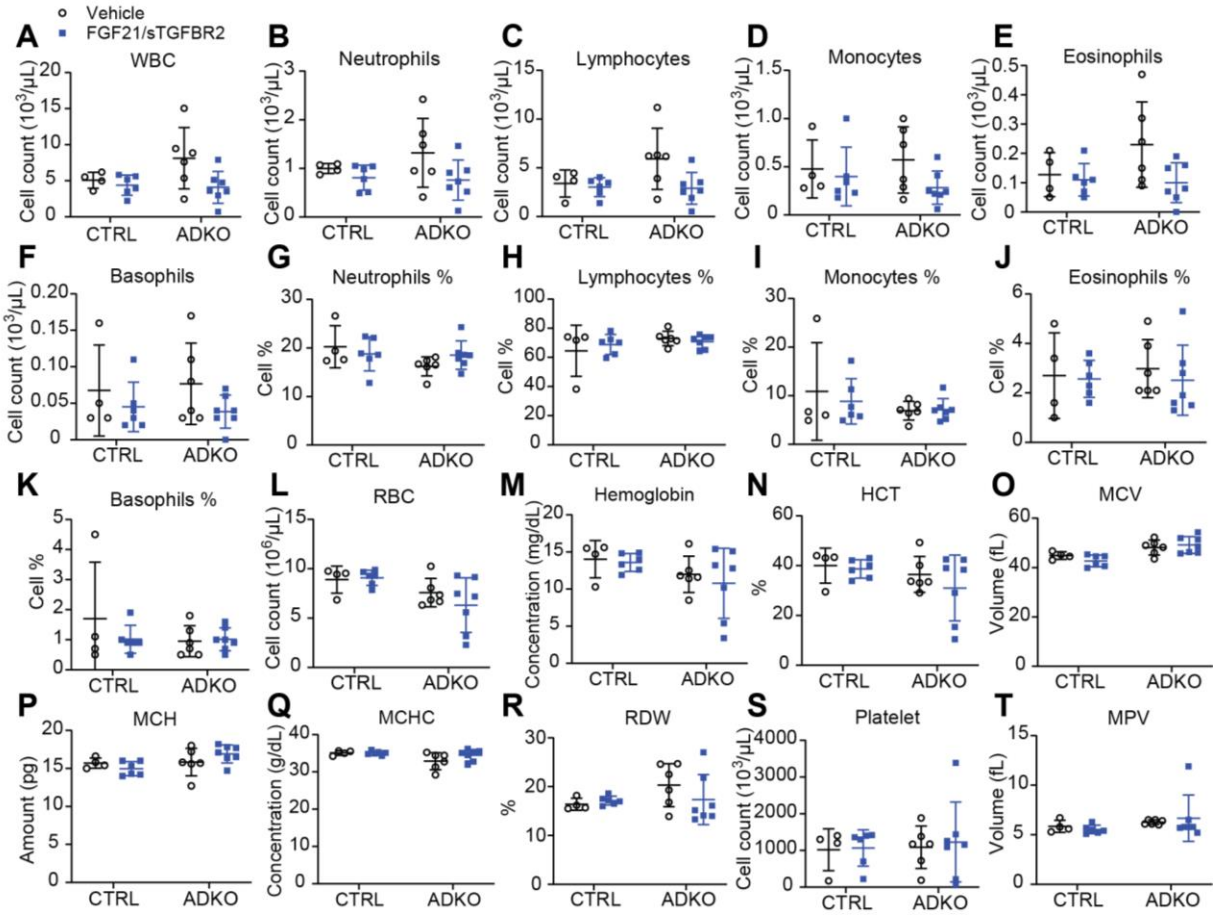
Supplemental Figure 3.2. FGF21/sTGFBR2 decreases diaphragm weights and kidney weights in HFD-induced obese mice. Female mice were euthanized ten weeks after FGF21/sTGFBR2 treatment (n = 5-7). Weights of (**A**) brain, (**B**) diaphragm, (**C**) kidneys, (**D**) spleen, (**E**) lungs, (**F**) heart, and (**G**) gastrocnemius muscle. (**H**) Quantification of AAV transduction in liver, psWAT, and BAT. (**I**) Plasma adiponectin immunoblot and (**J**) quantification relative to controls housed at 22°C. Statistical analyses were performed using two-way ANOVA, followed by Bonferroni's post-hoc test.



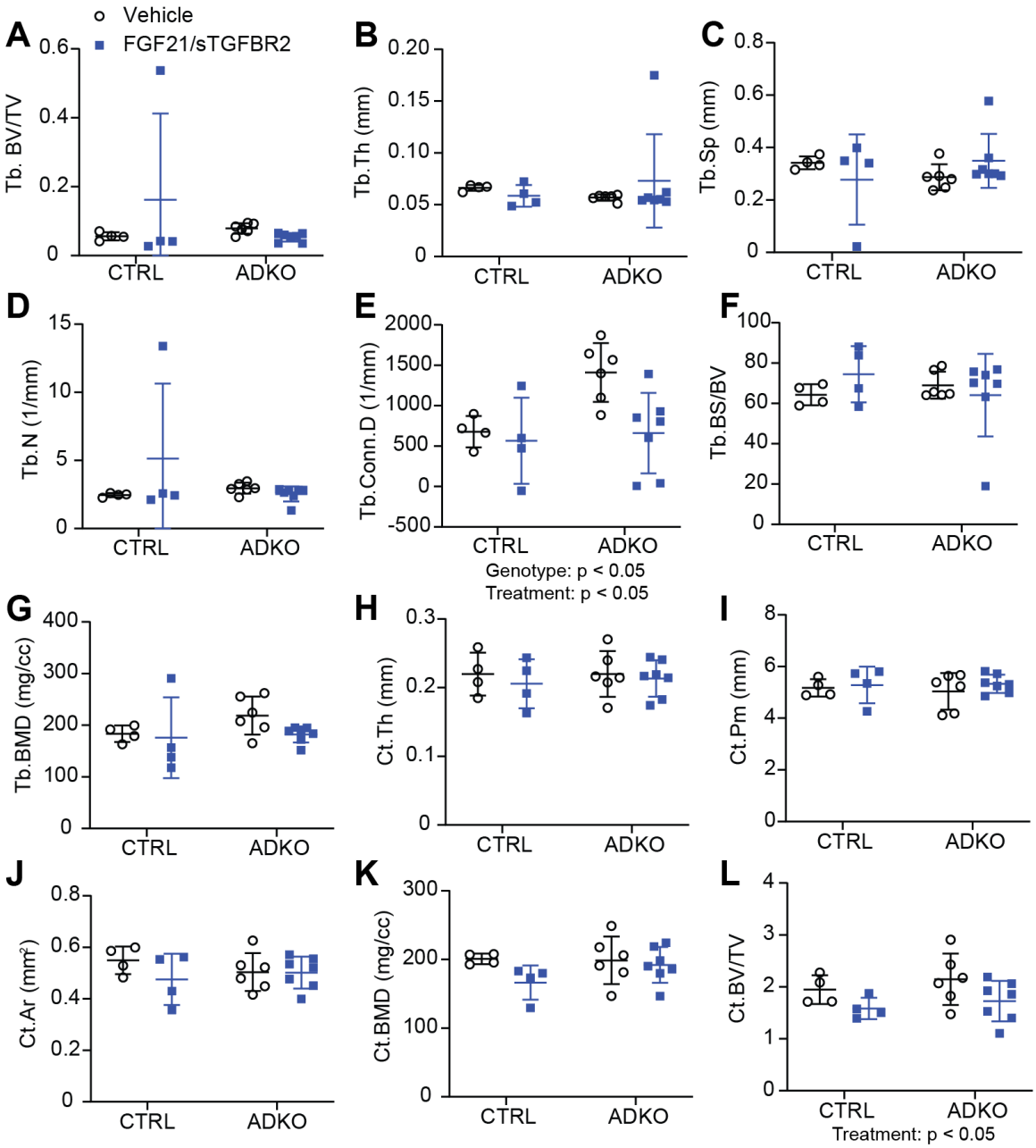
Supplemental Figure 3.3. FGF21/sTGFBR2 decreases tibial trabecular connectivity density and increases cortical perimeter. Female mice were euthanized ten weeks after FGF21/sTGFBR2 transduction (n = 4-7). Tibias were analyzed by nanoCT. (**A**) Cortical perimeter (Ct.Pm). (**B**) Cortical bone mineral density (Bt.BMD). (**C**) Trabecular bone volume fraction (Tb. BV/TV). (**D**) Trabecular thickness (Tb.Th). (**E**) Trabecular separation (Tb.Sp). (**F**) Trabecular number (Tb.N). (**G**) Trabecular connectivity density (Tb.Conn.D). (**H**) Trabecular specific bone surface (Tb.BS/BV). (**I**) Trabecular bone mineral density (Tb.BMD). *P < 0.05. Statistical analyses were performed using two-way ANOVA, followed by Bonferroni's post-hoc test.



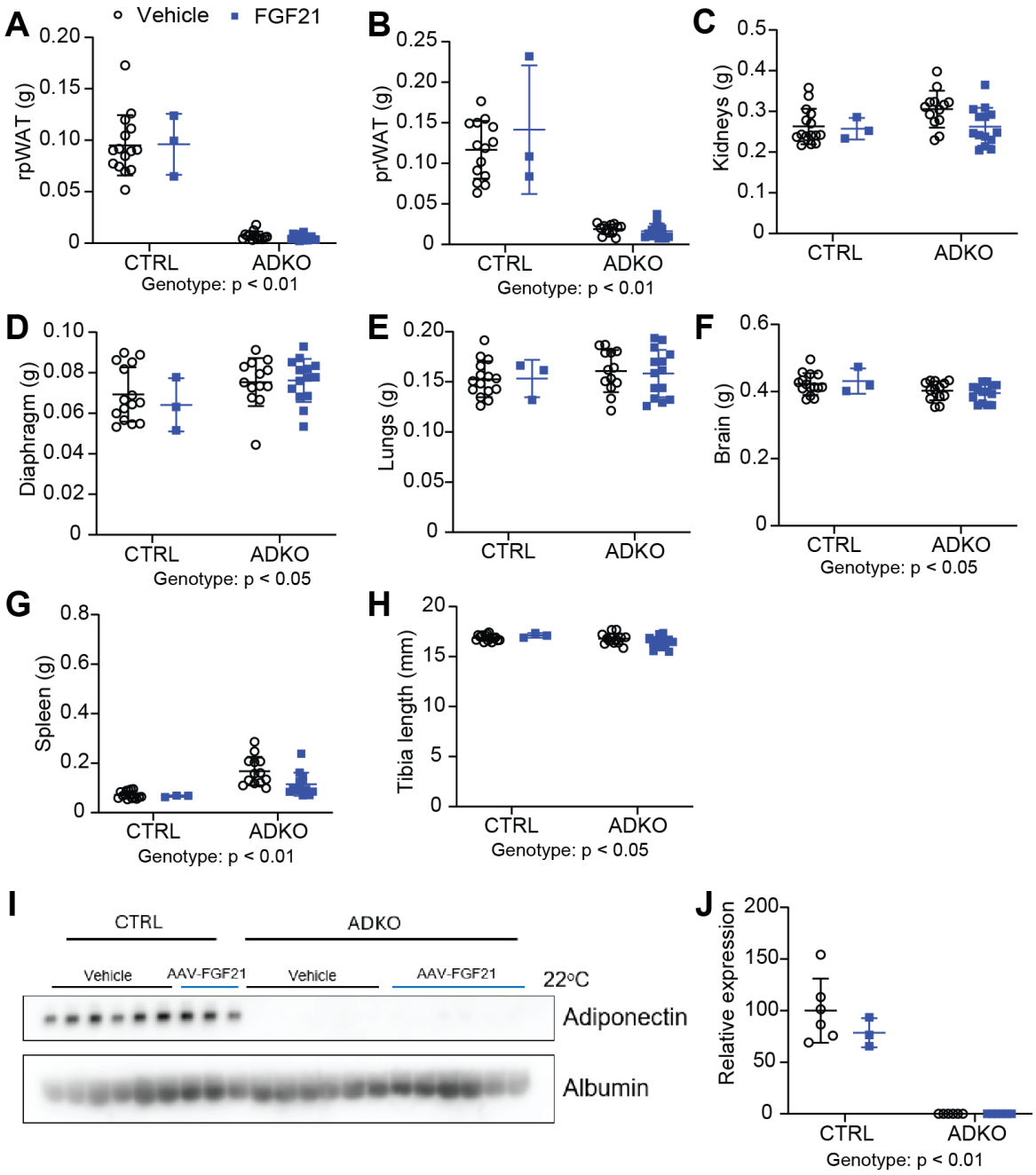
Supplemental Figure 3.4. FGF21/sTGFBR2 decreases kidney weights in lipodystrophic mice housed at 30°C. Female mice were euthanized 12 weeks after transduction with FGF21/sTGFBR2 (n = 4-7). Weights of (**A**) kidneys, (**B**) brain, (**C**) diaphragm, and (**D**) gastrocnemius muscle at euthanasia. (**E**) Immunoblot of plasma adiponectin with (**F**) quantification. (**G**) Fed leptin concentrations at euthanasia. *P < 0.05. Statistical analyses were performed using two-way ANOVA, followed by Bonferroni's post-hoc test.



Supplemental Figure 3.5. FGF21/sTGFBR2 does not change complete blood counts in lipodystrophic mice. Blood was taken at euthanasia 12 weeks after transduction with FGF21/sTGFBR2 (n = 4-7). Total cell counts of (**A**) white blood cells, (**B**) neutrophils, (**C**) lymphocytes, (**D**) monocytes, (**E**) eosinophils, and (**F**) basophils. Cellular percentage of (**G**) neutrophils, (**H**) lymphocytes, (**I**) monocytes, (**J**) eosinophils, and (**K**) basophils. (**L**) Red blood cell count. (**M**) Hemoglobin concentrations. (**N**) Hematocrit (HCT). (**O**) Mean corpuscular volume (MCV). (**P**) Mean corpuscular hemoglobin (MCH) amount. (**Q**) Mean corpuscular hemoglobin concentrations. (**R**) Red blood cell distribution width. (**S**) Platelet count. (**T**) Mean platelet volume. Statistical analyses were performed using two-way ANOVA, followed by Bonferroni's post-hoc test.



Supplemental Figure 3.6. FGF21/sTGFBR2 decreases tibial trabecular connectivity density and cortical bone volume fraction in lipodystrophic mice housed at thermoneutrality. Female mice were euthanized ten weeks after FGF21/sTGFBR2 transduction (n = 4-7). Tibias were analyzed by nanoCT. (**A**) Trabecular bone volume fraction (Tb. BV/TV). (**B**) Trabecular thickness (Tb.Th). (**C**) Trabecular separation (Tb.Sp). (**D**) Trabecular number (Tb.N). (**E**) Trabecular connectivity density (Tb.Conn.D). (**F**) Trabecular specific bone surface (Tb.BS/BV). (**G**) Trabecular bone mineral density (Tb.BMD). (**H**) Cortical thickness (Ct.Th). (**I**) Cortical perimeter (Ct.Pm). (**J**) Cortical area (Ct.Ar). (**K**) Cortical bone mineral density (Ct.BMD). (**L**) Cortical specific bone surface (Ct.BS/BV). Statistical analyses were performed using two-way ANOVA, followed by Bonferroni's post-hoc test.



Supplemental Figure 3.7. FGF21 has little effect on organ weights in lipodystrophic mice housed at 22°C. Female mice were euthanized eight weeks after FGF21 treatment (n = 3-15). Weights of (**A**) rpWAT, (**B**) prWAT, (**C**) kidneys, (**D**) diaphragm, (**E**) lungs, (**F**) brain, (**G**) spleen. (**H**) Tibia length. (**I**) Plasma adiponectin immunoblot with (**J**) quantification. Statistical analyses were performed using two-way ANOVA, followed by Bonferroni's post-hoc test.

3.7 References

1. Rubino, F. *et al.* Definition and diagnostic criteria of clinical obesity. *Lancet Diabetes Endocrinol.* 13, 221–262 (2025).
2. GBD 2015 Obesity Collaborators *et al.* Health Effects of Overweight and Obesity in 195 Countries over 25 Years. *N. Engl. J. Med.* 377, 13–27 (2017).
3. Piché, M.-E., *et al*. Obesity Phenotypes, Diabetes, and Cardiovascular Diseases. *Circ. Res.* 126, 1477–1500 (2020).
4. Akinci, B., *et al*. Lipodystrophy Syndromes: Presentation and Treatment. in *Endotext* (eds. Feingold, K. R. et al.) (MDText.com, Inc., South Dartmouth (MA), 2000).
5. Besci, O. *et al.* Deciphering the Clinical Presentations in LMNA-related Lipodystrophy: Report of 115 Cases and a Systematic Review. *J. Clin. Endocrinol. Metab.* 109, e1204–e1224 (2024).
6. Gonzaga-Jauregui, C. *et al.* Clinical and Molecular Prevalence of Lipodystrophy in an Unascertained Large Clinical Care Cohort. *Diabetes* 69, 249–258 (2019).
7. Garg, A. Lipodystrophies: Genetic and Acquired Body Fat Disorders. *J. Clin. Endocrinol. Metab.* 96, 3313–3325 (2011).
8. Pfeffer, M. A. *et al.* Lixisenatide in Patients with Type 2 Diabetes and Acute Coronary Syndrome. *N. Engl. J. Med.* 373, 2247–2257 (2015).
9. Marso, S. P. *et al.* Liraglutide and Cardiovascular Outcomes in Type 2 Diabetes. *N. Engl. J. Med.* 375, 311–322 (2016).
10. Marso, S. P. *et al.* Semaglutide and Cardiovascular Outcomes in Patients with Type 2 Diabetes. *N. Engl. J. Med.* 375, 1834–1844 (2016).
11. Husain, M. *et al.* Oral Semaglutide and Cardiovascular Outcomes in Patients with Type 2 Diabetes. *N. Engl. J. Med.* 381, 841–851 (2019).
12. Xie, Y., *et al*. Mapping the effectiveness and risks of GLP-1 receptor agonists. *Nat. Med.* 31, 951–962 (2025).
13. Oral, E. A. *et al.* Leptin-replacement therapy for lipodystrophy. *N. Engl. J. Med.* 346, 570–578 (2002).
14. Brown, R. J. *et al.* Long-term effectiveness and safety of metreleptin in the treatment of patients with generalized lipodystrophy. *Endocrine* 60, 479–489 (2018).
15. Oral, E. A. *et al.* Long-term effectiveness and safety of metreleptin in the treatment of patients with partial lipodystrophy. *Endocrine* 64, 500–511 (2019).
16. Wang, J.-H., *et al*. Adeno-associated virus as a delivery vector for gene therapy of human diseases. *Signal Transduct. Target. Ther.* 9, 1–33 (2024).
17. Geng, L., *et al*. The therapeutic potential of FGF21 in metabolic diseases: from bench to clinic. *Nat. Rev. Endocrinol.* 16, 654–667 (2020).
18. Kharitonenkov, A. *et al.* FGF-21 as a novel metabolic regulator. *J. Clin. Invest.* 115, 1627–1635 (2005).
19. Kajdaniuk, D., *et al*. Transforming growth factor β1 (TGFβ1) in physiology and pathology. *Endokrynol. Pol.* 64, 384–396 (2013).
20. Ong, C. H., *et al.* TGF-β-induced fibrosis: A review on the underlying mechanism and potential therapeutic strategies. *Eur. J. Pharmacol.* 911, 174510 (2021).
21. Jimenez, V. *et al.* FGF21 gene therapy as treatment for obesity and insulin resistance. *EMBO Mol. Med.* 10, e8791 (2018).
22. Jimenez, V. *et al.* Reversion of metabolic dysfunction-associated steatohepatitis by skeletal muscle-directed FGF21 gene therapy. *Mol. Ther.* 32, 4285–4302 (2024).

23. Davidsohn, N. *et al.* A single combination gene therapy treats multiple age-related diseases. *Proc. Natl. Acad. Sci. U. S. A.* 116, 23505–23511 (2019).
24. Véniant, M. M. *et al.* FGF21 Promotes Metabolic Homeostasis via White Adipose and Leptin in Mice. *PLOS ONE* 7, e40164 (2012).
25. Dollet, L. *et al.* FGF21 Improves the Adipocyte Dysfunction Related to Seipin Deficiency. *Diabetes* 65, 3410–3417 (2016).
26. Xu, W. *et al.* The blockade of the TGF-β pathway alleviates abnormal glucose and lipid metabolism of lipodystrophy not obesity. *Pharmacol. Res. Perspect.* 12, e1160 (2024).
27. Seeley, R. J. & MacDougald, O. A. Mice as experimental models for human physiology: when a few degrees in housing temperature matter. *Nat. Metab.* 3, 443–445 (2021).
28. Overton, J. M. Phenotyping small animals as models for the human metabolic syndrome: thermoneutrality matters. *Int. J. Obes. 2005* 34 Suppl 2, S53-58 (2010).
29. Cannon, B. & Nedergaard, J. Nonshivering thermogenesis and its adequate measurement in metabolic studies. *J. Exp. Biol.* 214, 242–253 (2011).
30. Kasza, I. *et al.* 'Humanizing' mouse environments: Humidity, diurnal cycles and thermoneutrality. *Biochimie* 210, 82–98 (2023).
31. Jacobsen, J. M. *et al.* Housing mice near vs. below thermoneutrality affects drug-induced weight loss but does not improve prediction of efficacy in humans. *Cell Rep.* 43, 114501 (2024).
32. Keijer, J., *et al*. What is the best housing temperature to translate mouse experiments to humans? *Mol. Metab.* 25, 168–176 (2019).
33. Gaskill, B. N. *et al.* Heat or Insulation: Behavioral Titration of Mouse Preference for Warmth or Access to a Nest. *PLOS ONE* 7, e32799 (2012).
34. Corsa, C. A. S. *et al.* Adipocyte-Specific Deletion of Lamin A/C Largely Models Human Familial Partial Lipodystrophy Type 2. *Diabetes* 70, 1970–1984 (2021).
35. Zhao, Z. *et al.* Effects of ambient temperatures between 5 and 35 °C on energy balance, body mass and body composition in mice. *Mol. Metab.* 64, 101551 (2022).
36. Matsumoto, M. *et al.* An improved mouse model that rapidly develops fibrosis in non-alcoholic steatohepatitis. *Int. J. Exp. Pathol.* 94, 93–103 (2013).
37. Scheller, E. L. *et al.* Region-specific variation in the properties of skeletal adipocytes reveals regulated and constitutive marrow adipose tissues. *Nat. Commun.* 6, 7808 (2015).
38. Murray, S. A. *et al.* Whole transcriptome analysis and validation of metabolic pathways in subcutaneous adipose tissues during FGF21-induced weight loss in non-human primates. *Sci. Rep.* 10, 7287 (2020).
39. Gliniak, C. *et al.* FGF21 Promotes Longevity in Diet-Induced Obesity Through Metabolic Benefits Independent of Growth Suppression. *Cell Metab.* In press.,.
40. Sadler, D. G., *et al*. A modest change in housing temperature alters whole body energy expenditure and adipocyte thermogenic capacity in mice. *Am. J. Physiol.-Endocrinol. Metab.* 323, E517–E528 (2022).
41. Xiao, C., *et al*. Anti-obesity and metabolic efficacy of the β3-adrenergic agonist, CL316243, in mice at thermoneutrality compared to 22°C. *Obes. Silver Spring Md* 23, 1450–1459 (2015).
42. Stanic, S. *et al.* Prolonged FGF21 treatment increases energy expenditure and induces weight loss in obese mice independently of UCP1 and adrenergic signaling. *Biochem. Pharmacol.* 221, 116042 (2024).
43. Makowski, L. *et al.* Lack of macrophage fatty-acid-binding protein aP2 protects mice deficient in apolipoprotein E against atherosclerosis. *Nat. Med.* 7, 699–705 (2001).

44. Shimomura, I. *et al.* Insulin resistance and diabetes mellitus in transgenic mice expressing nuclear SREBP-1c in adipose tissue: model for congenital generalized lipodystrophy. *Genes Dev.* 12, 3182–3194 (1998).
45. Wong, K. *et al.* Sequencing and characterization of the FVB/NJ mouse genome. *Genome Biol.* 13, R72 (2012).
46. Almind, K. & Kahn, C. R. Genetic Determinants of Energy Expenditure and Insulin Resistance in Diet-Induced Obesity in Mice. *Diabetes* 53, 3274–3285 (2004).
47. Timmermans, S. & Libert, C. Overview of inactivating mutations in the protein-coding genome of the mouse reference strain C57BL/6J. *JCI Insight* 3, (2018).
48. BonDurant, L. D. *et al.* FGF21 Regulates Metabolism Through Adipose-Dependent and -Independent Mechanisms. *Cell Metab.* 25, 935-944.e4 (2017).
49. Zhong, L. *et al.* Single cell transcriptomics identifies a unique adipose lineage cell population that regulates bone marrow environment. *eLife* 9, e54695 (2020).
50. Chaffin, A. T. *et al.* FGF21 controls hepatic lipid metabolism via sex-dependent interorgan crosstalk. *JCI Insight* 7, e155848.
51. Potthoff, M. J. *et al.* FGF21 induces PGC-1α and regulates carbohydrate and fatty acid metabolism during the adaptive starvation response. *Proc. Natl. Acad. Sci.* 106, 10853–10858 (2009).
52. Wei, W. *et al.* Fibroblast growth factor 21 promotes bone loss by potentiating the effects of peroxisome proliferator-activated receptor γ. *Proc. Natl. Acad. Sci. U. S. A.* 109, 3143–3148 (2012).
53. Tang, Y. & Zhang, M. Fibroblast growth factor 21 and bone homeostasis. *Biomed. J.* 46, 100548 (2023).
54. Li, X. *et al.* FGF21 Is Not a Major Mediator for Bone Homeostasis or Metabolic Actions of PPARα and PPARγ Agonists. *J. Bone Miner. Res.* 32, 834–845 (2017).
55. Andersen, B. *et al.* FGF21 decreases body weight without reducing food intake or bone mineral density in high-fat fed obese rhesus macaque monkeys. *Int. J. Obes.* 42, 1151–1160 (2018).
56. Li, Z. *et al.* Constitutive bone marrow adipocytes suppress local bone formation. *JCI Insight* 7, e160915.
57. Hadadi, N. *et al.* Comparative multi-tissue profiling reveals extensive tissue-specificity in transcriptome reprogramming during thermal adaptation. *eLife* 11, e78556 (2022).
58. Huang, W., *et al*. Development of an adipose-tropic AAV capsid ablating liver tropism. *iScience* 27, 110930 (2024).
59. Sommer, N. *et al.* Gene therapy restores adipose tissue and metabolic health in a pre-clinical mouse model of lipodystrophy. *Mol. Ther. Methods Clin. Dev.* 27, 206–216 (2022).
60. Tiwari, M. *et al.* Preclinical evaluation of tissue-selective gene therapies for congenital generalised lipodystrophy. *Gene Ther.* 31, 445–454 (2024).
61. Moitra, J. *et al.* Life without white fat: a transgenic mouse. *Genes Dev.* 12, 3168–3181 (1998).
62. Mcilroy, G. D., *et al.* Female adipose tissue-specific Bscl2 knockout mice develop only moderate metabolic dysfunction when housed at thermoneutrality and fed a high-fat diet. *Sci. Rep.* 8, 17863 (2018).
63. Wang, A. S., *et al*. Tissue specific loss of A-type lamins in the gastrointestinal epithelium can enhance polyp size. *Differ. Res. Biol. Divers.* 89, 11–21 (2015).

64. Bagchi, D. P. & MacDougald, O. A. Identification and Dissection of Diverse Mouse Adipose Depots. *JoVE J. Vis. Exp.* e59499 (2019) doi:10.3791/59499.
65. Parlee, S. D., *et al*. Quantifying size and number of adipocytes in adipose tissue. *Methods Enzymol.* 537, 93–122 (2014).
66. Love, M. I., *et al*. Moderated estimation of fold change and dispersion for RNA-seq data with DESeq2. *Genome Biol.* 15, 550 (2014).
67. Mi, H., *et al*. PANTHER version 14: more genomes, a new PANTHER GO-slim and improvements in enrichment analysis tools. *Nucleic Acids Res.* 47, D419–D426 (2019).
68. Subramanian, A. *et al.* Gene set enrichment analysis: A knowledge-based approach for interpreting genome-wide expression profiles. *Proc. Natl. Acad. Sci.* 102, 15545–15550 (2005).
69. Scheller, E. L. *et al.* Use of Osmium Tetroxide Staining with Microcomputerized Tomography to Visualize and Quantify Bone Marrow Adipose Tissue *In Vivo*. in *Methods in Enzymology* (ed. Macdougald, O. A.) vol. 537 123–139 (Academic Press, 2014).
70. Ferrannini, E. The theoretical bases of indirect calorimetry: a review. *Metabolism.* 37, 287–301 (1988).
71. Riachi, M., *et al*. Percent relative cumulative frequency analysis in indirect calorimetry: application to studies of transgenic mice. *Can. J. Physiol. Pharmacol.* 82, 1075–1083 (2004).
72. Simonson, D. C. & DeFronzo, R. A. Indirect calorimetry: methodological and interpretative problems. *Am. J. Physiol.* 258, E399-412 (1990).
73. Tschöp, M. H. *et al.* A guide to analysis of mouse energy metabolism. *Nat. Methods* 9, 57–63 (2011).
74. Kaiyala, K. J. Mathematical model for the contribution of individual organs to non-zero y-intercepts in single and multi-compartment linear models of whole-body energy expenditure. *PloS One* 9, e103301 (2014).
75. Kaiyala, K. J. & Schwartz, M. W. Toward a more complete (and less controversial) understanding of energy expenditure and its role in obesity pathogenesis. *Diabetes* 60, 17–23 (2011).
76. Frayn, K. N. Calculation of substrate oxidation rates in vivo from gaseous exchange. *J. Appl. Physiol.* 55, 628–634 (1983).

Chapter 4 Creation and Characterization of Novel Pathogenic *Lmna* Variant Mouse Lines

4.1 Abstract

Familial partial lipodystrophy 2 (FPLD2) is a rare condition that induces adipose tissue loss and redistribution, accompanied by metabolic dysfunction. FPLD2 is caused by pathogenic variants in *LMNA*, encoding the nuclear lamina proteins lamin A/C, which play a role in nuclear structure, mechanosensing, and control gene expression. Mechanisms of adipocyte loss in FPLD2 continue to be unclear, as existing studies utilize models of *Lmna* knockout or overexpression of *Lmna* variants, which do not recreate the genetic basis of FPLD2 in humans. We created seven new *Lmna* knock-in variant mouse models harboring pathogenic FPLD2-causing variants to study how these mutations cause FPLD2: T10I, R482Q, P485R, K486N, S573L, N582H, and R584H. In *Lmna* T10I, R482Q, and R584H mice, no signs of lipodystrophy or metabolic dysfunction were observed. A small decrease in adipose tissue weights were observed in *Lmna* P485R and N582H mice. *Lmna* T10I and obese P485R mice had impaired voluntary running capacity, which were not driven by a decrease in maximum muscle strength or an inability to undergo forced running. Indirect calorimetry analyses revealed that energy expenditure and fat oxidation were decreased in *Lmna* T10I and R482Q mice, which may underlie decreased running capacity as observed in *Lmna* T10I mice. Finally, RNA-seq analyses of whole adipose tissue or floated adipocytes from *Lmna* T10I, R482Q, and P485R mice showed suppression of adipogenesis and fatty acid metabolism pathways, and an increase in mTORC1 signaling, protein translation, and cell cycle pathways. In summary, though *Lmna* variant mice do not have obvious signs of lipodystrophy, they have impaired exercise capacity and changes in whole-body metabolism, which may still be informative in studying FPLD2 phenotypes. These studies have potential to provide new genetic tools to study FPLD2 and to uncover molecular mechanisms underlying laminopathies more broadly.

4.2 Introduction

Familial partial lipodystrophy 2 (FPLD2) is a rare disease that causes progressive adipose tissue loss, dysfunction, and redistribution. In FPLD2, adipose tissue is lost subcutaneously in the arms, legs, and trunk, and is redistributed to the face and dorsocervical region, and sometimes viscerally[1]. Though rare, studying lipodystrophies are of considerable interest as they are seemingly the opposite of obesity but are accompanied by many of the same metabolic comorbidities (diabetes, fatty liver disease, cardiovascular disease) due to the lack of safe lipid storage[2]. Studying FPLD2 can reveal new therapeutic targets for patients and reveal how adipose tissue is maintained in the body, which could be important for obesity and metabolic disease targeting.

Pathogenic variants in *LMNA,* which encodes the proteins lamin A/C, underlies FPLD2, and are typically monoallelic and inherited in an autosomal dominant manner. Lamin A/C are type V intermediate filaments and are part of the nuclear lamina, which interacts closely with the inner nuclear membrane. Lamin A/C facilitate nuclear transport, provide nuclear structure and stability, are important in mechanosensing, and bind to DNA at lamina-associated domains (LADs)[3]. More broadly, pathogenic variants in the lamin A/C gene can cause other diseases, termed laminopathies. These laminopathies include dilated cardiomyopathy (DCM), Emery-Dreifuss muscular dystrophy (EDMD), Hutchinson-Gilford progeria syndrome (HGPS), and peripheral neuropathy Charcot-Marie-Tooth Disorder Type 2 (CMT2)[4–7]. It is still unclear how variants throughout the lamin A/C gene can lead to a heterogenous group of tissue-specific disorders. Therefore, study of FPLD2 and the effect of pathogenic variants on lamin A/C biology may provide insights into molecular mechanisms of other laminopathies.

The mechanisms of adipocyte loss in FPLD2 are still unclear. Many groups have studied *Lmna* KO mouse embryonic fibroblasts (MEFs) and *Lmna* global KO mice to investigate the fundamental role of lamin A/C in tissue homeostasis, but many studies have contradicting data and effects of *Lmna* KO have proven difficult to study due to confounding factors, like runting and premature death in global *Lmna* KO mice[8–11]. Our lab has created a model of adipocyte-specific lamin A/C knockout (KO) in mice ($Lmna^{ADKO}$), which recapitulated many features of FPLD2, including the development and subsequent loss of WAT, accompanied by insulin resistance and hepatic steatosis[12]. From our other work (**Chapter 2**), we have determined that adipocytes lacking lamin A/C shrink and disappear and have decreased lipogenesis and increased

inflammation gene expression. These investigations into lamin A/C deficiency in adipocytes have been illuminating in revealing the fundamental role of LMNA in adipocyte maintenance but are confounded by the full deletion of lamin A/C rather than expression of a mutated lamin A/C, which is what occurs in FPLD2 and in laminopathies. Therefore, more refined and translational mouse models are needed to understand mechanisms of lipodystrophy and pathology of other laminopathies.

Two lab groups have created mice overexpressing human lamin A harboring the R482Q mutation driven by the aP2 (FABP4) promoter[13,14]. R482Q mice created by Wojtanik et al. had reduced fat mass and WAT weights compared to control mice, but development of lipodystrophy was slow and subtle, and required 32 weeks of HFD challenge[13]. These mice had insulin resistance and hepatic lipid accumulation, like patients with FPLD2. The other R482Q mice created by Le Dour et al. in 2017 did not develop lipodystrophy or metabolic dysfunction, even when challenged with HFD[14]. However, the Le Dour et al. paper showed that R482Q lamin A WAT had an increase in fibrosis and TGFb1 signaling. These studies were informative and helpful for the field in studying the effect of primary lamin mutations on WAT in mice, but had multiple caveats, including 1) the use of the aP2 promoter, expressed in not just adipocytes but also macrophages[15], 2) overexpression instead of endogenous expression levels of the lamin A R482Q variant, and 3) only lamin A harboring the mutation, instead of both lamin A and C.

Animal models to study other laminopathies beyond FPLD2 have been created, including numerous lamin A/C knock-in models: *Lmna* H222P mice to study muscular dystrophy and cardiomyopathy[16], *Lmna* L530P to study muscular dystrophy and progeria[17], *Lmna* R541C[18] and N195K[19] to study DCM, *Lmna* del.32K to study CMD and EDMD[20], and *Lmna* R249W to study congenital muscular dystrophy (CMD)[21]. Surprisingly, most of these models expressing knock-in *Lmna* variants did closely recapitulate features of muscular dystrophy and cardiomyopathy, with many of these mouse models suffering from premature death and obvious skeletal abnormalities, unlike the models of FPLD2 mentioned above. Progeroid syndromes have been studied in detail using the *Lmna* G609G mice, which also phenocopy HGPS closely[22]. The discrepancy in different *Lmna* variants causing disease in mice but not FPLD2-causing variants may highlight differences between mouse and human lamin A/C and underscores certain amino acid residues crucial for lamin functioning in mice. These new lamin A/C variant models are helpful in

studying DCM and EDMD, but models to study molecular mechanisms of lipodystrophy when lamin A/C is mutated are still lacking.

Our goal was to create more refined mouse models to study FPLD2 and other associated laminopathies by knocking in known lamin A/C mutations into mice. Using CRISPR-Cas9, we targeted three different exons to create seven new variant mouse lines. Exon 1 was targeted to create *Lmna* T10I mice – this variant in patients causes generalized lipodystrophy, diabetes, progeroid features, and cardiomyopathy[23]. Exon 8 was targeted to create *Lmna* R482Q, P485R, and K486N mice. *LMNA* R482 is the most commonly mutated residue in FPLD2, and the R482Q variant causes typical FPLD2 symptoms like decreased subcutaneous WAT, increased WAT around the face and neck, and metabolic syndrome[24]. The *Lmna* P485R variant causes partial lipodystrophy and progeroid symptoms[25], and the K486N variant causes typical FPLD2 features[26]. We created variants S573L, N582H, and R584H in exon 11, which only affects lamin A. The *LMNA* S573L variant causes generalized lipodystrophy, progeroid features, and arthropathy[27]. The R584H variant causes typical FPLD2 features and loss of subcutaneous adipose tissue[28]. We tried to create the FPLD2-causing R582H variant in mice, but due to a three amino acid difference in length between human and mouse lamin A/C, the 582nd residue in mice is N582. Therefore, N582H is not a pathogenic variant that causes FPLD2 in patients, but we were interested in studying this novel variant to see its effect on lamin biology. In this study, we explored the effect of these various *Lmna* variants on fat mass, energy expenditure and substrate oxidation, and on the WAT transcriptome. We found that though lipodystrophy phenotypes are mild or non-existent across different *Lmna* variant mice, much of the adipose tissue molecular signature is shared between various mutations.

4.3 Results

To study the effects of pathogenic *Lmna* variants in mice, and to see if these variants in mice phenocopy human laminopathies and FPLD2, we created seven new *Lmna* variant lines using CRISPR-Cas9 (**Figure 4.1 A**). These variants are *Lmna* T10I (Exon 1), R482Q, P485R, K486N (Exon 8), and S573L, N582H, and R584H (Exon 11). We validated the presence of the variant via sequencing, and ensured there were no off-target mutations. All variants had the single amino acid mutation and no off-target mutations besides R584H, which contained the R584H variant in addition to the downstream deletion of two base pairs and additional base pair mutation, which should produce a truncated lamin A/C – we will designate this variant R584H*. We re-bred the R584H founder to produce the real R584H line with no other off-target mutations, which was validated via sequencing.

To investigate phenotypes across the seven newly created variant lines, we performed body composition analyses. We did not see any difference in body weight, fat mass, or lean mass of adult male or female T10I, R482Q, P485R, N582H, or R584H mice compared to controls (**Figure 4.2**). We continued to investigate *Lmna* T10I mice, as this variant causes the most severe phenotype in patients out of the seven variants we created in mice. We euthanized the T10I cohort shown in **Figure 4.2 A** and performed necropsy analyses. We saw no difference in body weight, body length, fed glucose concentrations, or weights of posterior subcutaneous white adipose tissue (psWAT), gonadal white adipose tissue (gWAT), or liver of *Lmna* T10I/+ heterozygous mice compared to controls (**Figure 4.3 A, B, Supplemental Figure 4.1 A-D**). Weights of other organs and depots like spleen, heart, retroperitoneal white adipose tissue (rpWAT), perirenal white adipose tissue (prWAT), brown adipose tissue (BAT), and diameter of the gastrocnemius muscle were not changed in variant mice compared to controls (**Supplemental Figure 4.1 C-H**). Since we saw no obvious lipodystrophy phenotype in *Lmna* T10I variant mice housed at 22°C and fed normal chow (NC) (**Figure 4.3 B, C**), we challenged T10I mice by changing environmental temperature and diet. We put male *Lmna* T10I mice on a 60% high-fat diet (HFD), with the hopes that overloading WAT with lipid may cause adipose dysfunction and lipodystrophy, and housed them at a thermoneutral 30°C, which better mimics human housing conditions[29]. We placed male mice on HFD when they were four to six-weeks-old, and monitored them for multiple months after – we saw no change in body weight (**Supplemental Figure 4.1 I**), fat mass (**Figure 4.3 E**) or lean mass (**Figure 4.3 F**), or fasted

glucose at 15-17 weeks of age (**Supplemental Figure 4.1 J**) in T10I/+ or T10I/T10I (homozygous) variant mice compared to controls. We took female *Lmna* T10I mice and kept them on NC but housed them at thermoneutrality, and measured their body weight, fat mass, lean mass, and fasted glucose, which was not different regardless of genotype (**Figure 4.3 G, H, Supplemental Figure 4.1 K, L**). We then analyzed serum expression of circulating adiponectin in female mice at 15-17 weeks of age and observed no difference in adiponectin with genotype (**Supplemental Figure 4.1 M**). We euthanized both the male and female cohorts to evaluate whether these mice had lipodystrophy or other phenotypes of laminopathies. WAT, BAT, and liver weights and circulating triacylglycerols (TAG) were not different in male *Lmna* T10I mice compared to controls (**Figure 4.3 I, J**), and neither were other organ weights (**Supplemental Figure 4.1 N**). The same observation held for female mice, which also had no change in WAT or organ weights, or TAG concentrations (**Figure 4.3 K, L, Supplemental Figure 4.1 O**). Taken together, *Lmna* T10I mice do not have obvious signs of lipodystrophy or other laminopathies in male or female mice, regardless of whether the variant is present as monoallelic or biallelic.

T10I variant mice did not have any obvious changes in WAT weights, which we hypothesized may be due to loss and turnover of T10I adipocytes, accompanied by compensation of newly formed adipocytes to maintain the depot. To test this, we utilized the mTmG reporter system, crossed with Adiponectin-CreERT2 in either +/+, T10I/+, or T10I/T10I mice[30]. In the mTmG system, cells express membrane tdTomato globally, but if Cre is present, cells express membrane GFP. Therefore, we can track the fate of GFP positive cells that have Cre activity (in this case, only adipocytes in a tamoxifen-inducible manner) while monitoring formation of new cells, marked with tdTomato. We injected all mice with tamoxifen and imaged their WAT 12 weeks later and observed no obvious changes in the GFP vs. tdTomato ratio of adipocytes or in adipocyte morphology in psWAT (**Figure 4.4 A**) or gWAT (**Figure 4.4 B**). We quantified the percentage of GFP+ and tdTomato positive cells in psWAT (**Figure 4.4 C**) and gWAT (**Figure 4.4 D**) and confirmed there was no difference in *Lmna* T10I mice compared to controls. Therefore, under the conditions evaluated, the *Lmna* T10I variants does not affect adipocyte maintenance, morphology, or turnover rate.

We next evaluated the presence of molecular changes that occur with the *Lmna* T10I variant in WAT. Previous studies have shown that *Lmna* T10I cardiomyocytes have altered chromatin-lamin interactions, which disorganizes lamina-associated domains (LADs) and

dysregulates gene expression[31]. We performed bulk RNA-sequencing (RNA-seq) on gWAT from male and female mice fed NC housed at 22°C (**Figure 4.2 A-C**) and from female mice fed NC housed at 30°C (**Figure 4.3 G, H**) to evaluate the effects of sex, temperature, and the T10I variant on the WAT transcriptome. We observed that there were ~12500 differentially expressed genes when comparing male vs. female WAT regardless of genotype, underscoring the importance of sex as a biological variable. Next, we saw that ~9000 genes were altered when comparing 22°C vs. 30°C housing temperatures, indicating a full remodeling of the WAT transcriptome with changes in environmental temperature. When we controlled for sex and environmental temperature, we only observed eight differentially expressed genes between T10I/+ and +/+ mice, and ten changed genes between T10I/T10I and +/+ mice. Therefore, we performed Gene Set Enrichment Analysis (GSEA) to understand shifts in gene expression patterns not dependent on differentially expressed genes[32]. When comparing T10I/+ and control WAT, we observed downregulation of pathways related to adipogenesis, myogenesis, and inflammation, accompanied by an increase in ribosome, protein translation, and DNA repair pathways (**Figure 4.4 E**). We saw similar pathways altered in the T10I/T10I vs. control comparison, with decreased skeletal muscle, endothelial cell, and inflammatory pathways and upregulated ribosome, DNA repair, and mTORC1 signaling pathways (**Figure 4.4 F**). Therefore, in lieu of a lipodystrophy phenotype, we observed subtle transcriptomic changes in *Lmna* T10I variant WAT, which may serve as hints to understand the effects (or the lack of) expressing this amino acid mutation *in vivo*.

Patients with the *Lmna* T10I variant have lipodystrophy accompanied by other symptoms, like progeroid-like features, cardiomyopathy, and muscular dystrophy[23]. Therefore, we decided to explore other potential phenotypes beyond lipodystrophy, and challenged *Lmna* T10I mice with exercise to investigate any primary muscle or cardiac defects. We placed female mice into cages with running wheels and monitored voluntary exercise. We observed that homozygous T10I/T10I mice ran less time per day (**Figure 4.5 A**), less distance per day (**Figure 4.5 B**) at a lower average speed (**Figure 4.5 C**), but T10I/T10I mice were able to reach the same daily maximum speed as T10I/+ and control mice (**Figure 4.5 D**). We calculated the cumulative time (**Figure 4.5 E**) and distance ran (**Figure 4.5 F**) over 30 days and observed that T10I/T10I mice ran less than their control or heterozygous counterparts. Lower voluntary running could be driven by multiple factors, including 1) impaired muscle strength, 2) decreased cardiac

health/output, 3) impaired substrate release/utilization, 4) increased pain, or 5) reduced motivation/desire to exercise. We first tested maximum muscle strength via a grip strength assay and saw no difference in exerted force with genotype (**Figure 4.5 G**). We then evaluated forced running capacity via uphill treadmill running and again saw no change between genotype groups (**Figure 4.5 H-J**). We then ran mice downhill, which causes muscle damage and inflammation, but we observed no decrease in running capacity in T10I variant mice (**Figure 4.5 K-M**). In summary, *Lmna* bilallelic T10I mice run less voluntarily, but have no change in maximum muscle strength or forced running capacity.

Next, we investigated whole-body metabolism of *Lmna* T10I mice when running to investigate whether there were changes in substrate utilization during exercise, which may explain the defect in voluntary running in T10I bilallelic mice. We placed female mice into SABLE Promethion indirect calorimetry cages with a running wheel and confirmed that T10I/T10I mice ran less than control mice; we also saw that T10I/+ mice ran less than controls (**Figure 4.6 A, B**). These analyses also revealed that homozygote T10I/T10I mice had decreased energy expenditure during the dark cycle when compared to controls (**Figure 4.6 C, D**). Respiratory exchange ratio (RER) was not changed between genotypes (**Figure 4.6 E, F**) but fat oxidation was reduced in T10I/+ and T10I/T10I mice, specifically at the start of the dark cycle (**Figure 4.6 G, H**). Control mice have a spike in fat oxidation at the start of the dark cycle as they start to wake and begin physical activity and wheel running but have been eating little throughout the light cycle – therefore, mice must undergo fat oxidation to provide fuel for exercise before the post-absorptive state provides fuel for exercise. The lack of fat oxidation in T10I/+ and T10I/T10I mice may be driving the reduction in wheel running, or the decreased running activity may cause the decrease in fat oxidation. In summary, homozygous T10I variant mice have reduced energy expenditure and fat oxidation, which may underlie their decreased voluntary wheel running.

Beyond wheel running, we were interested in the effect of other metabolic stressors on *Lmna* T10I variant mice, like fasting and changes in environmental temperature. Therefore, we designed a regimen within the SABLE Promethion cages: two days of baseline measurements, a 12-hour dark cycle fast followed by a 36 hour refeed period, one day of cold exposure (10°C), one day back to ambient temperature (22°C), and one day of thermoneutrality (30°C). We placed female mice into the indirect calorimetry cages, this time with no running wheel, and monitored

their response to these metabolic stressors. First, we observed that even without the running wheels, homozygous T10I/T10I mice traveled less distance within the cage compared to T10I/+ and control mice, specifically during the baseline measurement period (**Figure 4.7 A**). We then monitored energy expenditure and saw that T10I/T10I mice had reduced metabolism compared to controls or T10I/+ mice, which held across all temperatures of 10°C, 22°C, and 30°C (**Figure 4.7 B**). We observed that RER seemed to trend lower in T10I/+ and T10I/T10I mice compared to controls across different stressors, but data were variable (**Figure 4.7 C**). Fat oxidation in T10I/T10I mice tended to decrease during baseline measurements and after being refed (**Figure 4.7 D**). Therefore, *Lmna* T10I biallelic mice have decreased energy expenditure and fat oxidation compared to controls, revealing a subtle but consistent energy imbalance.

Beyond studying the T10I variant, we were also particularly curious about the effects of the *Lmna* R482Q variant, as mutations at this residue causes 80-90% of FPLD2 incidences[33]. Other groups have knocked in the *Lmna* R482W variant to mice and have not observed a lipodystrophy phenotype (personal correspondence, unpublished data). We euthanized 10–12-week-old male and female R482Q mice (**Figure 4.2 D-F**) and observed no change in body weight, fed glucose, psWAT or gWAT weights in R482Q/+ mice compared to controls (**Figure 4.8 A-D**). We then challenged R482Q/+, as we did the *Lmna* T10I, with mice a 60% HFD or a western-style diet (WSD) with 45% fat and 17% sucrose. We also housed mice at 26°C to better "humanize" their environmental temperatures. With the 60% HFD challenge, we saw no significant change in body weight, fat mass, or lean mass in male or female variant mice compared to controls (**Figure 4.8 E-J**). WSD challenge in male and female mice also did not cause any significant changes in body weight, fat mass, or lean mass dependent on genotype (**Figure 4.8 K-P**). Therefore, NC feeding at 22°C, or HFD or WSD challenge at 26°C does not induce lipodystrophy in *Lmna* R482Q mice.

We next evaluated changes in circulating adiponectin, and again did not see any differences in expression between genotypes in female or male mice (**Figure 4.9 A, B**). Insulin concentrations were also unchanged in adult female mice between R482Q/+ and controls (**Figure 4.9 C**). While breeding cohorts by pairing male and female R482Q/+ mice, we observed that no weaned and genotyped mice had the R482Q/R482Q homozygous genotype. Inspection of breeding cages at postpartum day 12 to 14 (P12-14) revealed runted and lethargic mice, often with kinked tails; these mice all died by the end of P14 (**Figure 4.9 D**). Genotype analyses

demonstrated that these runted mice were biallelic R482Q/R482Q. Further necropsy and histological analyses revealed no obvious defects in organ development in homozygous R482Q mice, other than every tissue being smaller than that of their heterozygous or control counterparts. These mice may have cerebellar dysfunction, which was not histologically visible at this early mouse age but may occur later in life if the mice were able to survive longer. Therefore, these data suggest that the R482Q variant causes loss of function of lamin A/C, as their phenotype is very similar to that of the global *Lmna* knockout mice, which have muscular dystrophy and die by three to eight weeks of age[8,9].

Further analyses of psWAT, pmWAT and rpWAT crossed onto the Adiponectin-CreERT2 and mTmG backgrounds did not reveal changes in adipocyte turnover in R482Q/+ mice four weeks post-tamoxifen (**Figure 4.9 E**). Finally, we floated adipocytes from psWAT of control and heterozygous R482Q/+ male and female mice and performed bulk RNA-seq to investigate adipocyte-specific transcriptomic changes. When comparing effects of just sex, ~2200 genes were differentially expressed between male and female psWAT adipocytes. When we analyzed effects of genotype, only 21 genes were differentially expressed between R482Q/+ mice and controls, including downregulation of *Mc5r, Fkbp5, Saa1*, *Saa2*, and *Tmem52,* and upregulation of *Muc15*, *Foxa1, Tmem30b,* and *Map2*. Due to this small number of differentially expressed genes, we performed GSEA to analyze large pattern changes in gene expression. GSEA revealed that heterozygous R482Q mice had decreased adipogenesis, oxidative phosphorylation, and fatty acid metabolism pathways, with increased inflammation and epithelial mesenchymal transition (EMT) pathways (**Figure 4.9 F**). Taken together, WAT from R482Q/+ mice has a molecular signature indicating possible dysfunction of adipose tissue, similar to that of T10I/+ and T10I/T10I mice (**Figure 4.4 E, F**).

We were curious to see if the decreased voluntary running phenotype was consistent across different variant mouse models, like that of the *Lmna* T10I mice. When we ran female R482Q/+ and control mice, there was no change in time, distance, or speed on the running wheel between genotypes (**Supplemental Figure 4.2 A-F**). Grip strength and forced running capacity was also not changed in R482Q/+ variant mice compared to controls (**Supplemental Figure 4.2 G-J**). Therefore, we saw no evidence of decreased exercise capacity or muscle strength in R482Q variant mice.

To follow up on the bulk RNA-seq analyses of R482Q/+ psWAT adipocytes, we placed ~1 year old female control and heterozygous mice into SABLE Promethion indirect calorimetry cages to follow their whole-body metabolism. We took two days of baseline measurements, then fasted the mice for 12 hours, re-fed for 36 hours, and cold exposed them to 10°C for one day. With this regimen, we observed a tending increase in energy expenditure in R482Q/+ mice compared to controls, especially during cold exposure (**Figure 4.10 A**). We observed that RER was increased in R482Q/+ mice vs. controls across the different metabolic stressors (**Figure 4.10 B**). Following the RER data, fat oxidation tended to decrease (**Figure 4.10 C**), and glucose oxidation was increased in R482Q/+ mice compared to controls (**Figure 4.10 D**). These changes in substrate utilization were most apparent during the fasted state and cold exposure. Therefore, R482Q/+ mice tend to have increased energy expenditure and glucose oxidation, demonstrating a potential metabolic reprogramming or compensatory mechanism to maintain homeostasis.

Analyses of *Lmna* T10I and R482Q variant mice have not yet revealed an obvious lipodystrophy phenotype. However, our screening of another line, P485R, did show promising hints of fat loss, with a reduction in fat mass via body composition analyses in female homozygous P485R/P485R mice but not in heterozygous or control mice, and no change in body weight or lean mass with genotype (**Figure 4.11 A-C**). Necropsy data at euthanasia revealed no change in body weight, length, or fed glucose concentrations, but did show a trending decrease in psWAT and pmWAT weights of homozygous P485R mice (**Figure 4.11 D-H**). Other WAT depots like rpWAT and prWAT were not changed in weight with genotype (**Figure 4.11 I, J**). Weights of liver, heart, and BAT were not altered regardless of genotype, and neither was gastrocnemius muscle diameter (**Figure 4.11 K-N**). Analysis of circulating TAG, insulin, and adiponectin did not reveal changes with genotype (**Figure 4.11 O-Q**). Therefore, *Lmna* homozygous P485R mice may have a small decrease in WAT weights, but do not closely phenocopy FPLD2 in patients.

Like the other lines analyzed thus far, we performed bulk RNA-seq on whole psWAT from +/+, P485R/+, and P485R/P485R mice. When comparing P485R/+ or P485R/P485R mice compared to controls, only one gene was differentially expressed in either comparison: predicted pseudogene 8730 (*Gm8730*). We then performed GSEA and observed suppression of pathways related to adipogenesis, oxidative phosphorylation, fatty acid metabolism, and inflammation in either heterozygous or homozygous WAT compared to controls (**Figure 4.11 R, S**). Activated

pathways were related to EMT, chromosome segregation, and DNA replication (**Figure 4.11 R, S**). These GSEA patterns closely align with the RNA-seq pathways identified in adipose from *Lmna* T10I and R482Q mice, highlighting the consequence of single amino acid *Lmna* variants in altering the WAT transcriptome.

We next challenged 12-week-old *Lmna* P485R mice housed at 26°C with 60% HFD when housed at 26°C and monitored mice over time. We saw no change in body weight, fat mass, or lean mass with genotype (**Figure 4.12 A-C**). Therefore, we challenged P485R mice with exercise and placed them into cages with voluntary running wheels. We kept mice on 60% HFD for two weeks, and then changed their diet to NC to see if diet influenced running activity. We observed that homozygous P485R mice ran less time and distance, and at a lower speed than control or heterozygous mice (**Figure 4.12 D-I**). However, this decrease in running time was not driven by muscle weakness as measured by grip strength (**Figure 4.12 J**). When we ran non-obese NC-fed P485R mice in a separate experiment, P485R variant mice had no change in running capacity compared to controls (**Supplemental Figure 4.3 A-E**). Therefore, at least for the *Lmna* P485R line, there is an interplay of diet and exercise that is required to see decreased running capacity in homozygous variants.

We have screened other variant lines to see if other *Lmna* mutations cause lipodystrophy or other laminopathy phenotypes. *Lmna* K486N mice did not have an impairment in running capacity or grip strength, even when the variant was biallelic (**Supplemental Figure 4.3 F-J**). We have also analyzed a small cohort of male and female monoallelic *Lmna* N582H variant mice, and saw a decrease in psWAT and gWAT weights, and an increase in heart weights in variant mice versus controls (**Supplemental Figure 4.4 D, E, J**). No other organs or WAT depots were changed in weight in N582H mice (**Supplemental Figure 4.4 A-C, F-I, K, L**). Though this variant has not been observed to cause disease in humans, it likely impacts lamin A/C functioning in mice, causing a mild lipodystrophy.

Finally, we analyzed *Lmna* R584H*, which does not occur in humans, but we were interested in studying to see effects of a truncated lamin A/C protein *in vivo*. We saw no change in WAT or organ weights in male or female variant mice housed at 22°C fed NC compared to controls (**Supplemental Figure 4.5**). Challenge with HFD at 30°C in male mice (**Supplemental Figure 4.6**) or analysis of females kept on NC housed at 30°C (**Supplemental Figure 4.7**) revealed no difference in WAT or organ weights with genotype. Therefore, though R584H*

causes additional mutations within lamin A/C and an early truncation of the lamin A protein, mice are surprisingly resistant to these changes and can maintain homeostasis.

4.4 Discussion

In this study, we explored changes in fat mass, lean mass, and body weight across different *Lmna* variant lines under standard conditions (NC, 22°C), and at various housing temperatures (26°C, 30°C) with diet changes (HFD, WSD). We also carefully dissected multiple cohorts across different experimental conditions to screen for lipodystrophy or signs of other laminopathies. Generally, *Lmna* variant mice across mutations (T10I, R482Q, R584H, R584H*), regardless of whether mutations were monoallelic or biallelic, did not exhibit obvious signs of lipodystrophy or adipose tissue loss. Only *Lmna* P485R and N582H mice had hints of decreased fat mass, highlighting the potential importance of those amino acid residues in normal mouse lamin A/C functioning. Why are pathogenic *Lmna* variants that cause disease in humans not causing obvious lipodystrophy phenotypes in mice? An obvious answer is that mice are not humans, and have very different physiologies and lifestyles, including lifespan, metabolic rate, size, housing conditions, and genetic inbred background[34]. Furthermore, when considering adipose tissue biology specifically, fat pad organization is drastically different in mice and humans, with mice lacking an equivalent human visceral depot[35]. Adipocyte half-life is about 10 years in humans, and about one year in mice, which may explain differences in depot maintenance and adipocyte turnover[36]. BAT depots play a large role in thermogenesis in mice, but are less relevant in adult humans, which causes differences in lipid oxidation and glucose utilization between species[35]. Taken together, species differences likely play a large role in the lack of *Lmna* variants phenocopying human disease.

The lack of phenotype in *Lmna* variant mice is particularly puzzling because mouse and human lamin A/C have 96% homology in their amino acid sequences, with differences only present at the C-terminus tail. However, differences must exist in the requirement of certain amino acid residues for normal lamin A/C function. Lamin A/C is required for whole-body health, development, and homeostasis, as global *Lmna* KO causes muscular dystrophy and death by eight weeks of age[8,9]. It may be that pathogenic variants that cause EDMD and DCM in humans can also be phenocopied in mice due to their essential role in maintaining nuclear lamina structure or in mechanosensing – EDMD and DCM-causing mutations are often located within the rod domain, which is a region crucial for lamin A/C structure and assembly. Other *Lmna* variant models have shown inconsistencies between human and mouse disease phenotypes: for example, the CMT2-causing *LMNA* variant R298C has been knocked into mice but did not cause

clinical features seen in humans, like peripheral neuropathy changes or signs of decreased muscle strength[37]. A potential reason for these discrepancies are highlighted by a recent study investigating effects of two *LMNA* variants on lamina-chromatin interactions[31]. The investigators expressed the T10I or R541C variant in human induced pluripotent stem cells (hiPSCs) and differentiated cells into cardiomyocytes, adipocytes, or hepatocytes and performed chromatin immunoprecipitation sequencing (ChIP-seq) to map lamin-DNA interactions. The resulting *LMNA* T10I or R541C mutant cardiomyocytes had impaired physiology and remodeled chromatin architecture, but that T10I and R541C hepatocytes or adipocytes did not have altered nuclear structure or LAD changes[31]. This study reveals that pathogenic *LMNA* variants disrupt physiology in a cell-type specific manner and may explain why laminopathies are often tissue-specific – our studies should thus include analyses of not just adipose tissue, but other tissues that may be influenced by lamin mutations.

We observed that homozygous *Lmna* T10I and HFD-fed *Lmna* P485R mice had decreased voluntary wheel running compared to heterozygous or control mice, which was not due to obvious muscle weakness as measured by grip strength. Multiple reasons could underlie this decrease in voluntary running, including a reduced desire to run, cardiac issues, pain, impaired coordination, or impairment of substrate utilization. Our studies have yet to reveal a clear reason for reduced running in *Lmna* variant mice, but it may be related to decreased fat oxidation as observed in homozygous T10I mice via indirect calorimetry. Future studies will investigate changes in sensory nerve density and amount, pain testing, *in vivo* cardiac testing including echocardiograms, and balance tests. Additional skeletal muscle analyses will be required to test if muscle fiber composition is changed with global *Lmna* mutations and if single muscle fibers have reduced force production. Other mouse models of lipodystrophy like the global *Bscl2* (seipin) KO mice also have reduced voluntary running, underscoring the importance of functional adipose tissue to facilitate long-term exercise[38]. Additionally patients with FPLD2 have decreased abdominal muscle strength, and reduced heart rate and power at peak exercise compared to controls when they underwent cardiopulmonary testing on a stationary bike[39]. Grip strength was also reduced in patients with FPLD2[39]. Few studies investigating exercise capacity in patients with lipodystrophy exist, and should be of future focus in the field, as patients with FPLD2 often mention issues with endurance exercise and can harbor symptoms of other laminopathies like CMD and muscular dystrophy (personal correspondence, Dr. Elif Oral).

Our studies also revealed changes in energy expenditure, RER, and substrate utilization in *Lmna* T10I and R482Q mice. We observed that with presence of a running wheel, homozygous *Lmna* T10I mice expended less energy and had decreased fat oxidation, especially at the beginning of each light cycle (**Figure 4.6**). During cold (10°C) and thermoneutrality (30°C) exposure, *Lmna* T10I/T10I mice again had reduced energy expenditure (**Figure 4.7 B**), with variable changes in fat oxidation. This reduction in energy expenditure is likely simply due to decreased movement (**Figure 4.7 A**). *Lmna* T10I mice may have slightly impaired fatty acid oxidation in adipose tissue or muscle, which should be investigated in the future by testing fatty acid oxidation enzyme expression, and lipid and acylcarnitine amounts. Furthermore, understanding whether reduced running in T10I/T10I mice is responsible for reduced fat oxidation or if impaired fat oxidation causes a decrease in running should also be investigated. In *Lmna* R482Q mice, we saw reduced fat oxidation and increased glucose oxidation when compared to controls, especially during cold exposure (**Figure 4.10**). Like *Lmna* T10I mice, this may suggest impaired fatty acid oxidation accompanied by a compensatory utilization of glucose for fuel. Patients with lipodystrophy tend to have an increased RER, with preference for glucose utilization over fatty acids[40]. Therefore, though our *Lmna* variant mice do not have obvious signs of lipodystrophy, subtle metabolic shifts suggest potential adipose tissue or global metabolism dysfunction.

Beyond *in vivo* phenotyping, we investigated transcriptomic changes in *Lmna* variant WAT across three models: T10I, R482Q, and P485R. Though very few genes were differentially expressed in variant mice compared to controls, GSEA revealed changes in certain biological pathways. Across all models, pathways related to adipogenesis, fatty acid metabolism, and lipid catabolism were decreased. These data align closely with RNA-seq datasets of WAT from patients with FPLD2 and from mice with adipocyte-specific *Lmna* KO (**Chapter 2**). Variant mice had changes in inflammatory pathways, but inflammation either went up (R482Q) or down (P485R, T10I). A common transcriptomic pattern noticed in other models of lipodystrophy involve increased inflammation, so these changes in inflammatory pathways may be indicative of adipose dysfunction, even before obvious lipodystrophy phenotypes. Other upregulated pathways across models included protein translation, mTORC1 signaling, and epithelial to mesenchymal transition (EMT). These changes may be important in the ability of *Lmna* variant mice to maintain homeostasis even when harboring a global missense mutation. Finally, *Lmna*

T10I mice had suppression of muscle cell development and myogenesis pathways. No published studies have investigated how muscle-related genes can be expressed in adipose tissue – our data may be revealing a consequence of adipose-muscle crosstalk or may be a novel finding about the requirement of functional lamin A/C to control skeletal muscle gene expression in WAT. Given the decreased running observed in *Lmna* T10I, we cannot rule out changes in adipose-muscle crosstalk in this model, which should be investigated further.

Future studies will continue to characterize *Lmna* variant mice, including strains not discussed in detail here, like K486N, S573L, and R584H. Experiments to "humanize" or stress mice may be required to reveal a lipodystrophy phenotype, as humans undergo countless stressors daily – one of these stressors could be a trigger that interacts with an underlying genetic susceptibility to cause FPLD2. Evidence for this idea is potentially supported by the large age range of FPLD2 onset – ranging from five years old up to mid-to-late-twenties[1]. Stressors like a change of housing conditions, social isolation, noise, mechanical insults, or infection/immune insult may be needed to induce lipodystrophy. Insights from our studies will hopefully reveal fundamental differences between mouse and human lamin A/C, how to model human diseases in mice, and serve as future models to understand mechanisms of FPLD2 and other laminopathies.

4.5 Materials and methods

Animals

Lmna variant mice were generated using CRISPR-Cas9 with the University of Michigan Molecular Genetics Core. Guide RNAs were uniquely designed to target exon 1, 8, or 11 using Crispor. Three guides were tested by zygote injection to confirm DNA cutting. After confirming successful DNA targeting, Cas9 (1081060, IDT) and guides (Synthego), and a designed editing oligo were injected into 150 zygotes. Founder tail DNA was genotyped via PCR and sequencing to confirm editing oligo insertion. Founders (G0) were bred onto the C57BL6/J background and G1 pups were sequenced to confirm presence of correct mutation. Mice analyzed in this study were between G3 and G4 (mixed background), besides *Lmna* T10I which were G6 and congenic for C57BL6/J. Adipoq-CreERT2 mice (025124) and mTmG mice (007576) were from the Jackson Laboratory. Mice were intraperitoneally injected with tamoxifen (50 mg/kg; 13258, Cayman Chemical) in sterile corn oil for five consecutive days to induce recombination followed by a 10-day washout. Mice were euthanized by inhaled isoflurane overdose and death was assured via cervical dislocation or bilateral pneumothorax. Fat and lean mass was measured in live animals with an EchoMRI-100H (EchoMRI LLC). Animals were group housed under standard conditions (22°C, 30-60% humidity) unless otherwise noted, with a 12-hr light:dark cycle and free access to water and chow. All animal studies were performed in compliance with policies of the University of Michigan Institutional Animal Care and Use Committee (protocol no. PRO00011544). Daily care of mice was overseen by the Unit for Laboratory Animal Medicine at the University of Michigan.

mTmG imaging and analyses

Tissues were collected from mice and placed in light-protected tubes with cold PBS on ice before imaging. Whole mount tissues were imaged in an imaging chamber in 1x PBS with an inverted confocal microscope (Nikon A1si) and 20x oil objective. mTmG images were analyzed using Fiji and the Cell Counter plugin to count red (tdTomato+) and green (GFP+) adipocytes. At least 300 adipocytes were counted over four to seven images per individual mouse.

Serum measurements

Blood was collected from tail vein or at sacrifice via inferior vena cava and was allowed to coagulate on ice for 2 hours. After centrifugation at 2000 x g for 20 minutes at 4°C, serum was collected and stored at -80°C. ELISA was used to measure circulating concentrations of insulin (90080, Crystal Chem), and triacylglycerols were measured via colorimetric assay (10010303, Cayman Chemical). Serum adiponectin concentrations were measured via immunoblot.

Adipocyte fractionation for RNA-seq analyses

WAT depots were excised from mice, minced with scissors, and digested with 533.3 U/mL collagenase type I (LS004197, Worthington). Digestion was done in Krebs-Ringer-HEPES (KRH) buffer, pH 7.4 containing 1 g/L glucose and 500 nm adenosine for 30 minutes at 37°C shaking horizontally at 100 rpm. Adipocytes were separated from the stromal vascular fraction by filtering through 300 μm filters and centrifuging at 100 x g for 7 minutes. Floating adipocytes were transferred to 5 mL tubes and washed 3 times with KRH buffer by removing the infranatant from beneath the adipocyte layer with a 5 mL syringe and 21G needle. Adipocyte fractions were flash frozen for further analyses.

Bulk RNA-sequencing from mouse WAT or floated adipocytes

Total RNA was isolated and purified from mouse WAT or floated adipocytes using RNA STAT-60 (CS-110, amsbio) according to the manufacturer's instructions. After DNAse treatment, samples were submitted to Beijing Genomics Institute (BGI) for quality control, library preparation, and sequencing using the DNBSEQ Sequencing System. Raw read data quality was checked using FastQC (v0.11.9). Reads were aligned to the UCSC reference genome using STAR (v2.7.10a). FastQC was used for quality control post-alignment. Differential expression analyses were done using featureCounts/DESeq2 using UCSC build mm10 as the reference genome sequence. Gene Set Enrichment Analysis was run for the Hallmark and Gene Ontology gene set databases[32].

Voluntary wheel running assays

Mice were singly placed in cages with voluntary running wheels (no. 0297-0521; Columbus Instruments, Columbus, OH) to measure exercise performance. Voluntary running wheel exercise was monitored daily or every two days with an odometer to record the number of

running wheel revolutions, the total distance run per 24 hours, average speed, and maximum speed on the wheel.

Grip strength assay

Forelimb grip strength was measured using a grip strength meter. Mice were held by the tail and gently lowered toward the metal grip bar of the apparatus. Once the mouse had grasped the bar with its forelimbs, it was pulled backward by the base of the tail in a horizontal plane until it released the bar. The peak tension in grams was recorded automatically. Each mouse underwent five consecutive trials with at least 30 seconds of rest between each trial to prevent fatigue, and five trials were averaged to determine grip strength per mouse.

Uphill treadmill running assay

Mice were exercised on an Exer-3/6 adjustable variable-speed belt treadmill (no. 0257-901M; Columbus Instruments, Columbus, OH) with the shock grid at the back of the treadmill set to deliver shocks at an intensity of ~0.4 mA in 200-ms pulses separated at a maximum rate of 11 shocks per 10 seconds. Before functional testing, mice were first acclimated to treadmill running by being exercised for a total of 15 minutes, starting at a speed of 8 m/min for 5 minutes and followed by 5 minutes at 12 m/min and 5 minutes at 15 m/min. Mice were ran until exhaustion: exhaustion was defined by one of these criteria being satisfied: 1) spending greater than 50% of its time on the shock grid or 2) the third time a mouse is willing to sustain 2 seconds or more of shocking rather than attempting to return to the treadmill.

Downhill treadmill running assay

Mice were acclimated to the treadmill undisturbed for 15 minutes with the treadmill on at a low speed without the shock plate on. The treadmill was angled at -5-15 degrees. The shocking grid at the back of the treadmill was set to deliver shocks at an intensity of ~0.4 mA in 200-ms pulses separated at a maximum rate of 11 shocks per 10 seconds. The shock plate was then turned on and belt speed set to 7 m/min. The belt was then accelerated 3 m/min every two minutes until the belt was turning at 21 m/min. The mice were then exercised at this speed for up to 1 hour or until the point of exhaustion.

Indirect calorimetry

Mice were housed individually and allowed to acclimate for three days, Mice were then placed into an indirect calorimetry system (Promethion Core, Sable Systems International), and their O_2 consumption and CO_2 production, in-cage activities, food and water intake were measured at room temperature (22°C, 41% humidity) or at 10°C or 30°C as noted (12-12 hours 5:00PM~5:00AM) dark-light cycles). All animals had free access to food and water unless fasted. For *Lmna* T10I mice, a voluntary running wheel was placed in the cage. Oxygen consumption (VO_2), carbon dioxide production (VCO_2), spontaneous motor activity was measured using the Promethion System, an integrated open-circuit calorimeter equipped with an optical beam activity monitoring device. The Promethion system features high precision sensors measuring food, water intake & body weight in real time. The system was routinely calibrated each time before the experiment using a standard gas (20.5% O_2 and 0.5% CO_2 in N_2). VO_2 and VCO_2 in each cage were sampled sequentially for 30 seconds in five-minute intervals and the motor activity was recorded every second in X, Y, and Z dimensions. The air flow rate through the chambers was adjusted at the level to keep the oxygen differential around 0.3% at resting conditions. Respiratory exchange ratio (RER) was calculated as VCO_2 / VO_2. Total energy expenditure, carbohydrate oxidation, and fatty acid oxidation were calculated respectively based on the values of VO_2, VCO_2, without the estimation of protein breakdown (which is usually estimated from urinary nitrogen excretion)[41–47].

Statistics

All data was presented as mean ± SD. Two-way ANOVA with Bonferroni's post-hoc test was performed mouse data with two variables presented in the study. One-way ANOCA with Bonferroni's post-hoc test was performed for data with one variable and three groups. Student's t test was used when comparing mouse data between two genotypes. All analyses were conducted using GraphPad Prism version 10. For statistical comparisons, $p < 0.05$ was considered significant.

4.6 Figures and legends

Figure 4.1

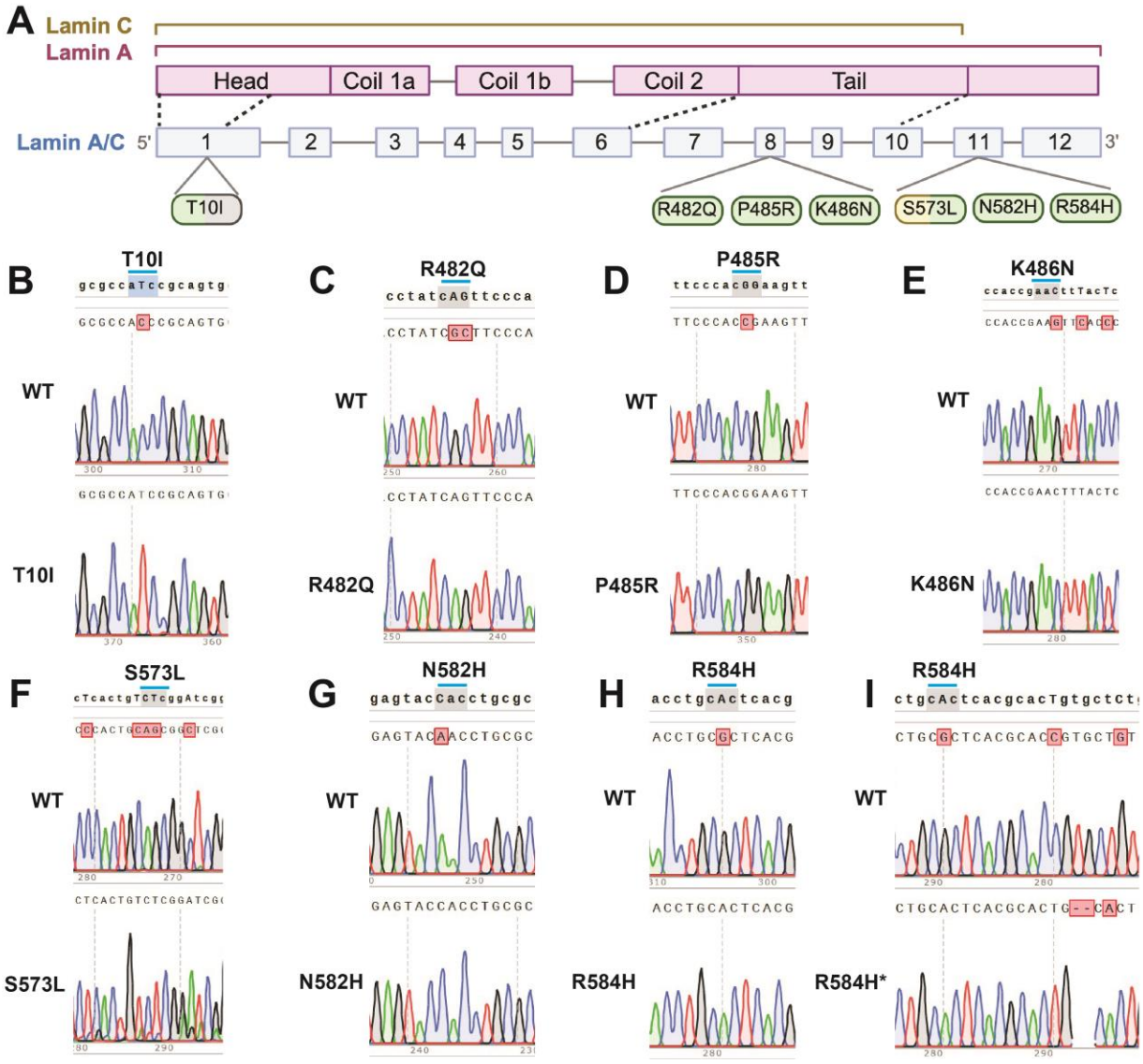


Figure 4.1. Creation and validation of seven pathogenic *Lmna* variant mouse lines. (**A**) Schematic of lamin A/C and location of seven amino acid mutations knocked into mice. Sequencing validation of (**B**) T10I, (C) R482Q, (D) P485R, (E) K486N, (F) S573L, (G) N582H, (H) R584H, (I) R584H*. Some wobble sites in WT sequences were changed back to the normal WT sequence, as marked in red. R584H* has two base pair deletions and one substitution downstream of R584H mutation site.

Figure 4.2

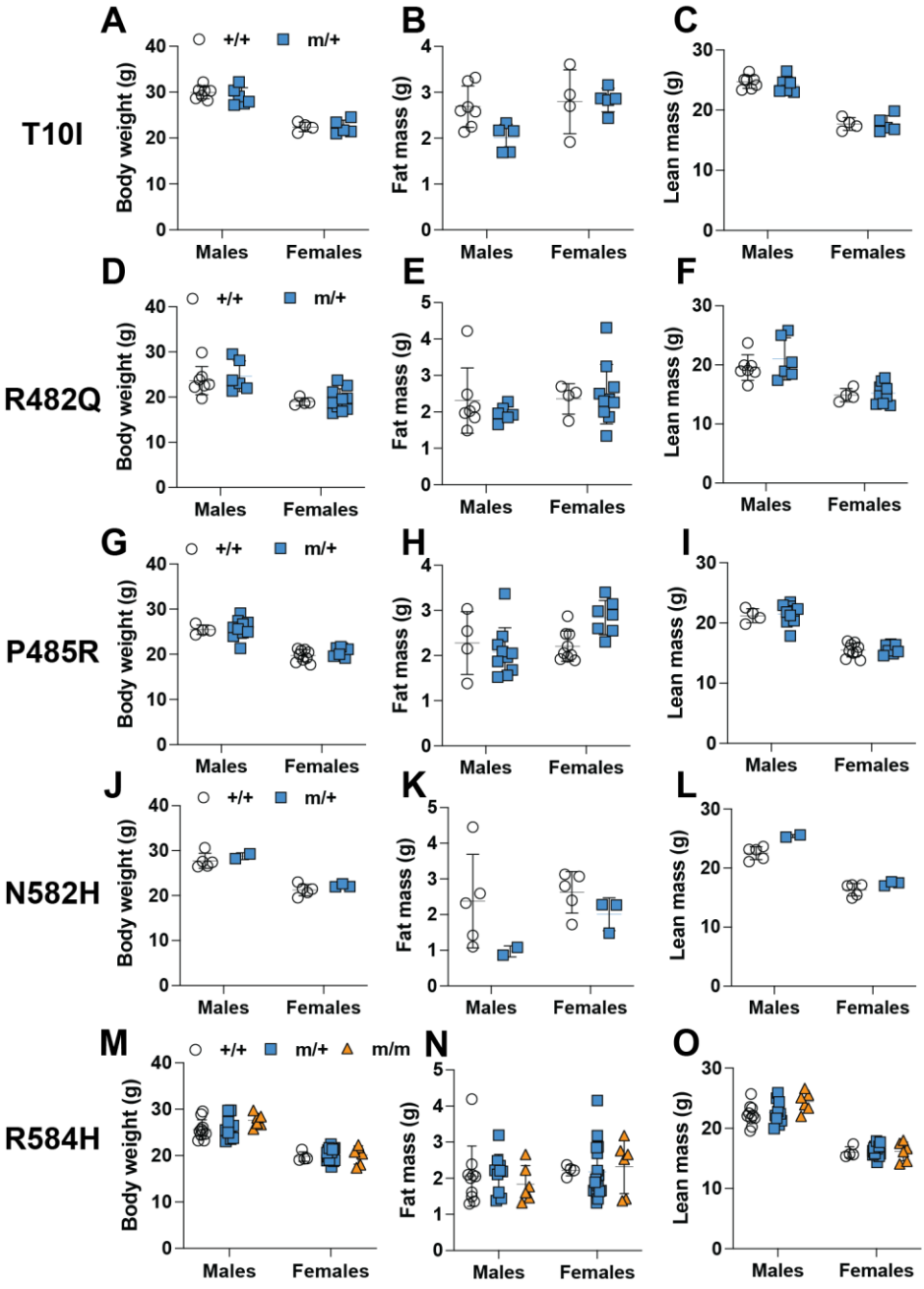


Figure 4.2. Body composition analyses of different *Lmna* variant lines revealed no changes in body weight, fat mass, or lean mass. All mice were on normal chow and housed at 22°C and were 20 weeks of age. +/+ = wildtype controls, m/+ = heterozygous, m/m = homozygous. (**A**) Body weight, (**B**) fat mass, and (**C**) lean mass in male and female *Lmna* T10I mice as measured by EchoMRI. (**D**) Body weight, (**E**) fat mass, and (**F**) lean mass in 10-week-old male and female *Lmna* R482Q mice. (**G**) Body weight, (**H**) fat mass, and (**I**) lean mass in 12-week-old *Lmna* P485R mice. (**J**) Body weight, (**K**) fat mass, and (**L**) lean mass in 16-week-old *Lmna* N582H mice. (**M**) Body weight, (**N**) fat mass, and (**O**) lean mass in 14-week-old *Lmna* R584H mice. All data represented as mean ± SD. Data were analyzed with two-way ANOVA with a Bonferroni post-hoc test.

Figure 4.3

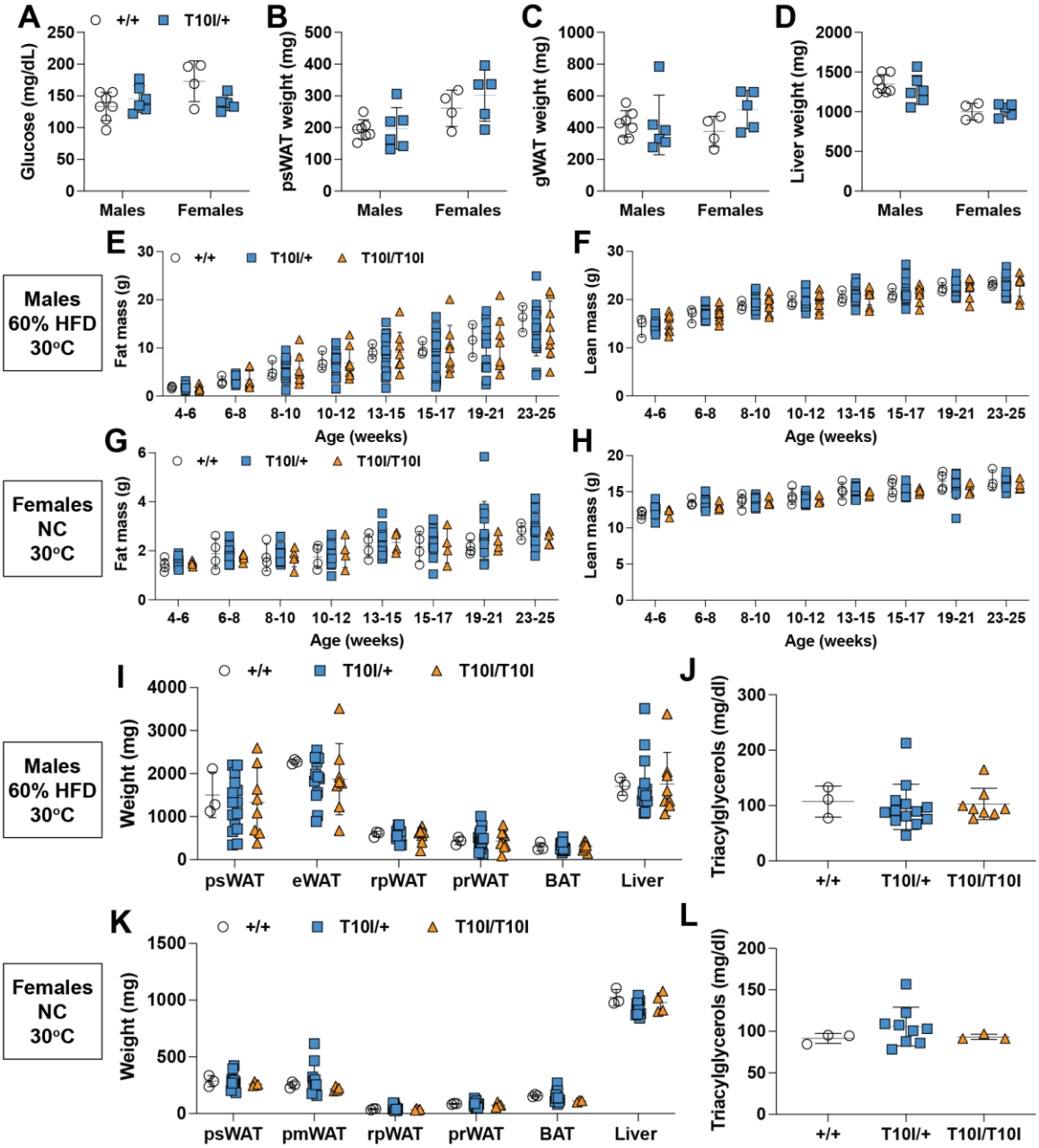


Figure 4.3. *Lmna* T10I mice had no change in white adipose tissue (WAT) mass in males or females on normal chow (NC) or high-fat diet (HFD) at 22°C or 30°C. Necropsy data of male and female *Lmna* T10I mice on NC at 22°C at 20 weeks of age, including (**A**) fed glucose, (**B**) posterior subcutaneous white adipose tissue (psWAT) weights, (**C**) gonadal white adipose tissue (gWAT) weights, and (**D**) liver weights. Male mice were challenged with 60% HFD and housed at 30°C, and (**E**) fat mass and (**F**) lean mass were measured. Female mice were housed at 30°C, with their (**G**) fat mass and (**H**) lean mass measured. Data at euthanasia of T10I male mice at 26 weeks of age: (**I**) psWAT, epididymal white adipose tissue (eWAT), retroperitoneal white adipose tissue (rpWAT), perirenal white adipose tissue (prWAT), and brown adipose tissue (BAT), and (**J**) fasted triacylglycerol concentrations. Data at euthanasia of female T10I mice at 26 weeks of age of (**K**) adipose depots and liver, and (**L**) fasted triacylglycerol concentrations. All data represented as mean ± SD. Data were analyzed with two-way ANOVA with a Bonferroni post-hoc test.

Figure 4.4

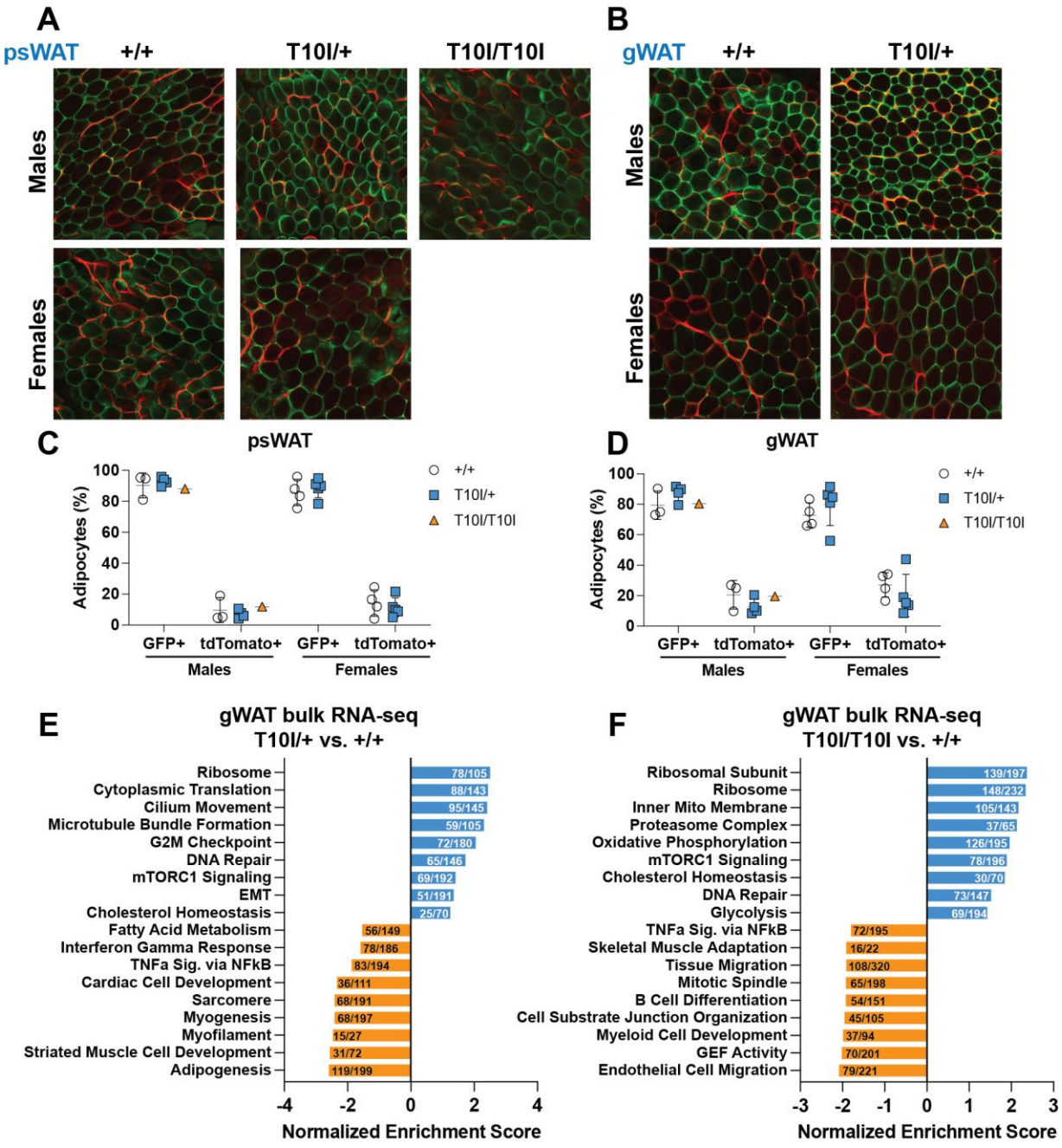


Figure 4.4. No difference in adipocyte turnover rates but bulk RNA-seq analyses reveal *Lmna* T10I WAT has decreased adipogenic and skeletal muscle pathways, and increased protein translation and mTORC1 signaling pathways. Adiponectin-CreERT2 and mTmG background crossed with T10I mice: 24-week-old *Lmna* T10I WAT 12-weeks post-tamoxifen from male and female mice and imaged fresh via confocal of (**A**) psWAT and (**B**) gWAT, with quantification of GFP+ and tdTomato+ adipocytes in (**C**) and (**D**). Gene set enrichment analysis (GSEA) of bulk RNA-seq performed on gWAT from male and female T10I mice housed at 22°C and 30°C, with comparisons of (**E**) T10I/+ vs. +/+ and (**F**) T10I/T10I vs. +/+. Numbers on bars are the number of genes driving each pathway. All data represented as mean ± SD. Data were analyzed with two-way ANOVA with a Bonferroni post-hoc test.

Figure 4.5

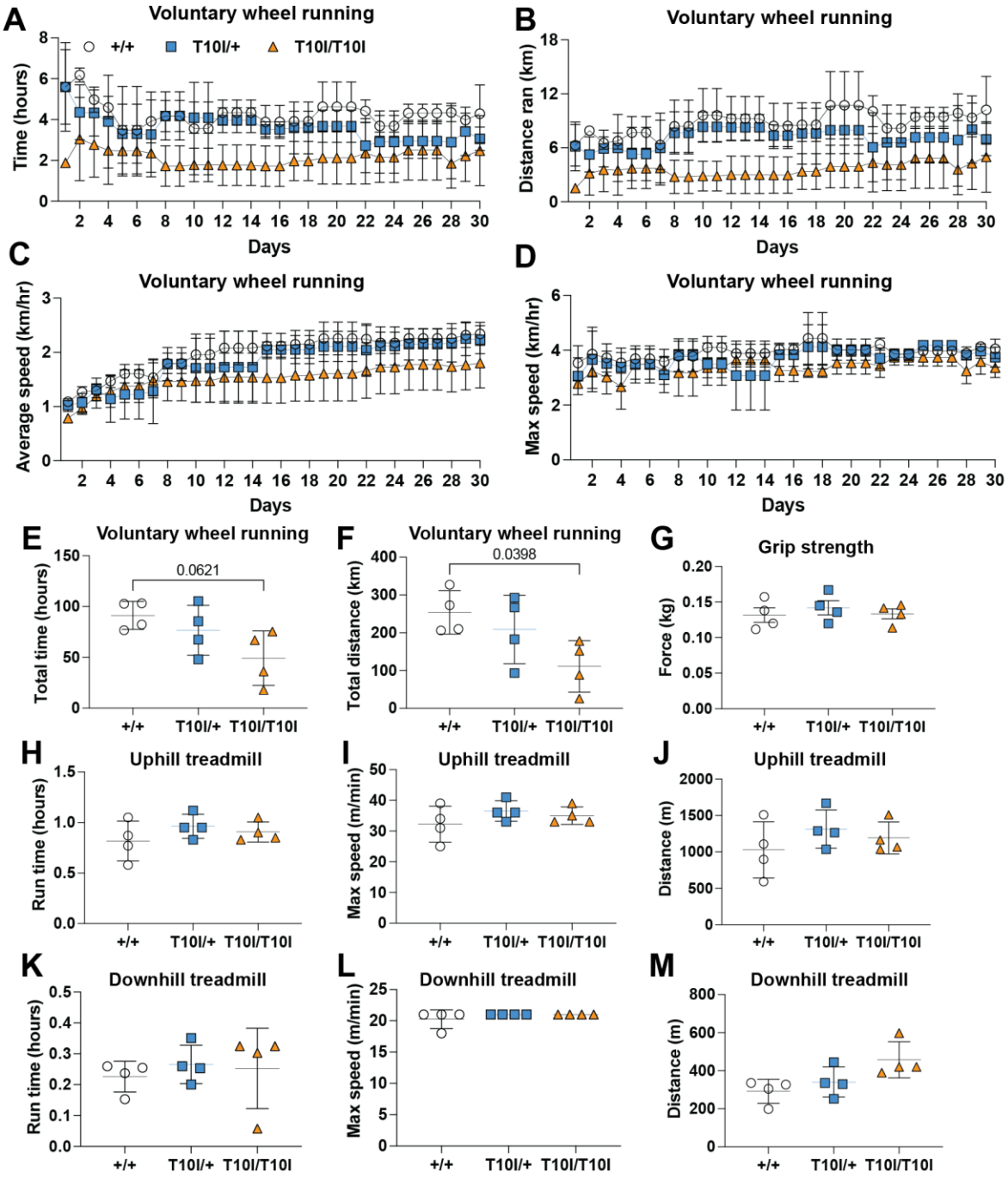


Figure 4.5. *Lmna* T10I homozygous mice run less voluntarily but have no impairment in muscle strength or forced running capacity. At 20 weeks of age, female *Lmna* T10I mice were placed in cages with running wheels, and (**A**) time ran per day, (**B**) distance ran per day, (**C**) average speed, and (**D**) maximum (max) speed was measured. (**E**) Total time ran over 30 days. (**F**) Total distance ran over 30 days. (**G**) Grip strength measurements in 24-week-old *Lmna* T10I mice. Uphill treadmill assay was performed on female *Lmna* T10I mice and (**H**) total run time, (**I**) max speed, and (**J**) total distance on treadmill was measured. A downhill treadmill assay was performed to cause muscle injury, and (**K**) run time, (**L**) max speed, and (**M**) distance ran was measured. All data represented as mean ± SD. Data were analyzed with two-way ANOVA with a Bonferroni post-hoc test.

Figure 4.6

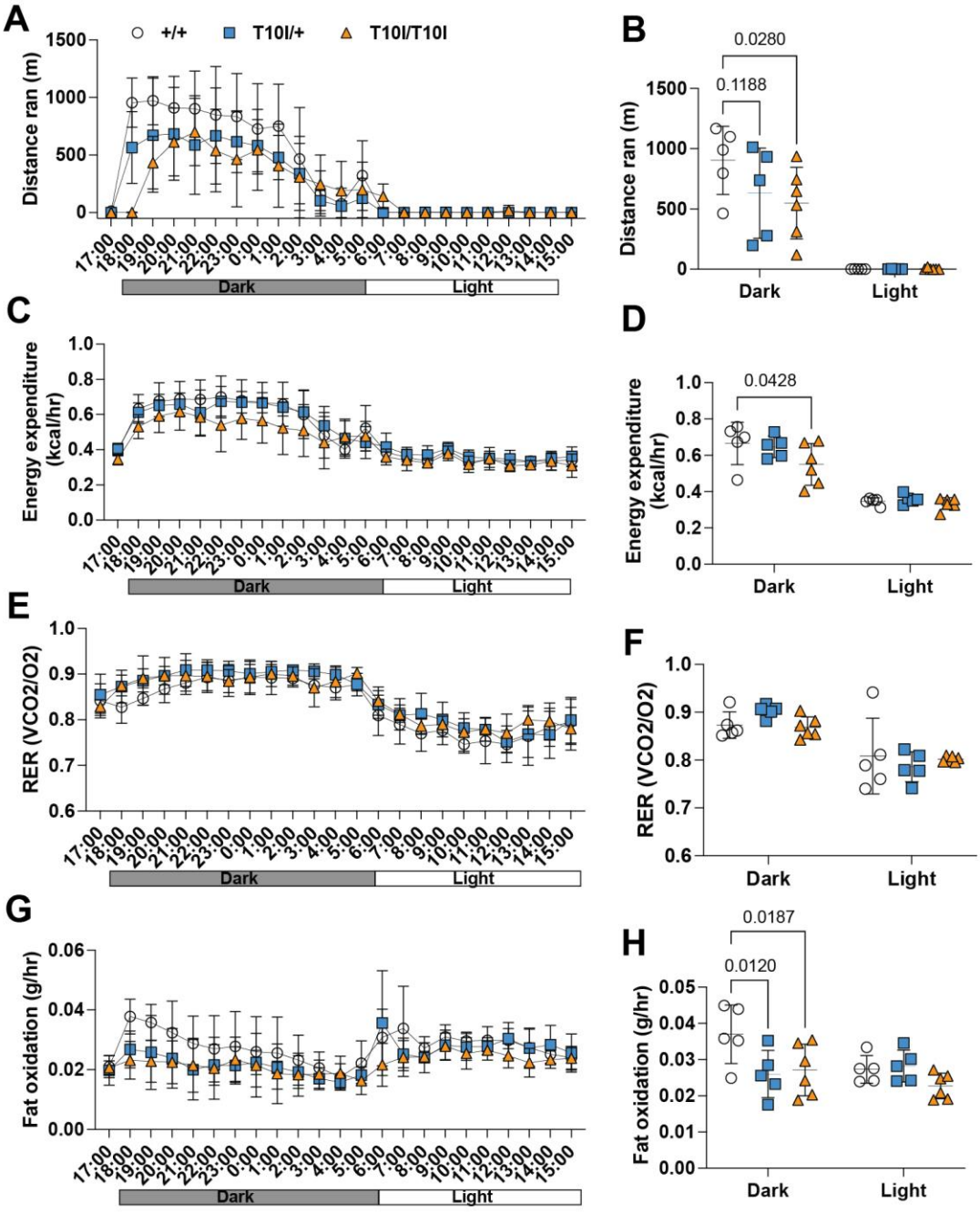


Figure 4.6. Female *Lmna* T10I mice have decreased running activity, energy expenditure, and fat oxidation. At 20 weeks of age, mice were placed into SABLE Promethion cages for three days with a running wheel, data shown is from the third day of indirect calorimetry. (**A**) Distance ran on running wheel was measured over time. (**B**) Total distance ran on the third day. (**C**) Energy expenditure over time. (**D**) Average energy expenditure for the six middle hours of each light cycle on the third day. (**E**) Respiratory exchange ratio (RER) over time. (**F**) Average RER during the eight middle hours of each light cycle. (**G**) Fat oxidation measured over time. (**H**) Average fat oxidation for first four hours of each light cycle. All data represented as mean ± SD. Data were analyzed with two-way ANOVA with a Bonferroni post-hoc test.

Figure 4.7

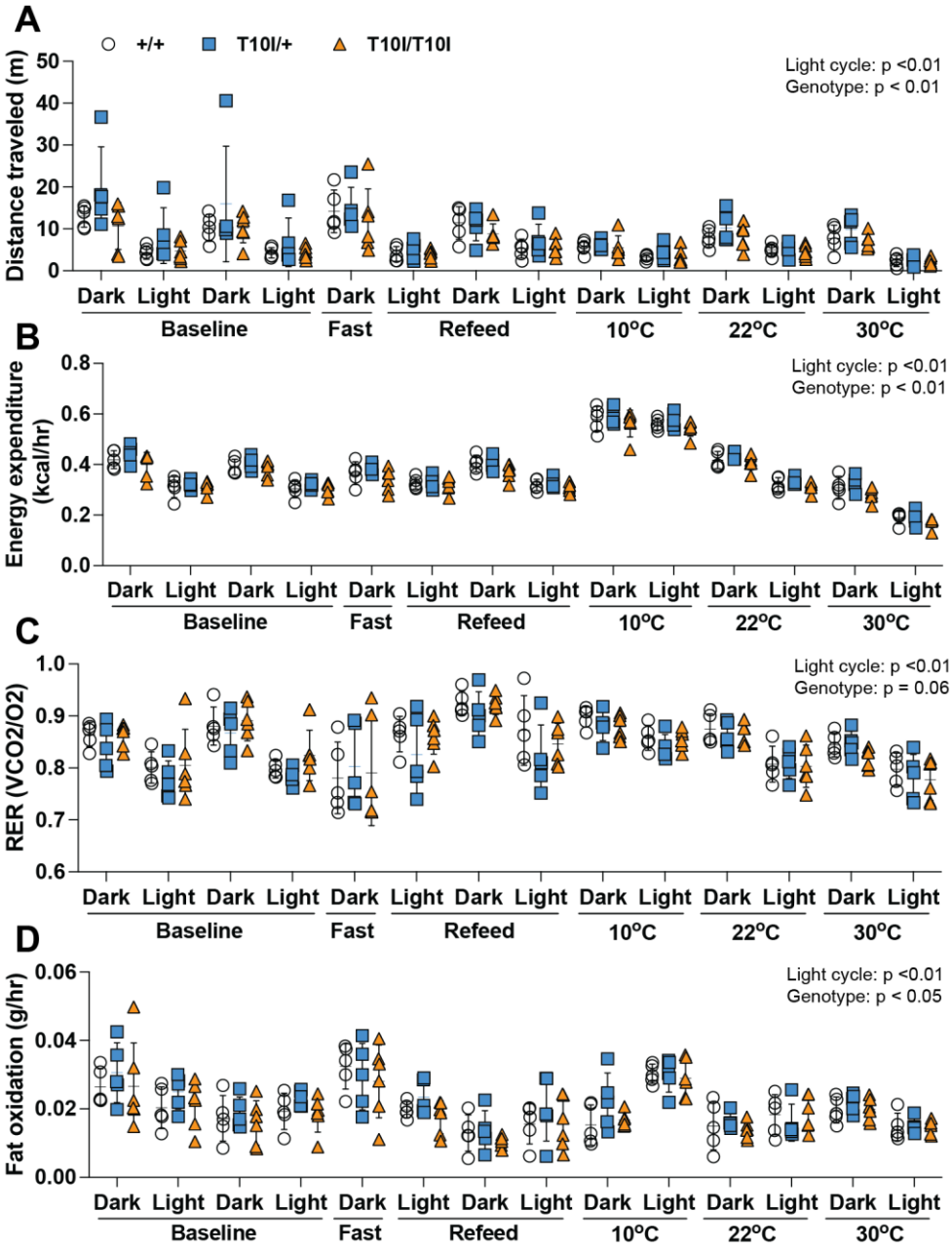


Figure 4.7. Female *Lmna* T10I mice have decreased energy expenditure and fat oxidation during different metabolic stressors. Mice at 20 weeks of age were placed into SABLE Promethion cages for seven days, and metabolic responses to fasting, refeeding, and the indicated temperature changes were determined. All data was averaged over the full 12 hours of each light cycle. (**A**) Distance traveled. (**B**) Energy expenditure. (**C**) RER. (**D**) Fat oxidation. All data represented as mean ± SD. Data were analyzed with two-way ANOVA with a Bonferroni post-hoc test.

Figure 4.8

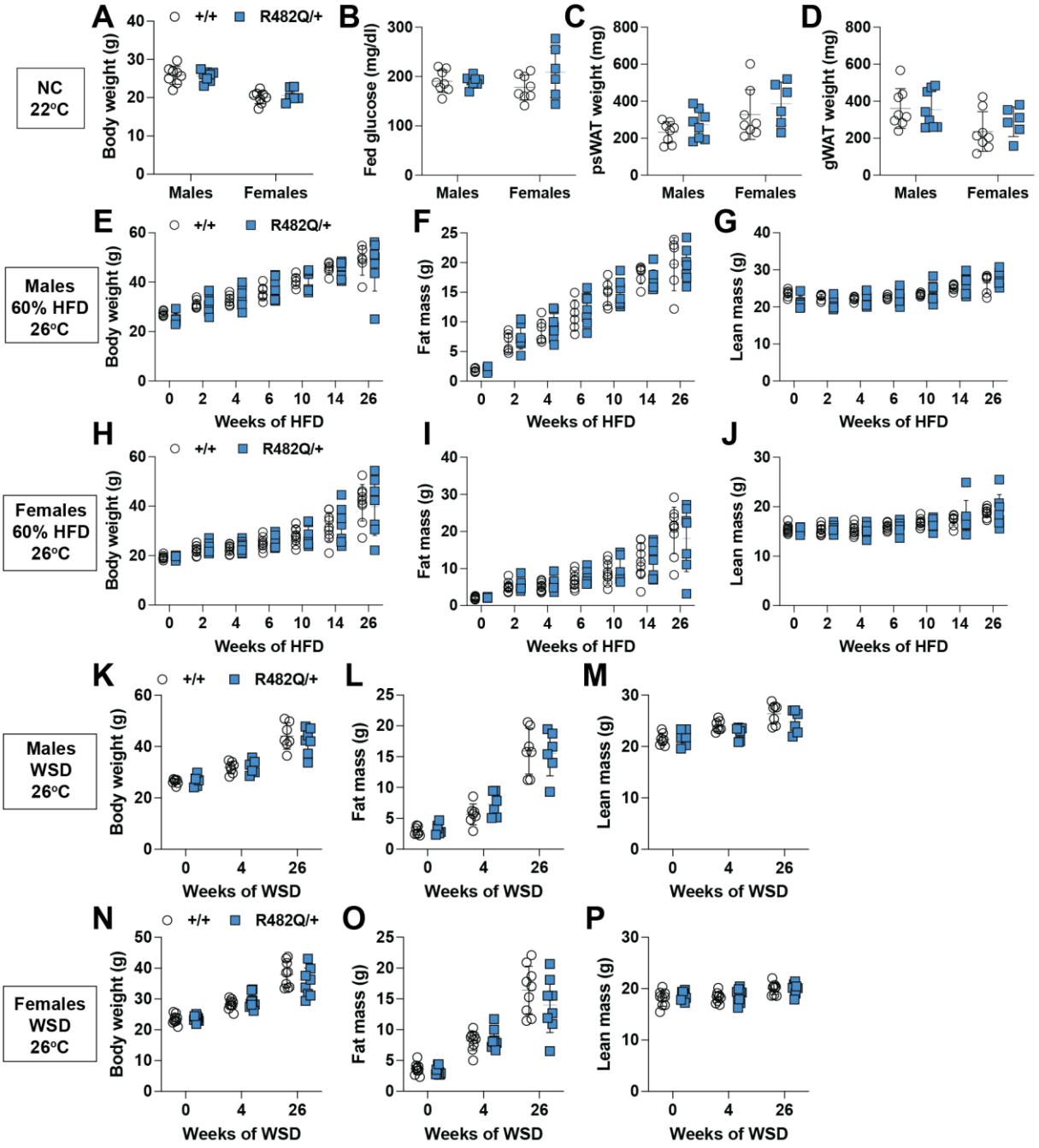


Figure 4.8. *Lmna* R482Q mice do not have lipodystrophy when fed normal chow, HFD, or western-style diet (WSD). Male and female mice at 10 to 12 weeks of age on normal chow housed at 22°C were euthanized. (**A**) Body weight. (**B**) Fed glucose. (**C**) psWAT weights. (**D**) gWAT weights. Eight to 10-week-old male *Lmna* R482Q mice were challenged with 60% HFD at 26°C with measures of (**E**) body weight, (**F**) fat mass, and (**G**) lean mass. Eight to 10-week-old female *Lmna* R482Q mice were challenged with 60% HFD housed at 26°C and (**H**) body weight, (**I**) fat mass, and (**J**) lean mass determined. Male mice at 20 weeks of age were challenged with WSD at 26°C and (**K**) body weight, (**L**) fat mass, and (**M**) lean mass was measured. Female mice at 20 weeks of age were challenged with WSD at 26°C and (**N**) body weight, (**O**) fat mass, and (**P**) lean mass was measured. All data represented as mean ± SD. Data were analyzed with two-way ANOVA with a Bonferroni post-hoc test.

Figure 4.9

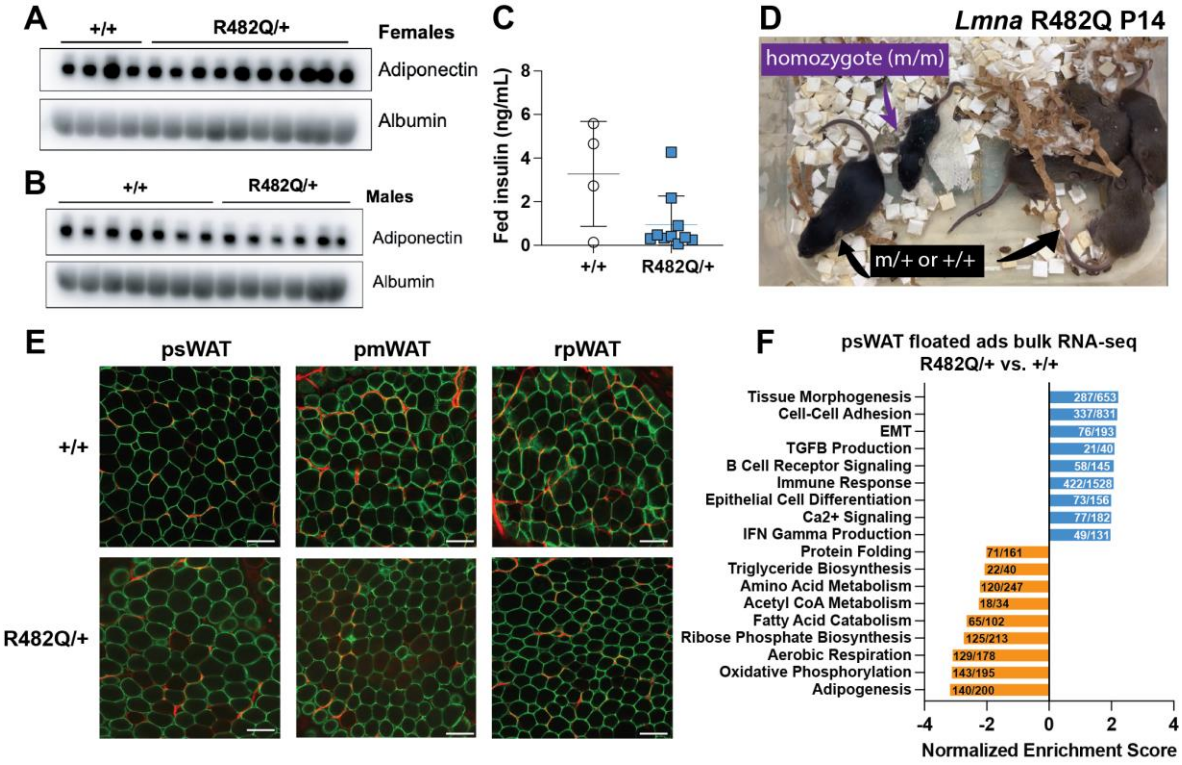


Figure 4.9. Homozygous *Lmna* R482Q mice die by P14, and RNA-seq analyses of Lmna R482Q/+ adipocytes reveal decreased adipogenesis and metabolism pathways, and an increased inflammatory signature. Serum adiponectin in 10-12-week-old (**A**) female and (**B**) male mice. (**C**) Fed serum insulin concentrations in 10-12-week-old female mice. (**D**) Image of homozygous R482Q mice compared to +/+ and R482Q/+ littermates at post-partum day 14 (P14). (**E**) Adiponectin-CreERT2 and mTmG background crossed with +/+ or R482Q/+ mice and imaged four weeks post-tamoxifen via confocal microscopy. Scale bar = 50 µm. (**F**) Bulk RNA-seq analyses of floated adipocytes (ads) from psWAT of male and female mice at 10 to 12 weeks of age. Numbers on graph bars are the number of genes driving each pathway. All data represented as mean ± SD. Data were analyzed with two-way ANOVA with a Bonferroni post-hoc test.

Figure 4.10

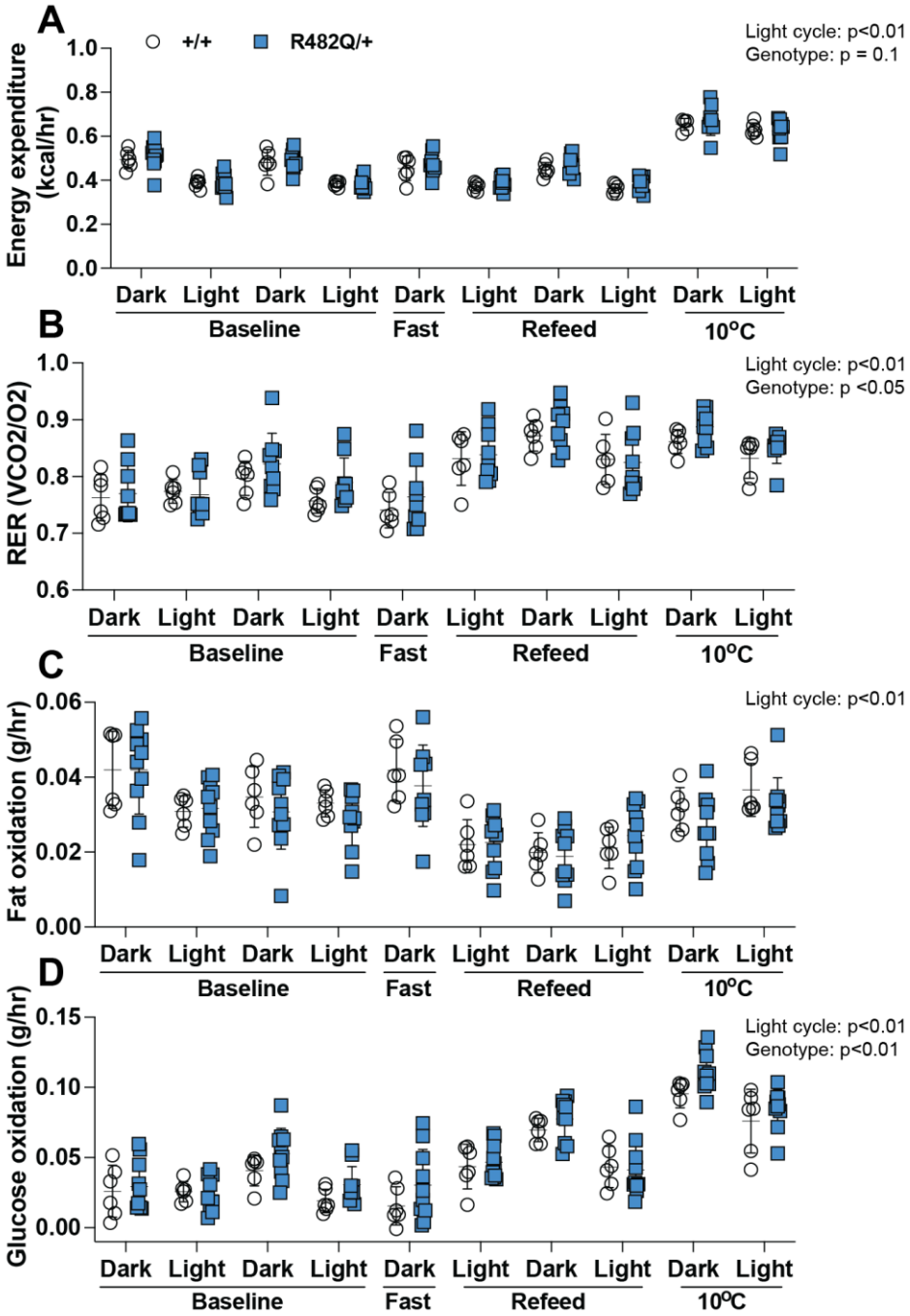


Figure 4.10. Female *Lmna* R482Q mice have decreased fat oxidation and increased glucose oxidation when fasted and exposed to cold temperatures. One year old female mice were placed into SABLE Promethion cages for five days and exposed to metabolic stressors like fasting, refeeding, and cold exposure. (**A**) Energy expenditure. (**B**) RER. (**C**) Fat oxidation. (**D**) Glucose oxidation. All data represented as mean ± SD. Data were analyzed with two-way ANOVA with a Bonferroni post-hoc test.

Figure 4.11

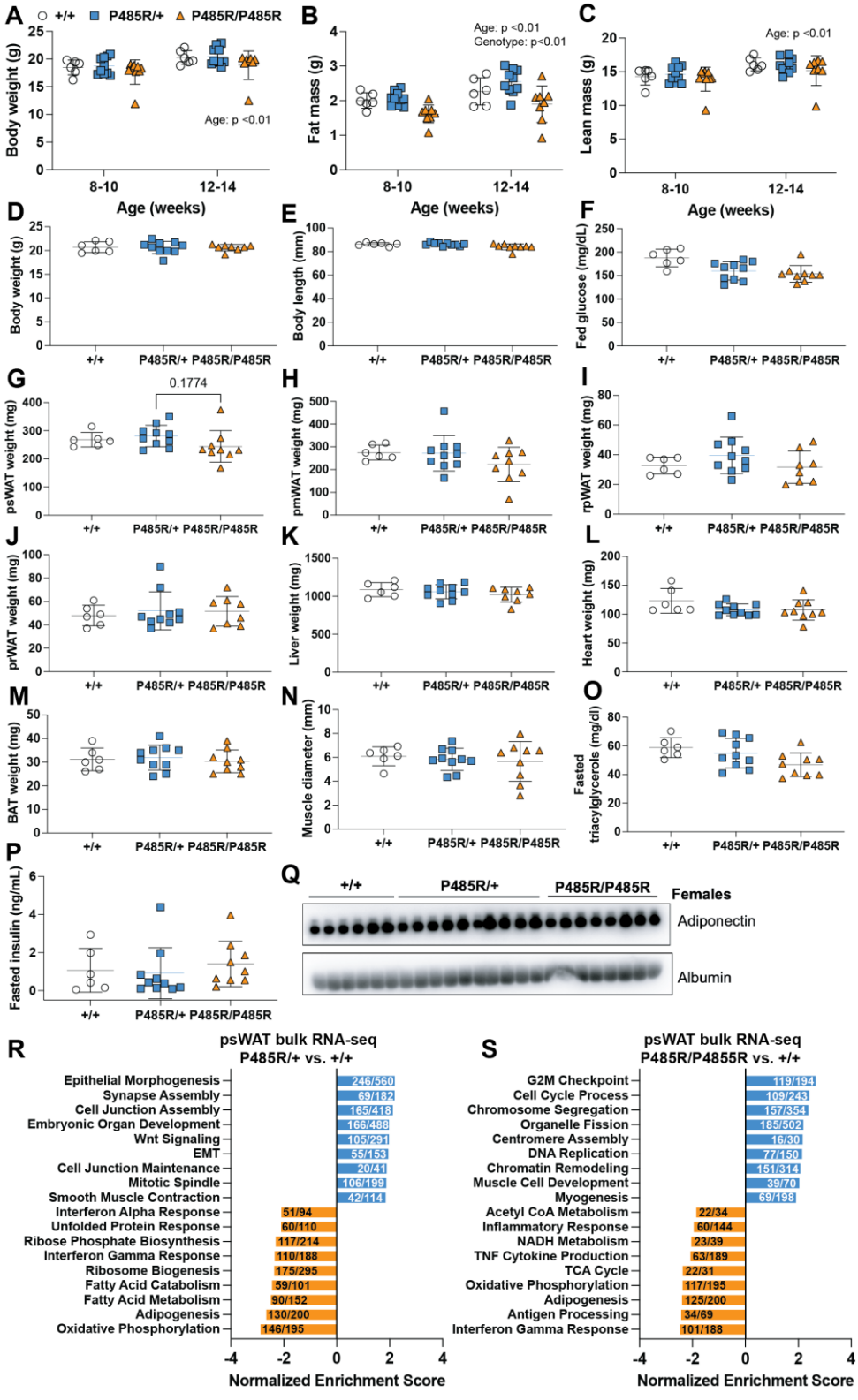


Figure 4.11. Female *Lmna* P485R mice have a trending decrease in WAT weights, accompanied by decreased adipogenic and oxidative phosphorylation gene pathways in WAT. Body composition of P485R mice over time

on NC housed at 22°C: (**A**) Body weight, (**B**) fat mass and (**C**) lean mass. Necropsy data at euthanasia of female *Lmna* P485R mice at 17 to 19 weeks of age. (**D**) Body weight. (**E**) Body length. (**F**) Fed glucose. (**G**) psWAT weight. (**H**) Parametrial white adipose tissue (pmWAT) weight. (**I**) rpWAT weight. (**J**) prWAT weight. (**K**) Liver weight. (**L**) Heart weight. (**M**) BAT weight. (**N**) Gastrocnemius muscle diameter. Fasted serum (**O**) triacylglycerol and (**P**) insulin concentrations before euthanasia. (**Q**) Serum adiponectin immunoblot. Bulk RNA-seq performed on psWAT of 17-19-week-old female *Lmna* P485R mice and analyzed with GSEA. (**R**) P485R/+ vs. +/+ comparison. (**S**) P485R/P485R vs. +/+ comparison. All data represented as mean ± SD. Data were analyzed with one or two-way ANOVA with a Bonferroni post-hoc test.

Figure 4.12

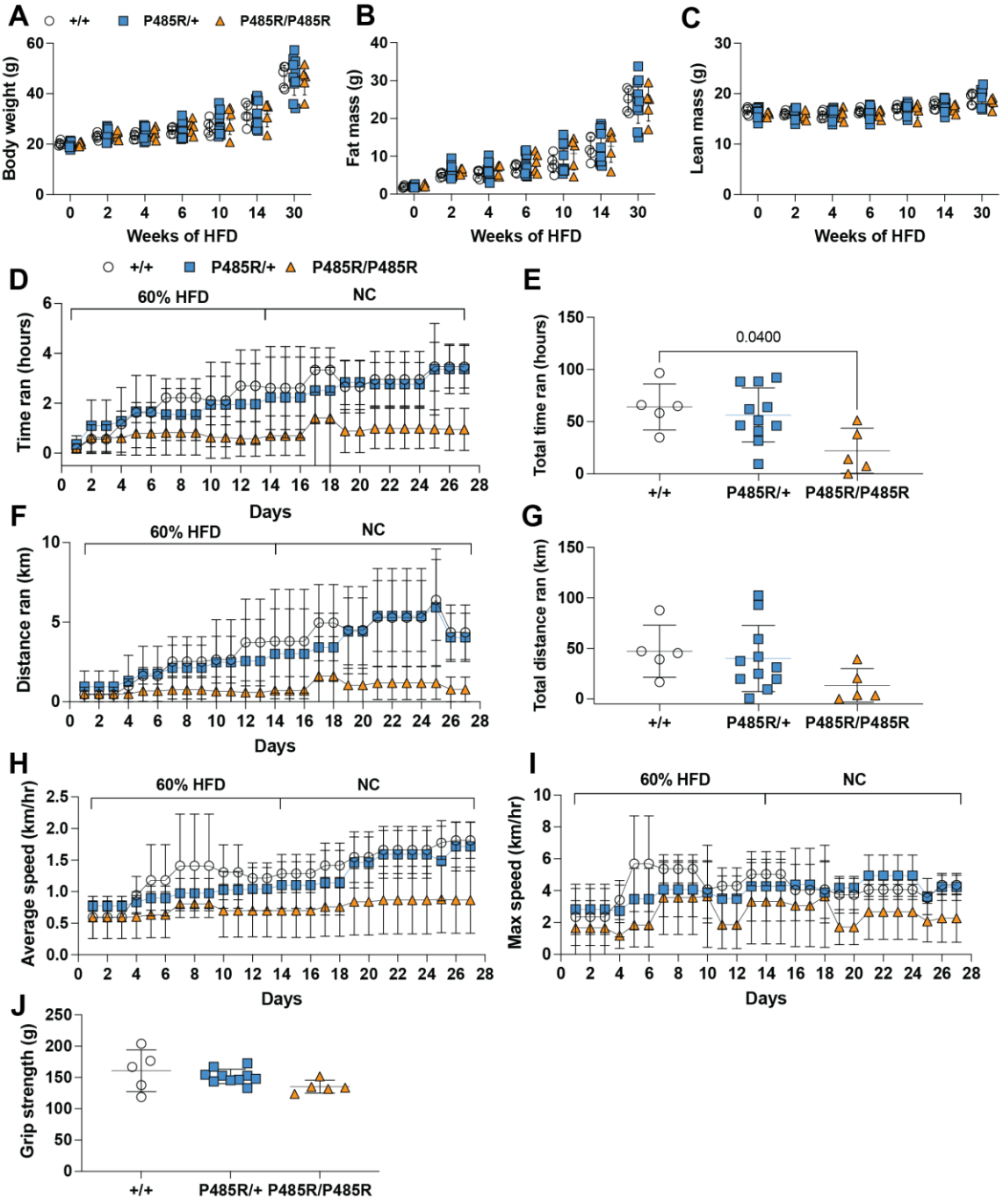
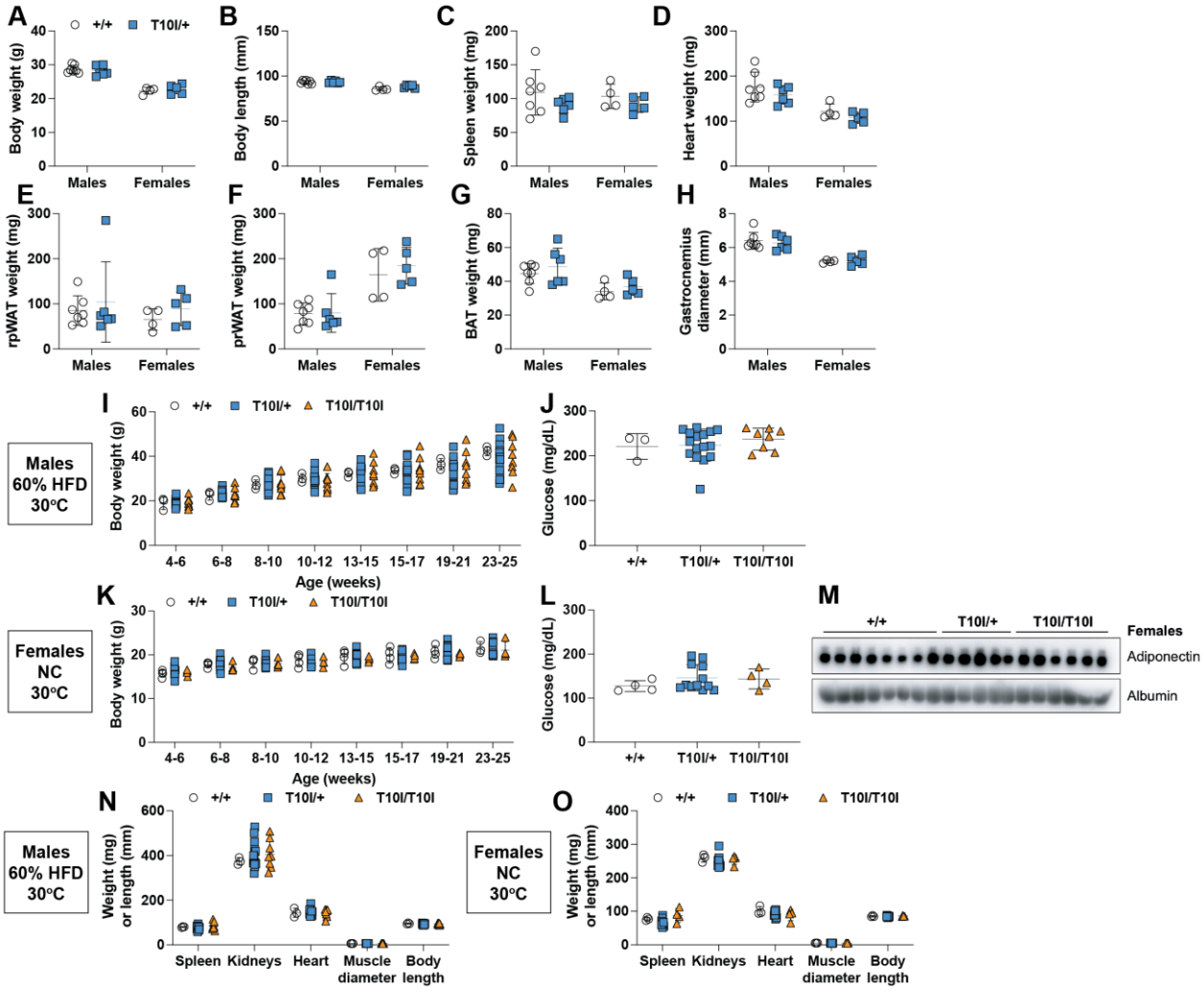
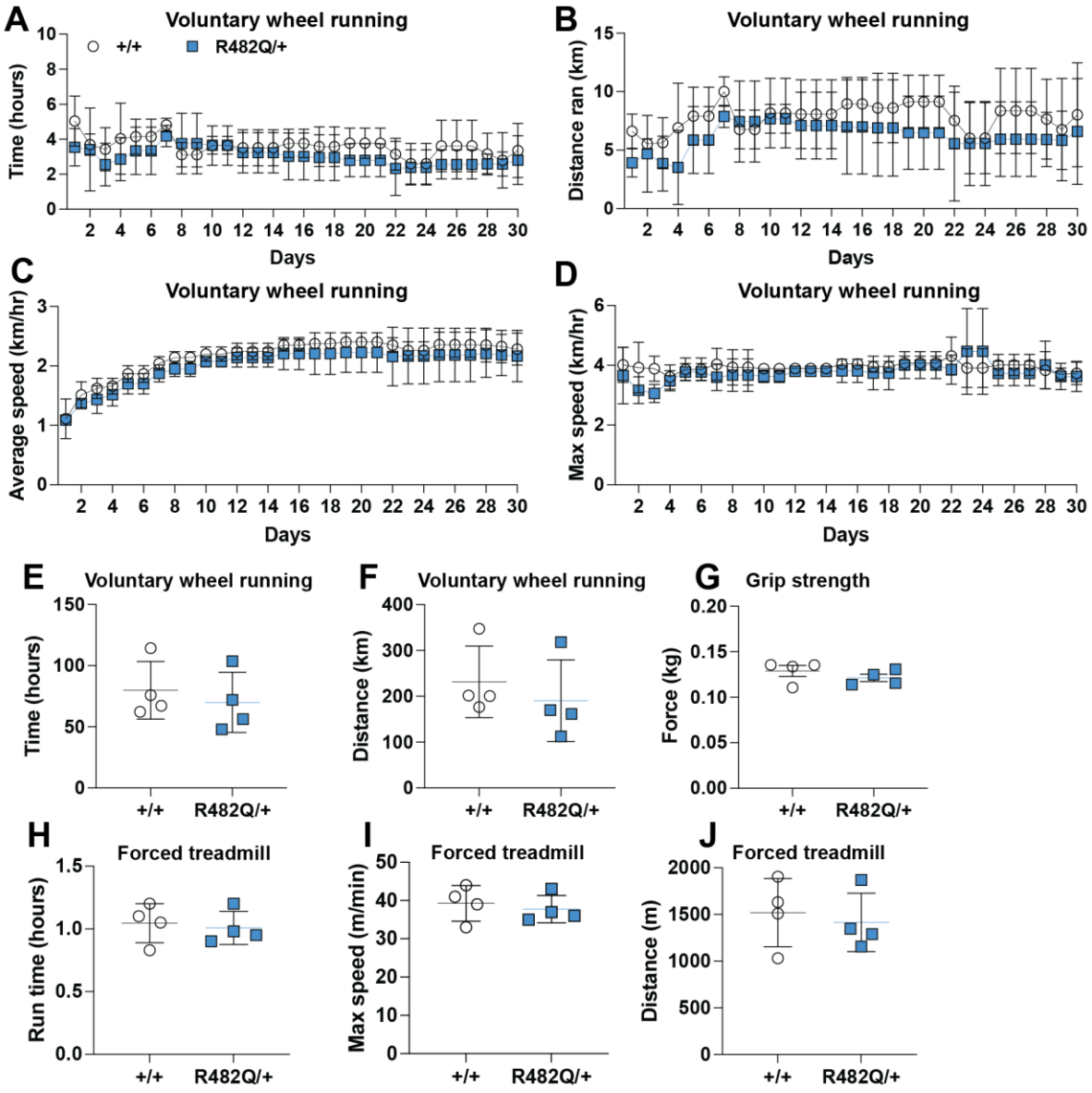


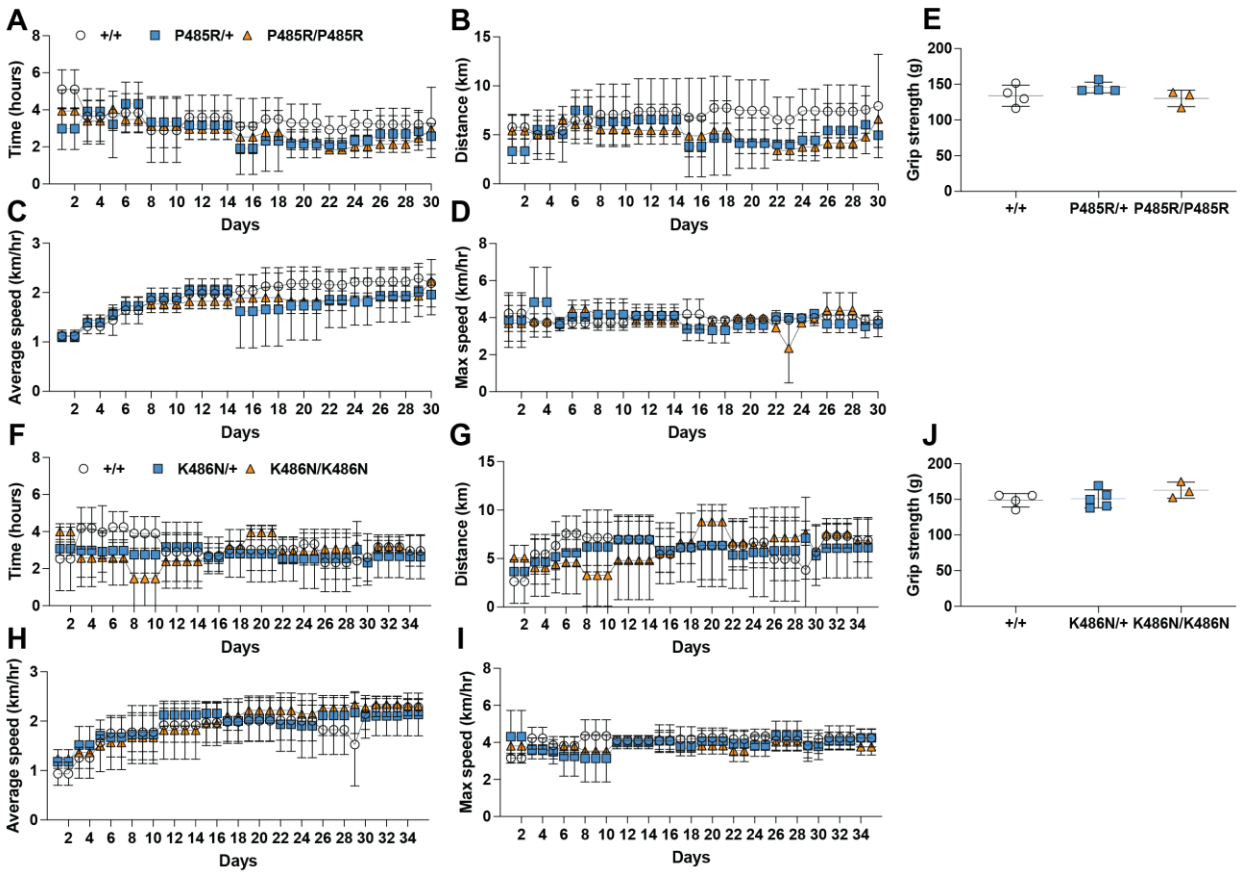
Figure 4.12. Female HFD-fed *Lmna* P485R mice have no change in fat mass but have decreased voluntary running capacity. Mice were started on HFD at 12 weeks of age and housed at 26°C. (**A**) Body weight, (**B**) fat mass, and (**C**) lean mass was measured over time. Mice were then placed into cages with voluntary running wheels when they were at 40 weeks of age. Mice were kept on HFD for 14 days of running, and then were switched to NC. (**D**) Time ran per day. (**E**) Cumulative time ran for 28 days. (**F**) Distance ran per day. (**G**) Cumulative distance ran for 28 days. (**H**) Average speed and (**I**) maximum speed per day. (**J**) Grip strength measured in mice at 44 weeks of age. All data represented as mean ± SD. Data were analyzed with two-way ANOVA with a Bonferroni post-hoc test.



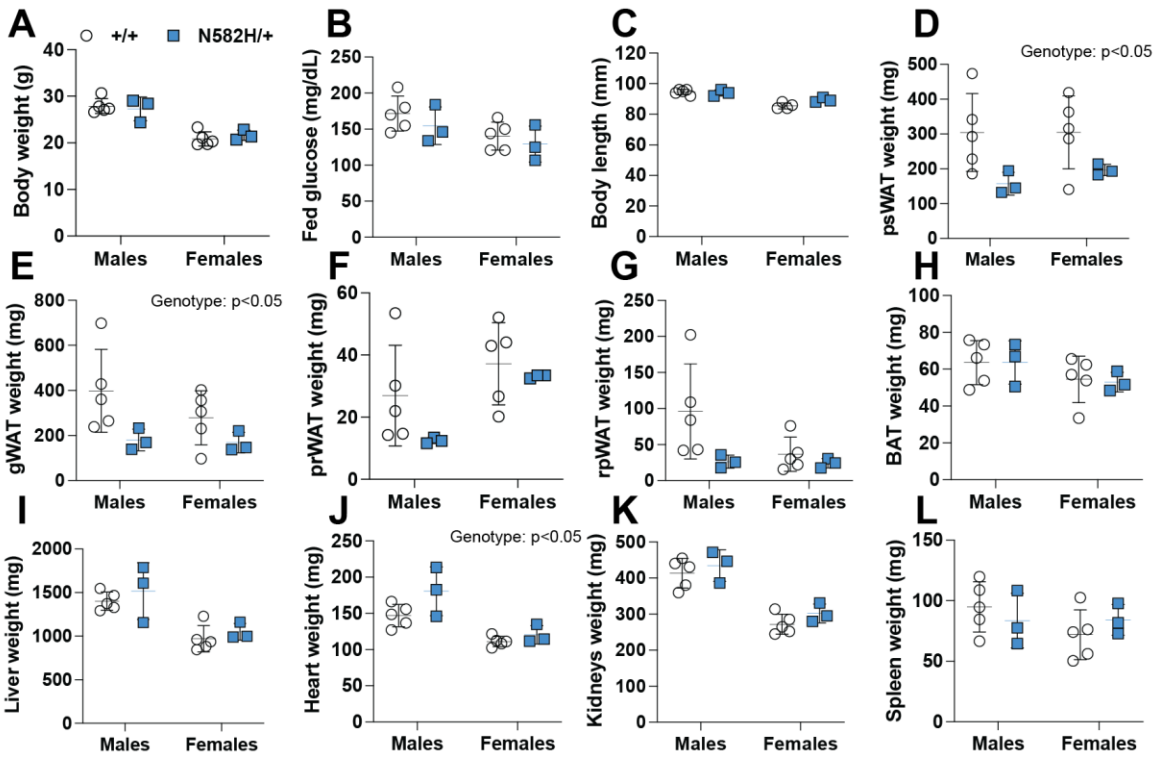
Supplemental Figure 4.1. T10I mice have no change in WAT or organ weights on NC or HFD. Necropsy data of male and female *Lmna* T10I mice at 20 weeks of age on NC at 22°C, including (**A**) body weight, (**B**) body length, (**C**) spleen weights, (**D**) heart weights, (**E**) rpWAT weights, (**F**) prWAT weights, (**G**) BAT weights, and (**H**) gastrocnemius muscle diameter. Male mice were challenged with 60% HFD and housed at 30˚C. (**I**) Body weight over time. (**J**) Fasted glucose concentrations at 15-17 weeks of age. Female mice were housed at 30°C and (**K**) body weight and (**L**) fasted glucose at 15-17 weeks of age was measured. (**M**) Serum adiponectin in females at 15-17 weeks of age. Data at euthanasia of 26-week-old T10I male mice of (**N**) spleen, kidneys, heart, gastrocnemius diameter and body length. Data at euthanasia of 26-week-old female T10I mice of (**O**) spleen, kidneys, heart, gastrocnemius diameter and body length. All data represented as mean ± SD. Data were analyzed with two-way ANOVA with a Bonferroni post-hoc test.



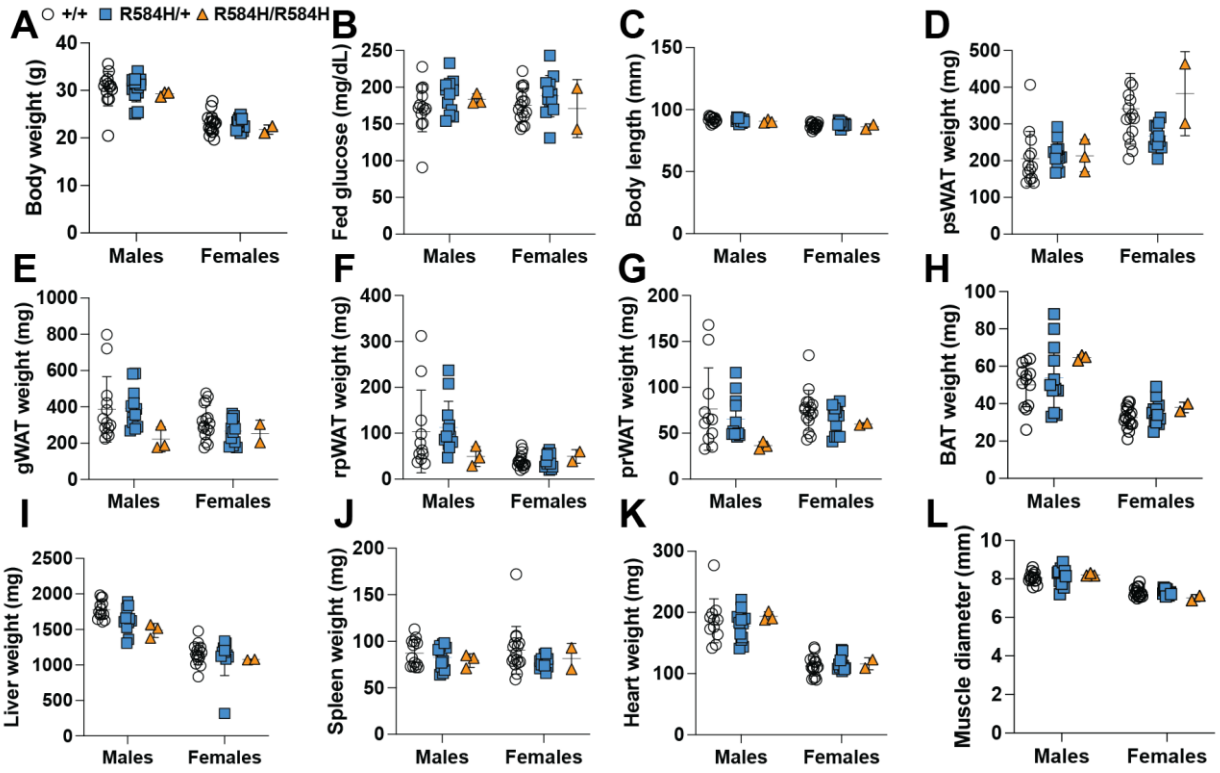
Supplemental Figure 4.2. Female *Lmna* R482Q mice do not have detectable change in voluntary running capacity or grip strength. At 22 weeks of age, mice were placed into cages with voluntary running wheels, and (**A**) time ran per day, (**B**) distance ran per day, (**C**) average speed, and (**D**) maximum speed were measured. (**E**) Cumulative time ran and (**F**) cumulative distance ran for 30 days. (**G**) Grip strength was measured in mice that were 26 weeks of age. Mice underwent forced treadmill running, and (**H**) run time, (**I**) max speed, and (**J**) distance was measured. All data represented as mean ± SD. Data were analyzed with two-way ANOVA with a Bonferroni post-hoc test.



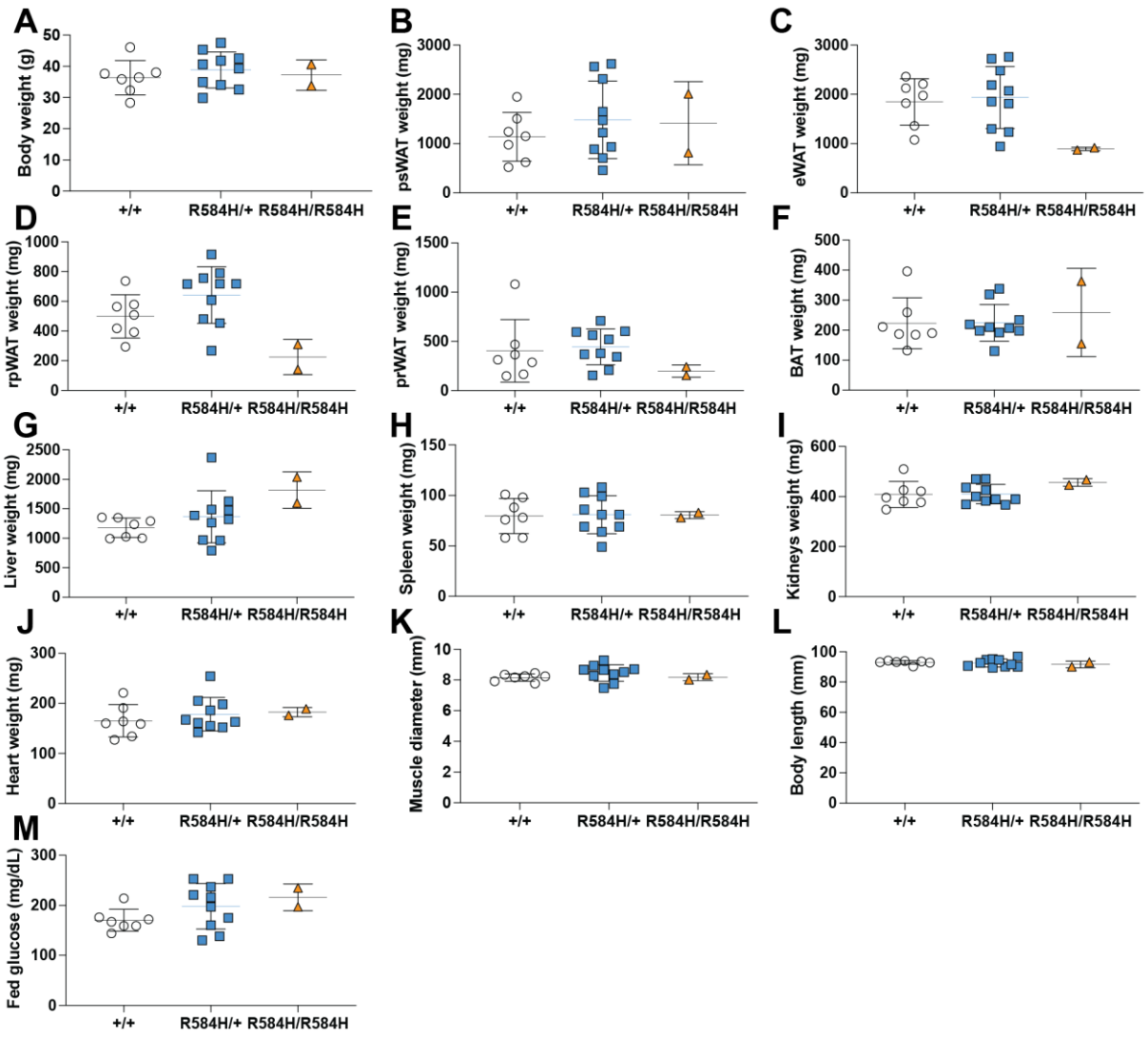
Supplemental Figure 4.3. *Lmna* P485R and K486N mice fed NC have no change in voluntary running capacity. At 32 weeks of age, female mice fed NC at 22°C were placed into cages with voluntary running wheels. (**A**) Time ran per day, (**B**) distance per day, (**C**) average speed and (**D**) max speed were measured in *Lmna* P485R mice. (**E**) Grip strength was measured in 36-week-old mice. (**F**) Time ran per day, (**G**) distance ran per day, (**H**) average speed, and (**I**) max speed were measured in *Lmna* K486N mice. (**J**) Grip strength was measured in 36-week-old mice. All data represented as mean ± SD. Data were analyzed with two-way ANOVA with a Bonferroni post-hoc test.



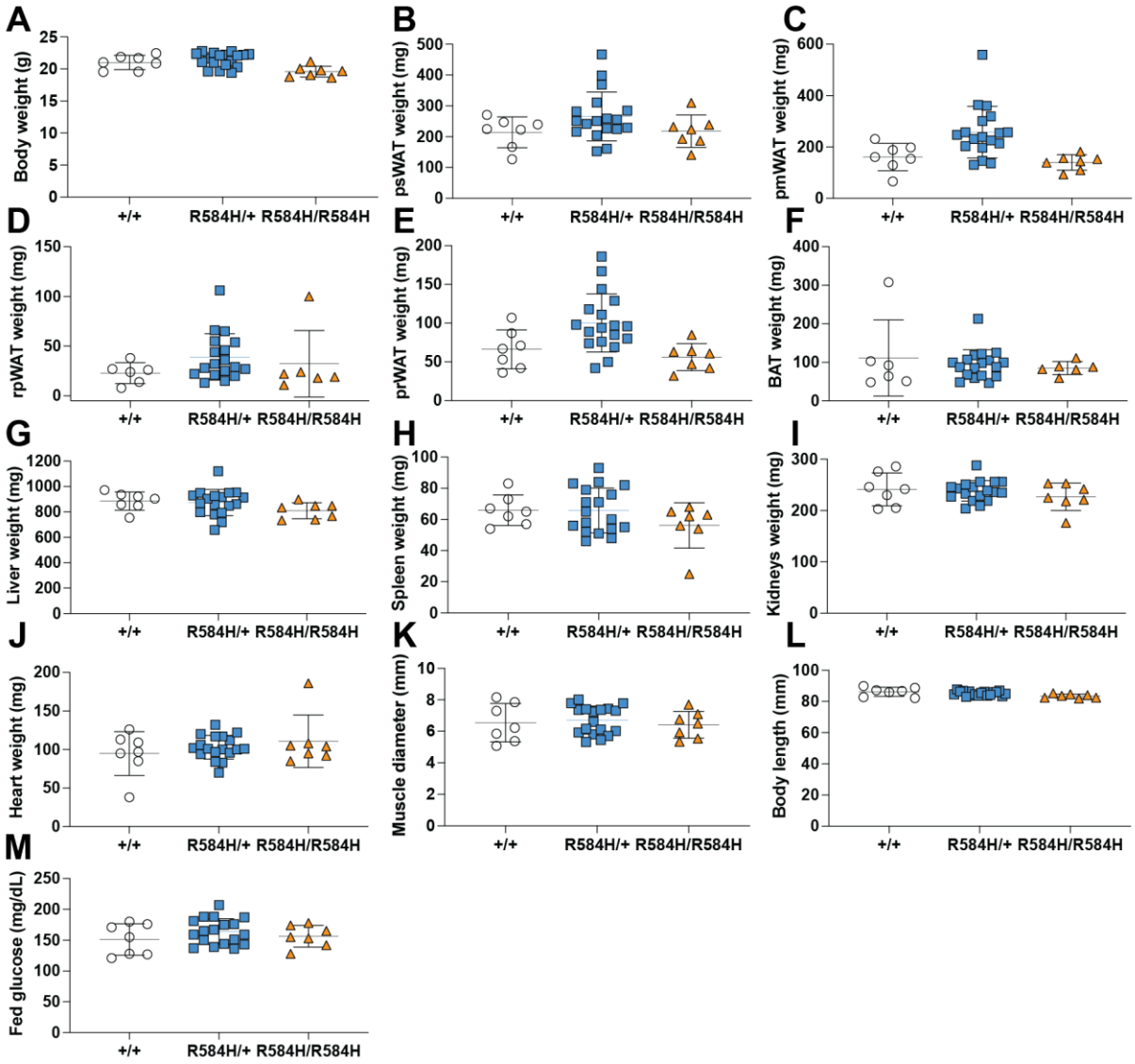
Supplemental Figure 4.4. *Lmna* N582H mice have reduced WAT weights and increased heart weights. At 16 weeks of age, male and female mice fed NC at 22°C were euthanized. (**A**) Body weight. (**B**) Fed glucose. (**C**) Body length. (**D**) psWAT weight. (**E**) gWAT weight. (**F**) prWAT weight. (**G**) rpWAT weight. (**H**) BAT weight. (**I**) Liver weight. (**J**) Heart weight. (**K**) Kidneys weight. (**L**) Spleen weight. All data represented as mean ± SD. Data were analyzed with two-way ANOVA with a Bonferroni post-hoc test.



Supplemental Figure 4.5. I R584H* mice have no change in WAT or organ weights. At 24 weeks of age, male and female *Lmna* R584H* (additional off-target mutations besides R584H) were euthanized. (**A**) Body weight. (**B**) Fed glucose. (**C**) Body length. (**D**) psWAT weight. (**E**) gWAT weight. (**F**) rpWAT weight. (**G**) prWAT weight. (**H**) BAT weight. (**I**) Liver weight. (**J**) Spleen weight. (**K**) Heart weight. (**L**) Gastrocnemius muscle diameter. All data represented as mean ± SD. Data were analyzed with two-way ANOVA with a Bonferroni post-hoc test.



Supplemental Figure 4.6. *Lmna* R584H* male mice fed a HFD for five months housed at 30°C had no change in WAT or organ weights. Male *Lmna* R584H* mice at 28 weeks of age were euthanized. (**A**) Body weight. (**B**) psWAT weight. (**C**) eWAT weight. (**D**) rpWAT weight. (**E**) prWAT weight. (**F**) BAT weight. (**G**) Liver weight. (**H**) Spleen weight. (**I**) Kidney weight. (**J**) Heart weight. (**K**) Gastrocnemius muscle diameter. (**L**) Body length. (**M**) Randomly-fed glucose concentrations. All data represented as mean ± SD. Data were analyzed with two-way ANOVA with a Bonferroni post-hoc test.



Supplemental Figure 4.7. *Lmna* R584H* female mice on NC housed at 30°C had no change in WAT or organ weights. Female *Lmna* R584H* mice at 28 weeks of age were euthanized. (**A**) Body weight. (**B**) psWAT weight. (**C**) eWAT weight. (**D**) rpWAT weight. (**E**) prWAT weight. (**F**) BAT weight. (**G**) Liver weight. (**H**) Spleen weight. (**I**) Kidney weight. (**J**) Heart weight. (**K**) Gastrocnemius muscle diameter. (**L**) Body length. (**M**) Random-fed glucose. All data represented as mean ± SD. Data were analyzed with two-way ANOVA with a Bonferroni post-hoc test.

4.7 References

1. Akinci, B., *et al*. *Lipodystrophy Syndromes: Presentation and Treatment*. *Endotext [Internet]* (MDText.com, Inc., 2018).
2. Lim, K., *et al*. Lipodystrophy: A paradigm for understanding the consequences of 'overloading' adipose tissue *Physiol. Rev.* **101**, 907-993 (2021).
3. Dittmer, T. A. & Misteli, T. The lamin protein family. *Genome Biol.* **12**, 222 (2011).
4. Bonne, G. *et al.* Mutations in the gene encoding lamin A/C cause autosomal dominant Emery-Dreifuss muscular dystrophy. *Nat. Genet.* **21**, 285–288 (1999).
5. Fatkin, D. *et al.* Missense mutations in the rod domain of the lamin A/C gene as causes of dilated cardiomyopathy and conduction-system disease. *N. Engl. J. Med.* **341**, 1715–1724 (1999).
6. Sandre-Giovannoli, A. D. *et al.* Homozygous Defects in LMNA, Encoding Lamin A/C Nuclear-Envelope Proteins, Cause Autosomal Recessive Axonal Neuropathy in Human (Charcot-Marie-Tooth Disorder Type 2) and Mouse. *Am. J. Hum. Genet.* **70**, 726–736 (2002).
7. De Sandre-Giovannoli, A. *et al.* Lamin A Truncation in Hutchinson-Gilford Progeria. *Science* **300**, 2055–2055 (2003).
8. Sullivan, T. *et al.* Loss of A-type lamin expression compromises nuclear envelope integrity leading to muscular dystrophy. *J. Cell Biol.* **147**, 913–920 (1999).
9. Kubben, N. *et al.* Post-natal myogenic and adipogenic developmental: defects and metabolic impairment upon loss of A-type lamins. *Nucl. Austin Tex* **2**, 195–207 (2011).
10. Lammerding, J. *et al.* Lamin A/C deficiency causes defective nuclear mechanics and mechanotransduction. *J. Clin. Invest.* **113**, 370–378 (2004).
11. Lammerding, J. *et al.* Lamins A and C but Not Lamin B1 Regulate Nuclear Mechanics *. *J. Biol. Chem.* **281**, 25768–25780 (2006).
12. Corsa, C. A. S. *et al.* Adipocyte-specific deletion of lamin A/C largely models human familial partial lipodystrophy type 2. *Diabetes* (2021) doi:10.2337/db20-1001.
13. Wojtanik, K. M. *et al.* The role of LMNA in adipose: a novel mouse model of lipodystrophy based on the Dunnigan-type familial partial lipodystrophy mutation. *J. Lipid Res.* **50**, 1068–1079 (2009).
14. Le Dour, C. *et al.* Extracellular matrix remodeling and transforming growth factor-β signaling abnormalities induced by lamin A/C variants that cause lipodystrophy. *J. Lipid Res.* **58**, 151–163 (2017).
15. Makowski, L., *et al*. The fatty acid-binding protein, aP2, coordinates macrophage cholesterol trafficking and inflammatory activity. Macrophage expression of aP2 impacts peroxisome proliferator-activated receptor gamma and IkappaB kinase activities. *J. Biol. Chem.* **280**, 12888–12895 (2005).
16. Arimura, T. *et al.* Mouse model carrying H222P-Lmna mutation develops muscular dystrophy and dilated cardiomyopathy similar to human striated muscle laminopathies. *Hum. Mol. Genet.* **14**, 155–169 (2005).
17. Mounkes, L. C., *et al*. A progeroid syndrome in mice is caused by defects in A-type lamins. *Nature* **423**, 298–301 (2003).
18. Yang, L. *et al.* The LMNA p.R541C mutation causes dilated cardiomyopathy in human and mice. *Int. J. Cardiol.* **363**, 149–158 (2022).
19. Mounkes, L. C., *et al*. Expression of an LMNA-N195K variant of A-type lamins results in cardiac conduction defects and death in mice. *Hum. Mol. Genet.* **14**, 2167–2180 (2005).

20. Bertrand, A. T. *et al.* DelK32-lamin A/C has abnormal location and induces incomplete tissue maturation and severe metabolic defects leading to premature death. *Hum. Mol. Genet.* **21**, 1037–1048 (2012).
21. Gómez-Domínguez, D. *et al.* CRISPR/Cas9-mediated elimination of the LMNA c.745C>G pathogenic mutation enhances survival and cardiac function in LMNA-associated congenital muscular dystrophy. *bioRxiv* (2025).
22. Osorio, F. G. *et al.* Splicing-directed therapy in a new mouse model of human accelerated aging. *Sci. Transl. Med.* **3**, 106ra107 (2011).
23. Hussain, I. *et al.* A Novel Generalized Lipodystrophy-Associated Progeroid Syndrome Due to Recurrent Heterozygous LMNA p.T10I Mutation. *J. Clin. Endocrinol. Metab.* **103**, 1005–1014 (2018).
24. Cao, H. & Hegele, R. A. Nuclear lamin A/C R482Q mutation in Canadian kindreds with Dunnigan-type familial partial lipodystrophy. *Hum. Mol. Genet.* **9**, 109–112 (2000).
25. Saha, B. *et al.* A Novel LMNA Mutation Causes Altered Nuclear Morphology and Symptoms of Familial Partial Lipodystrophy (Dunnigan Variety) with Progeroid Features. *Mol. Syndromol.* **1**, 127–132 (2010).
26. Santos, J. L., *et al*. Case Report: Concurrent de novo pathogenic variants in the LMNA gene as a cause of sporadic partial lipodystrophy. *Front. Genet.* **15**, 1468878 (2024).
27. Van Esch, H., *et al*. A homozygous mutation in the lamin A/C gene associated with a novel syndrome of arthropathy, tendinous calcinosis, and progeroid features. *J. Clin. Endocrinol. Metab.* **91**, 517–521 (2006).
28. Mory, P. B. *et al.* Phenotypic diversity in patients with lipodystrophy associated with LMNA mutations. *Eur. J. Endocrinol.* **167**, 423–431 (2012).
29. Seeley, R. J. & MacDougald, O. A. Mice as experimental models for human physiology: when a few degrees in housing temperature matter. *Nat. Metab.* **3**, 443–445 (2021).
30. Muzumdar, M. D., *et al*. A global double-fluorescent Cre reporter mouse. *Genes. N. Y. N 2000* **45**, 593–605 (2007).
31. Shah, P. P. *et al.* Pathogenic LMNA variants disrupt cardiac lamina-chromatin interactions and de-repress alternative fate genes. *Cell Stem Cell* **28**, 938-954.e9 (2021).
32. Subramanian, A. *et al.* Gene set enrichment analysis: A knowledge-based approach for interpreting genome-wide expression profiles. *Proc. Natl. Acad. Sci.* **102**, 15545–15550 (2005).
33. Broers, J. L., *et al*. Nuclear lamins: laminopathies and their role in premature ageing. *Physiol. Rev.* **86**, 967–1008 (2006).
34. Perlman, R. L. Mouse models of human disease. *Evol. Med. Public Health* **2016**, 170–176 (2016).
35. Börgeson, E., *et al.* Of mice and men: Pinpointing species differences in adipose tissue biology. *Front. Cell Dev. Biol.* **10**, 1003118 (2022).
36. Spalding, K. L. *et al.* Dynamics of fat cell turnover in humans. *Nature* **453**, 783–787 (2008).
37. Poitelon, Y. *et al.* Behavioral and Molecular Exploration of the AR-CMT2A Mouse Model LmnaR298C/R298C. *NeuroMolecular Med.* **14**, 40–52 (2012).
38. McGrath, C. *et al.* Exercise Increases Bone in SEIPIN Deficient Lipodystrophy, Despite Low Marrow Adiposity. *Front. Endocrinol.* **12**, 782194 (2022).
39. Monteiro, L. *et al.* Health-Related Physical Fitness in Women with Dunnigan Lipodystrophy with Mutation in LMNA Gene. *Rev. Port. Endocrinol. Diabetes E Metab.* 22 (2017) doi:10.26497/2017.000008.000105.

40. Chan, J. L. & Oral, E. A. Clinical Classification and Treatment of Congenital and Acquired Lipodystrophy. *Endocr. Pract.* **16**, 310–323 (2010).
41. Ferrannini, E. The theoretical bases of indirect calorimetry: a review. *Metabolism.* **37**, 287–301 (1988).
42. Riachi, M., *et al*. Percent relative cumulative frequency analysis in indirect calorimetry: application to studies of transgenic mice. *Can. J. Physiol. Pharmacol.* **82**, 1075–1083 (2004).
43. Simonson, D. C. & DeFronzo, R. A. Indirect calorimetry: methodological and interpretative problems. *Am. J. Physiol.* **258**, E399-412 (1990).
44. Tschöp, M. H. *et al.* A guide to analysis of mouse energy metabolism. *Nat. Methods* **9**, 57–63 (2011).
45. Kaiyala, K. J. Mathematical model for the contribution of individual organs to non-zero y-intercepts in single and multi-compartment linear models of whole-body energy expenditure. *PloS One* **9**, e103301 (2014).
46. Kaiyala, K. J. & Schwartz, M. W. Toward a more complete (and less controversial) understanding of energy expenditure and its role in obesity pathogenesis. *Diabetes* **60**, 17–23 (2011).
47. Frayn, K. N. Calculation of substrate oxidation rates in vivo from gaseous exchange. *J. Appl. Physiol.* **55**, 628–634 (1983).

Chapter 5 Discussion and Future Perspectives

This dissertation aimed to address key gaps in our understanding of FPLD2, laminopathies, and lamin A/C biology. Building upon our lab's previous work, we first examined the essential role for lamin A/C in adipocyte homeostasis and fate upon lamin A/C deficiency (**Chapter 2**)[1]. We also analyzed subcutaneous adipose biopsies from patients with FPLD2 to characterize morphological and transcriptional changes associated with disease progression (**Chapter 2**). Then, we tested a novel dual gene therapy treatments to mitigate metabolic dysfunction in lipodystrophic mouse models and evaluated how environmental temperature influenced therapeutic response (**Chapter 3**). Finally, we saw the need for more sophisticated mouse models to study mechanisms of FPLD2 and created seven new mice with global knock-in pathogenic *Lmna* variants that cause disease in humans (**Chapter 4**). In this chapter, I will briefly summarize and synthesize the major findings from Chapter 2 to 4 and highlight future directions for continuing work.

In Chapter 2, we observed that *Lmna*-deficient adipocytes in mice shrink and disappear in a manner consistent with apoptosis, accompanied by compensatory adipogenesis. Lamin A/C KO adipocytes exhibited cell-autonomous reductions in lipid metabolism, particularly in lipogenesis, alongside upregulation of inflammatory genes, reduced mitochondrial respiration, and ultrastructural mitochondrial abnormalities. These signatures were recapitulated in biopsies from patients with FPLD2: both bulk and snRNA-seq revealed decreased lipid metabolism and increased inflammatory gene programs across multiple cell types. Every analyzed cell type showed suppressed OXPHOS and mitochondrial-related gene programs, and pro-inflammatory signatures were especially enriched in adipocytes and T cells. These findings were strikingly conserved between human and mouse WAT, and were also evident in *Lmna* KO MEFs, which had changes in lipid metabolism and inflammatory gene pathways, correlated with alterations in chromatin accessibility. Notably, work from Chapter 4 further supported these signatures, as three *Lmna* variant mouse lines demonstrated transcriptional shifts in lipid metabolism, adipogenesis, mitochondrial function, and inflammation. These cross-species, cross-model

findings suggest a conserved transcriptomic program driving adipocyte loss in FPLD2. Future studies will investigate the molecular basis for these shared transcriptomic programs.

In Chapter 3, we evaluated a dual AAV-delivered gene expressing FGF21 and sTGFBR2 expression to treat metabolic dysfunction in a lipodystrophic mouse model. At thermoneutrality (30°C), FGF21/sTGFBR2 reduced hepatic steatosis but adipose tissue was required to improve insulin resistance. FGF21 administration alone was sufficient to ameliorate hepatic steatosis and insulin resistance in lipodystrophic mice housed at 22°C. Hepatic transcriptomic analyses of FGF21-treated lipodystrophic mice showed increased hepatic mitochondrial metabolism and protein translation pathways and decreased cellular proliferation gene programs. These findings underscore the therapeutic potential of targeting multiple pathways and emphasize the need to account for housing temperature in metabolic studies.

Finally, Chapter 4 introduced seven *Lmna* variant knock-in mouse lines. While most variants did not exhibit overt lipodystrophy, homozygous *Lmna* T10I and obese *Lmna* P485R mice had impaired voluntary running capacity. In *Lmna* T10I and R482Q mice, energy expenditure and fat oxidation were decreased, which may underlie the observed impairment in voluntary running. Transcriptomic analyses of WAT revealed a subtle shift in gene programs related to adipogenesis, protein translation, and inflammation across three different *Lmna* variant mouse lines. Future studies will investigate the basis of impaired voluntary exercise capacity and decreased energy expenditure and fat oxidation, as well as experimental strategies to unmask latent phenotypes in these models.

5.1 Molecular basis of shared transcriptomic signatures in lipodystrophic WAT

One of the most striking observations from this work was the conserved transcriptomic signature of decreased lipid metabolism and mitochondrial gene expression, along with increased immune-related gene programs in *Lmna*^{iADKO} and FPLD2 WAT. In *Lmna* KO MEFs, we observed both up- and downregulation of lipid metabolism and inflammatory-related genes, accompanied by corresponding changes in chromatin accessibility as measured by ATAC-seq (**Chapter 2**). These findings underscore a fundamental role for lamin A/C in regulating chromatin accessibility and gene expression. However, the overlap of differentially-expressed genes across cell culture, mouse, and human models was relatively small, typically only involving two to seven genes per pathway. This likely reflects the differing cell type contexts:

Lmna KO MEFs are fibroblasts, with distinct transcriptional baselines and chromatin landscapes compared to adipocytes.

To better define the molecular drivers of these conserved transcriptional changes in WAT, future experiments should include single nuclei ATAC-seq (snATAC-seq) or single nuclei chromatin immunoprecipitation-sequencing (snChIP-seq). These approaches would allow mapping of chromatin accessibility and lamin A/C-chromatin interactions in both lamin A/C KO and variant models. As part of the LEAD-ABC study, longitudinal WAT biopsies from patients with developing FPLD2 (Group B) will be collected annually over five years, offering a unique opportunity to track chromatin and transcriptional remodeling during disease progression. In the context of limited biopsy material, snATAC-seq is more feasible than snChIP-seq, as less starting material is needed. Integrations of these chromatin accessibility data with our existing snRNA-seq will enable us to determine which differentially accessible regions correspond to changes or stability in gene expression. Importantly, not all open chromatin regions lead to transcriptional activation, thus, combined multi-omic analyses are essential[2]. Our goal is to define regulatory regions that are differentially accessible in WAT harboring *LMNA* variants versus controls, and across distinct *LMNA* variants, as well as across depots (upper neck vs. abdomen). We hypothesize that altered chromatin accessibility at binding sites of lipid metabolism regulators such as *MLXIPL* or *SREBF1,* or mitochondrial regulators like *NRF1/2*, *ERRa,* CREB, or TFAM transcription factors may impair transcription of genes involved in lipogenesis and OXPHOS[3]. Identifying these specific transcriptional regulators and their enhancer landscapes would 1) tell us whether a change in *LMNA* function causes a primary change in chromatin, causing gene expression alterations and 2) whether changes in regulators of lipid metabolism gene expression precede mitochondrial dysfunction, and exactly what cells these changes are occurring in.

In parallel to our lipid and mitochondrial findings, inflammatory transcription factors, like IRFs, NF-kB, AP-1, and STAT family members warrants deeper investigation[4]. A key question is whether lamin A/C directly regulates chromatin accessibility at immune gene loci, thereby priming or restraining inflammation. If loss of functional lamin A/C leads to a primary disruption of immune-related gene regulation, this would explain the robust inflammation that occurs in adipocytes upon lamin A/C deficiency or pathogenic variant. Furthermore, whether

inflammation can cause defects in lipid metabolism or lipogenesis *in vivo* is of particular interest, as this has been shown in cultured 3T3-L1 cells[5,6].

Following chromatin accessibility and gene expression integrations, validation experiments should identify whether transcription factors implicated in lipid metabolism or inflammation are directly misregulated by lamin A/C. ChIP-seq or ChIP-qPCR analyses using antibodies against lamin A/C or B1 will confirm that transcription factor loci do indeed bind to the nuclear lamina. Lamin B1 is often used as a proxy for LAD binding, as antibodies for ChIP are well-validated and lamin B1 is only present at the nuclear periphery, unlike lamin A/C which is also present in the nucleoplasm[7]. These experiments would reveal direct interactions of transcription factor loci with the nuclear lamina and allow analysis of histone marks indicative of enhancer (e.g H3K27ac) or repressor (e.g. H3K27me3) activity. Similar analyses have shown a direct interaction between SREBP1 and lamin A/C, which may be part of the lipogenic gene expression changes we observe upon lamin A/C KO or mutation[8]. CUT&RUN sequencing is a viable alternative to ChIP when tissue is limited, as it requires less input material. CUT&RUN uses an antibody to a relevant target, and a nuclease cleaves the DNA located at the antibody's location to allow for DNA fragmentation purification and sequencing to precisely map DNA-binding protein locations[9]. For this project, important targets would be Additional imaging confirmation would be performed via DNA-FISH, which allows physical location visualization of a particular enhancer or transcription factor within the nucleus – this would reveal nuclear repositioning of a locus either towards or away from the nuclear lamina, which has been a useful tool in other models of lipodystrophy in mice[10].

Once candidate transcription factors or loci are identified through chromatin profiling, gain- or loss-of-function experiments could be performed in cultured human adipocytes from either primary cells or precursors edited to contain *LMNA* variants. For example, knocking out *SREBF1* in *LMNA* R482Q cultured human adipocytes would test whether this deficiency is sufficient to induce mitochondrial dysfunction or inflammation. Conversely, overexpressing *SREBF1* or creating a constitutively active form would assess whether restoration of lipogenic transcriptional signaling is sufficient to rescue mitochondrial dysfunction and/or suppress inflammation. These approaches could be generalized to any transcription factor implicated from ATAC-seq analyses.

Given limitations with human adipose tissue yield, additional mechanistic insights would be gained by using *Lmna*^{iADKO} WAT. We would perform snChIP-seq or bulk ChIP-seq on floated adipocytes from this mouse model, 3-, 7-, 10-, and 14-days post-tamoxifen, using lamin B1 antibodies. This would enable temporal mapping of chromatin-lamina interactions during adipocyte loss. We have previously tried to analyze changes in inflammation, lipid metabolism, and mitochondria protein expression at the timepoints listed above to see which dysfunctional process occurs first, but suppression of lipid metabolism/mitochondria and activation of inflammation occurred simultaneously by 10 days post-tamoxifen. Our ChIP-based analyses would reveal whether changes in chromatin binding at certain transcription factor, enhancer, or repressor loci occurs before 10 days post-tamoxifen, and which loci change first. Imaging-based confirmation via DNA-FISH would further determine whether spatial repositioning of key loci correlates with altered LAD binding. Finally, rescue experiments would be technically easier with the use of *Lmna*^{iADKO} WAT: genetic knockouts or overexpression via AAV would be administered in an adipose-tissue specific manner to evaluate whether restoration (or loss) of a particular gene program could rescue or prevent WAT loss. Identifying early, targetable gene programs before overt tissue loss would offer therapeutic potential for pre-symptomatic patients in FPLD2.

A more nuanced model for studying LMNA function in adipose tissue lies in the seven knock-in variant mouse lines we generated. RNA-seq analysis of three of these models: *Lmna* T10I, R482Q, and P485R, revealed few to no significantly differentially expressed genes in WAT. Despite this, pathway analysis uncovered consistent alterations in gene programs related to adipogenesis, inflammation, OXPHOS, muscle-related genes, and protein translation. The absence of robust differentially-expressed genes may stem from multiple causes. First, the changes within specific WAT cell types, such as adipocytes, may be diluted by transcriptomic stability of other resident cells, reducing statistical power to detect differentially expressed genes in bulk RNA-seq. Second, WAT may be undergoing major compensation: for example, if SREBP1-controlled genes are suppressed in *Lmna* variant WAT, but ChREBP senses the deficiency and responds to upregulate many of the affected genes, the overall transcriptional output may appear unchanged[11–13]. This type of compensatory regulation could mask gene-level differences, despite alterations in regulatory networks.

Given these limitations, snATAC-seq represents a more powerful strategy to investigate molecular changes in *Lmna* variant WAT. This approach reveals broad changes in chromatin accessibility, rather than mapping physical interactions between chromatin and the nuclear lamina, as these may not be changed. snATAC-seq would be particularly insightful in detecting accessibility changes without transcriptional changes, pointing to regulatory priming, in which chromatin structure would be modified before transcription occurs[14]. Furthermore, changes in chromatin accessibility would occur at silencer or gene-poor regions that are not directly tied to active gene expression, of which characterizes the majority of LADs[15]. Additionally, opposing changes in accessibility at enhancer and promoter regions within the same gene locus would neutralize transcriptional output, explaining the lack of differentially expressed genes despite regulatory remodeling. Performing snATAC-seq on *Lmna* variant WAT would thus provide critical insight into epigenetic and architecture changes that precede or accompany transcriptomic remodeling. Integration with human biopsy snATAC-seq would highlight conserved and species-specific responses to lamin A/C dysfunction. Though 96% of the amino acid sequence is conserved between mice and human LMNA, only human *LMNA* variants consistently cause lipodystrophy. Perhaps lamin A/C has different roles in mouse adipocyte maintenance versus human adipocytes, or there are stronger compensatory mechanisms to help prevent WAT transcriptomic changes and eventual lipodystrophy in mice. Taken together, chromatin accessibility profiling, especially snATAC-seq, offers a powerful approach to uncover regulatory alterations in *Lmna* variant WAT that may not manifest as differentially-expressed genes. This will reveal molecular underpinnings of lamin A/C genome control in WAT across species and would guide future investigation into LAD remodeling or alternative mechanisms of adipocyte loss, as discussed in the next section.

5.2 Other unexplored potential mechanisms of adipocyte loss in FPLD2

Whilst a significant portion of this dissertation has focused on chromatin architecture and gene regulation as the primary mechanisms of adipocyte and cellular dysfunction in FPLD2, it would be remiss to not explore other cellular disruptions beyond chromatin remodeling, as lamin A/C has diverse roles in nuclear and cellular biology (as detailed in Chapter 1).

Several lamin-binding partners reside in the inner nuclear membrane, including transmembrane proteins (TMEMs) classified as NETs. Of these, multiple TMEMs were downregulated in our *Lmna*^{iADKO} dataset, including *Tmem120a*, which has been previously

implicated in lipodystrophy[10]. Adipocyte-specific *Tmem120a* KO mice show reduced WAT mass and insulin resistance under HFD conditions. Loss of *Tmem120a* disrupts genome organization and induces myogenic gene expression through enhancer repositioning[10]. These findings suggest that adipocytes dysfunction may also be driven by loss of key chromatin regulators beyond lamin A/C itself. *Tmem120a* is proposed to function as a mechanosensitive ion channel involved in coenzyme A transport, highlighting its diverse roles beyond chromatin regulation[16].

We also identified changes in gene expression of several NETs in *Lmna*^{iADKO} WAT, like emerin (log2fold change (FC) 0.245), lamin B receptor (log2FC 0.197), SUN1 (log2FC -0.209), SUN2 (log2FC -0.174), and lamina-associated polypeptide 2 beta (LAP2b) (log2FC 0.177). Although these changes are modest, even subtle alterations in inner nuclear membrane components have potential to disturb nuclear integrity and signaling. SUN1 downregulation in human adipocyte precursors impairs adipogenesis, partially due to reduced nuclear localization of PPARg[17]. The lamin B receptor is essential for cholesterol synthesis[18] and emerin KO enhances adipogenesis[19], suggesting that altered NET expression would contribute to adipocyte dysfunction. Future experiments may include double KO mouse models of *Lmna* and other NETs like emerin or SUN1 or AAV-mediated overexpression in WAT to assess whether modulation of NETs exacerbates or rescues the lipodystrophic phenotype.

Lamin A/C also associates with NPC components, and its dysfunction weakens interactions between nucleoporins and the nuclear lamina[20]. Lamin loss can result in NPCs mislocalization[21]. While these studies did not assess NPC function directly, disrupted lamina-NPC interactions would plausibly impair nucleocytoplasmic transport. In *Lmna*^{iADKO} WAT, six nucleoporin transcripts are significantly upregulated, hinting at NPC remodeling in disease progression. Functional assays are needed to determine whether nuclear transport is compromised. One example of this would include floating adipocytes from *Lmna*$^{fl/fl}$ and *Lmna*^{iADKO} WAT at multiple timepoints post-tamoxifen and performing subcellular fractionation to evaluate nuclear versus cytoplasmic localization of proteins like STATs, ChREBP, or SREBP1 via immunoblotting. An alternative *in vitro* approach would be to study *Lmna* KO or variant ear mesenchymal stem cells (eMSCs) differentiated into adipocytes, with expression of a tagged GFP with either a nuclear localization signal or a nuclear export signal: localization of this GFP can be measured via live cell imaging. If there is mislocalization of either GFP, we can conclude that import or export to/from the nucleus is disrupted[22]. Study of nuclear transport upon

Lmna variant or KO would reveal valuable insight into how lamin A/C disruption affects broader cellular signaling and transcript trafficking.

Lamin A/C connects to the cytoskeleton via the LINC complex to sense and respond to cellular mechanical stresses. As detailed in Chapter 1, multiple studies have shown disruptions in microtubule organization, actin stress fibers, and mechanosensing upon *Lmna* KO *in vitro*. In our hands, mechanical stress applied to *Lmna* KO differentiated eMSCs did not cause an increase in cell death or nuclear damage compared to controls (data not shown). However, further studies are required to analyze whether LINC complexes or the cytoskeleton are disrupted in *Lmna* KO or variant adipocytes, which may also contribute to cellular dysfunction. As mentioned above, SUN1/2 proteins were modestly downregulated in *Lmna*^{iADKO} WAT, but nesprin proteins, another LINC complex component, were not changed in expression. Immunofluorescence for actin, LINC components, and cytoskeletal markers in *Lmna*^{iADKO} or variant WAT paraffin sections would reveal whether structural changes occur. Atomic force microscopy can measure mechanical properties of primary adipocytes or of isolated adipocyte nuclei to measure nuclear elasticity and stiffness[23,24]. Mechanical stress and force transmission assays *in vitro* would be applied to *Lmna* KO or variant cultured adipocytes. Though we saw no change in nuclear damage after mechanical stress experiments previously in *Lmna* KO adipocytes, the type of cyclical tension applied to the adipocytes may not have been sufficient to cause damage. Other types of mechanical stresses include compression or by tuning substrate stiffness (of hydrogels or extracellular matrix components) *in vitro*, which would be accompanied by assessment of nuclear damage or cytoskeleton reorganization via immunofluorescence staining. In summary, disruption of nuclear health upon *Lmna* KO or variant, including altering chromatin architecture, nuclear transport, or mechanical stress, would contribute to adipocyte loss in FPLD2, which should be followed up on in the future.

5.3 How do *Lmna*-deficient adipocytes eventually disappear and die?

Our findings show that *Lmna* KO adipocytes delipidate, shrink, and disappear by six weeks post-knockout. Most of our mouse work focused on characterizing the early triggering events that preceded adipocyte loss, as this is analogous to the "developing FPLD2" patient state we also studied. However, the terminal fate of shrunken and disappearing adipocytes remains unclear.

The shrunken shape and intact membrane of *Lmna* KO adipocytes is consistent with apoptosis. Typically, apoptosis does not cause inflammation, and is accompanied by membrane blebbing, condensed chromatin, and cleaved caspase expression[25]. While we observed membrane blebbing and potential hints of chromatin condensation in our *Lmna* KO adipocytes, we were not able to cleaved caspase 3 in *Lmna*^{iADKO} WAT, potentially due to the asynchronous nature of cell death or a low proportion of dying adipocytes. It is still largely unknown how adipocytes die, but irradiation-induced cell death of adipocytes caused macrophage recruitment and crown-like structure formation[26]. Alternatively, activation of caspase 8 in adipocytes (FAT-ATTAC mice) caused adipocyte death which that was non-inflammatory[27]. In our model, we see that *Lmna* KO adipocytes have cell-autonomous upregulation of inflammatory genes, no increase in macrophage or T cell activation, and no formation of crown-like structures[1].

Future experiments should prioritize identifying the specific cell death pathways involved. This would include fluorescent-activated cell sorting (FACS) analyses on *Lmna*^{iADKO} mTmG WAT to isolate the GFP+ adipocytes (KO) versus the tdTomato+ (intact lamin A/C) for subsequent proteomics analyses to identify any cell death signatures in the GFP+ adipocytes. Immunofluorescence staining on WAT sections would assess cleaved caspase 3/7/9 or utilize a TUNEL assay for apoptosis, RIPK1/3 for necroptosis, caspase 1 for pyroptosis or GPX4 for ferroptosis. We have previously performed immunoblots for GPX4 in total *Lmna*^{iADKO} WAT and saw no difference compared to controls (data not shown). Ultrastructural analyses via TEM would distinguish between forms of cell death: chromatin condensation and apoptotic bodies for apoptosis, organelle swelling and nuclear rupture in necroptosis, or increased autophagic vesicles for autophagy-associated cell death. While TEM quantification is challenging, systematic analysis of multiple timepoints post-tamoxifen would help resolve the sequence and nature of adipocyte death. In summary, although our work focused on early cellular stressors triggered by *Lmna* deficiency, future work should elucidate the precise mechanisms underlying adipocyte death. These insights will be essential for linking the transcriptomic and epigenetic stress responses we observed to the eventual disappearance of adipocytes in both mouse models and FPLD2 patient tissue.

5.4 Is FGF21/sTGFBR2 gene treatment a viable option for patients with FPLD2?

In Chapter 3, we evaluated a dual gene therapy using AAV-mediated delivery of FGF21 and sTGFBR2 to ameliorate metabolic dysfunction in a mouse model of FPLD2. This treatment

significantly improved hepatic steatosis, hyperlipidemia, and insulin resistance in obese mice, and showed therapeutic promise in the context of lipodystrophy[28]. However, this study raises two key questions: 1) is AAV-mediated gene therapy a feasible therapeutic option in humans, and 2) is FGF21/sTGFBR2 a viable target for treating FPLD2 in patients?

Several AAV-based therapies are already approved by the Food and Drug Administration for conditions such as spinal muscular atrophy, retinal dystrophies, and hemophilia[29]. AAVs offer tissue specificity, long-term expression, and a relatively favorable safety profile. However, challenges remain, including pre-existing immunity to AAV serotypes and high manufacturing costs. Still, more than 200 clinical trials are ongoing to utilize AAV-based gene therapies in a wide variety of diseases, including muscular dystrophy, cardiomyopathy, and neurological diseases[29]. Importantly, preclinical studies of lipodystrophy have demonstrated therapeutic benefit from AAV delivery. For instance, AAV-mediated *BSCL2* restoration in CGL mice, improved metabolic health[30]. Therefore, gene therapy is a potential option for treatment of diseases like FPLD2 and other laminopathies, particularly when the target gene (e.g. FGF21) can modulate multiple aspects of disease physiology.

FGF21 has been studied extensively and shown to improve insulin sensitivity, lower liver fat, and reduce inflammation in both rodent and primate models of metabolic disease[31–34]. Several FGF21 analogs have entered clinical trials in humans, where they improved hepatic steatosis and insulin sensitivity, particularly in patients with non-alcoholic steatohepatitis or cirrhosis[35]. The combination of FGF21 with an anti-TGFb strategy (sTGFBR2) would offer synergistic effects – improving insulin sensitivity while reducing fibrosis and inflammation, as we observed in mice. However, safety considerations are essential. FGF21 has been associated with bone loss in some studies, which should be of concern, especially in post-menopausal women[36–38]. The most frequent adverse events reported in trials of FGF21 analogs are gastrointestinal issues or injection-site reactions[35]. Similarly, drugs that target TGFb1 show promise as an anti-fibrotic therapy, but side effects include potential spontaneous autoimmunity and impaired wound healing[39]. These side effects would need to be thoroughly evaluated in preclinical and clinical settings.

Our preclinical model of FPLD2 and trials of dual gene therapy were enlightening in understanding the potential for FGF21/sTGFBR2 treatment in lipodystrophy. Further mouse experiments should be focused on better characterizing mechanisms of FGF21 and sTGFBR2 in

improving hepatic steatosis and insulin resistance. Liver transcriptomic data from FGF21-treated lipodystrophic mice showed that FGF21 decreased cellular proliferation, a likely mechanism for decreasing liver weights after FGF21 treatment. However, the precise mechanism by which hepatic lipids are cleared remains unsolved. Surprisingly, we observed increased sterol biosynthesis in FGF21-treated lipodystrophic livers, which was unexpected given the loss of hepatic lipid accumulation. In other studies, FGF21 has been shown to decrease *de novo* lipogenesis and increase fatty acid oxidation, contributing to improved hepatic steatosis in obese mice[40]. Does this same mechanism happen in mice with lipodystrophy? Further molecular analyses of expression of lipogenic and fatty acid oxidation-related proteins would help clarify this. Furthermore, indirect calorimetry studies of treated vs. untreated lipodystrophic mice would reveal whether changes in whole-body energy expenditure and fat oxidation contribute to metabolic improvements.

Although our dual gene therapy improved hepatic and systemic parameters, adipose tissue did not show robust improvement, as leptin and adiponectin levels remained low. It remains unclear whether adipocyte gene expression programs, particularly those related to lipogenesis or mitochondrial function, are partially restored. Extended treatment durations or later timepoints post-AAV delivery may be needed to detect subtle improvements. WAT should be evaluated histologically and via RNA-seq to confirm any restoration of health. Future experiments should also compare monotherapies (FGF21 or sTGFBR2) against the dual treatment to disentangle their respective contributions to efficacy and side effects. Such comparisons would refine our mechanistic understanding and may allow for more tailored treatment strategies based on patient phenotype or disease stage. Taken together, AAV-based delivery of FGF21 and sTGFBR2 holds promise as a treatment strategy for FPLD2. FGF21 is already under clinical investigation for other metabolic conditions, and gene therapy offers a durable delivery platform. However, further preclinical studies are needed to dissect individual versus synergistic effects of FGF21 and sTGFBR2 and assess safety profiles. FGF21/sTGFBR2 gene therapy would become a viable and impactful approach to treating the metabolic complications of FPLD2.

5.5 Impaired exercise capacity in *Lmna* T10I variant mice

In Chapter 4, we observed a consistent phenotype in *Lmna* variant mouse models, biallelic T10I and HFD-fed P485R mice, both of which demonstrated reduced voluntary running

capacity. Interestingly, grip strength was unaffected, suggesting that maximal muscular strength remains intact. This phenotype mirrors clinical observations in patients with lipodystrophy, particularly those with CGL, who frequently report fatigue and pain with endurance exercise[41,42]. In the case of FPLD2, this reduced exercise tolerance may stem from impaired fat oxidation during energy-demanding states. However, given the involvement of *LMNA* in both muscular and cardiac laminopathies, we cannot exclude the possibility that these variants have primary effects on skeletal muscle or cardiac tissue.

To determine whether reduced running in *Lmna* T10I or P485R mice reflects physical limitation versus behavioral aversion, treadmill-based endurance testing should be performed. Using a no incline treadmill set at average speed typical to what mice run on a voluntary running wheel (~2-4 km/hour), we can evaluate whether these mice are unable to sustain prolonged endurance running, or whether they are choosing not to run. Following this assessment, if homozygous variant mice have confirmed endurance impairment, muscle phenotyping should follow. This should include evaluating changes in muscle fiber composition via immunofluorescence in various skeletal muscles, like the gastrocnemius, soleus, and tibialis anterior muscles. A shift from oxidative (Type I and Type IIa fibers) to glycolytic fibers (Type IIb), would explain decreased endurance running[43]. Careful histological analyses of skeletal muscle would reveal features of muscle pathology, including increased fiber size variability, muscle fibrosis, or localization of myonuclei towards the fiber center, signs of muscle dysfunction or muscular dystrophy[44,45]. Finally, direct measurements of contractile force from individual muscle fibers mounted to a force transducer would elucidate whether muscle weakness underlies reduced exercise[46]. Bulk RNA-sequencing and ATAC-sequencing in parallel may be a helpful tool to determine if muscle integrity and homeostasis is decreased, which may reveal, for example, reductions in mitochondrial genes or other regulators of muscle homeostasis. Comparative transcriptomic and epigenomic analyses across multiple tissues in *Lmna* variant mice, such as adipose, skeletal muscle, and cardiac tissue, versus tissues typically spared in laminopathies, would reveal molecular mechanisms underlying the tissue-specific manifestations of these diseases.

Cardiovascular impairments would also cause decreased running, including reduced heart contractility, arrythmias, heart fibrosis, or conduction abnormalities. To assess these in *Lmna* variant mice, electrocardiography would be performed to assess conduction capacity or presence

of arrythmias. Additionally, echocardiograms would identify changes in heart chamber sizes, valve anatomy, and contractile function. Furthermore, histology would determine whether *Lmna* variant mice have cardiomyopathy or fibrosis deposition. Patients harboring the *Lmna* T10I variant often have cardiomyopathy, so further study of the cardiovascular system in these mice are warranted[47].

In *Lmna* T10I mice, forced treadmill assays did not reveal a decrease in maximum running capacity. This fast-paced assay requires considerable coordination by mice, but coordination can be further tested via the Rotarod assay, which evaluates motor coordination and balance in mice. Furthermore, mice would undergo a pole test, which assess locomotion and motor coordination as they climb down a pole, or would walk across a horizonal bar, which would test balance and coordination[48,49]. Subtle changes in coordination, though not expected in our *Lmna* variant mice, would lead to reduced voluntary running. We should also consider the potential for decreased motivation or desire to run. Laboratory mice are known to have a strong desire to run, with a range of 5 to 30 km per day – this would be reduced with a behavioral issue[50]. Tests like the progressive ratio task in which mice have to exert increasing amounts of work to earn an award, would measure reward seeking in variant mice[51]. Furthermore, a forced swim test would determine whether mice have decreased motivation or depressive-like symptoms if they have a higher duration of immobile/non-swimming time[52]. Finally, anxiety-like behaviors can be tested by the open field test – perhaps *Lmna* variant mice have increased anxiety when singly housed and in a novel environment[53]. Taken together, further investigations into underlying causes for decreased exercise would elucidate molecular underpinnings of decreased endurance exercise capacity in patients with FPLD2.

Another possibility is that *Lmna* variant mice experience heightened peripheral pain, which discourages running. To test this, mechanical or heat stimuli can be administered to mice, with behavioral responses such as limb withdrawal, vocalization, or grooming interpreted as pain-like behavior[54]. Given that *LMNA* variants can also cause peripheral neuropathy, sensory neuron function and integrity should also be evaluated[55]. Histological or molecular analyses of dorsal root ganglia or peripheral nerves may provide insights into sensory dysfunction.

Notably, *Lmna* T10I mice exhibit reduced fat oxidation and energy expenditure, which coincides with the observed running phenotype. Similar features were observed in *Lmna* R482Q mice, even in the absence of wheel access, suggesting a potential metabolic defect. Therefore, we

should determine whether reduced voluntary running is secondary to an impaired substrate utilization. Measurements of lactate, glucose, free fatty acids, and ketones before, during, and after forced running would be of particular interest. Elevated lactate would suggest increased glycolysis, and reduced ketones or free fatty acids may reflect impaired fat utilization[56]. To distinguish whether this defect lies in lipid mobilization versus oxidation, mitochondrial function assays such as Seahorse or Oroboros Oxygraph-2K analyses should be performed on isolated adipocytes, skeletal muscle, or purified mitochondria. This would assess oxygen consumption and respiratory capacity with various substrates. Finally, quantification of protein expression in cardiac tissues and skeletal muscle would reveal whether key transporters (e.g. GLUT4, CD36) are impaired. Taken together, *Lmna* variant mice, particularly those harboring the T10I variant, display impaired endurance capacity. This phenotype would arise from multiple overlapping mechanisms, including skeletal muscle or cardiac dysfunction, altered substrate metabolism, neuropathy, or motivational deficits. Comprehensive phenotyping encompassing exercise physiology, muscle and cardiac function, mitochondrial biology, and behavioral neuroscience is necessary to elucidate the molecular underpinnings of this complex trait. These investigations may ultimately reveal conserved mechanisms driving exercise intolerance in patients with FPLD2 and other laminopathies.

5.6 How can we trigger lipodystrophy in *Lmna* variant mice?

A notable, though often classified as a "negative" finding, is that *Lmna* variant mice do not exhibit obvious signs of FPLD2. Although P485R and N582H mice may be exceptions, our highly studied mouse variants do not lose much adipose tissue, if any, and do not develop metabolic dysfunction. This observation brings up multiple questions: 1) why do *Lmna* variant mice not develop lipodystrophy? 2) Is there a secondary trigger required to unmask lipodystrophy in the presence of pathogenic *Lmna* variants? These questions reflect another major unanswered question in the field: what initiates FPLD2? Onset is often coincident with puberty but can vary widely in timing, suggesting that lamin A/C dysfunction may require an external or developmental cue to manifest as lipodystrophy.

One explanation is the inherent physiological differences between mice and humans. Although human and mouse LMNA are highly conserved at the sequence level, there may be specific differences in assembly, post-translational modifications, chromatin interactions, or their binding partners and function. Though these differences have yet to be uncovered, this may be

informative for basic lamin biology studies. Utilization of high-resolution scanning electron microscopy may reveal fundamental structural differences between the mouse and human nuclear lamina. As detailed in Chapter 1, other models of laminopathies often phenocopy human diseases in mice, including muscular dystrophies and cardiomyopathies. Mouse adipose tissue is likely able to compensate for the presence of knock-in point mutations, which should be kept in mind for future studies of lipodystrophy. As detailed in the beginning of this chapter, comparative snATAC-seq analyses of mouse and human WAT may reveal chromatin accessibility or enhancer landscape differences that underpin these compensatory mechanisms.

Importantly, there may be unknown environmental triggers that are necessary to induce lipodystrophy. Unlike humans, laboratory mice are raised in a tightly controlled environment, with enrichment, group housing, consistent environmental temperature, and consistent access to food and water, with minimal physical or psychological stressors. In contrast, humans experience developmental, metabolic, mechanical, and environmental fluctuations that potentially interact with *LMNA* mutations to trigger lipodystrophy. These include pubertal hormonal shifts, fluctuations in environmental temperature and humidity, infection or immune challenges, exercise, diets, psychological stress, mechanical stress (e.g. sitting, stretching). It is plausible that such multifactorial stressors precipitate adipose tissue loss in genetically predisposed individuals. In this context, *Lmna* variant mice may require specific "secondary hits" to phenocopy FPLD2. Future studies would introduce variables such as cold exposure or thermogenic stress, low-grade inflammation, mechanical stress, and corticosterone administration. Additionally, genetic background likely influences disease penetrance. Humans are genetically heterogenous, while most *Lmna* variant mouse models are maintained on inbred strains. Breeding *Lmna* pathogenic variant mice onto an outbred backgrounds may unmask lipodystrophy phenotypes. In summary, the absence of lipodystrophy in *Lmna* variant mice likely reflects a combination of species-specific differences, compensatory mechanisms, and absence of environmental stressors. Triggering lipodystrophy may require combinatorial approaches that incorporate physiological and environmental challenges.

5.7 Final remarks

The findings presented in this dissertation extend beyond FPLD2, offering insights into broader mechanisms underlying lipodystrophies and laminopathies. This work underscores the essential role of lamin A/C in maintaining adipocyte homeostasis and highlights the value of

integrating patient-derived samples into mechanistic research. Our studies demonstrate both the promise and limitations of mouse models in recapitulating human diseases and emphasize the importance of studying human tissue to identify relevant biological pathways and therapeutic targets. Through the development and analysis of novel mouse models and the assembly of the largest known biopsy cohort of patients with FPLD2, we uncovered molecular mechanisms driving disease pathogenesis in both species. These findings lay the groundwork for future studies and therapeutic advances that we hope will translate into meaningful clinical advances. Our ultimate goal is that this work contributes not only to the scientific understanding of lamin A/C dysfunction, but also to improve outcomes and quality for life of patients affected by FPLD2 and laminopathies.

5.8 References

1. Corsa, C. A. S. *et al.* Adipocyte-specific deletion of lamin A/C largely models human familial partial lipodystrophy type 2. *Diabetes* (2021) doi:10.2337/db20-1001.
2. Maynard, S. *et al.* Lamin A/C impairments cause mitochondrial dysfunction by attenuating PGC1α and the NAMPT-NAD+ pathway. *Nucleic Acids Res.* gkac741 (2022) doi:10.1093/nar/gkac741.
3. Lee, J., *et al.* Mitochondrial Nuclear Receptors and Transcription Factors: Who's Minding the Cell? *J. Neurosci. Res.* **86**, 961–971 (2008).
4. Ahmed, A. U., *et al* . Transcriptional Activation of Inflammatory Genes: Mechanistic Insight into Selectivity and Diversity. *Biomolecules* **5**, 3087–3111 (2015).
5. Beutler, B. *et al.* Identity of tumour necrosis factor and the macrophage-secreted factor cachectin. *Nature* **316**, 552–554 (1985).
6. Torti, F. M., *et al*. A macrophage factor inhibits adipocyte gene expression: an in vitro model of cachexia. *Science* **229**, 867–869 (1985).
7. Shah, P. P. *et al.* Pathogenic LMNA variants disrupt cardiac lamina-chromatin interactions and de-repress alternative fate genes. *Cell Stem Cell* **28**, 938-954.e9 (2021).
8. Lloyd, D. J., *et al*. A novel interaction between lamin A and SREBP1: implications for partial lipodystrophy and other laminopathies. *Hum. Mol. Genet.* **11**, 769–777 (2002).
9. Kong, N. R., *et al*. A modified CUT&RUN protocol and analysis pipeline to identify transcription factor binding sites in human cell lines. *STAR Protoc.* **2**, 100750 (2021).
10. Czapiewski, R. *et al.* Genomic loci mispositioning in Tmem120a knockout mice yields latent lipodystrophy. *Nat. Commun.* **13**, 321 (2022).
11. Song, Z. *et al*. Regulation and Metabolic Significance of De Novo Lipogenesis in Adipose Tissues. *Nutrients*. **10**, 1383 (2018).
12. Crewe, C. *et al.* SREBP-regulated adipocyte lipogenesis is dependent on substrate availability and redox modulation of mTORC1. *JCI Insight* **4**, (2019).
13. Witte, N. *et al.* The Glucose Sensor ChREBP Links De Novo Lipogenesis to PPARγ Activity and Adipocyte Differentiation. *Endocrinology* **156**, 4008–4019 (2015).
14. Maytum, A. *et al.* Chromatin priming elements direct tissue-specific gene activity before hematopoietic specification. *Life Sci. Alliance* **7**, e202302363 (2023).
15. Yáñez-Cuna, J. O. & van Steensel, B. Genome–nuclear lamina interactions: from cell populations to single cells. *Curr. Opin. Genet. Dev.* **43**, 67–72 (2017).
16. Rong, Y. *et al.* TMEM120A contains a specific coenzyme A-binding site and might not mediate poking- or stretch-induced channel activities in cells. *eLife* **10**, e71474.
17. Fan, T. *et al.* SUN1 inhibits osteogenesis and promotes adipogenesis of human adipose-derived stem cells by regulating α-tubulin and CD36 expression. *J. Cell. Mol. Med.* **28**, e70143 (2024).
18. Tsai, P.-L., *et al*. The Lamin B receptor is essential for cholesterol synthesis and perturbed by disease-causing mutations. *eLife* **5**, e16011.

19. Tilgner, K., *et al*. Dynamic complexes of A-type lamins and emerin influence adipogenic capacity of the cell via nucleocytoplasmic distribution of beta-catenin. *J. Cell Sci.* **122**, 401–413 (2009).
20. Han, M. *et al.* Lamin A mutation impairs interaction with nucleoporin NUP155 and disrupts nucleocytoplasmic transport in atrial fibrillation. *Hum. Mutat.* **40**, 310–325 (2019).
21. Guo, Y. & Zheng, Y. Lamins position the nuclear pores and centrosomes by modulating dynein. *Mol. Biol. Cell* **26**, 3379–3389 (2015).
22. Lu, J. *et al.* Types of nuclear localization signals and mechanisms of protein import into the nucleus. *Cell Commun. Signal.* **19**, 60 (2021).
23. Haase, K. & Pelling, A. E. Investigating cell mechanics with atomic force microscopy. *J. R. Soc. Interface* **12**, 20140970 (2015).
24. Shoham, N. *et al.* Adipocyte Stiffness Increases with Accumulation of Lipid Droplets. *Biophys. J.* **106**, 1421–1431 (2014).
25. Zubair, M. & Bokhari, S. R. A. Apoptosis. in *StatPearls [Internet]* (StatPearls Publishing, 2025).
26. Lindhorst, A. *et al.* Adipocyte death triggers a pro-inflammatory response and induces metabolic activation of resident macrophages. *Cell Death Dis.* **12**, 579 (2021).
27. Pajvani, U. B. *et al.* Fat apoptosis through targeted activation of caspase 8: a new mouse model of inducible and reversible lipoatrophy. *Nat. Med.* **11**, 797–803 (2005).
28. Davidsohn, N. *et al.* A single combination gene therapy treats multiple age-related diseases. *Proc. Natl. Acad. Sci. U. S. A.* **116**, 23505–23511 (2019).
29. Wang, J.-H., *et al*. Adeno-associated virus as a delivery vector for gene therapy of human diseases. *Signal Transduct. Target. Ther.* **9**, 78 (2024).
30. Tiwari, M. *et al.* Preclinical evaluation of tissue-selective gene therapies for congenital generalised lipodystrophy. *Gene Ther.* **31**, 445–454 (2024).
31. Anderson, J. M. *et al.* Long-term effects of a fat-directed FGF21 gene therapy in aged female mice. *Gene Ther.* **31**, 95–104 (2024).
32. Geng, L., *et al*. The therapeutic potential of FGF21 in metabolic diseases: from bench to clinic. *Nat. Rev. Endocrinol.* **16**, 654–667 (2020).
33. Jimenez, V. *et al.* Reversion of metabolic dysfunction-associated steatohepatitis by skeletal muscle-directed FGF21 gene therapy. *Mol. Ther. J. Am. Soc. Gene Ther.* **32**, 4285–4302 (2024).
34. Xu, J. *et al.* Acute glucose-lowering and insulin-sensitizing action of FGF21 in insulin-resistant mouse models--association with liver and adipose tissue effects. *Am. J. Physiol. Endocrinol. Metab.* **297**, E1105-1114 (2009).
35. Harrison, S. A., *et al*. FGF21 agonists: An emerging therapeutic for metabolic dysfunction-associated steatohepatitis and beyond. *J. Hepatol.* **81**, 562–576 (2024).
36. Wei, W. *et al.* Fibroblast growth factor 21 promotes bone loss by potentiating the effects of peroxisome proliferator-activated receptor γ. *Proc. Natl. Acad. Sci. U. S. A.* **109**, 3143–3148 (2012).
37. Tang, Y. & Zhang, M. Fibroblast growth factor 21 and bone homeostasis. *Biomed. J.* **46**, 100548 (2023).
38. Li, X. *et al.* FGF21 Is Not a Major Mediator for Bone Homeostasis or Metabolic Actions of PPARα and PPARγ Agonists. *J. Bone Miner. Res.* **32**, 834–845 (2017).
39. Varga, J. & Pasche, B. Anti-TGF-ß therapy in fibrosis: recent progress and implications for systemic sclerosis. *Curr. Opin. Rheumatol.* **20**, 720–728 (2008).

40. Coskun, T. *et al.* Fibroblast growth factor 21 corrects obesity in mice. *Endocrinology* **149**, 6018–6027 (2008).
41. Dantas de Medeiros, J. L. *et al.* Impaired functional exercise capacity and greater cardiovascular response to the 6-min walk test in congenital generalized lipodystrophy. *BMC Cardiovasc. Disord.* **22**, 384 (2022).
42. Akinci, B., *et al*. Phenotypic and Genetic Characteristics of Lipodystrophy: Pathophysiology, Metabolic Abnormalities, and Comorbidities. *Curr. Diab. Rep.* **18**, 143 (2018).
43. Booth, F. W. & Thomason, D. B. Molecular and cellular adaptation of muscle in response to exercise: perspectives of various models. *Physiol. Rev.* **71**, 541–585 (1991).
44. Cotta, A. *et al.* Muscle biopsy essential diagnostic advice for pathologists. *Surg. Exp. Pathol.* **4**, 3 (2021).
45. Bonne, G., *et al*. Emery-Dreifuss Muscular Dystrophy. in *GeneReviews®* (eds. Adam, M. P. et al.) (University of Washington, Seattle, Seattle (WA), 1993).
46. Bonetto, A., *et al*. Assessment of muscle mass and strength in mice. *BoneKEy Rep.* **4**, 732 (2015).
47. Hussain, I. *et al.* A Novel Generalized Lipodystrophy-Associated Progeroid Syndrome Due to Recurrent Heterozygous LMNA p.T10I Mutation. *J. Clin. Endocrinol. Metab.* **103**, 1005–1014 (2018).
48. Deacon, R. M. J. Measuring motor coordination in mice. *J. Vis. Exp. JoVE* e2609 (2013) doi:10.3791/2609.
49. Eltokhi, A., *et al*. Comprehensive characterization of motor and coordination functions in three adolescent wild-type mouse strains. *Sci. Rep.* **11**, 6497 (2021).
50. Goh, J. & Ladiges, W. Voluntary Wheel Running in Mice. *Curr. Protoc. Mouse Biol.* **5**, 283–290 (2015).
51. Cambre, E., *et al*. Measuring Motivation Using the Progressive Ratio Task in Adolescent Mice. *Curr. Protoc.* **3**, e776 (2023).
52. Can, A. *et al.* The Mouse Forced Swim Test. *J. Vis. Exp. JoVE* 3638 (2012) doi:10.3791/3638.
53. Seibenhener, M. L. & Wooten, M. C. Use of the Open Field Maze to Measure Locomotor and Anxiety-like Behavior in Mice. *J. Vis. Exp. JoVE* 52434 (2015) doi:10.3791/52434.
54. Deuis, J. R., *et al*. Methods Used to Evaluate Pain Behaviors in Rodents. *Front. Mol. Neurosci.* **10**, 284 (2017).
55. Larson, C. M., *et al*. The Study of Pain in Rats and Mice. *Comp. Med.* **69**, 555–570 (2019).
56. Lønbro, S. *et al.* Reliability of blood lactate as a measure of exercise intensity in different strains of mice during forced treadmill running. *PLOS ONE* **14**, e0215584 (2019).